Development of 3D Background Oriented Schlieren with a Plenoptic Camera

by

Abhishek Bichal

A dissertation submitted to the Graduate Faculty of
Auburn University
in partial fulfillment of the
requirements for the Degree of
Doctor of Philosophy

Auburn, Alabama
August 01, 2015

Keywords: Tomographic Density Measurement, Background Oriented Schlieren, Plenoptic
Camera, Depth Perception, Three-dimensional

Approved by

Brian Thurow, Chair, Associate Professor of Aerospace Engineering
Anwar Ahmed, Professor of Aerospace Engineering
Roy Hartfield, Professor of Aerospace Engineering
Bertram Zinner, Associate Professor of Mathematics and Statistics

Abstract

This dissertation investigates a novel idea of implementing background oriented schlieren (BOS) with a plenoptic camera along with its application for 3-dimensional (3D) density measurement and for depth perception (DP) of inhomogeneous structures in an inhomogeneous flow field. In the process, the mathematical implementation of BOS was reworked to address the sensitivity of the measurement technique when used in constrained laboratory conditions. The current equation describing the BOS analysis suggests that the sensitivity of the BOS measurement technique is a function of the focal length of the lens used on the camera. When the conditions of a laboratory were imposed on the BOS experiment, it was found that the f-number on the lens of the camera and the circle of confusion used in setting up the experiment influenced the sensitivity of the experiment. This dissertation also provides guidelines for setting up an effective BOS experiment in a laboratory. Plenoptic cameras are light field based cameras that capture light fields and the images are called plenoptic images. These images once captured can be computationally processed after the fact to generate multiple perspective views. For the first time, in this dissertation, the idea of implementing BOS with the plenoptic camera was explored. The major advantages of BOS with a plenoptic camera is that, multiple perspective are captured with a single camera and the ease with which they are captured. The multiple perspective views obtained from BOS with a plenoptic camera show disparity in the captured images which results in the disparity of the BOS data generated from these images. The ability to generate multiple perspective views from a single plenoptic image and the disparity between them were used in the development of the DP and 3D density measurement capabilities of the BOS with a plenoptic camera. The DP capability of the BOS with a plenoptic camera was successfully demonstrated by measuring the location of a cone shock with less than 3% error. The cone shock was generated with a

cone placed in a Mach 2.0 flow. The 3D density measurement capability was demonstrated with both simulated and physical experiments. From these experiments, it was learned that the BOS with a plenoptic camera can accurately measure the 3D density distribution of an inhomogeneous flow field as long as the angle between the inhomogeneous structure and the optical axis of the camera is in the range of the viewing angles of the camera. But, as all the perspective views generated from the plenoptic image are captured through the aperture of the camera lens, the range of the viewing angles obtained in the perspectives is small. This small range of viewing angles limits the 3D density measurement applicability of the BOS with a plenoptic camera.

Acknowledgments

The work presented in this dissertation was made possible with the help of many people. I want to take this opportunity to acknowledge and offer my sincerest gratitude to them.

I want to thank Dr. Brian Thurow, for his patience, guidance, support, knowledge, and expertise throughout my PhD program. I want to express my gratitude to Dr. Anwar Ahmed and Dr. Roy Hartfield for their advice and encouragement which was invaluable for the work conducted in this dissertation.

I would also like to thank my colleagues in the advanced flow diagnostic laboratory, present and past, who spent their time and shared their knowledge with me.

This list is incomplete without mentioning my family and friends for all of their support all through my graduate studies. Also, I want to thank my wife Mridula for her unconditional love and unwavering support she showed throughout my PhD program.

Table of Contents

List of Figures

xviii

List of Tables

<div align="center">List of Abbreviations</div>

d_{far} displacement measured at the farthest plane in the DOF

∇ $\partial/\partial x \hat{i} + \partial/\partial y \hat{j} + \partial/\partial z \hat{k}$

ϕ optical path length

ρ density

ε wavefront distortion angle

b distance between the plane of effective refraction and the background

c_i circle of confusion at image

c_o circle of confusion at the object

d_a aperture diameter

d_i measured distortion

f focal length of the camera lens

$f\#'$ image side f-number

G vector with discretized density from the VOI

g function defining the distribution of measured property in the VOI

h_i image height

h_{near} height of the DOF at the plane nearest to the camera

h_o object height

I	measured property of a projection
K	Gladstone-Dale constant
l	distance between the camera lens and the plane of effective refraction
M_{vox}	no. of voxels in the VOI
N	no. of projections
n	refractive index
n_s	number of pixels under a microlens
p	pixel size
Px	number of pixels
S	light path
s_{far}	distance between the camera lens and the farthest plane in the DOF
s_i	image distance
s_{near}	distance between the camera lens and the nearest plane in the DOF
s_o	object distance
2D	two-dimensional
3D	three-dimensional
3DDMT	3-dimensional density measurement technique
4D	four-dimensional
5D	five-dimensional
AFDL	advanced flow diagnostic laboratory

ART	algebraic reconstruction technique
AU	Auburn University
BOS	background oriented schlieren
BOSS	background oriented stereoscopic schlieren
CGBOS	colored grid background oriented schlieren
CT	computed tomography
DOF	depth of field
EMML	estimation maximization maximum likelihood
f#	f-number
FBP	filtered back projection
FFT	fast Fourier transform
FOV	field of view
IR	index of refraction
IRF	index of refraction
LFBOS	light field background oriented schlieren
LFI	light field imaging
LFIT	light field imaging toolkit
M	Magnification of the setup
MART	multiplicative algebraic reconstruction technique
MMD	minimum measurable deviation

MRS	molecular Rayleigh scattering
MTF	modulation transfer function
NDT	non-destructive testing
OPL	optical path length
OTF	optical transfer function
PIV	particle image velocimetry
PLIF	planar light induced fluorescence
PT-BOS	plenoptic tomographic background oriented schlieren
SFR	spatial frequency response
SH	Shack-Hartmann
SNR	signal to noise ratio
SOR	successive over relaxation
SVD	singular value decomposition
VI	volume with inhomogeneity
VOI	volume of interest
W	weighting matrix

Chapter 1

Introduction

Most real flows are unsteady, three-dimensional (3D) and compressible in nature. Any considerable change in the velocity and pressure or change in temperature of the flow field also result in density variations. The effects of these density variations is the area of interest in many fields such as aero-optics, astronomy, oceanography etc.. Performance of the aero-optic systems such as optical seekers in missiles, airborne telescopes, airborne free-space communication systems, and airborne laser weapon systems suffer significantly with density fluctuations around them [1, 2]. In astronomy, compressible and turbulent nature of the atmospheric air causes image distortions [3–5]. In oceanography, studying the density fluctuations can help study the marine ecology [6] or in search and rescue [7, 8] operations etc.. This dissertation is primarily motivated by the need to visualize compressible flow fields; however, this work is presented in a general manner so as to be useful to a more general audience.

Measuring the density fluctuations in a flow field can help understand the observed inefficiencies and distortions. Measurement techniques involving probes are point measurement techniques and are not always practical. Placing them in the flow field also changes the nature of the flow field around the probe. Optical measurement techniques are non-intrusive, robust and have predictable accuracy. Developments in laser technology and fast computing systems made them the measurement techniques of choice for most flow fields. With the advancements in the high speed, high resolution and low light camera technology, their applications are further extended to high speed flows.

Current measurement techniques used for measuring density fluctuations present in the flow field are based on planar light induced fluorescence (PLIF) [9, 10], molecular Rayleigh

scattering (MRS) [11], interferometry [12, 13], Shack-Hartmann [14], or background oriented schlieren (BOS) [15, 16]. PLIF and MRS are planar measurement techniques. The Shack-Hartmann, BOS or interferometry based techniques are aero-optic measurement techniques that utilize the interaction between the light and air to measure the inhomogeneities present in the flow field. The aero-optic techniques can be extended to measure the 3D density information of the flow field. The 3D information of the flow field can be measured by capturing the flow field information from multiple directions. When capturing the information from multiple directions, the volume of interest needs to be calibrated for a good correlation of the information from different directions. Capturing the information from multiple directions simultaneously can be cost prohibitive. A detailed discussion on the current density measurement techniques is presented in Chapter-2.

The above discussion illustrates the challenges associated with the current density measurement techniques. The 3D density measurement techniques are expensive and require complex setup and calibration. For the first time, this dissertation work looks at the application of BOS with the plenoptic camera in an attempt to address the concerns associated with the existing measurement technique.

1.1   Idea

The application of BOS for density measurement of a compressible flow field was shown with both, multiple camera setup [16] and single camera setup [15, 17]. In both implementations, BOS information from multiple directions was used in the reconstruction of the 3D density distribution of the flow field. The BOS data from multiple direction is similar to the information obtained in computed tomography (CT) which can be used with tomographic reconstruction techniques to reconstruct the inhomogeneous 3D volume in the field-of-view (FOV).

Plenoptic cameras are light field based imaging systems that capture light fields in a single plenoptic image which can be used to computationally generate multiple perspective

views. If, instead of using a regular camera for BOS imaging, a plenoptic camera is used, then the BOS information of the flow field from multiple directions can be obtained from a single plenoptic image. All the perspective views generated from the single plenoptic image capture the information of the flow field from the same instance. Thus, capturing multiple perspective views simultaneously whose data can be used for instantaneous reconstruction of the 3D density distribution of the flow field.

Implementation of the BOS technique with a plenoptic camera is a novel idea shown for the first time in this work, though a combination of the light field, concept behind the plenoptic camera, with BOS was implemented by Wetzstein et al. [18] in 2011. Wetzstein et al. [18] developed an alternative BOS technique using a calibrated light field background and a traditional camera, and called it light field background oriented schlieren (LFBOS). Sample images from their work are shown in Figure 1.1. In LFBOS, a four-dimensional (4D) probe instead of a high frequency random pattern is used as the background. The 4D probe varies the color or intensity of the light forming the image to quantify the direction and the location of the origin of the light on the background.
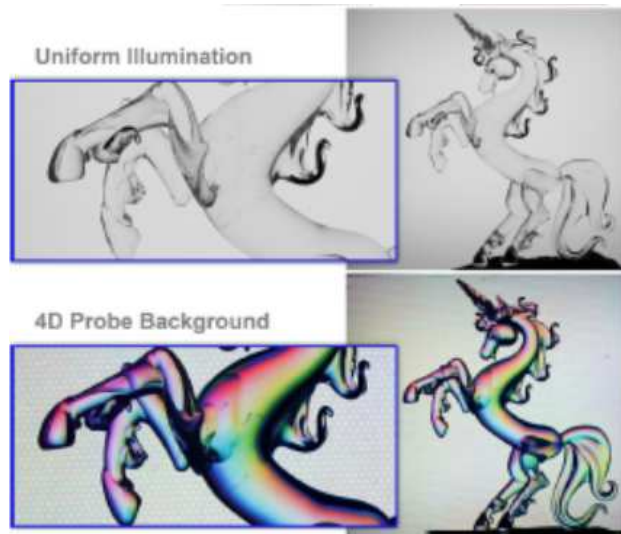
Figure 1.1: Image showing the 4D probe with a classic rainbow schlieren filter that codes the angles and magnitude of complex refractive events in hue and saturation [18].

The top pair of images in Figure 1.1 show the images of a figurine illuminated from the back without any filters. In these images, no information about the medium (figurine) is revealed. The bottom pair of images in Figure 1.1 are imaged with the 4D probe with a classic rainbow schlieren filter in the back. When calibrated, the colors in the images quantify the refraction experienced by the light rays due to the figurine.

In their paper, authors note that the LFBOS technique do not require any reference image and the total space required for the experimental setup is smaller than the space required for the BOS experiment. Authors also noted the limitations of the LFBOS technique in the current implementation. In the current form, LFBOS capability to measure a schlieren object is limited by the size of the optics on the light field probe. One of the major limitation of the technique is the choice of the application specific leneslet array. The setup used for demonstrating LFBOS was sensitive enough for liquids and solids, but not for gases and shock waves, areas of concentration in this dissertation.

In this section, a quick look at both BOS and the plenoptic camera are given. A detailed description of the two are given in Chapters 3 and 4 respectively.

1.1.1   Background Oriented Schlieren

Background oriented schlieren, as the name implies, is a schlieren based imaging technique. The method varies from traditional schlieren imaging, however, in the manner in which deflected light rays are detected. Figure 1.2 shows the setups for both the traditional schlieren and the BOS experiments. In traditional schlieren, use of a knife edge after the converging convex lens stops the light deflected due to the inhomogeneity in the flow field, present in the section where the light beam is parallel, from reaching the image sensor. Images thus captured, carry information about the inhomogeneity in gradients perpendicular to the knife edge.

The basic concept of BOS in an ideal situation is illustrated in Figure 1.2(b). As opposed to the gradient images captured in traditional schlieren, a distorted background image is
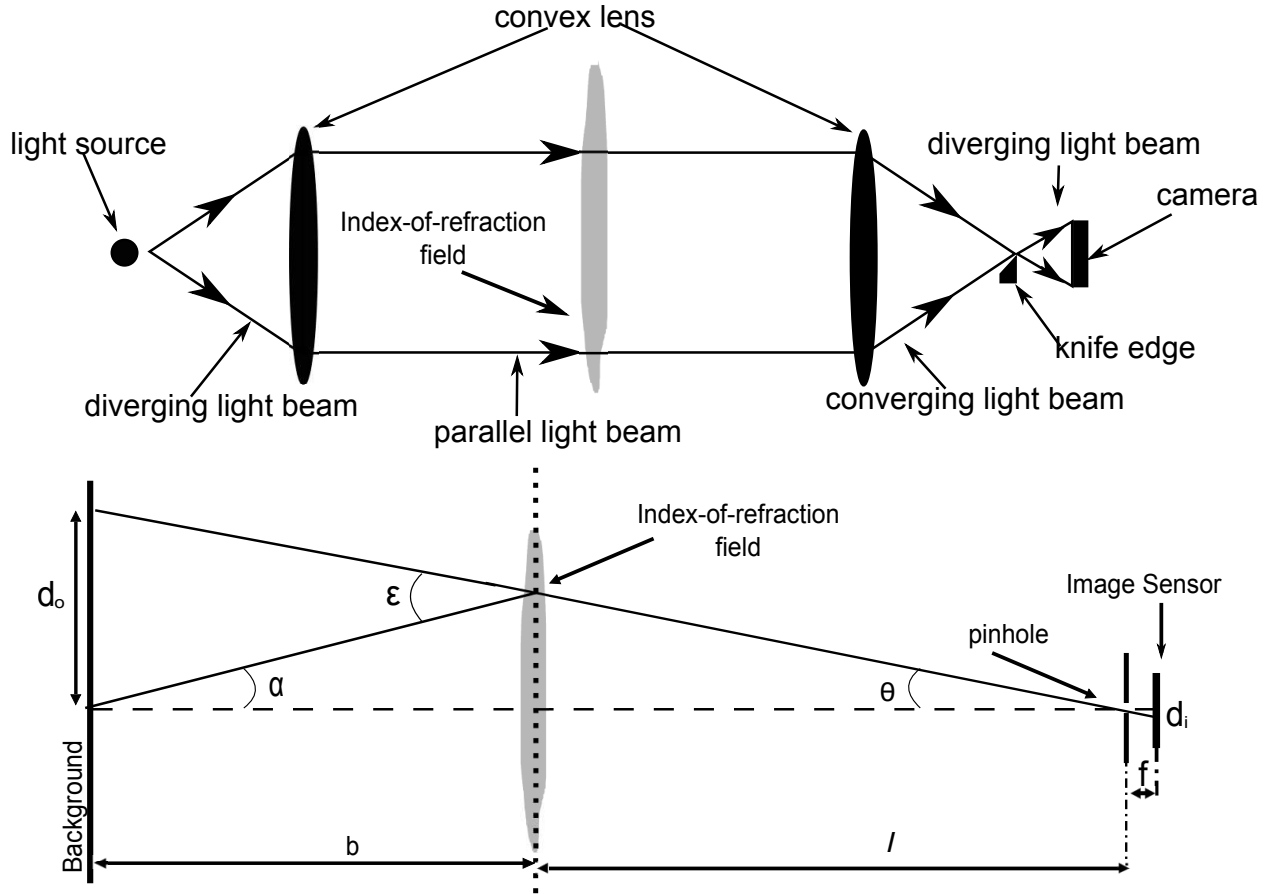
Figure 1.2: Experimental set up of (a) traditional schlieren and (b) BOS experimental techniques.

captured in BOS. This distorted background when compared with the original/reference background gives spatial deflections of the light beam caused due to the inhomogeneous flow field. In the ideal situation, the imaging system uses a pinhole lens approximation and assumes that the light rays originating from the background have paraxial nature. A random background is placed at a distance $(b+l)$ away from the camera lens, where l is the distance between the camera and the location of effective refraction and b is the distance between the location of the effective refraction and the background. In the absence of density gradients $(\nabla\rho = 0)$, a light ray emitted from the background reaches the image sensor without any refractions, as shown by the dashed line. In the presence of an inhomogeneous optical

5

medium ($\bigtriangledown\rho \neq 0$), however, the light ray is deflected by an angle ε, resulting in a shift in the location of incidence on the image sensor.

1.1.2 Plenoptic Camera

A plenoptic camera is a light field based camera. As defined by Arun Gershun in his classic paper, a light field is the amount of light traveling in every direction through every point in space [19]. A plenoptic camera differs from a regular camera in the manner in which the image information is captured. The presence of a microlens array, shown schematically in Figure 1.3, in front of the image sensor in the plenoptic camera causes the difference in the manner images are formed. The microlens array enables the plenoptic camera to capture angular information of the light along with the spatial information in an image. This information enables the user to computationally refocus the image to any point in the object space, change (or extend) the depth of field (DOF) of the image, and also change the perspective of the image after it is captured.
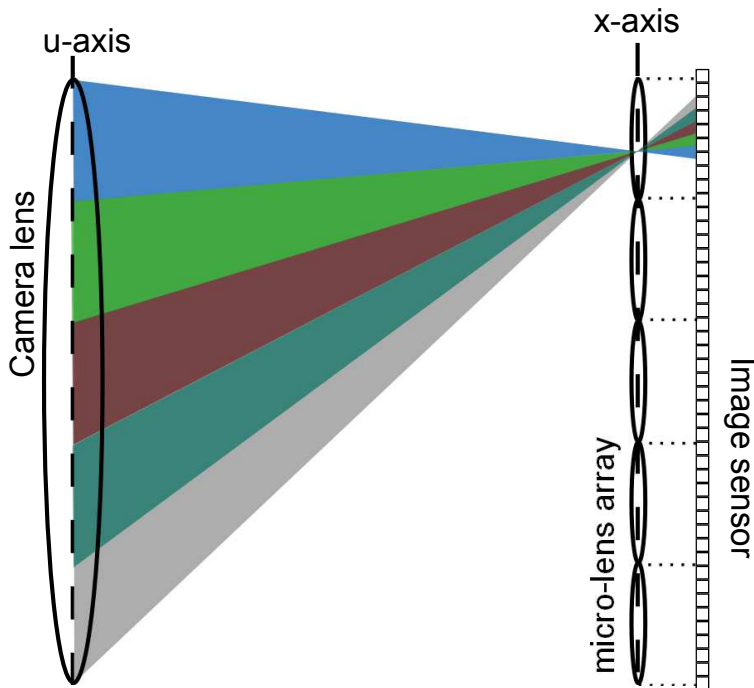
Figure 1.3: Schematic showing the effect of using a microlens array in a plenoptic camera.

In Figure 1.4, an image of figurines of three Star Wars characters, Robot C3PO, Darth Vader, and Stormtrooper, captured with a plenoptic camera is shown. A zoomed in view of the orange box in Figure 1.4, highlighting lightsaber's guard is shown in Figure 1.5. Each circle in Figure 1.5 represents the pixels behind a single microlens. The raw image, in Figure 1.4, can be manipulated computationally to change the focal plane, extend the DOF and change the perspective view.
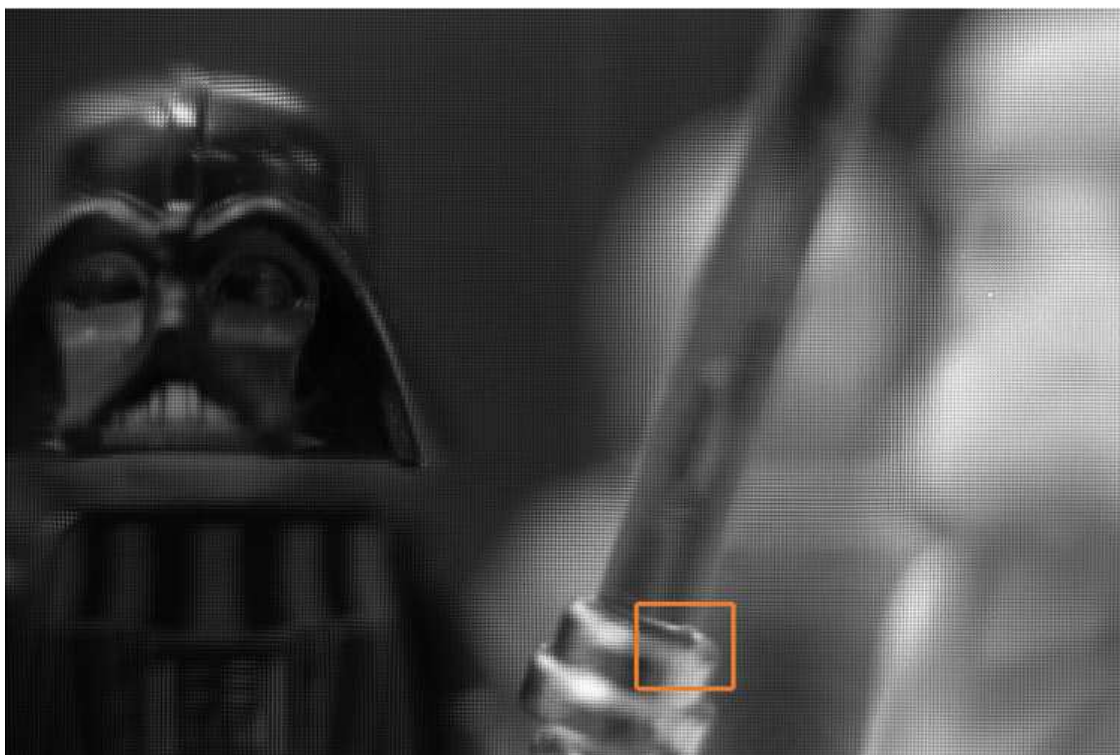
Figure 1.4: Picture of three Star Wars figurines imaged with a plenoptic camera [20]. A orange box in the image is highlighting the guard of the lightsaber. Zoomed in view of the box is shown in Figure 1.5.

In Figures 1.6 and 1.7, images, computationally generated from the raw plenoptic image are shown. In the raw image, Darth Vader is in focus whereas in Figure 1.6(a) robot C3PO is in focus, Darth Vader is in focus in Figure 1.6(b) and Stormtrooper in Figure 1.6(c). Images shown in Figure 1.7 have extended DOF, which means all three figurines are in focus. But, the perspective view changes from one to the other.
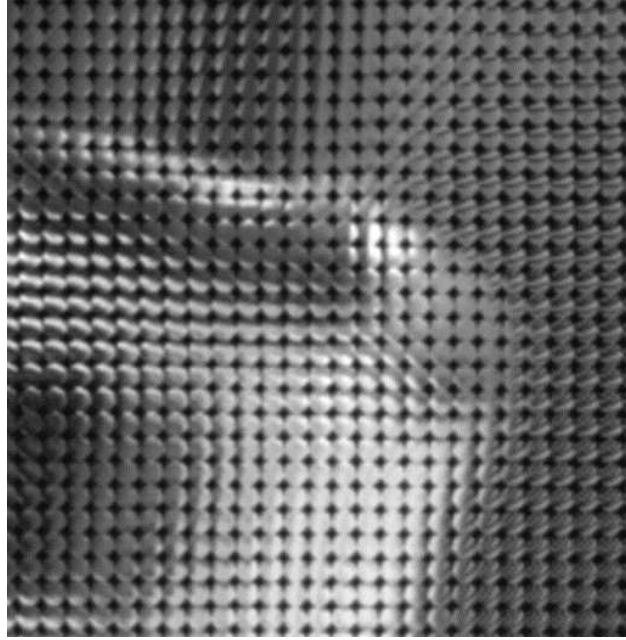
Figure 1.5: Zoomed in view of the lightsaber's guard [20].

Figure 1.6: In the above images three Star War figures, Robot C3PO in the back, Darth Vader in black and Stormtrooper in the front are imaged. a) Robot C3PO is in focus, b) Darth Vader is in focus and c) Stormtrooper in focus [20].

Figure 1.7: Computationally generated images from the raw plenoptic image showing the extended depth of field and change in perspective view from one to the other [20].

The ability to measure the integral effect of non-uniformity along the line of sight and the ability to generate multiple perspective views from a single image captured with a plenoptic camera present us with a unique opportunity. Information about the inhomogeneous field captured in the perspective views obtained from the plenoptic images can be used to locate the inhomogeneous structured or regenerate the 3D density distribution of the flow field using tomographic reconstruction techniques. In the following chapters a detailed discussion on how to computationally develop multiple perspective views from plenoptic images, the theory behind the integral measurement of BOS technique, and how to use this information to study 3D properties of the flow field is presented.

1.2   Dissertation Overview

In this research, a novel idea to perform BOS analysis with images captured with a plenoptic camera is explored and its application to study 3D properties of the flow field is investigated. In this chapter, the ideas along with the two measurement tools, BOS and plenoptic camera, were introduced. A survey of the literature discussing the current whole field density measurement techniques is presented in chapter 2. Advantages and disadvantages of these techniques are also discussed. In Chapter 3, use of BOS for aero-optic measurement of an inhomogeneous flow fields is presented. In Chapter 4, specifications of the plenoptic cameras available at Auburn University (AU) advanced flow diagnostic laboratory (AFDL) are given along with a discussion on computational techniques to process light fields obtained from a plenoptic camera. Chapter 5 takes a look at the different tomographic reconstruction techniques and discuss why a particular reconstruction technique is chosen for this work. The 3D reconstruction algorithm and the execution of the tomographic reconstruction used in this work are shown in Chapter 6. Chapter 7 details the performance of the developed 3-dimensional density measurement technique (3DDMT) using simulated experiments. Physical experiments exploring the application of BOS with the plenoptic camera

9

and the observations are presented in Chapter 8. Concluding remarks and the future work are given in Chapter 9.

Chapter 2

Literature Survey

Current density measurement techniques can be divided into two main categories, qualitative and quantitative measurement techniques. Measurement techniques such as schlieren and shadowgraph are qualitative in nature and only give a visual reference to the nature of the density distribution in a flow field. Quantitative measurement techniques can help quantify the density variation in the flow field. Quantitative measurement techniques can further be divided into two-dimensional (2D) and 3D techniques. The 2D density measurement techniques are based on either the molecular Rayleigh scattering (MRS) or the planar light induced fluorescence (PLIF) and the 3D density measurements are developed based on either the interferometry, schlieren technique or the Shack-Hartmann (SH) sensor. In this chapter, current measurement techniques that are capable of measuring quantitative density distribution in the flow field are discussed.

2.1 2D Measurement Techniques

2.1.1 Molecular Rayleigh Scattering

In molecular Rayleigh scattering (MRS), an external light shined on gas particles is scattered. The light scattered from the gas particles is the same as the incident light. This is called elastic scattering and causes no energy exchange between the incoming photons and the molecules in the flow field. In elastic scattering, the incident light causes an induced dipole moment on a gas molecule causing it to scatter the incident light in all directions [21].

In MRS, intensity of the scattered light is proportional to the density of the gas and the intensity of the laser. This relation between the density of the flow field and the irradiance

from scattering was first exploited in 1989 by Smith et al. [11] to measure the planar density distribution in a turbulent boundary-layer with Mach 2.5 flow. Figure 2.1 shows an instantaneous image of their boundary-layer with air flowing from right to left in the image. The dark region in the image is the high temperature low density region and the bright region is the colder free stream with higher density. They were able to image and study the density structures in a plane. The MRS based density measurement technique was also successfully employed by Miles and Lempert in 1990 [22], Fiedler et al. in 1997 [23], Panda and Seasholtz in 1999 [24], and Mielke et al. in 2006 [25].
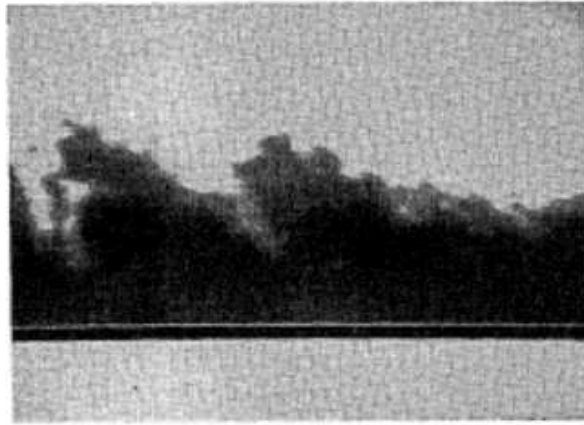
Figure 2.1: Streamwise density cross section normal to the boundary [11].

The biggest advantage of using the MRS technique for density measurement is that the process is free of any tracer molecules and the measurement has direct correlation to the imaged irradiance. In MRS, scattering is instantaneous, in the order of 10^{-12} seconds, as there is no energy exchange between the incident photons and the gas molecules. Although, the wavelength of the incident light in MRS can be arbitrarily selected, using UV radiation favors the experiments as the scattering intensity varies with the fourth power of the scattered light frequency [26].

Signal levels associated with the MRS are low, limiting the applicability of the technique. To address the issue of low signal levels, Dam et al. [27] used an intensified solid state camera, and Escoda and Long [28] and Dimotakis et al. [29] used extraneous gases with

12

higher scattering signal. But, the use of intensified camera resulted in complicated analysis to quantify the data and when using extraneous gases, densities were measured indirectly using the relationship between the density and the mixture fraction. Use of extraneous gases also assumes constant gaseous composition throughout the flow field.

2.1.2 Planar Laser Induced Fluorescence

In the planar laser induced fluorescence (PLIF) technique, tracer molecules are shined with a laser tuned to be absorbed by the tracer molecules. Tracer molecules absorbing the laser light are excited to an unstable state. These unstable molecules return to the stable or ground state by releasing short-term (fluorescence) and long-term (phosphorescence) radiation [21, 30]. PLIF is also used in reacting flows to measure tracer particles to indicate the underlying reaction [9, 10].

In 1984, Massey and Lemon [31] demonstrated the application of tunable ArF laser for oxygen (O_2) fluorescence to measure the temperature and density fluctuations to an accuracy of 1°K and 1% error respectively. LIF experiments using iodine as tracer molecules are independent of temperature, which were utilized in developing a pressure measurement technique by Lemoine and Leporcq [32]. Other tracer molecules either present in the gaseous mixture (such as NO, OH and CH) or externally added to the flow (such as acetone and biacetyl) are used to measure the concentrations of various gases in gaseous mixtures [33,34]. In 2013, Reid et al. [35] demonstrated the application of acetone-PLIF technique to measure the density distribution in a compressible flow field with uniform distribution of acetone. They studied the density variation by imaging the central plane in the wake of a hemisphere placed in a transonic flow. A sample image from their work is shown in Figure 2.2. In their observations, they reported successfully measuring the 2D density distribution with less than 10% error.

PLIF experiments are associated with tracer seeding disadvantages. In large scale facilities, uniform seeding of the flow field is difficult. Secondary scattering, sampling ambiguities,
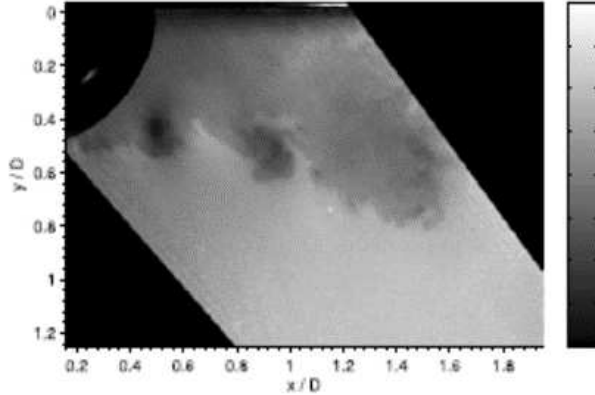
Figure 2.2: Normalized density fields of the centerline plane in the wake region. The color scale spanning from 0.4 to 1.2 [35].

and coherent scattering effects limit the observation of small-scale structures in flows. At high speeds and at high turbulence frequencies, tracer molecules may not follow the flow and therefore may not represent the true flow physics [26].

2.2 3D Measurement Techniques

Aero-optic techniques such as the interferometry, BOS and the Shack-Hartmann based methods are 2D techniques that can be extended to measure 3D properties of the flow field. In this subsection application of each aero-optic technique to measure 3D density distribution of the flow field is discussed.

2.2.1 Interferometry

Interest to investigate 3D inhomogeneity of a flow field using aero-optic measurement techniques, such as absorption or interferometric methods, combined with tomographic reconstruction appeared as early as the 70's. Inquiries included wide range of flow fields such as natural convection [36], turbulent jets [37], transonic aerodynamics [38], laminar jets [39, 40] etc. But, these early investigations measured only the time averaged properties of the flow fields. Earliest known unsteady tomographic measurements include a paper by Snyder and

Hesselink [41]. They used the interferometric tomography technique to measure density distribution in an unsteady helium jet.

The basic principle of interferometry is the wave property of light observed in the Young's double slit experiment. When light from a source is split and made to interfere with each other, a pattern of constructive and destructive interference fringe appears. The observed interference pattern is a function of the two interfering wavefronts.

Figure 2.3 shows a schematic of an experimental setup using interferometer for aerodynamic purposes. In the schematic shown, light from a laser beam is split into reference and test/distorted beam. The two beams are then joined at the second splitter right before the image is captured. Capturing of the interferogram by the camera is shown as the interferogram in the figure. The fringe pattern is captured in the interferogram without and with the presence of compressible flow in the test-section. The difference in the fringe pattern is qualitatively related to the density distribution in the flow field [42, 43].
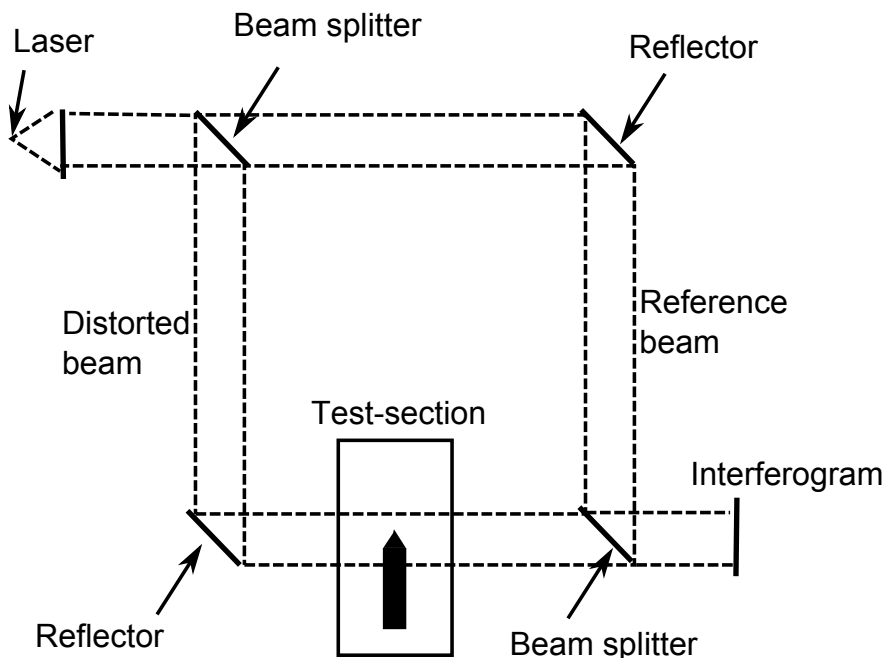
Figure 2.3: Schematic showing an experiment with interferometry setup.

Pedersen [13] researched the experimental applicability of the tomographic reconstruction technique to investigating turbulence in a warm jet emitting from a nozzle. Figure 2.4

15

shows the schematic of Pedersen's experimental setup. In his observations, Pedersen notes a reconstruction of the inhomogeneous refractive index distribution in the flow field with acceptable accuracy. Each interferogram provides slope of a wavefront in only one direction. To fully characterize the wavefront in 2D, two interferograms are required [44]. For good interferometric measurements, it is important

1. to have homogeneity in the refractive index and thickness of the beam splitters,

2. parallelism of the test-section windows, mirrors and beam splitters, and

3. exact mounting of the optical elements without any bending sagging or other mechanical deformations.

Thus, making the experimental setup complex and difficult [45]. Soller et al. [46] noted the limitation on the angular range that can be achieved in an experimental setup and its adverse effects on the reconstructed 3D volume. In a study comparing the shearing interferometry and shadowgraph by Jewell [47], author notes advantages of interferometry over shadowgraph, but, suggest the use of Shack-Hartmann sensors as more practical approach to 3D study of compressible flow fields.

2.2.2 Shack-Hartmann Sensor

The Shack-Hartmann (SH) sensor is the most commonly used wavefront sensor. The SH sensor is made of an array of lenslets, shown in Figure 2.5(a), to spatially discretize the wavefront and measure local deflections. A schematic of a distorted wavefront passing through the SH sensor is shown in Figure 5 2.5(b). In Figure 5 2.5(b), the solid sinusoidal wavefront left of the SH sensor represents a distorted wavefront. The function of each lenslet is to focus the light incident on it onto the image sensor. The displacement, d_k, of the spot measured behind the kth lenslet is a function of the average local tilt of the discretized portion of the wavefront incident on the lenlet and the focal-length of the lenslet [48, 49].
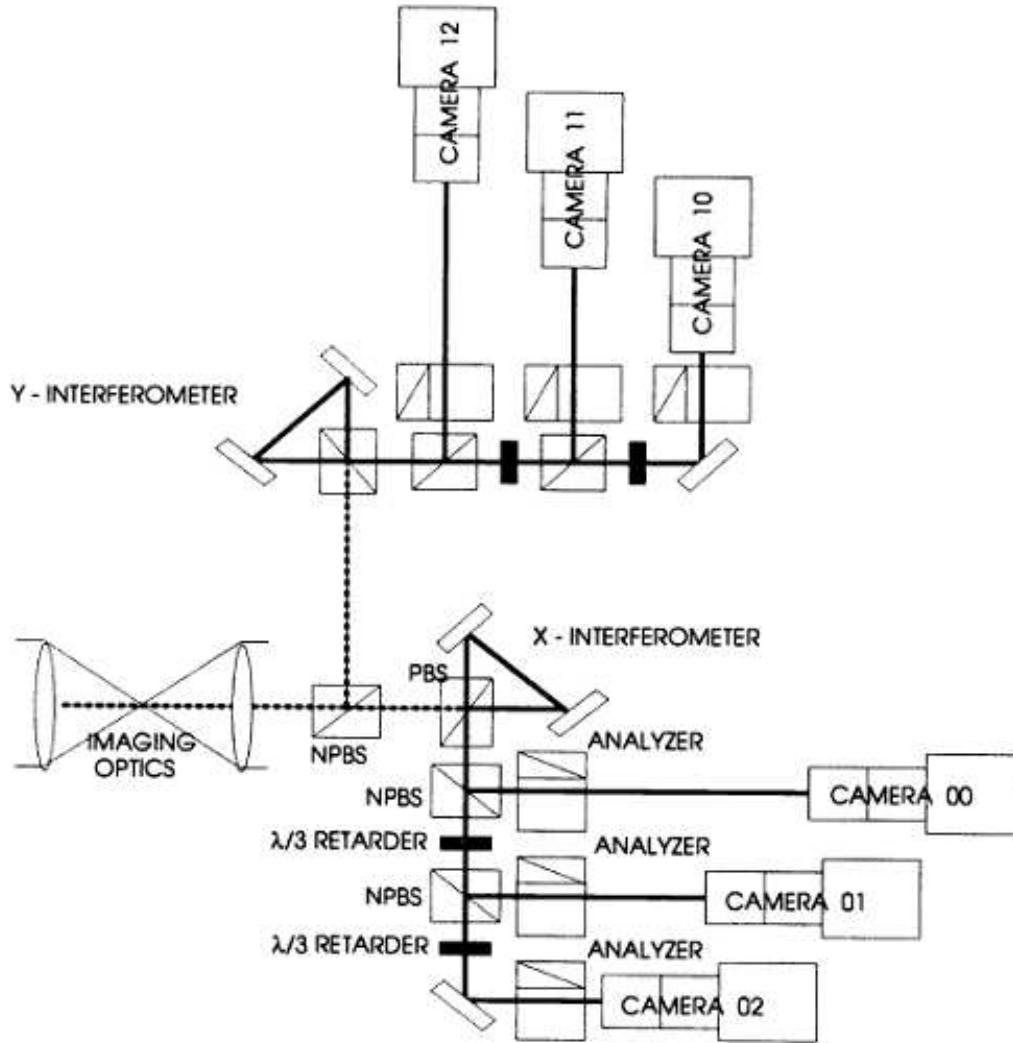
Figure 2.4: Schematic of the experimental setup used to capture tomographic shearing interpherometric wavefront data [13].

In the mid 90's, researchers at Air Force Research Laboratory (AFRL) Phillips site developed and used a tomographic density measurement technique using the SH wavefront sensor. In 1994, McMakin et al. [50] described the simulation of a tomographic measurement technique using the SH sensors. They characterized the performance of the system as a function of the number of projections, number of samples (lenslets) in each projection and the focal-length of the lenslets. In 1995, McMackin et al. [14] demonstrated the application of the SH sensor to measure density distribution. They used 1D SH sensors with 40 lenslets each to tomographically reconstruct cross-sectional planes of a vertical flow jet. Schematic
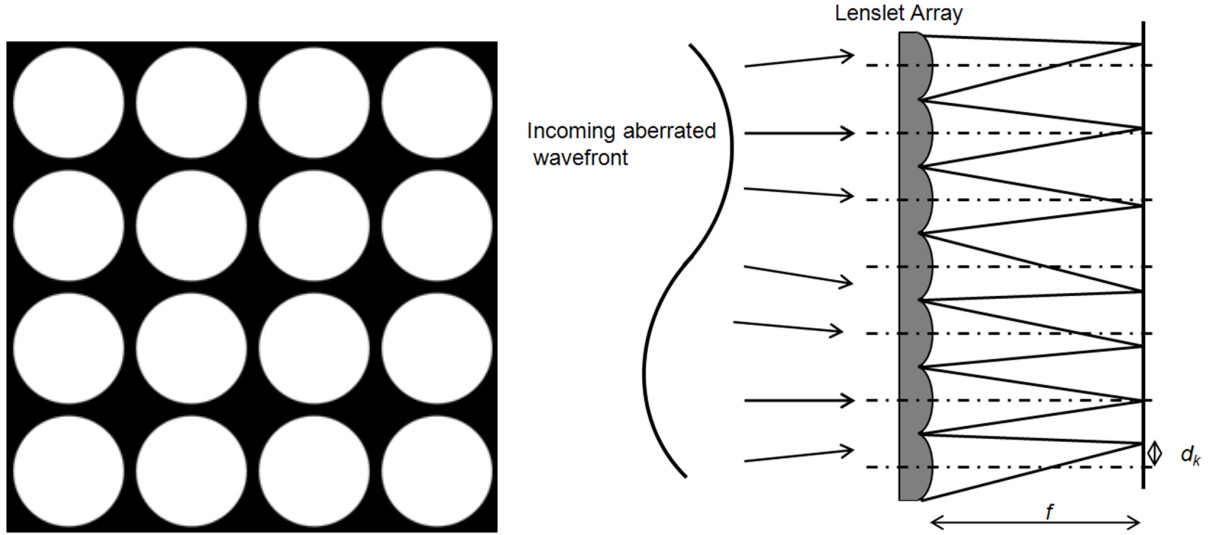
Figure 2.5: (a) Shack-Hartmann sensor lenslet and (b) Schematic showing the working of the Shack-Hartmann sensor.

of the experimental setup is shown in Figure 2.6. In this work, authors extended their study by simulating the experiments with varying number of SH sensors and the number of lenslets on each sensor to find the optimal setup required for an acceptable accuracy. They observed that to obtain an accuracy of 5.5%, a minimum of 9 simultaneous projections with at least 64 lenslets on each sensor are required. The authors also noted that the 2D reconstruction technique described can be extended to 3D reconstruction.

The tomographic reconstruction technique developed using the SH sensors at AFRL used 8 simultaneous projections, shown in Figure 2.6. This configuration was successfully used by Pierson et al. [52], Hugo et al. [53], Pierson et al. [54] and McMackin et al. [51]. In a 1999 work, McMackin et al. [55] were able to record data at 5 kHz to reconstruct temporally varying density in 2D planes.

In experiments involving the SH sensors, the number of simultaneous projections captured for instantaneous measurements are limited by:
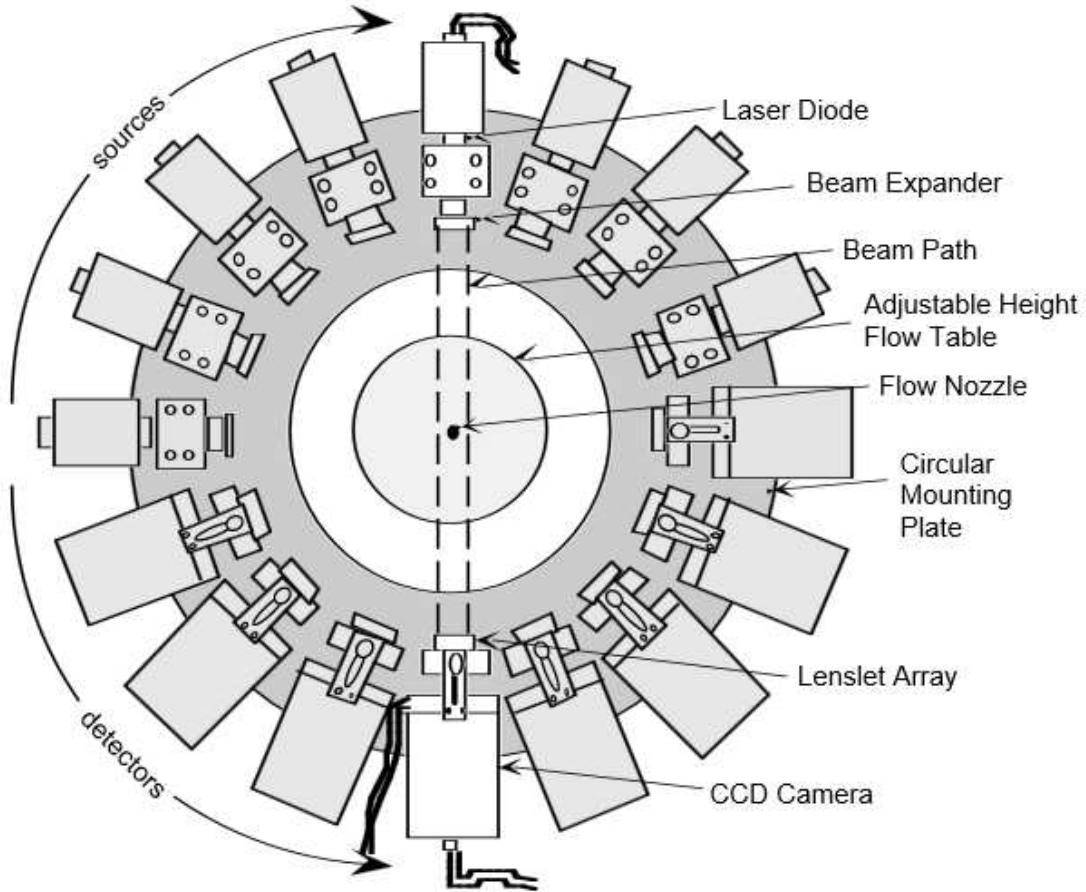
Figure 2.6: Schematic showing the setup for tomographic data acquisition of the jet data using the Shack-Hartmann sensors [51].

1. optical access to the flow field: when conducting experiments in wind-tunnels, limited number of windows on the tunnel limit the number of the SH sensors that are able to view the light coming from the other side of the tunnel,

2. space available for experimental setup, and

3. the SH sensors are relatively expensive: use of large number of sensors is cost prohibitive.

When using the SH sensors, resolution of the reconstructed date is limited by the number of lenslets on each sensor. Some of these disadvantages associated when using the SH sensors are addressed with the use of the BOS technique for tomographic measurements.

2.2.3 Background Oriented Schlieren

An introduction to BOS was given in Chapter 1. In the BOS experiments, an incoherent light source is used. Thus, the most expensive equipment in the BOS experiments is the image sensor/camera and collimating optics (if used [56]) which are inexpensive when compared with the apparatus required in the SH experiments. Use of cross correlation techniques that are used in particle image velocimetry (PIV) to calculate the deviation from the BOS images results in resolutions better than the data acquired from experiments using the SH sensors.

Few different implementation of BOS for tomographic measurement of a flow field density distribution can be found in the literature. Venkatakrishnan and Meier's [15] work in 2004 demonstrated the application of the traditional BOS technique to measure the time averaged density distribution around an axisymmetric symmetric cone placed in a Mach 2.0 flow. A Sony DSC F-707 camera with 5.1 megapixel resolution with the exposure time of 0.01 sec was used to capture the BOS images. These images were analyzed using PIV algorithms to obtained displacement data, which was then used to generate the integrated density field of each view with successive over relaxation (SOR) method described by Ehrlich in 1981 [57]. 19 projections thus generated were used with the filtered back projection (FBP) technique to reconstruct the averaged 3D density distribution of the flow field. This 3D density measurement technique (3DDMT) was also successfully used to study the average density distribution in an axisymmetric underexpanded jet flow [58] and later to measure the density field in an oblique shock-separated turbulent boundary flow [59].

In 2011, Ota et al. [17] implemented the tomographic BOS described by Venkatakrishan and Meier [15] with a few changes. Ota et al. used a variant of BOS called colored grid background oriented schlieren (CGBOS), to capture BOS images of an asymmetric cone placed in Mach 2.0 flow. The asymmetric shape of the model is seen in Figure 2.7(a). The background used in these experiments was made of a structured grid of vertical and horizontal lines drawn with two different colors, shown in Figure 2.7(a). A schematic of the

experimental setup is shown in Figure 2.8. Once captured, images were processed to separate individual color information to measure the displacement data. Images showing the green horizontal lines and red vertical lines separated from the original CGBOS image are shown in Figure 2.7(b) and 2.7(c) respectively. Displacements in the x-direction are obtained from the images with red vertical lines and in the y-direction are obtained from analyzing the images with green horizontal lines. Instead of the FBP used by Venakatakrishnan and Meier [15], Ota et al. [17] used algebraic reconstruction technique (ART) to reconstruct the 3D density distribution around the model.
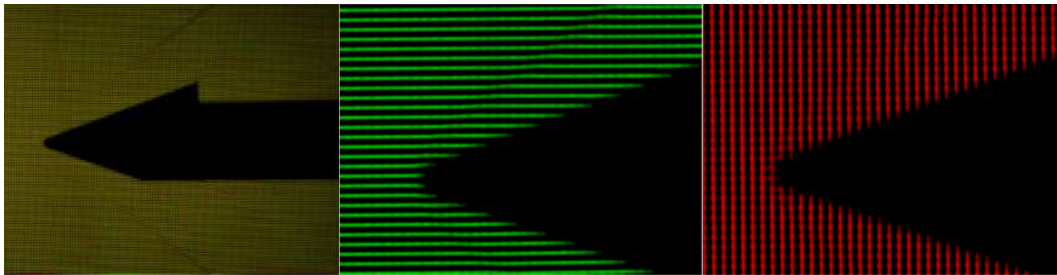
Figure 2.7: a) CGBOS image taken through Mach 2.0 flow, b) green horizontal lines of the CGBOS image and c) red vertical lines of the CGBOS image [17].
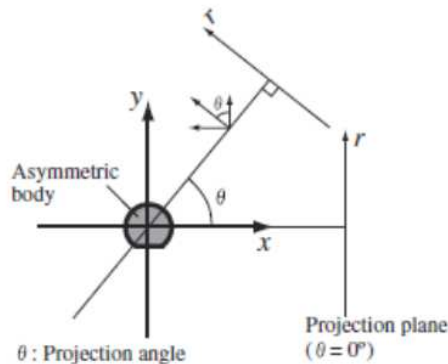
Figure 2.8: Projection angle and image plane [17].

In a 2008 study, Atcheson et al. [16] used the BOS technique to demonstrate its applicability to measure 3D density distribution in a time varying flow field. They captured 16 perspective view simultaneously using 16 Sony HDR-SR7 camcorders with 1/60 sec exposure. The captured perspective views had a maximum angular disparity of 180°. Figure 9

shows their setup with 16 cameras and the wavelet background used in their experiments. As they imaged flow due to buoyant hot air, the exposure was good enough to record turbulent structures in the flow field. They developed a tomographic reconstruction technique to reconstruct the 3D density distribution of the flow field which accounts for the sparseness in the captured data. This technique was also used to study turbulent gas flow in the presence of occluders [60] and using Microsoft's Kinect cameras [61].

Figure 2.9: Image acquisition system used by Atcheson et al. [16].

In the 3DDMT's using BOS, although averaged in some cases, the 3D density distribution of the flow field was successfully measured. These 3DDMT's are acceptable for either the steady or the low speed flows. All these techniques require a well calibrated physical space for reconstruction.

2.3   Summary

From the above discussion of the current state of the art 3d density measurement techniques, it is observed that they are expensive to measure unsteady compressible flow. Setting up experiments to capture multiple perspective views cameras is cumbersome and complex to calibrate and the number of perspective views that can be captured may be limited by the optical access to the flow field. To address these issues, in this dissertation, a novel idea to perform BOS with a plenoptic camera is explored along with its application to measure 3D density distribution in a compressible flow field addressing some of the challenges associated with the current measurement techniques.

Background Oriented Schlieren

In Chapter 1, the concept of BOS was introduced. A schematic showing the traditional BOS' experimental setup is shown in Figure 1.2(b) and shown here again in Figure 3.1, for convenience. With the paraxial and small angle approximation, the measured deviation is given by [62, 63]:

$$\varepsilon = \left(\frac{l}{b} + 1\right)\left(\frac{d_i}{f}\right) \tag{3.1}$$

where, d_i is the distortion measured at the image plane and f if the focal length of the lens on the camera. b and l are the distance between the effective refraction and the background and distance between the camera lens and the plane of effective refraction respectively.
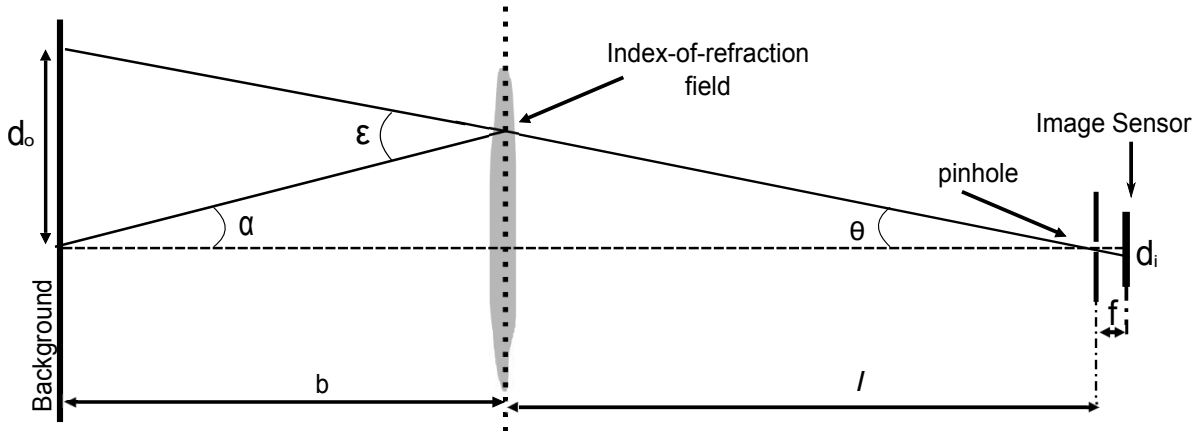
Figure 3.1: Experimental set up of traditional BOS experiments.

In this chapter, a look at previous works that studied BOS is presented in section 3.1. In section 3.2, the relationship between the aero-optic distortions of the light rays and the BOS measurements is discussed. The behavior of BOS in practical situation such as a laboratory setup is discussed in section 3.3 and section 3.4 presents the performance analysis study

of the BOS technique with an example showing the application to measure the integrated effects of index-of-refraction field (IRF).

3.1   Related Work

While a comprehensive review of BOS is beyond the scope of this work, a brief summary of related work is given here to provide the proper context for the current work. Meier [64] introduced the concept of BOS in his 1999 patent filing. It has the simplest setup amongst all types of schlieren based techniques.

In a typical BOS experiment conducted in a laboratory, a random background illuminated with an incoherent light source is placed on one side of the IRF and a camera with suitable lens on the other. As light propagates from the background to the camera, variations in the IRF cause the light rays to refract resulting in the imaged background to distort. The medium that causes the distortion, a compressible flow field in this work, is referred to as a schlieren object or an inhomogeneous flow field. The magnitude of the distortion can be quantified by comparing the distorted image with a reference image captured without the schlieren object in the FOV, although it should be noted that some techniques, such as the background oriented stereoscopic schlieren (BOSS) circumvent this issue by using two simultaneous measurements from different angles [63] or by using a calibrated light field background [17]. In general, the image distortion is determined using algorithms derived from the particle image velocimetry (PIV). PIV algorithms apply a 2D cross-correlation to a small interrogation window (typically on the order of 32×32 pixels) to determine the local displacement of the underlying image pattern; a review of these algorithms can be found in books by Raffel et al. [65] and Adrian and Westerweel [66]. More recent work has investigated the use of optical flow algorithms and optimized backgrounds, to determine displacement, which, taken together, have the potential to greatly improve the spatial resolution (in theory on the order of single pixel) beyond that achievable with PIV algorithms [16].

Following the original work of Meier [64], several authors demonstrated the use of BOS for visualization of various compressible flows. Some examples include the study of the tip vortices shed from helicopter blades [63, 67], visualization and propagation of shock waves generated by explosions [68], the study of the density variation in a variety of flows such as flame from Bunsen burner, supersonic jet, concentration measurement of gases, wake and vortex measurement, gunshot [69], 3D reconstruction of a double free jet [70], and the study of supersonic shear layers [71]. A significant feature of BOS highlighted in these works is its quantitative nature, which can be used to measure the inhomogeneity present in the flow field density distribution. Initially, a detailed understanding of the technique was obtained by drawing the similarities between laser speckle velocimetry and BOS [62]. More recent works, however, have focused directly on the physics of the technique and considered such things as the type of background and computational methods for determining the image displacement [16, 72, 73].

An important property of any BOS system is its sensitivity, which is taken as the magnitude of image distortion that will occur for a given index-of-refraction gradient. In general, it is well recognized that the sensitivity is directly dependent on the properties of the imaging system, the location of the schlieren object relative to the background and camera, and the resolution of the background and camera. These relationships are fairly well understood and presented, for example, by Goldhahn and Seume [70] who observed that increasing the focal length and positioning the schlieren object closer to the camera resulted in a more sensitive measurement. Furthermore, they comment that the overall length has a minor influence on the sensitivity.

While the basic understanding of these relationships is clear, the literature varies as to what constitutes an optimal experimental arrangement. This variation is largely due to different notions about limitations on the spatial resolution of the measurement at the schlieren object location. It is generally specified that the camera in the BOS setup should be focused on the background while the schlieren object is implicitly out-of-focus [63, 67].

Later studies noted that both the background and schlieren object should be in nominal focus. In both cases, the spatial resolution of the measurement is specified by the degree to which the schlieren object is in focus [69, 74]. Depending on the resolution requirements, this may restrict the allowable thickness of the schlieren object or the maximum distance between the background and the schlieren object, thus limiting the sensitivity of the measurements [74, 75].

As PIV algorithms have traditionally been used to determine the magnitude of image distortion, several authors have also considered the relationship between the size of the PIV interrogation window and the defocus of the schlieren object when the camera is focused on the background. Hargather and Settles [74] suggested that the optimal position of the object is halfway between the camera lens and the background. Richard et al. [62] suggest that blurring of the schlieren object be allowed as long as the blur is considerably smaller than the size of the interrogation window. Similar results were reported by Goldhahn and Seume [70]. Hargather and Settles [74] also suggested a thin flow field assumption for the thickness of the schlieren object. Klinge et al. [75] addressed this issue in even more detail and suggested that the optimal configuration is when the magnitude of the blurring is equal to the size of the interrogation window. They note that moving the object closer to the camera can lead to increased sensitivity, but at the expense of spatial resolution whereas moving the object further away decreases the sensitivity without providing any improvements in spatial resolution.

In the current work, the spatial resolution of the measurement is particularly important as it places important constraints on the experimental arrangement and sensitivity. As such, in this chapter, a new viewpoint on the optimal arrangement of a BOS experiment is provided that takes into account the FOV of the measurement as well as the resolution of both the background and the schlieren object. First, however, the theory relevant to the measurement is introduced.

3.2 Aero-optic Distortions

Aero-optics is the study of the interaction between light and air. To understand the application of the BOS technique for measuring the integrated effect of the compressible flow, OPD, on light rays, this section is divided into three parts. It starts with a simple description of the principle behind aero-optic distortions to help understand the relation between the optical path length (OPL) and the properties of air (or another medium). In the second section, BOS is explained. Finally, these two ideas, aero-optic distortions and BOS, are then tied together with a short comment in the third part.

3.2.1 Aero-optic wavefront distribution

The OPL (ϕ) of a light ray is given by integrating the refractive index (n) of the medium along the light's path (S).

$$\text{OPL} = \phi = \int_s (n) dS \tag{3.2}$$

n of a gas is a function of its density, and the relation is described by the Gladstone-Dale equation [76, 77]:

$$n(x, y, z, t) = 1 + K\rho(x, y, z, t) \tag{3.3}$$

where, K and ρ are the Gladstone-Dale constant and the gas density, respectively. K is a function of the wavelength of light and the gas composition, suggesting, for a given gas and light source, the index-of-refraction varies only with the density of the gas.

$\rho(x, y, z, t)$ in Equation 3.3 emphasizes that the density can vary in both space and time resulting in an unsteady, inhomogeneous IRF. Light rays propagating through this inhomogeneous medium experience refraction. The remainder of the analysis in this chapter is applicable to an inhomogeneous IRF associated with any medium and not just that associated with an air flow.

Equation 3.4 gives the amount of refraction experienced by a light ray after propagating an infinitesimal length (dS).

$$d\varepsilon = \triangledown n \cdot dS \tag{3.4}$$

where, $d\varepsilon$ is the angle of refraction and $\triangledown$ is the differential vector operator ($(\partial/\partial x \hat{i} + \partial/\partial y \hat{j} + \partial/\partial z \hat{k})$). Integrating Equation 3.4 along the light path, S, through the medium gives the total angular deflection [15,63]:

$$\varepsilon = \int_s \triangledown n \cdot dS \tag{3.5}$$

As shown in Equation 3.2, the OPL, ϕ, of the light ray is a function of the refractive index of the medium it passes through. Combining Equations 3.2 and 3.5 yields [78]:

$$\varepsilon = \int_s \triangledown n \cdot dS = \triangledown \int_s n \cdot dS = \triangledown \phi \tag{3.6}$$

Thus, the total angle of refraction of the light ray passing through the inhomogeneous index field is directly proportional to the local gradient of the OPL.

Given the nature of the space and time varying IRF, it is safe to assume that the OPL is a function of space (varying in x and y direction) and time too. Thus, the OPL of any two rays may or may not be the same. In schlieren experiments, it is not always possible to measure the absolute OPL, but, a relative difference in the OPL between two neighboring light rays is measured, OPD. The OPD for a wavefront, surface with constant phase, is defined as:

$$\hat{\phi} = \phi - \bar{\phi} \tag{3.7}$$

where, $\bar{\phi}$ is the spatially averaged OPL across a beam aperture.

Substituting ϕ from Equation 3.7 in Equation 3.6:

$$\varepsilon = \triangledown \phi = \triangledown \hat{\phi} \tag{3.8}$$

28

3.2.2 Traditional BOS

In an ideal BOS experiment, the setup shown in the schematic in Figure 3.1 is used for experiments. The angle of incidence of a light ray measured from the BOS images in such an experiment is given by Equation 3.1. Assuming the effective refraction of the light ray takes place at a distance l from the lens, the relation between the angles, ε, α and θ, shown in Figure 3.2, is given by:

$$\varepsilon = \alpha + \theta \tag{3.9}$$

Using trigonometric identity, the above equation can be expanded to:

$$\tan \varepsilon = \tan(\alpha + \theta) = \frac{\tan \alpha + \tan \theta}{1 - \tan \alpha \tan \theta} \tag{3.10}$$

Geometrically, α and θ are related to b and l as:

$$b \tan \alpha = l \tan \alpha \tag{3.11}$$

Substituting tan from Equation 3.11 in Equation 3.10 gives:

$$\tan \varepsilon = \frac{\left(\frac{l}{b} + 1\right) \tan \theta}{1 - \left(\frac{l}{b}\right) \tan^2 \theta} \tag{3.12}$$

For small angles (reasonable approximation for density variations in gaseous flow fields), this reduces to:

$$\tan \varepsilon = \varepsilon = \left(\frac{l}{b} + 1\right) \tan \theta \tag{3.13}$$

Substituting $\tan \theta$ from Figure 3.1 leads to [62, 63]:

$$\varepsilon = \left(\frac{l}{b} + 1\right) \left(\frac{d_i}{f}\right) \tag{3.14}$$

This equation is the same In Equation 3.14, b, l, and f are constants for a given experimental arrangement and give the relation between the total refraction of a light ray and the measured image displacement for small angular deflections. Deflection in Equation 3.14 measures the integral effect of the total refraction experienced by the light ray in the inhomogeneous IRF.

3.2.3 Relation between BOS and wavefront sensing

The effective angle of refraction (ε), shown in Figure 3.1 and in Equation 3.14, is the same as that in Equation 3.6, providing us with a direct measurement of the wavefront distortion for every point in the image:

$$\varepsilon = \bigtriangledown \phi = \left(\frac{l}{b} + 1 \right) \left(\frac{d_i}{f} \right) \tag{3.15}$$

Thus, BOS can be used for measuring the local gradients of the wavefront distortion that can be used to measure the OPD's of the wavefront. The following sections of the chapter investigate the challenges associated with the application of the BOS technique for measuring OPD's.

3.3 Practical Considerations

So far, the idealized analysis has been based on the following assumptions:

1. the lens on the camera has a pinhole aperture with infinite DOF, and

2. the wavefront distortions are described as deviations occurring at a thin interface from a nominally parallel beam.

In this section, the above assumptions are relaxed and a practical imaging system with finite depth-of-field (DOF) and converging beam is considered. The primary constraint in this analysis is the fact that both the test section, where the distorting medium is located, and the background should be kept in nominal focus. The following subsections look at

each constraint separately with the results from a BOS simulation model and experiment complementing the observations.

3.3.1 Spacing and Focusing

In an arbitrary laboratory arrangement, shown in Figure 3.2, there will be restrictions imposed by the total available laboratory space $(l + b)$, the required FOV and the DOF of the imaging system. In this section, the analysis in section 3.2 is continued to survey the effect of the constraints on the sensitivity of the BOS technique.
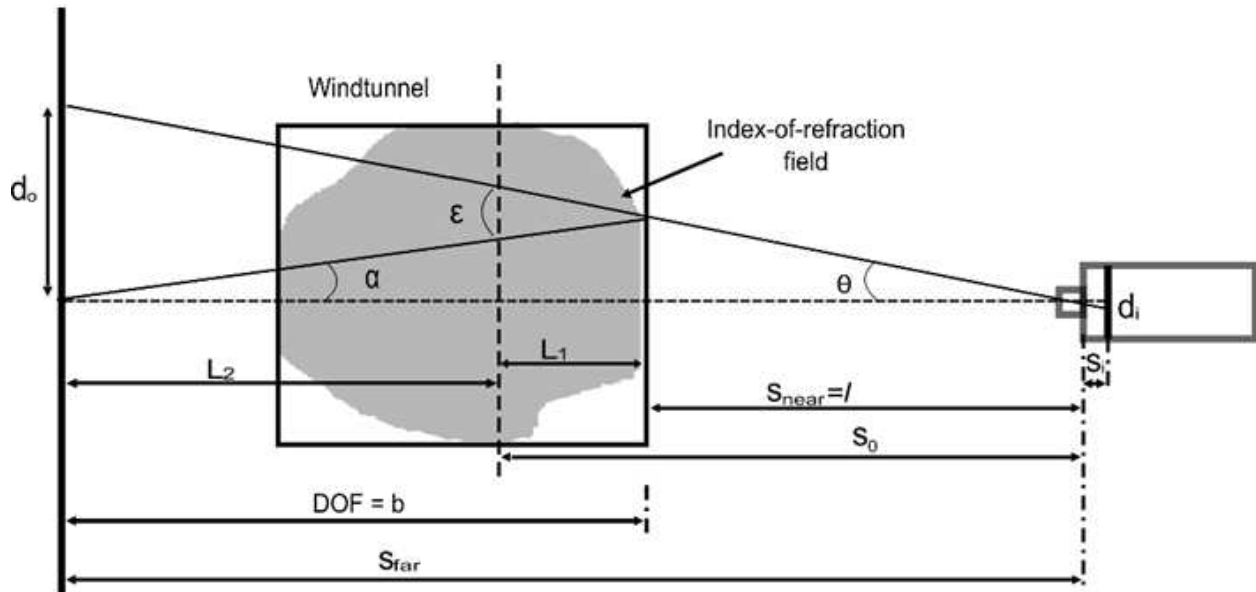
Figure 3.2: Illustration showing laboratory BOS configuration.

The independent variables used in a BOS experiment that can be adjusted by the user or are fixed properties of the instrumentation are:

1. f = focal length of the lens

2. d_a = diameter of the lens aperture

3. $f\# = f/d_a$ = f-number

4. h_i = image height = physical size of the image sensor

5. h_{near} = exit height = height of the desired FOV = height of the test-section

6. p = size of a single pixel on the image sensor

7. $c_i = k \times p$ = circle of confusion at the image sensor, k is generally an integer.

The goal is to rewrite Equation 3.14 in terms of these independent variables. To do so, geometric equations for the DOF and FOV that relate l and b to the above variables are introduced. Further, the constraint that the background is placed at the furthest most point of the DOF and that the exit plane of the inhomogeneous medium (i.e. the wavefront beam aperture, h_{near}) is at the nearest point in the DOF is imposed. As such, the condition that the spatial resolution of the background and the wavefront measurement are equal is explicitly imposed. When using PIV algorithms with large interrogation windows, this may be considered overly restrictive as the resolution at the exit plane can be as large as the size of the interrogation window as discussed by Klinge et al. [75]. The current analysis, however, is motivated by the potential of optical flow algorithms to achieve a spatial resolution that approaches that of the background image. As such, the analysis proceeds under the assumption that the background and exit plane must have equal resolution if spatial resolution is to be maximized.

The thin lens equation:

$$\frac{1}{s_i} + \frac{1}{s_o} = \frac{1}{f} \tag{3.16}$$

where, s_i and s_o are the image and object plane distances measured from the lens respectively and f is focal length of the imaging lens. The nominal magnification (M) of the setup is defined as:

$$M = \frac{s_i}{s_o} = \frac{h_i}{h_o} \tag{3.17}$$

where, h_i and h_o are the height of the image and the object respectively. It is important to note that the nominal focus is not fixed at the background plane, but, rather, to a plane between the background and the exit plane. Applying the properties of similar triangles to

the image plane, object plane and the exit plane, as seen in Figure 3.2, gives:

$$\frac{h_i}{s_i} = \frac{h_o}{s_o} = \frac{h_{near}}{s_{near}} \qquad (3.18)$$

The relation between the circle of confusion at the image plane and the object plane is given by:

$$c_o = \frac{c_i}{M} \qquad (3.19)$$

Equation 3.19 defines the effective spatial resolution of the measurement.

Kingslake [79] describes the approach used for developing the DOF relations adopted in this work. Figure 3.3 shows a schematic defining the DOF for a given aperture diameter, d_a, on the imaging lens. In this figure, the lens is set to focus on the plane located at a distance s_o from the lens such that all points originating from this plane form a sharp image on the image sensor. Rays originating from in front of or behind the focal plane will appear blurred. The DOF is defined by the conical set of rays that fill a spot size c_o (also known as the circle of confusion in the object plane, Figure 3.3) on the object plane such that the blurred spot is indistinguishable from a spot formed from a point source on the object plane. The size of the blur spot (at the image plane) is typically chosen to correspond to the size of a single (or integer multiple) pixel. As will be seen, allowing some image blur can have significant benefits to the overall experiment. s_{near} and s_{far} are the distances measured from the lens to the nearest and farthest planes in the DOF. Thus, DOF consists of the region between s_{near} and s_{far}. They are given by:

$$s_{far} = \frac{d_a s_o}{d_a - c_o} \qquad (3.20)$$

$$s_{near} = \frac{d_a s_o}{d_a + c_o} \qquad (3.21)$$

Figure 3.3: Schematic showing some of the variables used to describe the DOF in the paper.

Substituting Equations 3.17, 3.18 and 3.19 in 3.21, the height of the FOV at the focal plane is obtained.

$$h_o = \frac{d_a h_i h_{near}}{d_a h_i + c_i h_{near}} \tag{3.22}$$

This can further be used to calculate the magnification in Equation 3.1, and then the following quantities:

1. $s_i = (M + 1) f =$ image distance,

2. $s_o = \left(\frac{1}{M} + 1\right) f =$ object distance (distance of the focal plane from the lens),

3. $s_{near} = l =$ distance of the test-section from the camera lens,

4. $\text{DOF} = b = s_{far} - s_{near} = \frac{d_a s_o}{d_a - c_o} - \frac{d_a s_o}{d_a + c_o}$, and

5. $\frac{l}{b} = \frac{d_a M - c_i}{2c_i}$.

Substituting the above expressions into Equation 3.14 gives the deviation angle in terms of the independent variables:

$$\varepsilon = \left(1 + \frac{d_a M - c_i}{2c_i}\right) \left(\frac{d_i}{(1 + M) f}\right) \tag{3.23}$$

34

Further assuming $d_a M \gg c_i$, simplifies Equation 3.23 to:

$$\varepsilon = \left(\frac{d_i M}{2 c_i \left(1 + M \right) f\#} \right) \tag{3.24}$$

Equation 3.24 is equivalent to Equation 3.14, but expressed in terms of the independent variables with the DOF constraints described earlier. Equation 3.24 suggests that, for a given magnification, the sensitivity is directly proportional to the $f\#$ and the circle of confusion. This is directly due to the notion that increasing both parameters will increase the overall DOF of the imaging system, thus minimizing the ratio (l/b) found in Equation 3.14. Interestingly, the focal-length of the imaging lens and the overall length of the measurement system do not factor in. As such, one can conclude that, if appropriately set-up, a compact BOS system should perform just as well as a system with a larger footprint. Thus, BOS can be considered for applications where space is limited and other schlieren techniques are not applicable. An additional factor not accounted for here is that a compact system also places less of a demand on the illumination source for the background. In situations where the system length is fixed (e.g. background fixed to a wall), the above analysis can be used to determine the optimal settings for the cameras focus. As will be shown in Section 4, this can significantly improve the sensitivity of the measurement.

On the surface, this analysis is contrary to other analyses reported in the literature where it is implied or explicitly stated that increasing the focal-length of the imaging system will lead to increased sensitivity [63, 69, 70]. The current analysis indicates that focal-length does not directly affect the sensitivity. The key difference is that, in this work the desired FOV is known and is a fixed value whereas it is implicit in other works that increasing the focal length will lead to a reduced FOV.

3.3.2 Accounting for Converging Beam

In most typical schlieren experiments, collimating optics are used for parallelizing the beam from a point source, however they are not typically used in BOS, although use of collimating optics is seen in some BOS experiments in what is known as a schlieren mode of operation [56]. Thus, in a typical BOS experiment, the light beam originating from the background imaged in the BOS technique is converging (shown in Figure 3.4 with a concave wavefront), a feature which must be accounted for when considering the light beam distortion.

Figure 3.4 shows a minimalistic view of the BOS setup. Light rays originating from the background travel along a radial path to the camera to form an image. The wavefront thus formed of the converging beam, with no inhomogeneous IRF, has a nominal concave shape, shown by a solid wavefront in Figure 3.4. In the presence of an inhomogeneous field, a distorted concave wavefront is formed, shown with a dashed wavefront in the figure. For a given height of the IRF (i.e. for a given h_{near}), s_{near} is directly proportional to the focal length of the camera lens. This results in an inverse relationship between the cone angle formed by the incident light rays and the camera lens.
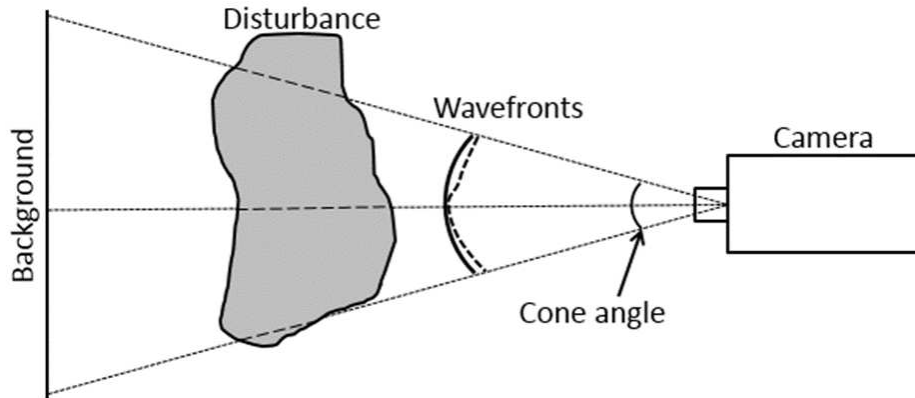
Figure 3.4: Concave shape of the wavefront.

Figure 3.5 shows the effect of the imaging lens focal-length on the measured distortion of the wavefront. In this case, the test object was a plano-convex lens (1000 mm focal length) placed between the background and the camera. Images were acquired with imaging lenses with 50 mm (bold line) and 75 mm (dashed line) focal-length. The magnitude of the distortion is displayed as function of radial distance from the center of the test object. In both cases, the f-number of 16 and a circle of confusion of 2 pixels was used to determine placement of the background relative to the test object and camera. As discussed in the previous section (and validated in the next section), these two configurations should lead to identical results; however, in this case, the use of a shorter focal-length imaging lens leads to a slight increase in the magnitude of the image distortion. This is not because the BOS system is more sensitive with the 50 mm lens compared with the 75 mm lens, but, rather, because the path of light rays through the index-of-refraction field (i.e. through the plano-convex lens) is different for the two different focal-length lenses. Here, the shorter focal-length imaging lens leads to a nominally more curved incident wavefront such that the light rays have a greater incident angle and longer path through the test object.

This observation represents a key difference between typical schlieren and a BOS imaging system. In both cases, the measured distortion is the integrated effect of the gradients in the index-of-refraction field along the line-of-sight. In the case of the schlieren technique, the light beam is parallel (planar wavefront) to light of sight. In the case of BOS imaging, the nominal wavefront is converging (converging lines-of-site) with a radius of curvature inversely proportional to that of the imaging lens focal-length.

3.4   Performance Analysis of BOS

Experiments, both simulated and physical, were conducted to validate BOS' applicability as a wavefront sensor and study its sensitivity to an inhomogeneous index field. To keep the experiments simple and repeatable, a known IRF, a 1,000 mm focal-length and 50.8 mm diameter plano-convex lens, was used. In the physical experiments, images were captured
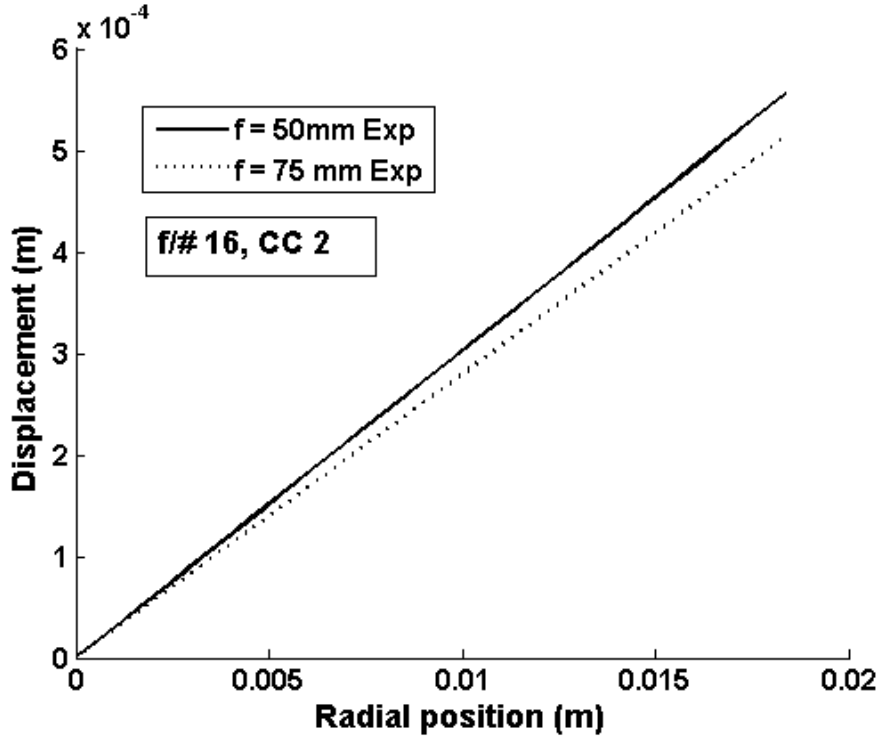
Figure 3.5: Figure showing the effect of concave wavefront when using different focal-length lenses.

using a Cooke corporation sensicam qe camera (1376 × 1024 pixel resolution and 6.45 um pixels) with interchangeable 25 mm, 50 mm and 75 mm lenses for imaging. The test object was physically placed between the camera and the background with all distances determined using the equations formulated in Section 3. In the simulated experiments, the distortion of a background image was computed based on the integration of the optical path length from a virtual background to a virtual camera with the plano-convex lens producing a known and specified geometry as given by the manufacturer. Experiments were designed to vary the focal-length, f-number and the circle of confusion (CC) with different combination of values shown in Table 3.1. Dependent variables, such as l, b, s_o, and s_i, used for the experiments were computed using the equations given earlier and are shown in Tables 3.2 and 3.3.

focal-length (mm)	25	50	75
f-number	8, 11, 16	8, 11, 16, 22	8, 11, 16, 22, 32
CC (px)	1, 2, 3	1, 2, 3	1, 2, 3

Table 3.1: Table showing focal length of each lens and the associated f-numbers and CC values for each lens.

3.4.1 Sensitivity Analysis

In this study, sensitivity is taken as the minimum measurable deviation (MMD) of the measurement. Here, this value is assumed to be equal to an image distortion of 0.1 pixels. This accuracy was assumed as it is generally consistent with accuracies observed using PIV image analysis software (used here), although, as will be seen, this is a conservative estimate. To study the effects of the parameters on MMD, experiments were simulated synthetically and the results validated by comparison with physical experiments conducted in the lab. The FOV of the synthetic experiments was fixed at 100 mm to emulate the particular lab conditions at AU. The input parameters of Table 3.1 were used with the analysis of Section 3.3 to determine the corresponding placement of the virtual camera, background and test object for each experiment.

Results from the synthetic experiments closely agree with physical observations and are plotted in Figure 3.6 and Figure 3.7.

Figure 3.6 shows the effect of the focal-length on MMD, expressed in radians. The data plotted in Figure 3.6 was obtained with the three camera lenses set at $f\#$ 16 to achieve a realistic DOF. The physical lengths used for setting up the experiments are shown in Table 3.2. As discussed earlier, changing the focal-length does not have an effect on the MMD, when the influence on the DOF is accounted for in determining the placement of the test object and the background.

To illustrate the importance of selecting the appropriate background location, two cases are shown in Figure 3.6: (i) plane of the effective refraction at the beginning of the DOF, s_{near}, and the background at the end of the DOF, s_{far}, represented as optimized, and (ii)

39
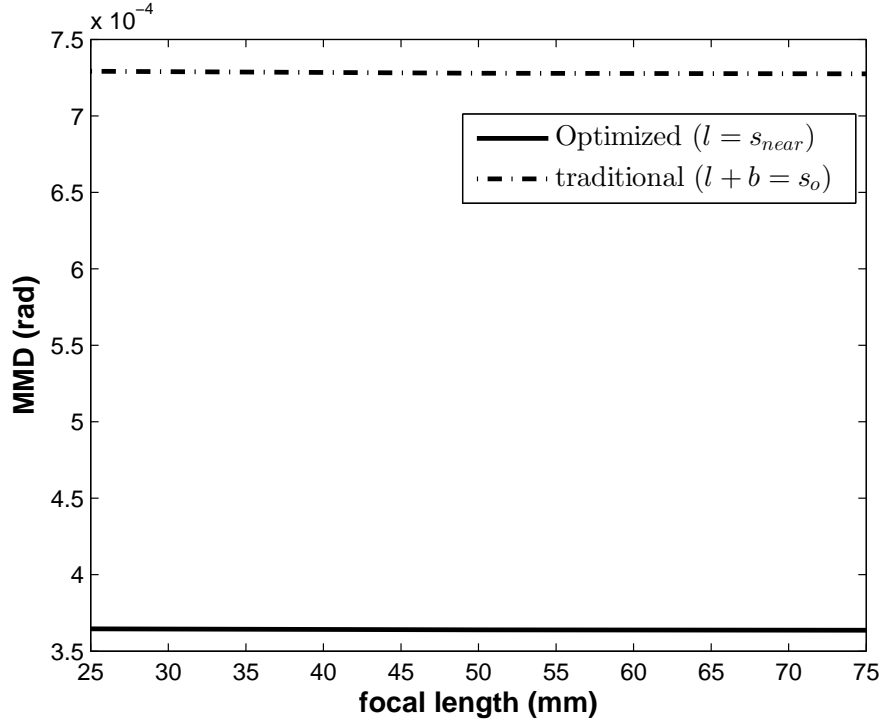
Figure 3.6: Effect on the MMD of the system with varying focal length lenses with the maximum f-number possible for each and keeping the 4" test-section in focus.

the background placed at the focal plane, s_o, and the effective refraction is placed at the beginning of the DOF, s_{near}, represented as traditional.

Focal length $(f) \rightarrow$	25 mm		50 mm		75 mm	
Properties ↓						
l	s_o	s_{near}	s_o	s_{near}	s_o	s_{near}
b (m)	0.0269	0.0575	0.0261	0.0537	0.0258	0.0526
$l + b$ (m)	0.4306	0.4596	0.8334	0.8595	1.2367	1.2620

Table 3.2: List of various properties associated with the data shown in Figure 3.7. Note the increase in overall length with increasing focal length.

From Figure 3.6, the optimized setup that exploits the full DOF of the imaging system is seen to have an MMD value half that obtained from the traditional set-up where the background is perfectly in focus. As discussed, the choice of the $f\#$ heavily influences the DOF and is directly proportional. The effects of increasing DOF with increasing $f\#$ on the

MMD are plotted in Figure 3.7. These results are for the optimized setup using a 75 mm focal-length imaging lens. The results are striking with nearly an order of magnitude improvement allowed by operating the lens at the highest possible $f\#$. For example, Table 3.3 shows the influence of $f\#$ on the DOF when a 75 mm focal-length lens is used on the camera with 1 pixel CC.
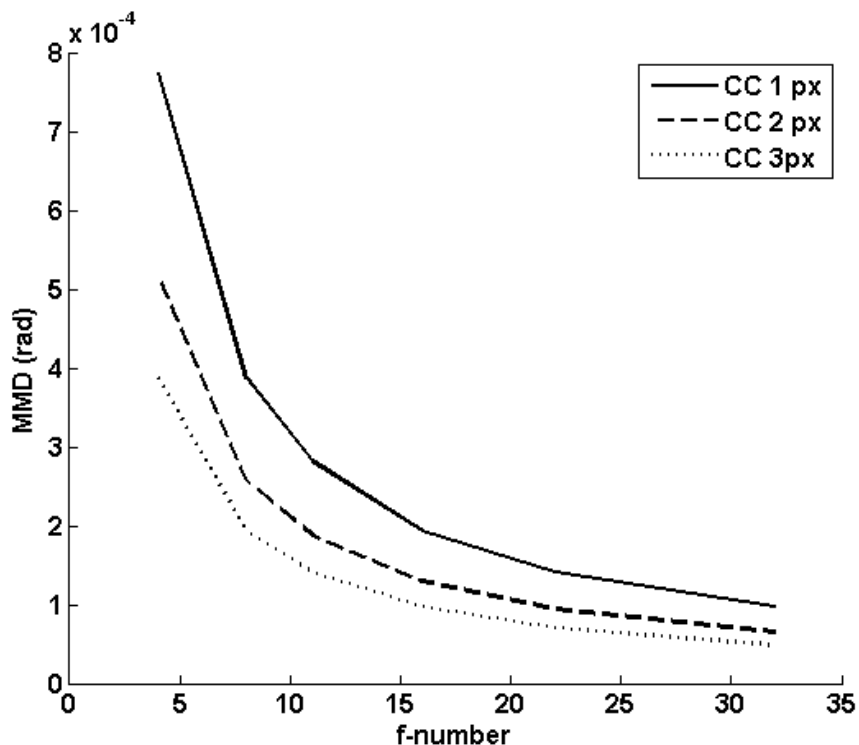
Figure 3.7: Effect of the size of the circle of confusion on the MMD.

f	4	5.6	8	11	16	22	32
b (m)	0.0127	0.0179	0.0258	0.0357	0.0526	0.0735	0.1098
$l + b$ (m)	1.2233	1.2283	1.2359	1.2456	1.2620	1.2823	1.3177
l/b	94.965	67.546	46.982	33.896	22.991	16.448	10.996
$(1 + l/b)\,(1/s_i)$ (rad/m)	1279.5	913.95	636.76	465.28	319.88	232.64	159.94

Table 3.3: List of various properties associated with the data shown in Figure 3.8 for circle of confusion 1 pixel. Note the increase in the ratio l/b with increasing f-number.

Increasing the DOF has two limitations. For one, at high $f\#$'s the image resolution will eventually be limited by diffraction as opposed to the geometrical analysis considered here.

41

Secondly, the amount of light passing through the aperture is inversely proportional to the square of the $f\#$. Increase in $f\#$ by one step decreases the amount of light passing through the aperture by half. Thus, increasing $f\#$ requires a brighter illumination source. This latter point is somewhat circumvented, however, by the realization that short focal length lenses can yield nearly the same MMD, thus allowing for the background to be placed much closer to the camera.

The effect of the CC on MMD is also studied by varying the size of CC between 1, 2 and 3 pixels. Observations from this analysis are also plotted in Figure 3.7. An increase in CC causes the DOF to increase, resulting in a more sensitive experimental setup. With the optimized setup, increasing CC also results in blurring of the background. This is in contrast to earlier works where the background is in the focal plane of the system for maximum resolution [63, 67]. There is evidence based on the imaging particles, however, that suggests that PIV algorithms actually achieve better results with some blurring with the recommended optimal particle size of 2-4 pixels [65, 66]. The use of wavelets in generating background demonstrated by Cook and DeRose [80] also shows little information loss with blurring. Thus, the current work suggests that mild blurring of the images can yield significant improvement to the sensitivity of the experiment.

3.4.2 OPD measurement and Error Analysis

Figure 3.8 shows an example of the raw images obtained of a background without and with the test object in the FOV. These images were captured using the 25 mm focal length lens with $f\#$ 16 and 3 pixel CC. It is hard to see the presence of any distortion with the naked eyes, but Figure 3.8(c) shows the displacement data obtained by processing these images using the cross-correlation algorithms used for PIV analysis with varying size of the interrogation region (detailed in random error subsection).

The aim of this section is to demonstrate the applicability of the BOS technique for wavefront sensing. This is done in two steps:
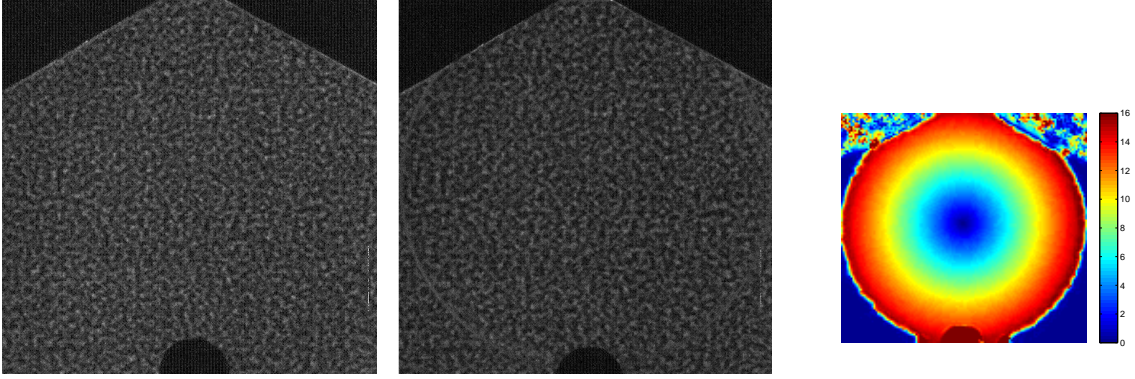
Figure 3.8: Sample images showing typical BOS data. a) Reference image of background without a disturbance; b) Distorted image of background caused by presence of a plano-convex lens between the background and the camera; c) Measured displacement of the image (color bar represents number of pixels displaced).

1. the displacement data, d_i, in units of pixels, determined from the cross-correlation algorithm is converted to angular distortion, ε, in units of radians, and

2. a reconstruction algorithm is applied to the angular distortion data to determine the local phase of the wavefront, expressed in terms of an optical path difference.

The displacement data, obtained from image processing, when divided by the magnification of the background gives the virtual displacements, d_{far}, seen at the background shown in Figure 3.2.

$$d_{far} = \frac{d_i}{M_{far}} \tag{3.25}$$

where, M_{far} is the magnification at the background. ε is then calculated from:

$$\varepsilon = \frac{d_{far}}{b} \tag{3.26}$$

In the above equation ε is assumed small. The wavefront distortion data thus obtained is directly used for wavefront reconstruction.

There are several techniques described for OPD measurement. Some of the techniques explored for this work were from computer vision which are described as Shape from Shading

[81] or Fast-Fourier techniques [82–84]. The outputs from these techniques are sensitive to the various parameters used, and are still the point of investigation. For this work, the iterative technique described by Southwell [85] which was used for successful wavefront reconstruction from SHWS data in earlier studies was elected.

Figure 3.9 shows an example of a reconstructed wavefront and the associated OPD distribution. Data used for this reconstruction was obtained with the plano-convex lens as the test object imaged with the 75 mm focal-length lens set at $f\#$ 16 and 2 pixel CC. The plot in Figure 3.9(a) shows the 3D wavefront distortion where the concave shape is consistent with the function of the plano-convex test object. OPD distribution on the wavefront is shown in Figure 3.9(b). The color bar shows the magnitude of the OPD in meters. For comparison, the expected/synthetic wavefront and associated OPD are shown in Figure 3.10. From a quick look, the data from the experiment qualitatively matches the synthetic data.
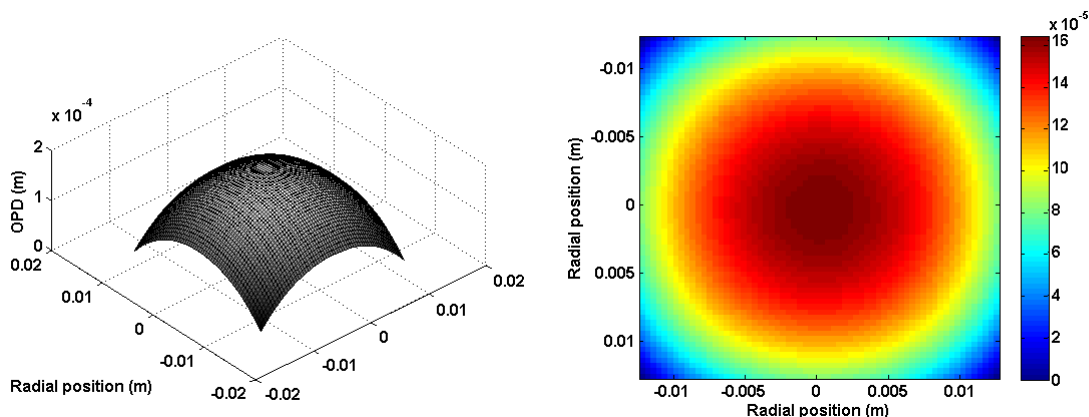
Figure 3.9: Figure showing a) the 3D reconstructed wavefront and a) the OPD distribution from the experimental data.

A better comparison of the magnitudes is given in Figure 3.11, where the distribution of the percentage difference at each point on the surface is shown. An error of $\pm 5\%$ is seen near the corners of the wavefront although the vast majority of the wavefront has an absolute error in the OPD on the order of 1%-2%. An uncertainty analysis was conducted focusing on the error in the reconstructions process.
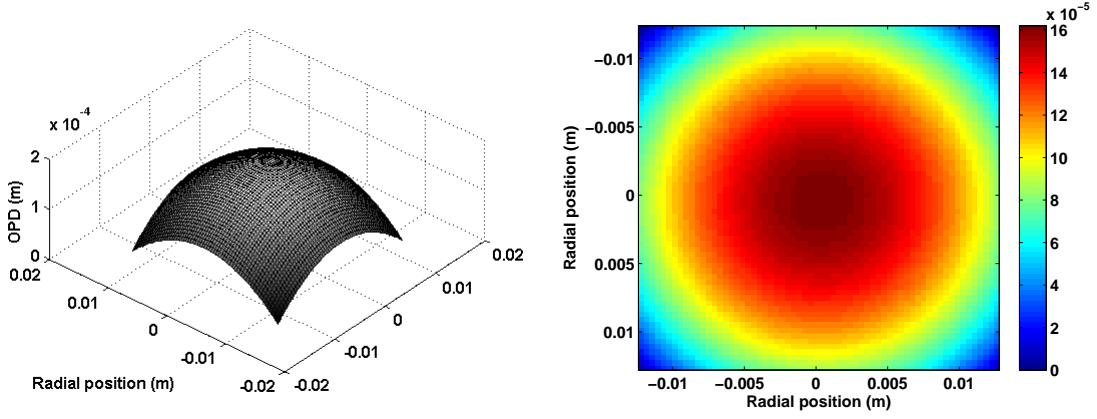
Figure 3.10: Figure showing a) the analytical wavefront and b) the OPD distribution.
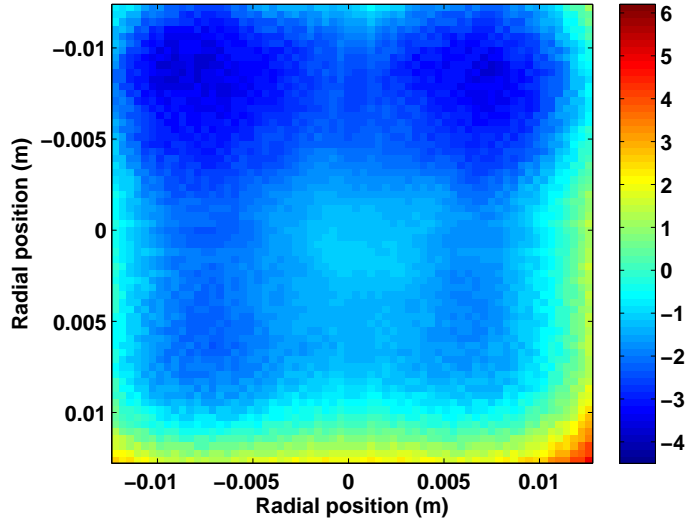
Figure 3.11: Figure showing the percentage error distribution in the calculated OPD.

To understand the error and its propagation, ε (given in Equation 3.14) is written in differential form as:

$$\partial \varepsilon = \partial l \left(\frac{1}{b}\right)\left(\frac{d_i}{s_i}\right) - \partial b \left(\frac{l}{b^2}\right)\left(\frac{d_i}{s_i}\right) - \partial s_i \left(\frac{l}{b} + 1\right)\left(\frac{d_i}{s_i^2}\right) + \partial d_i \left(\frac{l}{b} + 1\right)\left(\frac{1}{s_i}\right) \quad (3.27)$$

The first three terms on the right hand side of Equation 3.27 are associated with the physical geometry of the experimental arrangement and represent the uncertainty in the placement of the camera relative to the background and wavefront exit plane. These uncertainties affect the whole data and can be described as the systemic or biased uncertainties. The last term on the right hand side of the equation is the random uncertainty associate with PIV algorithms which is well documented [65, 66].

Bias/Systemic Error: It is easy to setup an experiment to precise values in an analytical/synthetic model, but setting it up physically induces errors due to human involvement.

As seen in Equation 3.27, uncertainty in l, b, and s_i result in a bias error. To investigate the effect of the individual terms, three different simulated experiments were conducted:

1. varying l with b and s_i fixed,

2. varying b with l and s_i fixed, and

3. varying s_i with l and b fixed.

Results from these experiments are plotted in Figure 3.12. In all the three experiments, 75 mm focal-length lens was used with aperture set at $f\#$ 22. The index field was generated to model the plano-convex lens. The error percentage in Figure 3.12(a) and 3.12(b) is defined as:

$$error\% = \frac{\varepsilon_e - \varepsilon_m}{\varepsilon_e} * 100 \tag{3.28}$$

where, the subscripts e and m denote the expected and the measured values.

For a given set of conditions (fixed f, $f\#$ and CC), Figure 3.12(a) shows systemic error in the measured deviation caused by the uncertainty in measuring l and Figure 3.12(b) shows systemic error due to error in measuring b. A linear relationship is seen in both plots. For the given Δl or Δb, blurring the images (i.e. increasing circle of confusion) is seen to reduce the error percentage as the overall length of the experiment is increased such that the relative, fixed error in positional accuracy is decreased. It is observed that increasing CC has a much

46

more significant effect on the error associated with b than it does with l. In addition, it was notice that the effect of Δb is significantly greater, by at least an order of magnitude, than the effect of Δl and Δs_i. Thus, an accurate measurement of b is important for better accuracy from BOS.

Evaluating the effects of error in measuring l and b is simpler than investigating the effect of the error in s_i, as there is no change in the magnification of the system with errors in l or b. Changes in s_i causes the magnification of the system to change, therefore, before looking at the effects of uncertainty in measuring s_i on ε, the relation between Δs_i and Δs_o is studied. Results from the simulated experiment are shown in Figure 3.12(c). This data was collected with the 75 mm lens with $f\# = 22$ and CC $= 2$ pixels. The x-axis in the plot represents Δs_o and y-axis represents Δs_i. From the figure, an error of 30 mm in measuring the nominal focal plane of the imaging lens results in an error of 0.36 mm in s_i. Fortunately, the error associated with these parameters is quite low. For example, when an error of 10 mm in measuring s_o was considered, an error of -0.26% was measured in the deviation angle.

Experimental results that match the best and worst with the expected output are presented in Figure 3.13. The x and y axes in these plots represent the radial position and the image displacement in meters respectively. In these plots, the dashed line with error bars represents the analytical/expected data and the solid line represents the data from the experiments. The error bars on the analytical data represents the range of the expected deviation values when the uncertainty in DOF, Δb, is 1 mm.

As expected, the experimental data shows the displacement values increase linearly when moving away from the lens axis along the radius. The experimental data in Figure 3.13(a) matches closely with the expected output, giving the best match from the set of experiments done and the data in Figure 3.13(b) shows the least matching results. Further evaluation of the data shows that a systemic error of -0.6 mm and 7.7 mm in the DOF, Δb, can explain the observed errors. In fact, it is not surprising that the best results were achieved with the 75 mm focal length imaging lens and worst with the 25 mm focal-length lens. The overall length

(a)

(b)

(c)
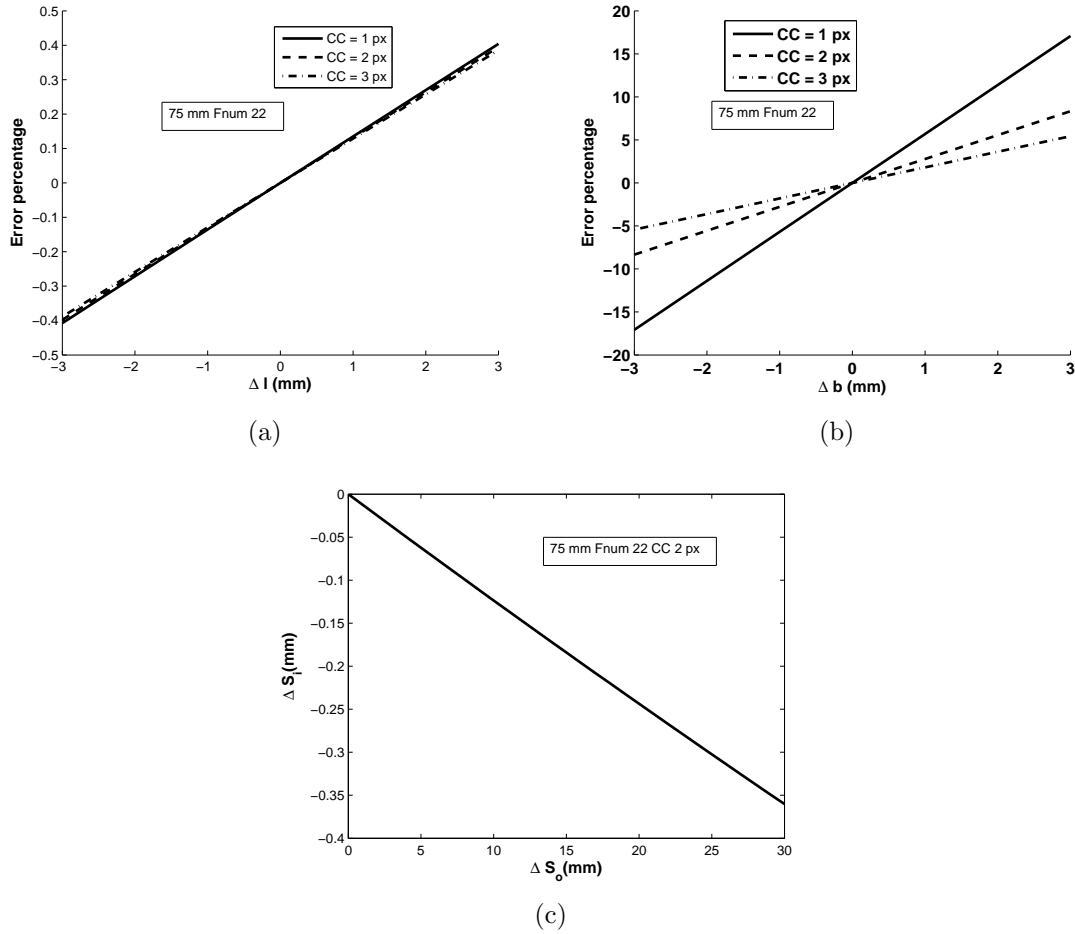
Figure 3.12: Plots show the error data from the synthetic models. Error percentage in the measured data when there is an error in measuring (a) l and, (b) b. Plot in (c) shows the error in s_i when there is an error in measuring s_o.

of the system is proportional to the imaging lens focal-length such that a longer focal-length tends to mask small positional errors whereas a short focal-length lens makes the same error appear large by comparisons.

As shown in Figure 3.14, when the error in Δb is accounted for, the measured results match the expected results. From Figures 3.13 and 3.14, it is observed that the error in measuring b affects the whole data and can be corrected for with good calibration images. In fact, a plano-convex lens with known focal-length is suggested here to be a good calibration target due to the linear relationship between deflection angle and radial position.
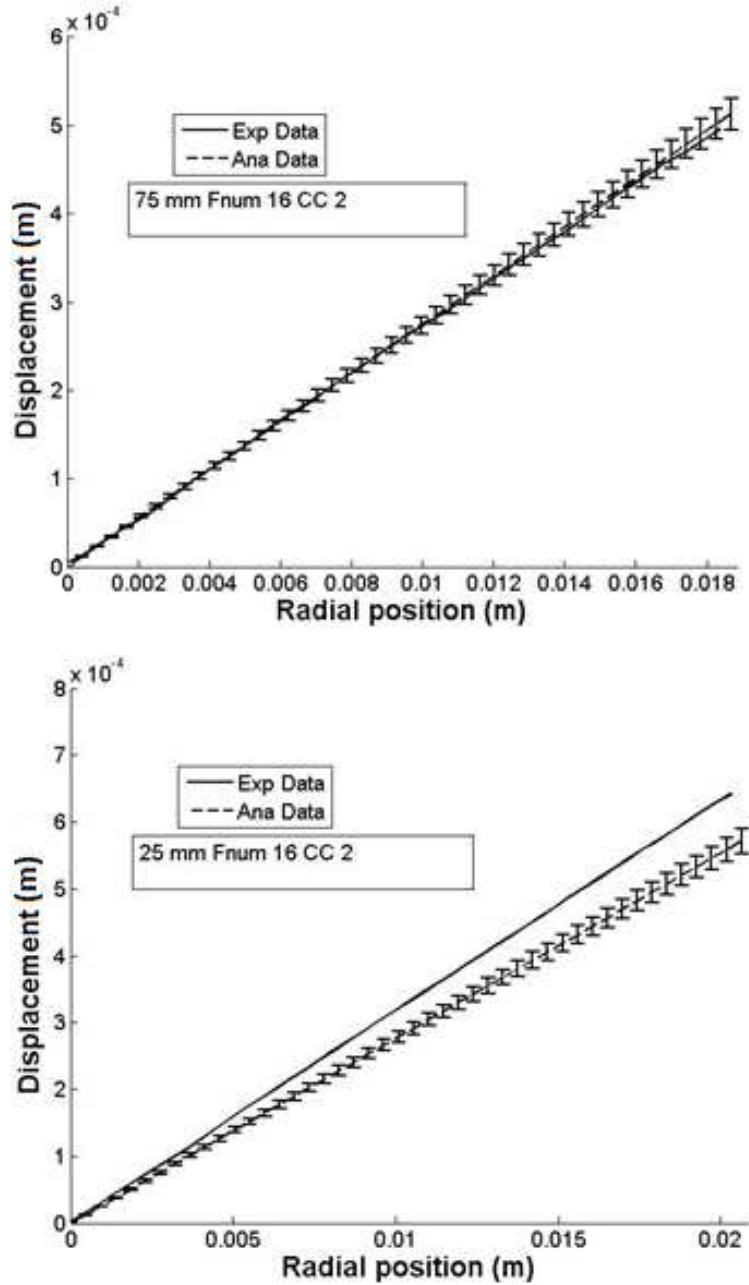
Figure 3.13: Plots show the experimental data compared to the expected data. a) Best and, b) worst match.

Random Error: To assess the random error associated with the image processing algorithms, statistical analysis was performed on both synthetically generated and experimental data. Images obtained synthetically and experimentally were processed using PIV algorithms. Displacement values measured by the PIV algorithms varied from 0-16 pixels.
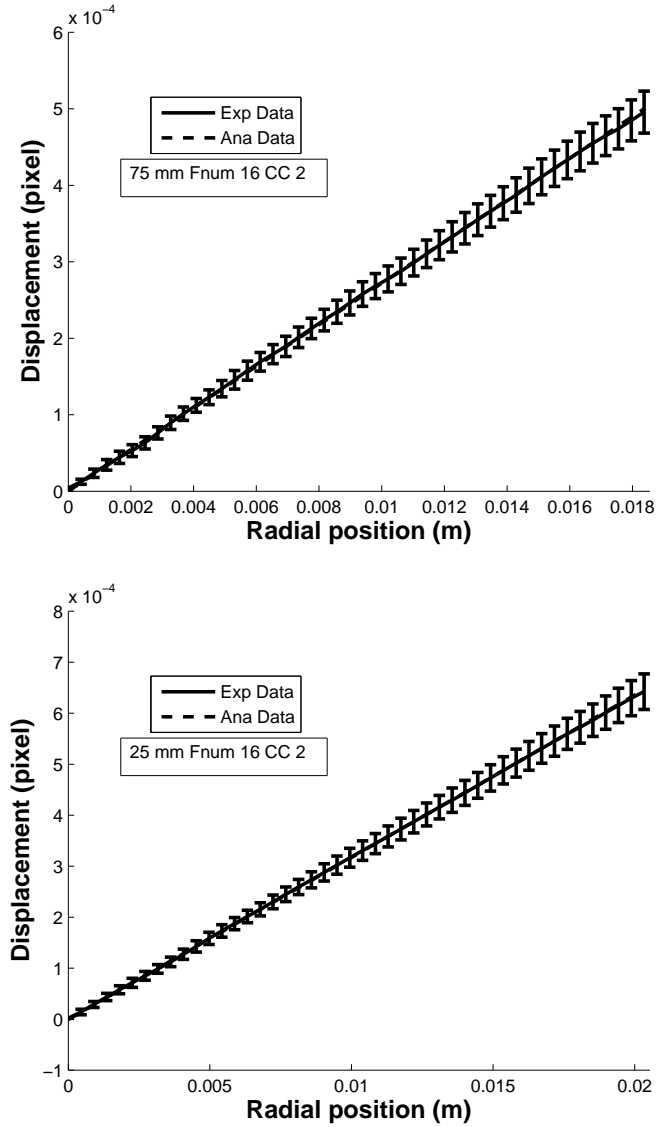
Figure 3.14: Plots show the experimental data compared to the expected data after accounting for the Δb calculated from calibration images. a) Best and, b) worst match.

To ensure the size of the measured displacement is less than 1/4 the size of the interrogation regions in PIV process, images were divided into two regions, one with the displacement value less than 8 pixel and the other where it was greater than 8. The portion of the image with less than 8 pixel displacement was processed with 32×32 pixel size interrogation regions and the rest with 64×64 pixel size interrogation regions. The overlap between the

neighboring interrogations was 75% and 87.5% respectively. Displacement data from the PIV process was then compared with the expected distortions to obtain the difference.

Synthetic data was obtained from processing two background images generated analytically, one without the influence of the index field in the image (reference) and the second with the influence causing the background to distort. Known properties of the plano-convex lens were used to analytically generate OPD caused by it. This OPD data was then used to obtain the distortion it would cause to the background image when captured with the 75 mm lens set at $f\#$ 16 and 2 pixel CC. Distortion data thus obtained was then used to warp the reference background with the method described by Brox et al. [86].

Statistical analysis was done on two sets of data. One set of data was collected from 360 radial lines through the center of the image each separated by 1° on a single correlated image pair. The other set of data was collected from a single radial line across a set of 330 correlated image pairs.

The standard deviation measured from processing the data obtained with 75 mm lens set at $f\#$ 16 and 2 pixel CC is shown in Figure 3.15. Figure 3.15(a) shows the plot from the analysis of the synthetic data and Figure 3.15(b) shows the plot from the analysis of the experimental data. The x-axis in both plots show the radial position on the plano-convex lens and the y-axis show the measured standard deviation, both measured in meters. When compared with the size of a single pixel of the camera used in the experiments, 6.45 um, values of the standard deviation measured on the synthetic data are less than 0.04 pixels, approximately 0.28 um. Standard deviation measured on the experimental data is less than 0.4 um, which approximately measures to 0.06 pixels. The accuracy measured in both, synthetic and experimental, data is better than 0.1 pixels. Similar results were obtained with other data sets.

Figure 3.16 shows the results from the same data, but after it has been converted to OPD. Data used for this reconstruction was taken from the experiments with 75 mm lens set at $f\#$ 16 and 2 pixel CC. In Figure 3.16, the OPD from a slice passing through the
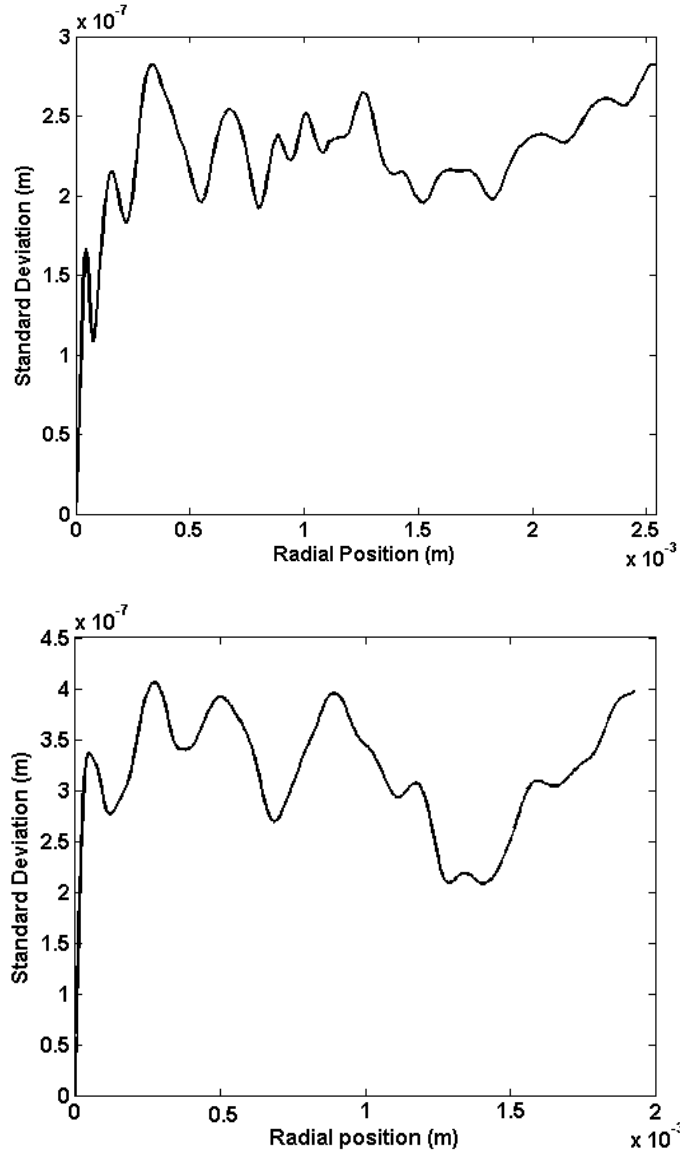
Figure 3.15: Plots showing the standard deviation measured on the displacement data obtained from image processing. a) Synthetic data, and b) experimental data

optical axis of the plano-convex lens is plotted. The solid line represents the synthetic data obtained from the simulated experiment and the dashed line with error bars represents the OPD from the physical experiments. Error bars account for the uncertainty in the shape of the plano-convex lens as specified by the manufacturer. When accounted for the uncertainty in manufacturing, the experimental OPD agrees quite closely with the synthetic OPD.

Fluctuations in the random error appear indiscernible in the experimental OPD data, but a closer look at the data when fitted with a low order polynomial curve reveal the fluctuations, shown in Figure 3.16(b). The norm of the residuals from the curve fitting is less than ±0.7um. This value is about two orders smaller than the OPD, implying an error percentage less than 0.12%, giving confidence in the application of BOS for OPD measurement.
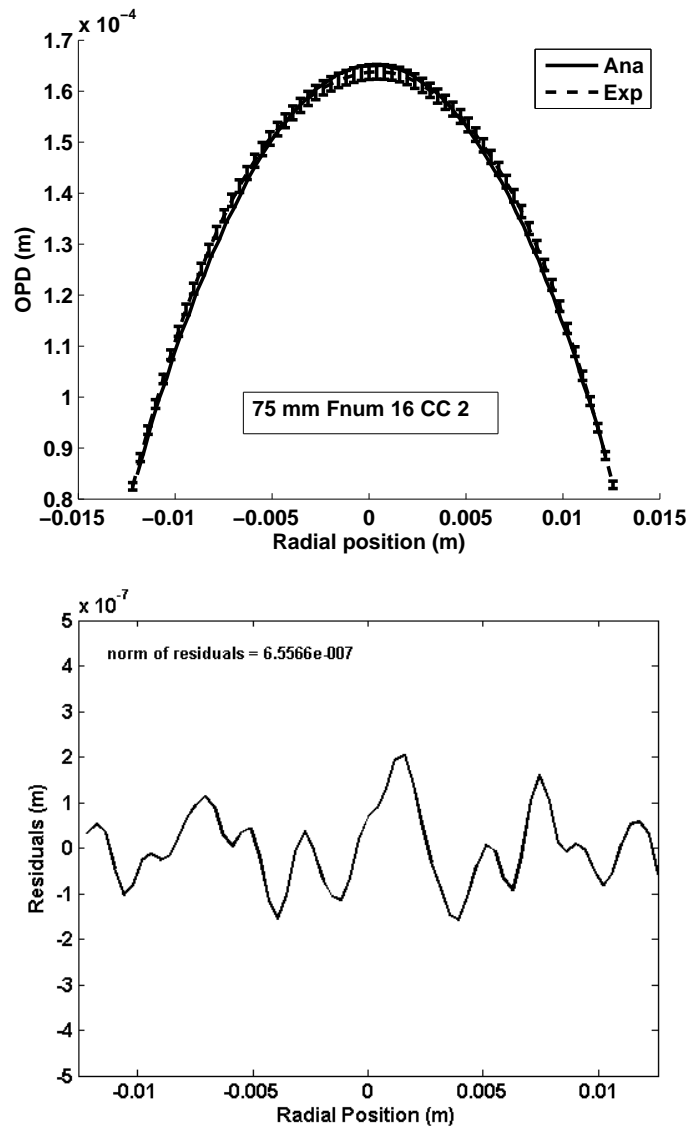
Figure 3.16: Figure showing the a) center line OPD comparison and b) standard deviation in the showing the small fluctuations in the measurements.

3.5 Summary

The feasibility of using a BOS imaging system for OPD measurements is clearly demonstrated in this chapter. As the distortion of a wavefront is governed by the same physical phenomena as BOS (refraction of light in an inhomogeneous medium), determination of OPD data from BOS data is a fairly straightforward process.

In the process of developing this relationship, some of the basic equations describing the BOS technique were reformulated in terms of variables typically accessible to researchers employing the technique. Specifically, the equations were written under the constraint that the imaging system has a fixed FOV and that the test object and background must be placed at front and back plane of the DOF as determined using geometrical optics. In this sense, the background and test object are considered as having the same spatial resolution. For the PIV algorithms used here, this constraint is overly strict; however, as the development of optical flow algorithms with high spatial resolution continues, this constraint is expected to be quite relevant, particularly if one is interested in optimizing the spatial resolution. In addition, it was found that the focal-length of the imaging lens does not affect the sensitivity of the BOS system as the DOF scales with focal-length. Rather, the sensitivity is better characterized by the relative DOF of the imaging system, which is best represented by the $f\#$ of the imaging lens and the desired resolution of both the background image and test object as given by the circle of confusion.

This reformulation is significant because it implies that BOS can be used for OPD measurements in space-limited environments and does not require the lengths normally associated with schlieren imaging experiments. In addition, the analysis offers guidelines for optimizing the sensitivity of a given experiment and demonstrates that placement of the background at the focal plane is a less than optimal condition. Along these lines, it is shown that allowing the background to be blurred slightly can yield significant improvements in the sensitivity.

These results were validated using both synthetic and real experimental data. The experimental data was also used to assess the uncertainty of both the BOS displacement data and the reconstructed data. In both cases, the accuracy was found to be quite good with the most significant errors being systemic errors associated with uncertainty in the alignment of the system components (camera, test object, background). It is suggested, however, that a calibration experiment using a known object, such as the plano-convex lens used here, can minimize this source of error. Random errors are associated with the uncertainty in determining the image displacement. It was found that a 0.1 pixel estimate is conservative under the conditions examined here although more detailed analysis would be needed for an arbitrary situation. When converted to wavefront data as represented by the optical path difference, the accuracy was better than 1% proving the feasibility and potential of the technique.

In this chapter, viability of BOS for wavefront sensing/OPD measurement was demonstrated. OPD measured from BOS is the integrated effect of the inhomogeneous nature of the flow field along the path of the light rays that originate at the background and form the image on the image sensor. This is similar to the energy dissipation observed in images obtained in CT. Thus, if the BOS data is obtained from multiple views for a flow field, simultaneously, this data can be used to reconstruct the instantaneous density distribution of the flow field. In Chapter 4, discussion on the use of a plenoptic camera to capture BOS images from multiple views is presented and in Chapters 5 and 6, discussions on the tomographic reconstruction technique used in this work for reconstructing the 3D density distribution of the flow field and its implementation are presented.

Chapter 4

Plenoptic Camera

Michael Faraday introduced the idea of light field in 1846 [19], but it was not until 1936 that the term light field was coined [87]. In 1986, Kajiya introduced the concept of light field to the field of computer graphics while working on generalizing the rendering equations [88]. The concept of light field imaging (LFI) was first introduced in 1991 by Adelson and Bergen [89]. In 1992, Adelson and Wang showed the stereo imaging capabilities of the plenoptic camera with a single camera lens [90]. Since its introduction, LFI has found applications in many areas such as hand-held photography [91,92], microscopy [19], consumer photography (Lytro), aerodynamics [93,94] and others.

Images captured with a conventional digital camera capture the spatial information of the FOV, whereas the images captured with a plenoptic camera capture both the spatial and angular information, i.e. the light field, of the FOV. As the data imaged in the plenoptic camera captures information of a volume, going forward this volume is referred to as the volume of interest (VOI). Once imaged, the light fields captured with the plenoptic camera can be used to computationally reconstruct the 3D spatial information of the VOI. Light fields can be used to computationally:

1. Generate perspective views looking of the VOI at different angles within the limits of the camera lens aperture,

2. Generate images with extended DOF, and

3. Refocus the captured plenoptic image to any desired plane in the VOI.

In this chapter, the design and working principles of the plenoptic camera with a discussion on how the information from the captured light fields are used to computationally achieve

56

one of the three above mentioned tasks is presented. Plenoptic cameras developed and constructed by the AU AFDL that are used in this research are also presented.

4.1 Plenoptic Function

The plenoptic function, as defined by Adelson and Bergen, allows the reconstruction of every possible view, at every moment, from every position, at every wavelength, within the bounds of the space-time-wavelength region under consideration [89].

$$L = L(x, y, \lambda, t, u, v, w) \tag{4.1}$$

In the above equation, L is the light field, (u, v, w) represents location of the camera aperture in every possible location, (x, y) represents every location on the image sensor, λ represents every wavelengths and t represents every time. When considering only the still imagery, plenoptic function can be defined as a five-dimensional (5D) function.

$$L = L(x, y, u, v, w) \tag{4.2}$$

Moon and Spencer [95] and Levoy and Hanrahan [96] found redundancy in the above equation when the (u, v) plane has a fixed location and reduced the 5D plenoptic function to a 4-dimenisional (4D) function.

$$L = L(x, y, u, v) \tag{4.3}$$

The 4D plenoptic function in Equation 4.3 is referred to with different names: photic field [95], 4D lumigraph [97] or 4D light field [96]. From here on, the use of the plenoptic function refers to the 4D plenoptic function given in Equation 4.3.

4.2 Plenoptic Camera

Adelson and Wang defined a plenoptic camera as the camera that records information about how the world appears from all possible viewpoints within the lens aperture [90]. Plenoptic images or light fields can be captured in a variety of ways [20]:

1. by mounting a camera on a gantry and taking images from different positions,

2. by using an array of cameras, or

3. by mounting a microlens array between the lens and the image sensor of the camera.

In this work, plenoptic cameras with microlens arrays mounted between the lens and the image sensor are used. A schematic of the plenoptic camera used in this research is shown in Figure 4.1(a).
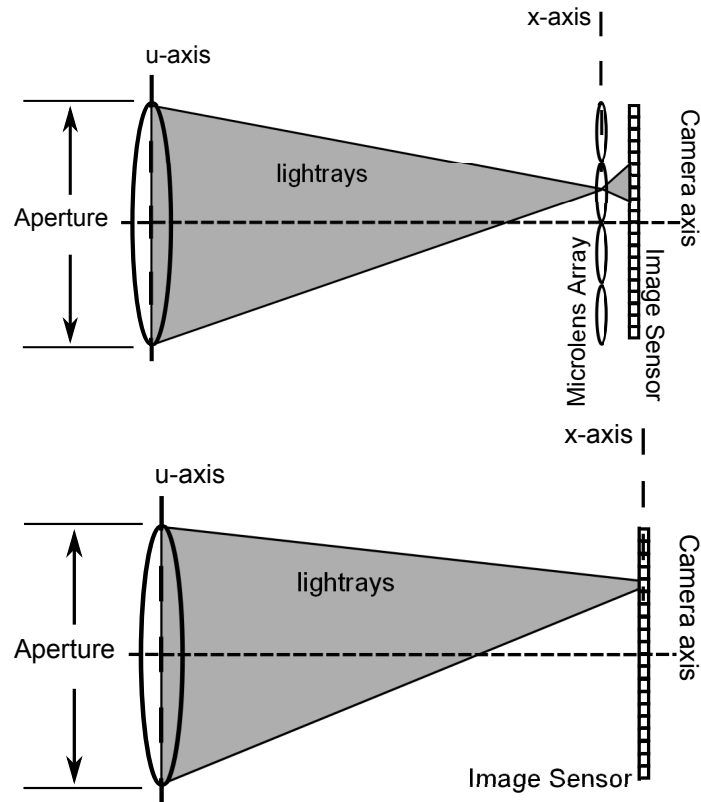
Figure 4.1: Images showing the schematic of a) plenoptic and b) conventional cameras.

The difference in the construction of the plenoptic camera from a conventional camera causes the difference in the way an image is formed on their image sensors. In a conventional camera, shown in Figure 4.1(b), light rays passing through the lens aperture converge on a pixel and the pixel value is a function of the weighted sum of light converging from the aperture. The weight here is a function of the angle between the incident ray and the normal of the image sensor plane. In integrating the light coming from the aperture, all the directional information of the light rays is lost. In plenoptic cameras, the use of the microlens array divides the image sensor into subregions of equal size. The light coming from the lens aperture converges on the microlens array as opposed to the conventional camera where the light converges on the image sensor. The image formed by each microlens is essentially an image of the main lens aperture such that each pixel in the subregion corresponds to a different point on the aperture, thus preserving the angular information of the light field.

In Figure 4.2, the idea of storing the information in a pixel from a particular region of the lens in the plenoptic cameras is seen. Extending the idea to demonstrate the effect and the difference in the image formation between a conventional and the plenoptic cameras, schematic images showing image formation when a light source is:

1. at the focal plane,

2. located closer to the camera than the focal plane, and

3. located farther away from the camera than the focal plane

are shown in Figures 4.3 and 4.4.

With the conventional camera, when the light source is at the focal plane of the camera setup, a sharp image is formed on the image sensor. Moving the light source closer or farther from the camera blurs the captured image. The two blurred images of the light show no difference when compared to each other. When imaging the same light source with the plenoptic camera, shown in Figure 4.4, the captured images in all three instances differ from one another. When the light source is placed at the focal plane, the light source's image fills

59

up a microlens on the microlens array and the pixels right behind it on the image sensor. As the source is moved away from the focal plane, either closer to or away from the camera, the image of the light source on the microlens array blurs and spreads to more than one microlens. As the incident angle of the light on the microlens array varies depending on whether it is moved closer to or farther away from the camera, only certain pixels under the microlens get illuminated as a function of the incident angle. Illumination of the pixels behind the microlens as a function of the incident angle varies the image formed on the image sensor. Thus the information captured in plenoptic cameras carry both spatial and angular information of the captured light.
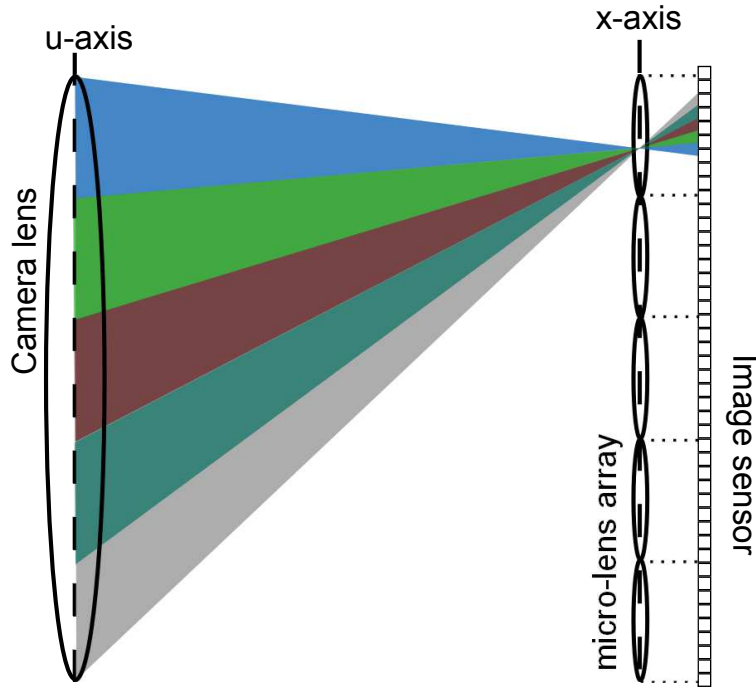
Figure 4.2: Image showing the preservation of angular information of a light field in plenoptic cameras.

4.3 Processing Light Fields

Images captured with plenoptic cameras are available for simulations of fully general imaging configurations, such as camera views where the lens and sensor are not parallel, or even non-physical models such as general linear cameras [98] or imaging where each pixel
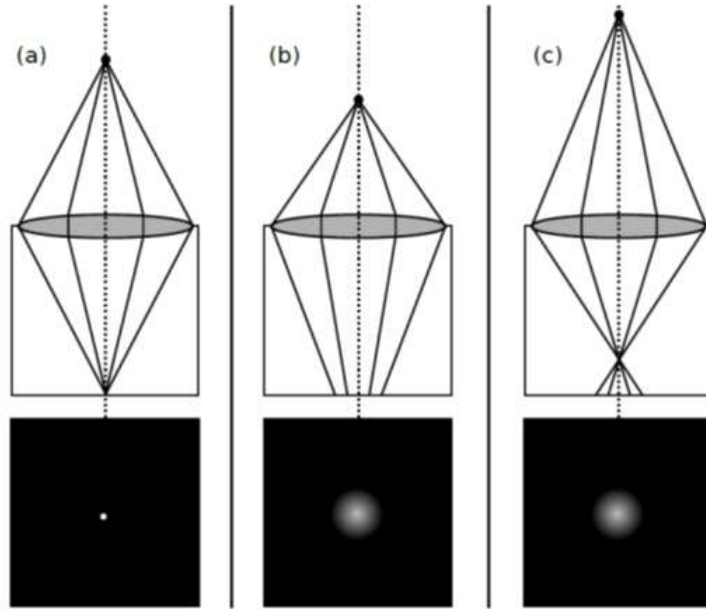
Figure 4.3: Images showing the schematic of image formation with a conventional camera when the light source is a) at the focal plane, b) closer to the camera than the focal plane and c) farther from the camera than the focal plane [93].
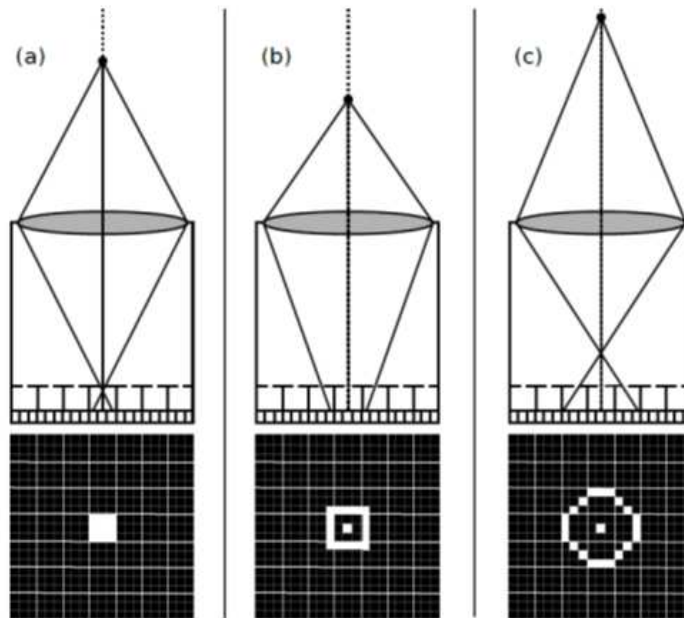
Figure 4.4: Images showing the schematic of image formation with a plenoptic camera when the light source is a) at the focal plane, b) closer to the camera than the focal plane and c) farther from the camera than the focal plane [93].

is focused at a different depth [91]. The focus in this work is to generate perspective view images with synthetic image sensors parallel to the original aperture and the image senor. Therefore, image synthesis assume that the original aperture plane, image sensor plane, and the synthetic image sensor plane are parallel to each other, as shown in Figure 4.5. Photographs are computed from the light fields as if they were taken with a conventional camera with synthetic setup that is different from the original setup. Original here refers to the conditions in which light fields are acquired.
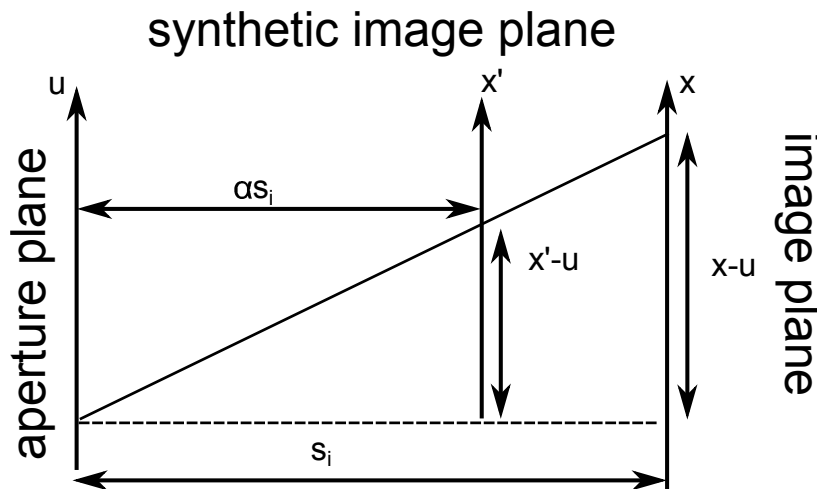
Figure 4.5: Schematic showing synthetic photography in 2D.

4.3.1 Sub-aperture Images

For the purpose of discussion, a plenoptic camera with $n_s \times n_s$ pixels in each subregion is assumed with the camera lens set at f-number $f\#$. The definition of the f-number of the plenoptic camera differs from that used in the conventional camera. As reasoned by Ng [92], the full potential of the plenoptic camera is utilized when the image behind each microlens occupies the maximum number of possible pixels without overlapping with the images formed from the neighboring microlenses. This condition is met when the effective f-number of the camera lens matches the f-number of the microlenses.

The f-number on the camera lens is given by:

$$f\# = \frac{f}{d_a} \tag{4.4}$$

Where, f is the focal length of the lens, d_a is the diameter of the aperture on the camera lens.

The effective f-number of a plenoptic image called the image side f-number, as defined by Ng [92], is given by:

$$f\#' = \frac{s_i}{d_a} \tag{4.5}$$

Where, $f\#'$ is the image side f-number and s_i is the distance between the principle plane of the lens and the plane with the microlens array.

From the lens equation,

$$s_i = f\left(1 + M\right) \tag{4.6}$$

Where, M is the magnification of the setup respectively.

Using Equations 4.5 and 4.6, the image side f-number in terms of the f-number of the lens is given by:

$$f\#' = \frac{f\#}{(1 + M)} \tag{4.7}$$

F-number of the microlens is defined as:

$$f\#'_{micro} = \frac{f_{micro}}{p_{micro}} \tag{4.8}$$

f_{micro} and p_{micro} in Equation 4.8 are the focal-length and pitch of the microlenses respectively. As suggested by Ng [92], for the efficient use of the plenoptic camera, f-numbers from Equation 4.7 and Equation 4.8 must match.

Coordinate systems used in partitioning the plenoptic image is shown in Figure 4.6. The plenoptic image/the microlens plane represents the (x,y) coordinate system. The subregions

corresponding to each microlens in the plenoptic image/ the region behind each microlens is represented by the (u,v) coordinate system. Because each microlens receives light from the full aperture of the camera lens and converges it onto the region behind it, the (u,v) coordinate system in the subregions is representative of the camera lens aperture.
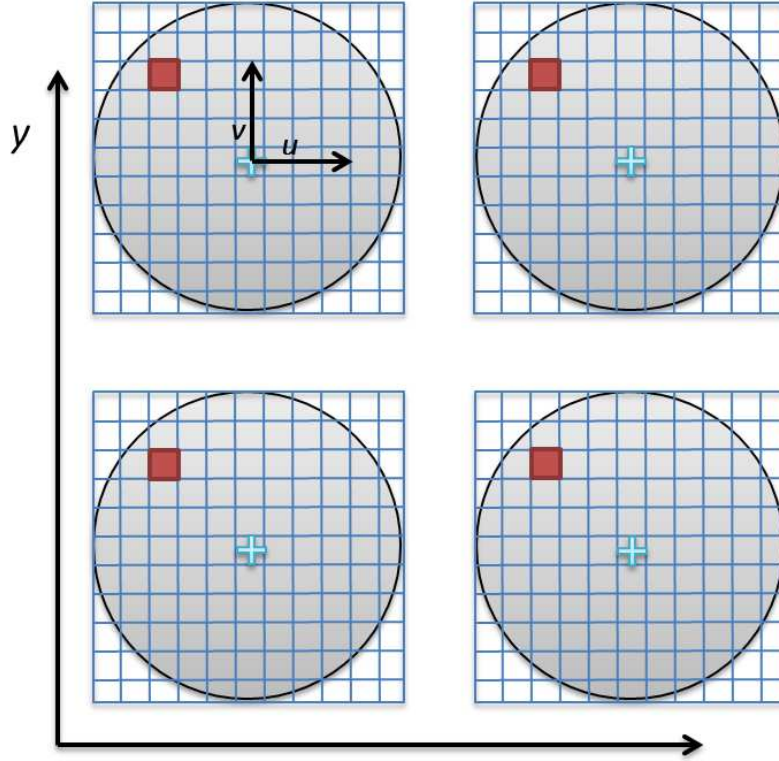
Figure 4.6: Schematic showing the coordinate systems used for partitioning the plenoptic image.

Synthetic subaperture images are computed by extracting data from the light field captured with the plenoptic camera with the above settings. A subaperture image is generated by extracting image information from each subregion in the plenoptic image with constant (u,v). This subaperture image mimics the image captured with a conventional camera with an f-number of $f\#' \times n_s$. The aperture of this virtual camera is centered at the (u,v) location on the aperture of the camera lens on the plenoptic camera. Changing the location from which data is extracted changes the location of the virtual camera in the (u,v) plane thus changing the perspective of the simulated image.

Choosing two different location on the (u,v) plane gives two different perspectives and the maximum distance between any two points on the (u,v) plane is equal to the diameter of the lens aperture, d_a. Thus, the maximum difference between any two perspective on the (u,v) is d_a. Given two conventional cameras separated by d_a and focused on the same object plane, angular disparity between the two is given by:

$$\theta = \tan^{-1}\left(\frac{d_a}{s_o}\right) \tag{4.9}$$

Where, s_o is the distance between the camera lens and the object plane.

An image of a scene with some cameras, their accessories and the book titled Introduction to Light Field Imaging placed on a table captured with the plenoptic camera is shown in Figure 4.7. Perspective views generated from this image are shown in Figure 4.8. The image in Figure 4.8(a) gives the perspective view of the scene from left when compared with the image in Figure 4.8(b). For a better visual reference, two arrows in the image points to two noticeable disparities in the perspective views. The perspective views generated with the method described above have an extended depth of field as they mimic conventional cameras with the f-number, n_s times higher than the image side f-number of the setup.

The number of pixels in each perspective view generated from the plenoptic image is equal to the number of microlenses in the microlens array used in the plenoptic camera. Thus, the resolution of the perspective views is n_s times smaller than the resolution of the image taken with the same camera without the microlens array. As seen, use of the microlens array in the camera makes it capable of capturing plenoptic images that have both the spatial and angular information of the light field at the cost of reduced spatial resolution.

As seen in Chapter 3, increasing the size of the circle of confusion results in an increased DOF allowing the user to set a more sensitive experiment. For the perspective views generated from the plenoptic camera, microlenses on the microlens array can be considered as the virtual pixels. Thus, giving users the ability to capture perspective views with large DOF

Figure 4.7: Picture of a scene with cameras, their accessories and a book placed on a table imaged with the plenoptic camera [99].

without penalizing the brightness of the image. Thus, the large size of the microlenses is an advantage in setting up BOS experiments.

4.3.2 Digital Refocusing

Stroebel et al. [100] expressed the image formation in a conventional cameras using classical radiometry as:

$$E_{s_i}(x, y) = \frac{1}{s_i^2} \int \int L_{s_i}(x, y, u, v) \cos^4 \theta \, du \, dv \tag{4.10}$$

s_i in the above equation is the distance between the aperture and the image sensor. L_{s_i} is the light field inside the camera body with separation s_i and defined as a function of
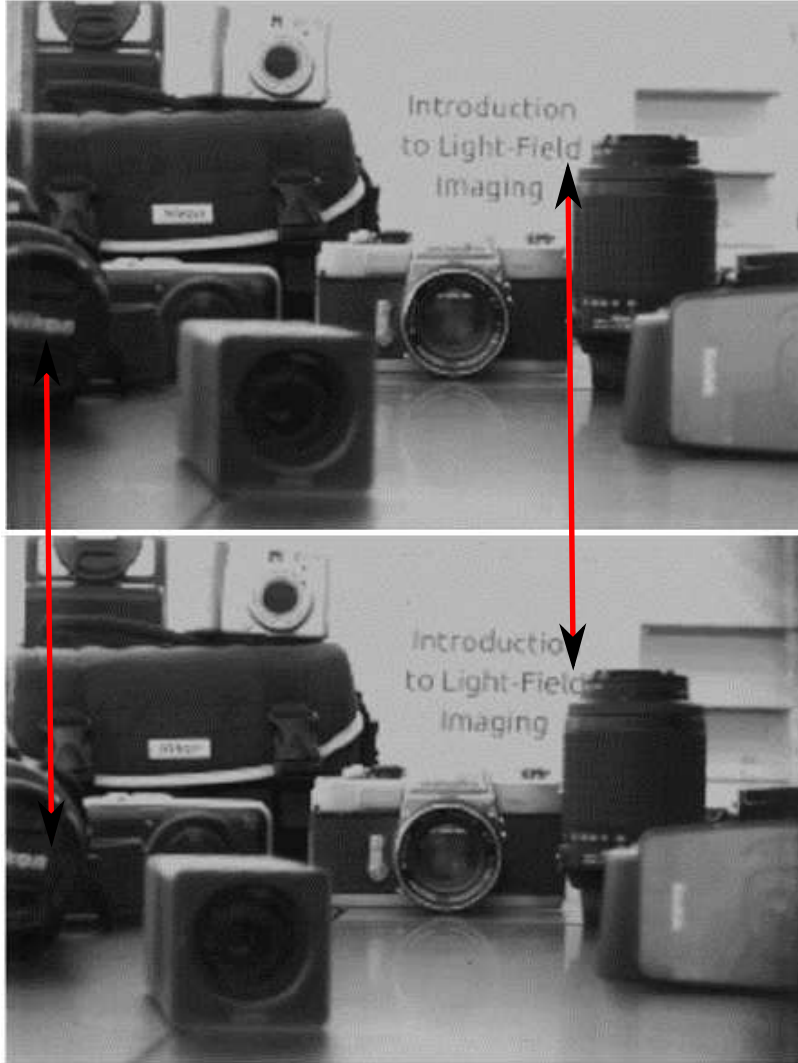
Figure 4.8: (a) Left and (b) right perspective views highlighting the disparity in them with the two red lines pointing to the test on the book in the back and the lens cap in the front of the focal plane [99].

(x,y,u,v). E_{s_i} is the irradiance distribution on the image sensor. θ is the angle the light ray, $L_{s_i}(x, y, u, v)$, makes with the optical axis of the camera.

An image formed in a conventional camera was defined as the weighted sum of light converging from the aperture. In Equation 4.10, $\cos^4 \theta$ is the weighting function describing the contribution of the light rays making an angle θ with the image sensor of the camera. The weighting function suggests that, in a cone beam converging on a pixel, the contribution of a light ray in image forming is inversely proportional to its angle of incidence. The incident

angle in Equation 4.10 is a function of (x,y,u,v) which can be used to reduce the imaging equation as:

$$L_{s_i}(x, y, u, v) = L_{s_i}(x, y, u, v) \cos^4 \theta \qquad (4.11)$$

and,

$$E_{s_i}(x, y) = \frac{1}{s_i^2} \int \int L_{s_i}(x, y, u, v) \, du dv \qquad (4.12)$$

Figure 4.5 shows a schematic illustrating the geometry used in refocusing the image to a virtual plane (x',y'). To refocus the image to the synthetic plane, $L_{\alpha s_i}(x', y', u, v)$ at the synthetic plane needs to be defined. Using similar triangle with the geometry shown in Figure 4.5, light rays passing through u and x' intersect with (x,y) plane at:

$$x = u + \left(x' - u\right) \frac{s_i}{\alpha s_i} = u + \left(x' - u\right) \frac{1}{\alpha} = u\left(1 - \frac{1}{\alpha}\right) + \frac{x'}{\alpha} \qquad (4.13)$$

and,

$$y = v\left(1 - \frac{1}{\alpha}\right) + \frac{y'}{\alpha} \qquad (4.14)$$

x and y thus calculated can be used to redefine the light field at the synthetic plane in terms of the original light field as:

$$L_{\alpha s_i}\left(x', y', u, v\right) = L_{s_i}\left(u\left(1 - \frac{1}{\alpha}\right) + \frac{x'}{\alpha}, v\left(1 - \frac{1}{\alpha}\right) + \frac{y'}{\alpha}, u, v\right) du dv \qquad (4.15)$$

Refocused images thus formed are given by:

$$E_{\alpha s_i}\left(x', y'\right) = \frac{1}{\alpha^2 s_i^2} \int \int L_{s_i}\left(u\left(1 - \frac{1}{\alpha}\right) + \frac{x'}{\alpha}, v\left(1 - \frac{1}{\alpha}\right) + \frac{y'}{\alpha}, u, v\right) du dv \qquad (4.16)$$

Sample images generated from a plenoptic image shown in Figure 4.9 are presented in Figure 4.10. In Figure 4.9, a scene of the room is captured with the plenoptic camera. A hat and a box with Imperx written on it are in nominal focus in the image. This plenoptic

image was then manipulated with Equation 4.16 to refocus the image to focus on the person in the background, shown in Figure 4.10(a) and the digital clock, shown in Figure 4.10(b).

Figure 4.9: Scene of a room captured with the plenoptic camera [101].
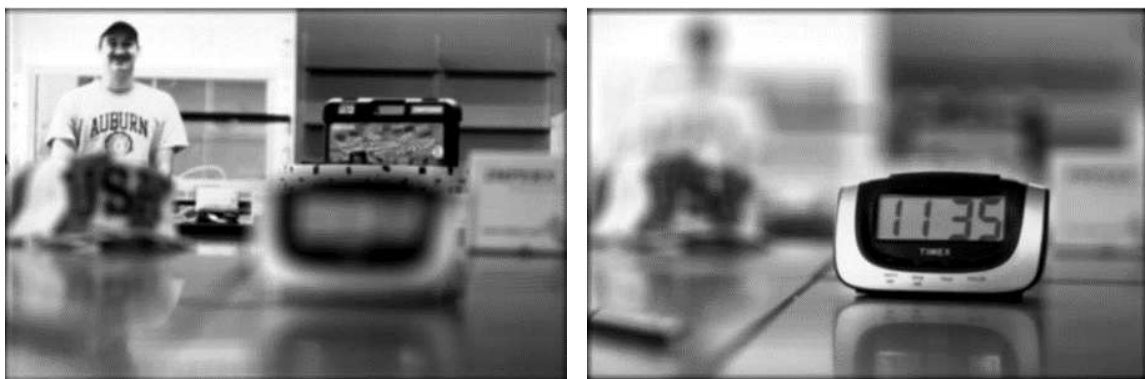
Figure 4.10: Images generated by refocusing the plenoptic image. (a) Person in the image is in focus, and (b) digital clock in the image is in focus [101].

4.4 Plenoptic Cameras at AU AFDL

The AFDL at AU has designed and constructed several plenoptic cameras with two different specifications, one with a 16 MP image sensor and the other with a 29 MP image sensor. Both models use camera bodies from Imperx's Bobcat series.

The Bobcat cameras are highly programmable with high density field-programmable gate array (FPGA) providing hundreds of programmable features. The Bobcat cameras used in this work have the capability to provide 8, 10, 12 or 14-bit outputs. The dual clock design of the cameras provides faster frame rates. The Bobcat 2.0 also includes many different triggering modes such as asynchronous, standard, fast, frame accumulation and double trigger (for PIV). Programmable exposure control allows the user to program the exact exposure time to 1 microsecond precision [102].

A picture of the 16 MP camera is shown in Figure 4.11. The 16 MP Imperx Bobcat ICL-B4820 and the 29 MP Imperx Bobcat B6640 are modified by placing microlens arrays in front of the image sensors to act as plenoptic cameras. Custom built mounts with series of positioning screws were used to mount the microlens arrays. The design of the camera is such that the microlenses are exactly focused on the sensor. An iterative adjustment is then made so that the image captured by the camera is an array of sharp points. An exploded view of the camera and the microlens array is shown in Figure 4.12. Although the basic construction of the two cameras is similar, they differ in the microlens arrays used and the size of the image sensors. Thus, capturing images with different image resolutions.

The 16 MP camera has an image sensor with a maximum resolution of 4904×3280 pixels with the pixel pitch of 7.40 um. The microlens array used with this camera has square shaped microlenses with the microlens pitch of 125 um. A schematic of the microlens array is shown in Figure 4.13(a). The microlens array has approximately 289×193 useable microlenses. These micro lenses divide the image sensor behind them into subregions with approximately 16×16 pixels in each subregion. Each microlens on the array has a focal-length (f_{micro}) of 500 um.

Figure 4.11: 16 MP Imperx Camera modified to act as a plenoptic camera [20].

ITEM	PARTS LIST
	DESCRIPTION
1	IMPERX ICL-B4820 (16MP) CAMERA BACK END
2	IMPERX M3.0 SET SCREWS (1.5mm HEX DRIVE)
3	IMPERX F-MOUNT ADJUSTMENT BARREL
4	IMPERX M2.5 FLAT HEAD SCREWS (PHILLIPS #1 DRIVE)
5	IMPERX F-MOUNT BEZEL (NEEDS A DIAMETER CLEARANCE C
6	#0-80 X 3/16" BUTTON HEAD SCREWS McM_92949A052 (.03
7	MLM COVER PLATE
8	MLM ADJUSTER-SCREWS
9	LEE SPRING PART#_CI 012B 02 S
10	MLM ADJUSTER
11	MICROLENS ARRAY SANDWICH
12	#0-80 X 3/8 SOCKET HEAD SCREWS McM_92200A057 (.050"
13	MLM BRACKET
14	LEE SPRING PART#_CI 012BC 04 S
15	IMPERX M2.0 FLAT HEAD SCREWS (PHILLIPS #1 DRIVE)
16	MLM BRACKET HOLDER

Figure 4.12: Exploded view of the camera and microlens array mounting apparatus [20].

In the 29 MP camera, a maximum resolution of 6600×4400 pixels can be achieved. The image sensor in this camera has the pixel pitch of 5.5 um. The microlens array used in this camera has hexagonal shaped microlenses, shown in Figure 4.13(b). The microlens array has 471×362 microlenses. Because of the unique shape and packing of the microlenses, pitch between the microlenses in the x-direction is 77 um and in the y-direction is 67.83 um. The microlens array used in the 29 MP camera divides the image sensor into subregions with approximately 14×14 pixels in each subregion. The microlenses on the microlens array used in the 29 MP camera has a focal length of 308 um.
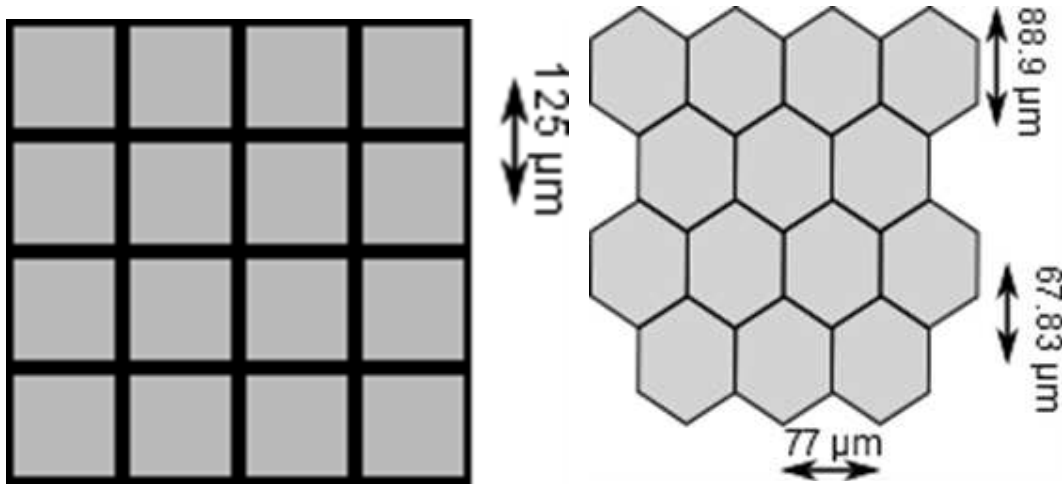
Figure 4.13: Schematic of micro lens arrays used in a) the 16 MP camera and b) the 29 MP camera.

Images captured with the plenoptic cameras for this research were processed using the software called the light field imaging toolkit (LFIT) developed at AU AFDL which is currently in version 2.21. The LFIT is developed in MATLAB. A screenshot of the LFIT software is shown in Figure 4.14.

The LFIT takes raw images captured with the plenoptic camera along with a calibration image to generate the perspective views. The calibration image is a plenoptic image of a white paper captured with a small aperture on the camera lens. The calibration image thus captured is an image of array of dots representing the centers of the subregions behind each

microlens in the microlens array. A sample calibration image is shown in Figure 4.15. Along with the calibration image, software takes inputs about the experimental setup such as the focal-length of the lens used on the plenoptic camera and the size of the FOV at the focal plane of the setup. The LFIT has the capability to process a single image or has a batch mode to process a batch of plenoptic images. The LFIT has separate modes to process the images obtained from the 16 MP camera and the 29 MP camera. When using the software, user is provided with an option to generate perspective views either with original resolution or with user specified super resolution. Images obtained from the 29 MP camera are by default set to a super resolution of factor 2. Images used in the experimental results were obtained from the 29 MP camera with the default super resolution settings.
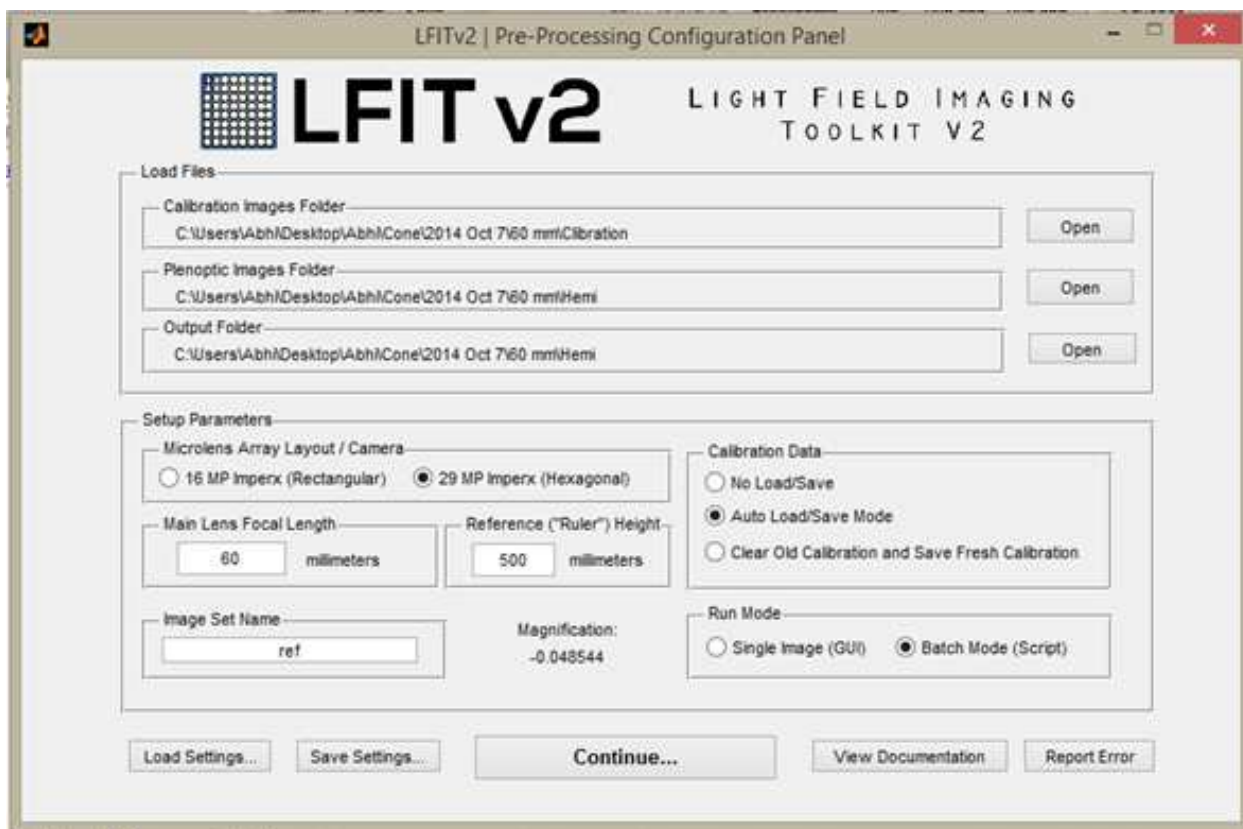
Figure 4.14: Screenshot of the Light Field Imaging Toolkit (LFIT).
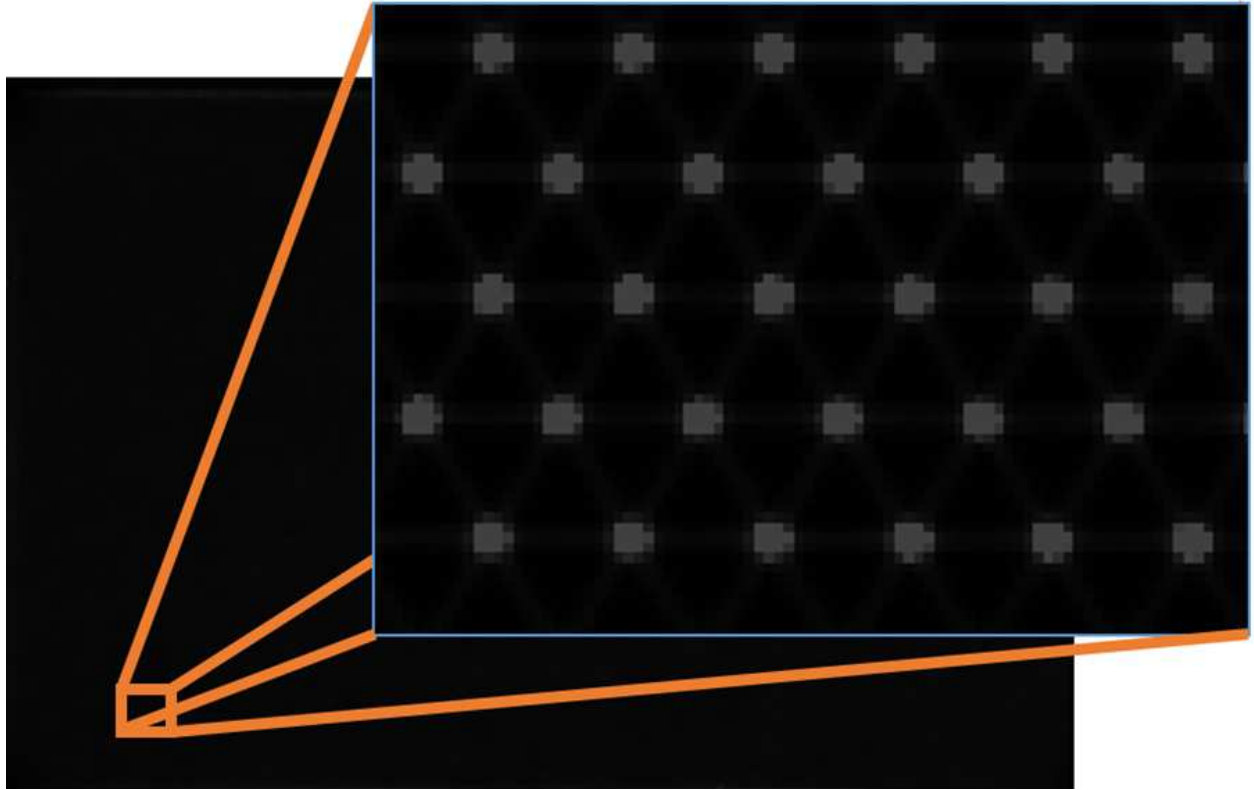
Figure 4.15: Sample calibration image.

Chapter 5

MART Equation

The purpose of this research is to visualize the 3D density distribution of a flow field using images obtained from a plenoptic camera. While the basic perspective views from a plenoptic camera provide some information about the depth (as will be shown in Chapter 8), alternative methods, such as those found in CT, for estimating the 3D density field are sought. The main challenge is that images generated from a plenoptic camera have limited resolution and limited angular information, which will place constraints on the type of CT algorithms that might be expected to provide reasonable approximations of the 3D density field. This chapter reviews various CT algorithms and assesses their suitability for use with plenoptic image data.

This chapter starts by defining the general problem of reconstruction in this work and then present a survey of the available reconstruction techniques from which a method is chosen that is believed to serve the most for this work. Finally, the chosen method is tested on simple sample problems and results are presented.

5.1   Problem of 3D Reconstruction

The concept of tomography was first introduced in 1940 by Gabriel Frank but it was not until 1972 when it was used for the first time to image the human head for medical purposes [103]. It has since been applied in different fields to measure the density distribution or as a method for non-destructive testing (NDT).

In tomography, light passing through a VOI is imaged at various angles. Depending on the relation between the light rays and the mass in the VOI, properties of the light coming out of the VOI interest change when compared with the light that enters. These changes

that can be measured from the images/projections formed from the light are then used to reconstruct the density of the VOI. The relation between the VOI and the projections is given by:

$$I_n(x, y) = \int_S g(x, y, z)ds \qquad n = 1, 2, 3...N \qquad (5.1)$$

I_n is the measured property of the nth projection. For example, I in X-ray CT is the amount of attenuated energy when the X-rays pass through a human tissue. N is the total number of projections. g is the function defining energy absorption as a function of the density distribution in the VOI and ds is the infinitesimal distance along the light's path in the VOI.

In this work, the aim is to use the OPD data obtained from processing the BOS images from the plenoptic camera to reconstruct the density distribution in the VOI. OPD for a projection is given by:

$$\hat{\phi}_n(x, y) = \phi_n(x, y) - \bar{\phi}_n \qquad (5.2)$$

where, $\hat{\phi}_n$ is the measured OPD from BOS, ϕ_n is the optical path length (OPL) of the projection, and $\bar{\phi}_n$ is the spatially averaged optical path length for the nth projection:

$$\bar{\phi}_n = \sum_{x=1, y=1}^{x=N_x, y=N_y} \phi_n(x, y) \qquad (5.3)$$

where, N_x and N_y are the total number of pixels in the x and y direction in each projection.

The plenoptic tomographic background oriented schlieren (PT-BOS) has some key differences when compared with the more traditional CT applications.

1. PT-BOS requires a flow field with varying index of refraction (IR), either due to compressibility or due to different species of gases,

2. PT-BOS requires reference projections of the background with uniform density in the VOI,

3. PT-BOS uses OPD for 3D reconstructing the volume whereas the traditional CT measures the total energy attenuation,

76

4. PT-BOS has limited viewing angles with limited resolution per projection,

5. When used for measuring a turbulent flow, the density in the VOI have voxels with both negative and positive fluctuations (relative to the mean) in the VOI, and

6. Average optical path length $(\bar{\phi}_n)$ for a given perspective view is independent of the average optical path length of any other perspective view.

In PT-BOS, comparing the distorted projections with the reference projections give the disparities/distortions between the two. These distortions obtained from processing BOS images are then used with the Southwell iterative technique, discussed in Chapter 3, to obtain the OPDs. The definition of the OPD suggests that the density of an individual voxel in a discretized VOI interest may have a positive or negative difference relative to the average density of the volume.

When defining the OPD in Equation 5.2, the average optical path length is used. The average optical path length measured for each perspective view is independent of the other. This introduces additional variables into the tomographic reconstruction problem for PT-BOS.

To address the specific challenges associated with PT-BOS, a survey of the various reconstruction techniques is presented in the next section and the one technique that best suits the needs of the PT-BOS technique being developed in this research is selected.

5.2 3D Reconstruction Techniques

There is a mountain of work with great contributions in the field of tomographic reconstruction techniques. In this work, only some of it is referred to, as it is not possible to cover it all here. To have a better understanding, a discussion on the types of data that are obtained from the projections and the reconstruction techniques that can be used for reconstruction is given.

Data obtained from tomographic projects can be categorized either as extensive or sparse data. Extensive data, as the name suggests has more than 180° of angular information with sufficiently small angular interval between the projections for a good reconstruction. Sparse data can be in two forms:

1. Projections with more than 180° of angular information with large angular interval between the projections, and

2. Projections from the VOI with limited angular access.

When using sufficient projections for reconstruction, transform based reconstruction techniques are used. But, when reconstructing from sparse data, series based or iterative reconstruction techniques are used.

5.2.1 Transform Based Techniques

The filtered back projection technique (FBT) is a fast Fourier transform (FFT) based reconstruction technique developed using the Fourier slice theorem, shown in Figure 5.1. The Fourier slice theorem states that the Fourier transform of a parallel projection of an image $f(x, y)$ taken at an angle θ gives a two-dimensional transform, $F(\eta, \xi)$, of a slice subtending an angle θ with the η-axis [104]. The first axis in Figure 5.1 shows the physical space with Cartesian coordinates and a projection making an angle θ being captured. The second axis shows the Fourier transform of the projection as a slice of the VOI making an angle θ in Fourier space.

By using the above definition, a perfect object space can be reconstructed using FBT when an infinite number of projections, each taken at a different angle, are given. In practice, only a finite number of projections are available for reconstruction which calls for interpolation of the missing data. The effect of interpolation for the missing data is greater for points away from the origin in the frequency domain. In simple words, any high frequency data, such as an edge or a shock is adversely affected by interpolation by causing them to blur or
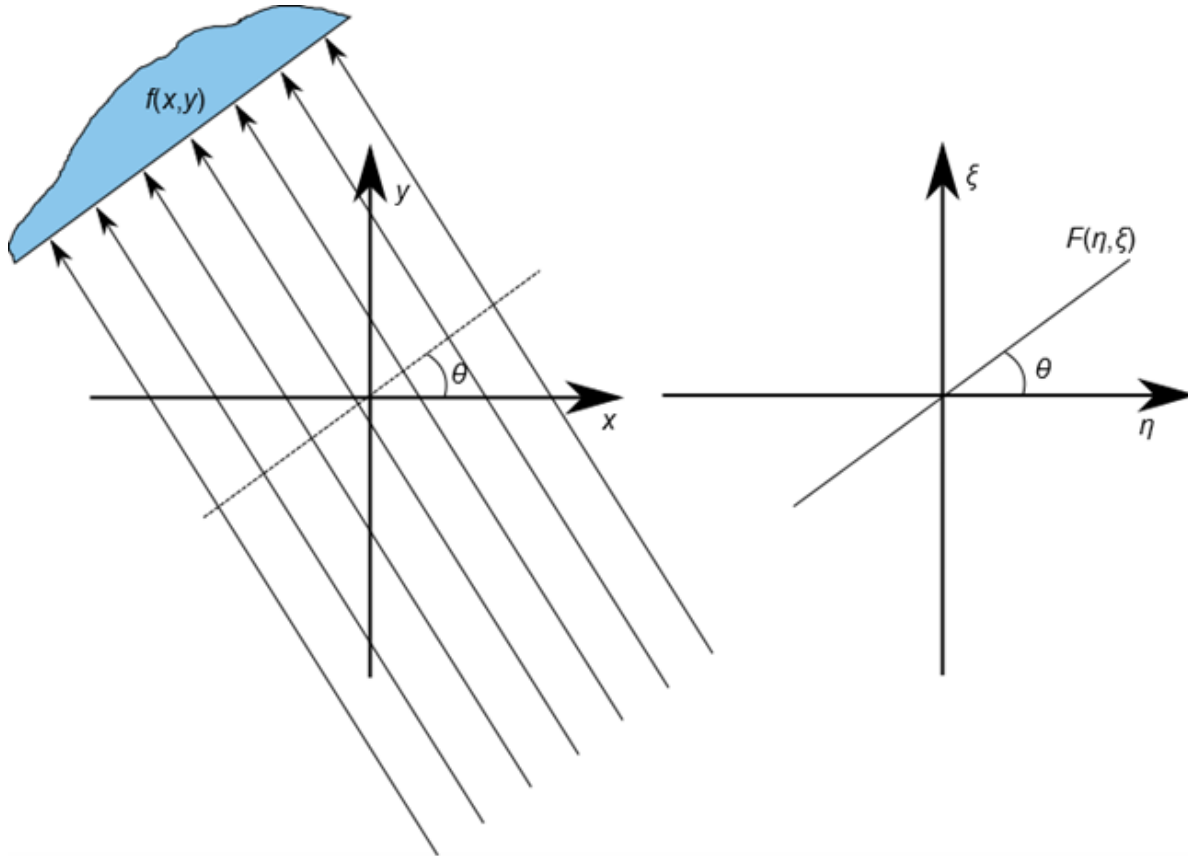
Figure 5.1: Fourier Slice theorem. Images showing a) the capturing of a projection making an angle θ with x-axis and b) its Fourier transform in the frequency plane.

diffuse. This effect grows with reducing number of projections. Thus, when the range of the projection angles is limited or the number of projections is limited, the available information is insufficient for using FBT reconstruction.

5.2.2 Series Based Techniques

In a given tomographic setup, let there be N projections with Px_x and Px_y number of pixels in x and y direction in each projection, and the VOI is discretized into M_{vox} voxels. Mathematically, tomographic projections can be expressed as:

$$I = WG \tag{5.4}$$

where, I represent the projection data from all projections as a vector with $N_T = N \times Px_x \times Px_y$ elements, W is the weight matrix (discussed in the next chapter) associated with the projections with $N_T \times M_{vox}$ elements and G is a vector with discretized density from the VOI with M_{vox} elements. Thus, there are N_T equations to solve for M_{vox} variables.

Given the sparse nature of the projection data, the number of equations are insufficient to solve all the variables in the VOI ($N_T < M_{vox}$). In the past 40-45 years researchers have developed iterative reconstruction techniques to solve this ill-posed inverse problem. These iterative algorithms address the problem of solving the above equation by minimizing the Kullback-Leibler distance (KL), given by [105–107]:

$$KL(WG, I) = (WG)log\frac{WG}{I} + I - WG \tag{5.5}$$

KL is not an actual distance in true sense. KL is the measure of the entropy difference between the two distributions over the same space. KL is always greater than or equal to 0 (KL 0). KL is a positive number when $WG \neq I$ and zero if $WG = I$.

In this section, a discussion on a few of the series based reconstruction techniques categorized into estimation maximization maximum likelihood (EMML), singular value decomposition (SVD) and algebraic reconstruction techniques (ART) is presented.

5.2.2.1 Estimation Maximization Maximum Likelihood

Rockmore and Macovski [108] first showed the application of estimation maximization (EM) algorithms to tomographic reconstruction. Since then, a few different variations of the EMML techniques have been developed [107,109–111]. The EMML reconstruction techniques have found a great success in positron emission tomography (PET), single photon emission computed tomography (SPECT) [112] and other fields.

The first EM algorithm was introduced in 1977 [113] for finding the maximum likelihood estimation of probabilistic models in statistics. The EM algorithms use a two step approach

to find the maximum likelihood solution. In the first step, referred to as the estimation step (E), log-likelihood of the estimations are calculated using the current estimates for the parameters. In the second step, referred to as the maximization step (M), parameters used for maximizing the log-likelihood found in step E are calculated. In tomography, the parameters in step M are the weights (discussed in Chapter 6), which are calculated prior to the iteration. Therefore, only the E step is left to iterate and obtain the distribution of g in the VOI. EMML is implemented in a few different variations and some are application specific.

The simple EMML iterative equation is given by:

$$g_j^{k+1} = g_j^k \sum_i w_{i,j} \frac{I_i}{wg^k} \tag{5.6}$$

where, k is the iteration counter, $i = 1, 2, 3N_T$ and $j = 1, 2, 3M_{vox}$. EM estimations are iterated to converge on the ML solution. But for multimodal problems, the solution tends to converge on the local minima and not on the global minima. This suggests that the solution depends on the initial guess. The above implementation of the EMML algorithm tends to rough solution, resulting in a noisy output [106]. With large data, implementation of the above EMML algorithm can be slow [107]. To address the speed of convergence of the EMML implementation, modified algorithms such as the block iterative EMML (BI-EMML) [107], the ordered set EM (OS-EM) [109], space-altering generalized expectation-maximization (SAGE) [114], the ABEMML [111] (where AB refers to the upper and lower bound limits for the solution from a priori knowledge) etc., were introduced. To address the noise in the reconstructed volume, a regularizing implementation of the EMML algorithm was suggested [105].

From the above discussion, EMML suffers from sensitivity to noise, rate of convergence is slow and the final reconstructed volume (solution) depends on the initial guess. The EMML algorithms also have the positivity constraint built into them which makes the EMML

algorithms not an ideal reconstruction technique for the problem in this work where, as both positive and negative values are expected in the reconstructed volume depending on the imaged flow field.

5.2.2.2 Singular Value Decomposition

In this sub-section, a definition of the singular value decomposition (SVD) equation is given and it's application to tomographic reconstruction is discussed. Detailed theory, applicability and examples are out of the scope of this work and can be found in books detailing matrix theory.

Any matrix, W, of size $m \times n$, where, $m \geq n$ can be factored as:

$$W = U\Sigma V^T \tag{5.7}$$

where, U is a $m \times m$ orthogonal matrix whose columns are the eigenvectors of WW^T and V is a $n \times n$ orthogonal matrix whose columns are eigenvectors of W^TW. Σ is a $m \times n$ element diagonal matrix. The diagonal elements, if denoted as σ_1, σ_2, σ_3, $\ldots \sigma_r \ldots$ are called the singular values of W and are bound by the constraint $\sigma_1 > \sigma_2 > \sigma_3 > \cdots > \sigma_r > 0$. The subscripts denote the row and r is the rank of W such that $r \leq n$.

Early application of SVD to tomography can be traced back to the 60's with Cormack's application to 2-dimensional Radon transforms [115]. In his work presented in 1983 [116], Davidson noted difficulties in reconstruction with an ill-conditioned problem caused due to limited viewing angles. He suggested conditioning of the problem for obtaining low quality reconstruction. The paper also noted the difficulty in using the priori knowledge about the volume in reconstruction as incorporating it may not have a natural expression in terms of singular functions. Caponnetto and Bertero [117] studied the properties and effect of singular values and functions on the aliasing effects and the resolution obtained from the reconstruction. They also concluded that if the number of projections in the setup are less

than a certain upper limit, then the resolution of the reconstruction is dependent on the number of projections.

Using the SVD algorithm for tomographic reconstruction provides an automatic system to handle the under and over determined system of equations gracefully. For a given tomographic setup, decomposition is determined only once. Though, the decomposition of the radon function is performed only once, because the SVD algorithms cannot take advantage of the prior knowledge or use the sparseness of the weighting function, execution of the SVD algorithms for iterative reconstruction is slow [118, 119].

5.2.2.3 Algebraic Reconstruction Techniques

Algebraic reconstruction technique is a class of iterative reconstruction techniques. They were first introduce by Gordon et al. [120] in 1970 for reconstructing 3 dimensional volume with small number of projections (5 to 10). In their paper they introduced two algebraic reconstruction techniques:

1. additive algebraic reconstruction technique is simply referred to as algebraic reconstruction technique (ART)

$$g_j^{k+1} = \max \left[g_j^k + \frac{I_i - \sum_{j=1}^{M_{vox}} w_{i,j} g_j^k}{M_{ivox}}, 0 \right] \tag{5.8}$$

where, M_{ivox} is total number of voxels in the VOI influencing the observed data i.

2. multiplicative algebraic reconstruction technique (MART).

$$g_j^{k+1} = g_j^k \frac{I_i}{\sum_{j=1}^{M_{vox}} w_{i,j} g_j^k} \tag{5.9}$$

In the original implementation, the value at each voxel is changed with the updated value calculated from every observed/measured data point [121]. This results in the salt and pepper noise in the reconstructed volume [104]. This issue of salt and pepper noise is addressed with either a relaxation parameter ($\mu < 1$) or with modified simultaneous ART (SIRT or simultaneous iterative reconstruction technique) [122] and multiplicative SIRT (MSIRT). In the modified versions (SIRT and MSIRT), instead of changing the value of a voxel with every observed data the value at the voxel is changed with the averaged sum of the changes obtained for the voxel with every observed data after each iteration. The SIRT equation is given by:

$$g_j^{k+1} = \max \left[g_j^k + \frac{\sum\limits_{i=1}^{N_j} I_i}{\sum\limits_{i=1}^{N_j} L_i} - \frac{\sum\limits_{i=1}^{N_j} \sum\limits_{j=1}^{M_{vox}} w_{i,j} g_j^k}{\sum\limits_{i=1}^{N_j} M_{ivox}}, 0 \right] \tag{5.10}$$

where, N_j is the number of observed data points influenced by j^{th} voxel and L_i is distance travelled by i^{th} ray in the VOI. The MSIRT equation is given by:

$$g_j^{k+1} = g_j^k \frac{\sum\limits_{i=1}^{N_j} I_i}{\sum\limits_{i=1}^{N_j} L_i} \times \frac{\sum\limits_{i=1}^{N_j} M_{ivox}}{\sum\limits_{i=1}^{N_j} \sum\limits_{j=1}^{M_{vox}} w_{i,j} g_j^k} \tag{5.11}$$

In their 1973 work, Herman et al. [121] introduced a modified ART equation given by:

$$g_j^{k+1} = g_j^k + \frac{I_i - \sum\limits_{j=1}^{M_{vox}} w_{i,j} g_j^k}{\sum\limits_{j=1}^{M_{vox}} w_{i,j}^2} \tag{5.12}$$

A detailed analysis of this method and a few more ART implementations are presented in Gordon's 1974 paper [123].

In 1984, Andersen and Kak [124] noted that the ART algorithm converged to the solution faster than SIRT, while the SIRT reduced the salt and pepper noise. To obtain the advantages of both methods, they introduces a modified algorithm and called it simultaneous algebraic reconstruction technique (SART). Mathematically SART is given by:

$$g_j^{k+1} = g_j^k + \frac{\sum_{i=1}^{N_j} \left[w_{i,j} \frac{I_i - \sum_{j=1}^{M_{vox}} w_{i,j} g_j^k}{\sum_{j=1}^{M_{vox}} w_{i,j}} \right]}{\sum_{i=1}^{N_j} \sum_{j=1}^{M_{ivox}} w_{i,j}} \tag{5.13}$$

The SART algorithm was observed to have better results when compared with ART and faster than SIRT. Though faster, the rate of convergence of SART algorithms is slower when compared with the MART algorithms. Going forward, the effort in this work is focused on the MART algorithms.

The original equation for MART given by Gordon et al. is shown Equation 5.9, but the MART equation has evolved ever since with different applications. The modified MART equation used in tomographic applications in the field of fluid dynamics is given by:

$$g_j^{k+1} = g_j^k \left(\frac{I_i}{\sum_{j=1}^{M_{vox}} w_{i,j} g_j^k} \right)^{\mu w_{i,j}} \tag{5.14}$$

where, μ is the relaxation parameter. With constant initial values and function $f > 0$, Censor [125] notes that the MART algorithm converges with Lent [126] noting that the algorithm maximizes Shannon entropy. Herman [127] observed that in an inconsistent case, the above equation may not maximize the entropy.

To address the issues associated with MART, Byrne [107] in 1995 introduced the simultaneous MART (SMART) algorithm which computed the $(k + 1)^{st}$ iteration values simultaneously from k^{th} values. In his work, he compares both MART and SMART algorithms and observes that the SMART algorithm addresses the question raised by Censor [125].

The simultaneous nature of the SMART algorithm also allows the implementation to be parallelized.

Badea and Gordon's [128] paper in 2004 presents a modified MART algorithm called the power MART:

$$g_j^{k+1} = g_j^k \left(\frac{I_i}{\sum\limits_{j=1}^{M_{vox}} w_{i,j} g_j^k} \right)^p \tag{5.15}$$

They studied the influence of power (p) on the performance of the algorithm and noticed that the value of the power $p > 2$ results in a diverging solution of the reconstruction process, $p = 2$ cycles the reconstruction between two false solutions and $p < 2$ results in a convergence solution.

All the variations of the MART technique seen so far, MART, MSIRT and SMART, impose the positivity constrain on the VOI. But, as discussed earlier, in a turbulent flow both positive and negative difference values (from the mean) in the VOI are expected. For the purpose of this research, use of power MART with $p = 1$, which is also equal to the original MART shown in Equation 5.9, allows the reconstructed volume to have either the positive or the negative difference in the VOI. To further study its applicability, the original MART equation is investigated in the following section.

5.3 Reconstruction of Choice

To test the reconstruction capabilities of the reconstruction technique of choice, two models were designed and tested. The models and the results from the reconstruction are presented in this section.

The two models were designed with the 16 MP plenoptic camera specifications in mind. To keep the design simple and test the reconstruction technique's capabilities in a computationally efficient manner, a reduced number of microlenses and reduced number of pixels behind each microlens were used. The virtual camera in these experiments had 100×100

microlenses with 7×7 pixels behind each microlens. The design of a virtual camera with these specifications provided 49 perspective views.

The VOI was discretize to have $100 \times 100 \times 100$ voxels. The VOI in each model had three small volumes of inhomogeneities of size $3 \times 3 \times 3$ voxels each. The index of refraction (IR) due to the inhomogeneity is these volumes was designed to have a difference of three thousandths from the rest of the volume. Two of the inhomogeneties are in line in the y-direction starting from 7th layer of the voxels when counting from the beginning of the VOI. The third inhomogeneity starts from the 80th layer and is in the line of sight of the lower volume when seen through the central perspective view of the plenoptic camera.

To account for the positive and negative differences expected in a turbulent flow field, the two models were designed as:

1. Model 1: All three volumes with inhomogeneity (VI) have IR 1.003 when the rest of the VOI have an IR of 1.0. This results in a positive difference between the VI and the average IR of the VOI.

2. Model 2: The two VIs starting from the 7th layer have an IR of 1.003 and the third VI has an IR value of 0.997. This results in the positive difference between the VIs starting at layer 7 and the average IR and a negative difference between the VI starting at the 80th layer and the average IR.

5.3.1 Case 1

In case 1, the reconstruction capability when using model 1 was tested. Figure 5.2 shows slices of the volume, taken perpendicular to z-axis. To view the IR difference distribution in the VOI, layer 1, 8, 50 and 81 are shown. Because there are no inhomogeneities in layers 1 and 50, a uniform IR distribution is observed in them. In layer 8 and 81, the inhomogeneities with positive difference are observed where the VIs in the volume are expected. In layer 8, two positive VIs one above the other in the y-direction are seen. In layer 81 only one VI with positive difference is seen.
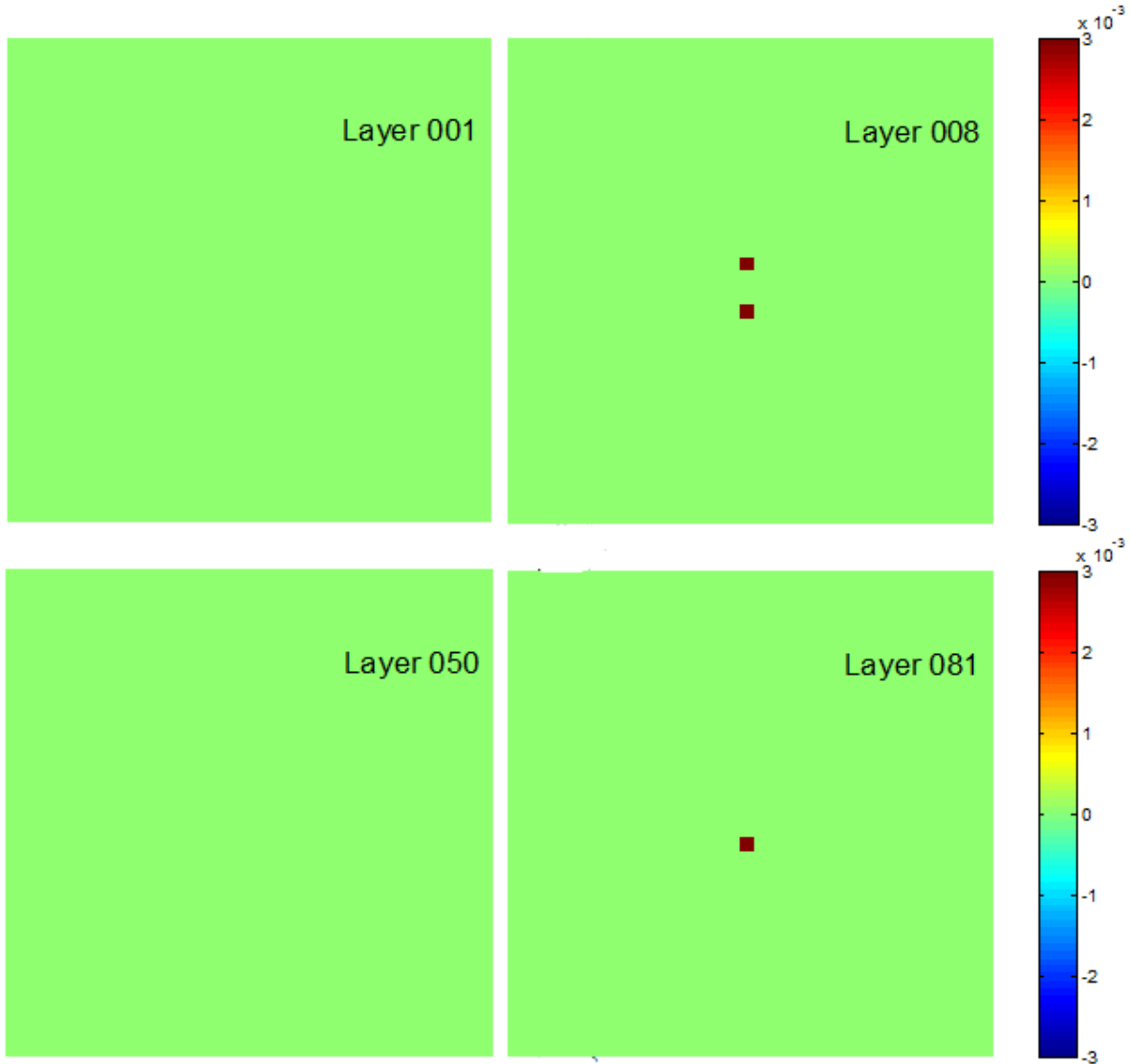
Figure 5.2: Slices of the modeled VOI for case 1 showing layers 1, 8, 50 and 81.

To simulate and test the reconstruction capabilities, each microlens is assumed to have 77 pixels under it, resulting in a 77 array of perspective views. The generated perspective views in the array are labelled from 1 to 49 as shown in Figure 5.3. The OPD for each perspective view was calculated by integrating the product of an infinitesimal distance and IR difference between each point on the line of sight and the average IR of the VOI. In Figure 5.4, the generated OPD distribution in perspective views 1, 7, 25, 43 and 49 are shown. The disparity in the measured OPD between any two perspective views is clearly

visible from the images. OPD data thus generated for each perspective view was used in the reconstruction of the VOI using the MART equation, shown in Equation 5.14.

1	2	3	4	5	6	7
8	9	10	11	12	13	14
15	16	17	18	19	20	21
22	23	24	25	26	27	28
29	30	31	32	33	34	35
36	37	38	39	40	41	42
43	44	45	46	47	48	49

Figure 5.3: Image showing how the cameras are labelled in the array.
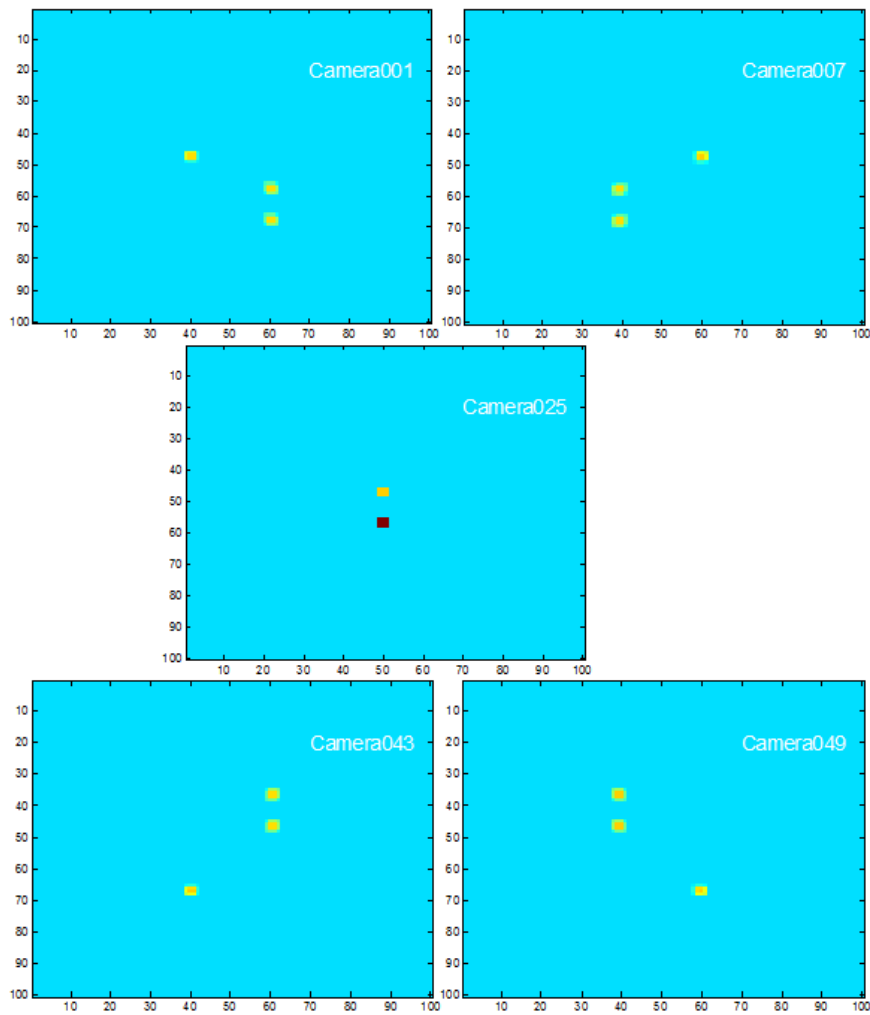
Figure 5.4: Perspective views 1, 7, 25, 42 and 49 for case 1.

In Figure 5.5 layers 1, 8, 50 and 81 from the reconstructed volume are shown for comparison with the layers shown in Figure 5.2. The reconstruction closely matches the generated model and the total error is less than 2%. From this example, it is observed that the reconstruction technique has acceptable performance when the inhomogeneities have positive difference. In the following subsection, observations from the investigation taking a look at the performance of the reconstruction technique when there are inhomogeneities with both positive and negative difference are present in the VOI.
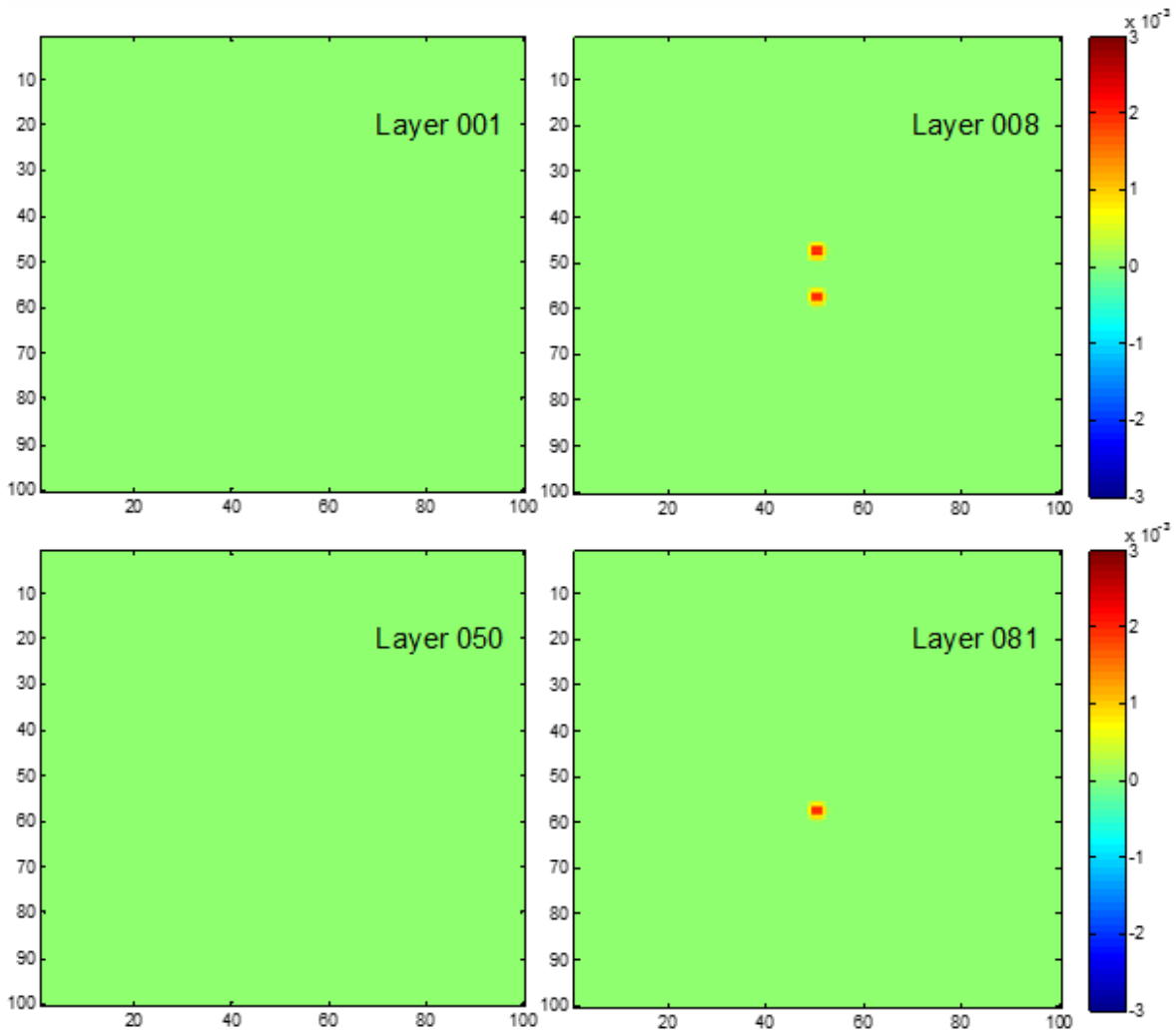
Figure 5.5: Image showing the layers 1, 8, 50 and 81 from the reconstructed volume for case 1.

5.3.2 Case 2

In case two, the second model that has negative difference in the third VI starting from layer 80 was used. Layers 1, 8, 50 and 81 from model 2 are shown in Figure 5.6 and the perspective views 1, 7, 25, 43 and 49 are shown in Figure 5.7. In perspective view 25, only one inhomogeneity is seen as the two VIs that are on the same line of sight but have a negative difference for one and a positive difference for the other cancel the effect of each other. Disparity between any two perspective views is again evident from the images in Figure 5.7.
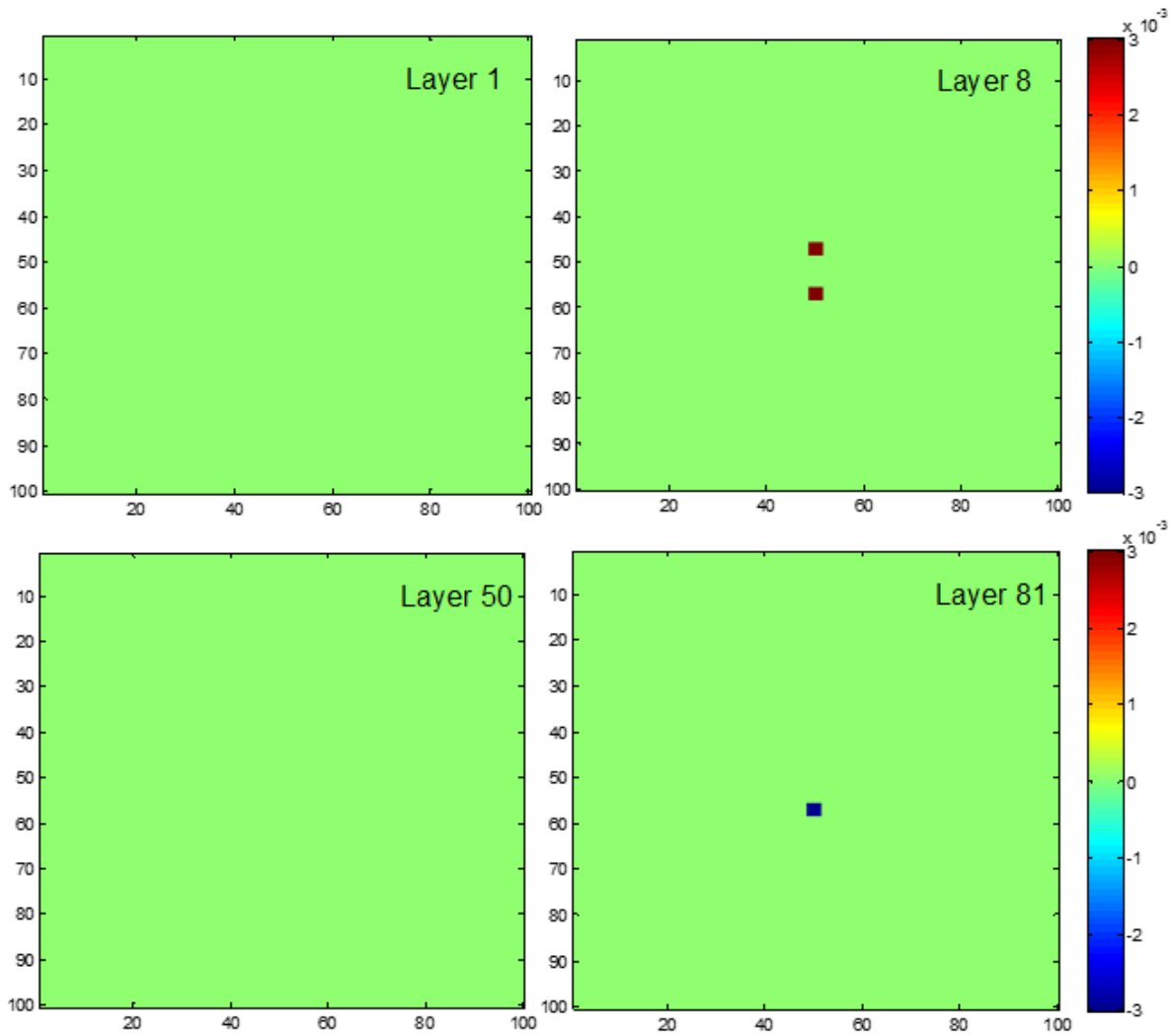
Figure 5.6: Slices of the modeled VOI for case 2 showing layers 1, 8, 50 and 81.
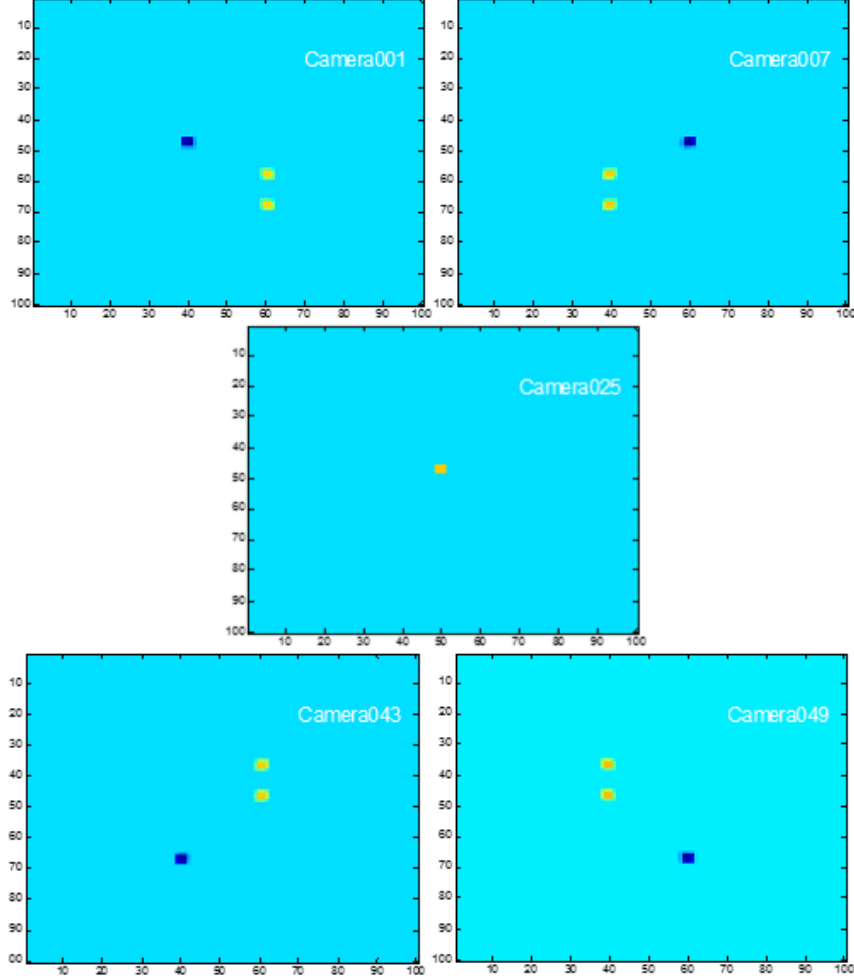
Figure 5.7: Perspective views 1, 7, 25, 42 and 49 for case 2.

The output from processing the plenoptic images with the BOS technique are the OPD values. The constant of integration or the average OPL ($\bar{\phi}_n$) for different perspective views is different and is unknown. As mentioned in the last section, the power MART equation with $p = 1$ is preferred in this work. To use the MART equation, it is important to quantify the difference. To achieve this, the reconstruction equation was modified to compensate for the integration constant as:

$$g\left(x_j, y_j, z_j\right)^{k+1} = g\left(x_j, y_j, z_j\right)^k \frac{1}{N_j} \sum_{i=1}^{N_T} \left(\frac{I\left(X_i, Y_i\right) + IC_i^k}{\sum_{j \in N_i} w_{i,j} g\left(x_j, y_j, z_j\right)^k} \right) \tag{5.16}$$

$$IC_i^k = \min\left[\sum_{j \in N_i} w_{i,j}\tilde{n}\left(x_j, y_j, z_j\right)^k, 0\right] \quad \text{for } k > 1$$

$$IC_i^k = 0 \qquad\qquad\qquad\qquad\qquad \text{for } k = 0$$

(5.17)

where, IC is the integration constant.

In tomographic reconstruction with an ill posed problem as the one in this work, there is more than one solution that satisfies the tomographic equations. Therefore, it is important to choose the appropriate OPD to start the reconstruction. In this section, two models are presented:

1. $\hat{\phi}_n' = \bar{\phi}_n - C_n$ where, C_n is a constant such that all values in $\hat{\phi}_n'$ are greater than or equal to zero,

2. $\hat{\phi}_n' = \bar{\phi}_n$.

$\hat{\phi}_n'$ is the OPD from n^{th} perspective view used in the reconstruction and $\hat{\phi}_n$ is the OPD obtained from BOS processing.

The output from the reconstruction using definition 1 and definition 2 are shown in Figures 5.8 and 5.9 respectively. In Figure 5.8, slices from layers 1, 8 and 50 closely match the model layers with some ghosting effects. The layer 81 in the reconstructed volume show uniform IR distribution, contrary to the inhomogeneity due to the negative difference expected from the simulated model. As there are no negative values used in the input data, no negative values in the reconstructed volume are observed. Though a faint VI is seen in layer 81, the difference between the VI and the rest of the volume is diffused as the minimum OPD value is taken as the reference measurement. Slices from the reconstructed volume using definition 2 for OPD are shown in Figure 5.9. Use of the second definition for OPD resulted in a more accurate reconstruction of the VOI. Even the VI with negative difference is more pronounced as compared to the one reconstructed using definition 1.
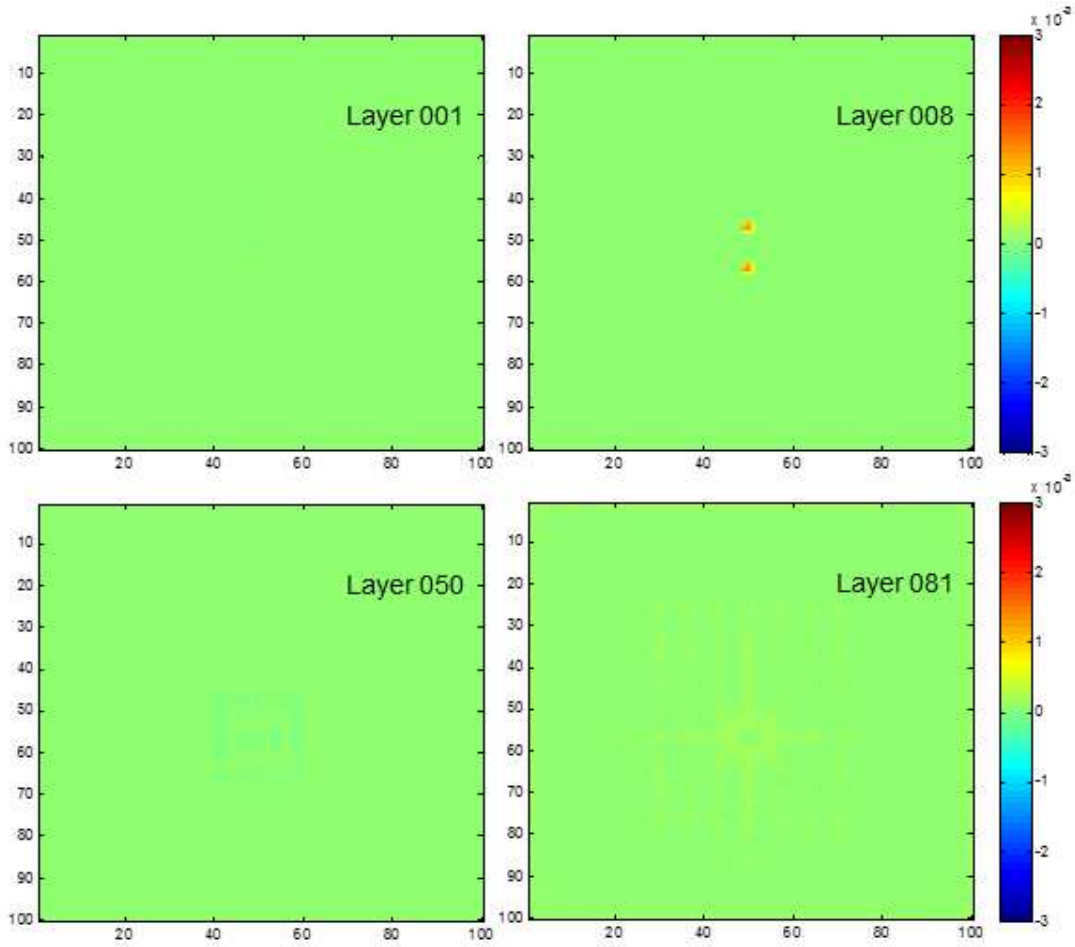
Figure 5.8: Image showing the layers 1, 8, 50 and 81 from the reconstructed volume for case 2 definition 1.

5.4 Summary

In this chapter, a survey of the current 3D reconstruction techniques that reconstruct a 3D volume from projections is presented. These reconstruction techniques can be divided into transformed based or series based techniques. The transform based techniques converge to a solution fast, but require extensive projection data for accurate reconstruction of the 3D volume. The series based reconstruction techniques are iterative and can reconstruct a 3D volume from limited projection data. The review of the series based reconstruction techniques showed that in most cases the reconstruction technique have positivity constrain
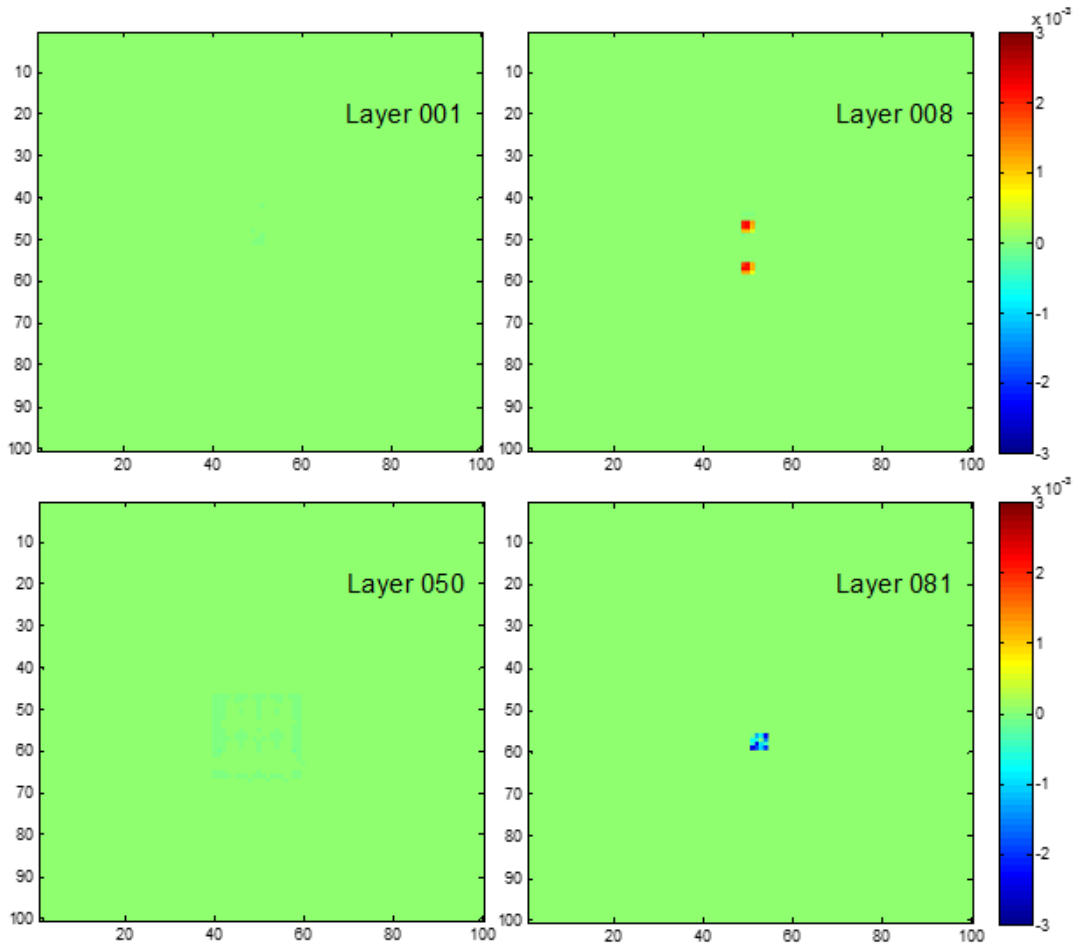
Figure 5.9: Image showing the layers 1, 8, 50 and 81 from the reconstructed volume for case 2 definition 2.

built into the reconstruction technique. If the reconstruction technique used for the 3DDMT being developed has positivity constraint in it, then the constraint limits the application of the developed 3DDMT to turbulent flow where turbulence can cause the density in the flow field can either decrease or increase. From the reconstruction techniques reviewed in this chapter, it was observed that the use of the original MART equation introduced by Gordon et al. [120] with the modification to accommodate for the integration constant works best for the current work. Defining the OPD with definition 2, reconstructed the volume more accurately. In the next chapter, the setup and execution of the MART algorithm for reconstruction used in this work are presented.

Chapter 6

MART Implementation

The discussion on the various reconstruction techniques and the reconstruction technique of choice for this work were presented in Chapter 5. After choosing a suitable reconstruction technique, it is important to discuss the implementation details. In this chapter, methods used for discretizing the VOI, calculating the weighting function and the implementation of the reconstruction algorithm as a whole are presented.

Before the specifics on the implementation of the MART equation are presented, the MART equation is given here for reference.

$$g\left(x_j, y_j, z_j\right)^{k+1} = g\left(x_j, y_j, z_j\right)^k \frac{1}{N_j} \sum_{i=1}^{N_T} \left(\frac{I\left(X_i, Y_i\right) + IC_i^k}{\sum_{j \in N_i} w_{i,j} g\left(x_j, y_j, z_j\right)^k} \right) \tag{6.1}$$

Where, g is the average refractive index difference between the refractive index in the voxel associated with (x_j, y_j, z_j) and the reference index (average refractive index of the volume), k is the iteration count, N_j is the total number of pixels that were influenced by the jth voxel, and $w_{i.j}$ is the weighting coefficient (defined in the next subsection) of the voxel associated with the pixel.

I in the above equation represents the data obtained from processing the images. In this work, I refers to the OPD data obtained from processing the background images with the BOS technique described in Chapter 3. (X_i, Y_i) refers to the ith pixel and its (X, Y) coordinate location on the individual camera.

6.1 Generating the Weighting Function

Calculating the weighting function requires an understanding of how the reconstruction problem is set, how the VOI is discretized and how the line of sight of each pixel in each perspective view interacts with the voxels in the VOI. This section starts by introducing the setup used for the experiments followed by the nomenclature used in calculating the weights. The setup and the nomenclature are then used to describe the challenges associated with calculating weights and how these were handled in this work.

6.1.1 Setup

Figure 6.1 shows the top view schematic of the experimental setup. In the figure, the camera is seen looking out to the VOI, without any parallelizing optics, suggesting that the FOV of the camera increases with increasing distance from the camera. From the schematic, the symmetry of the trapezoidal shaped VOI along the optical axis (z-axis) can be realized. The total volume of the VOI is given by:

$$\text{total vol} = \text{DOF}\frac{\text{FOV@}s_{near} + \text{FOV@}s_{far}}{2} \tag{6.2}$$

Where, s_{near} and s_{far} are the distances of the nearest and the farthest planes of the DOF measured from the camera lens.

Light originating from the background passes through an inhomogeneous volume, VOI, to reach the camera. The inhomogeneity in the VOI along the optical path of a light ray influences the optical path of the light ray. This influence is measured using the BOS technique. Ideally (in a continuous volume), measurements from the BOS technique can be mathematically expressed as:

$$\bigtriangledown \phi = \bigtriangledown \int_{S} n \cdot dS \tag{6.3}$$
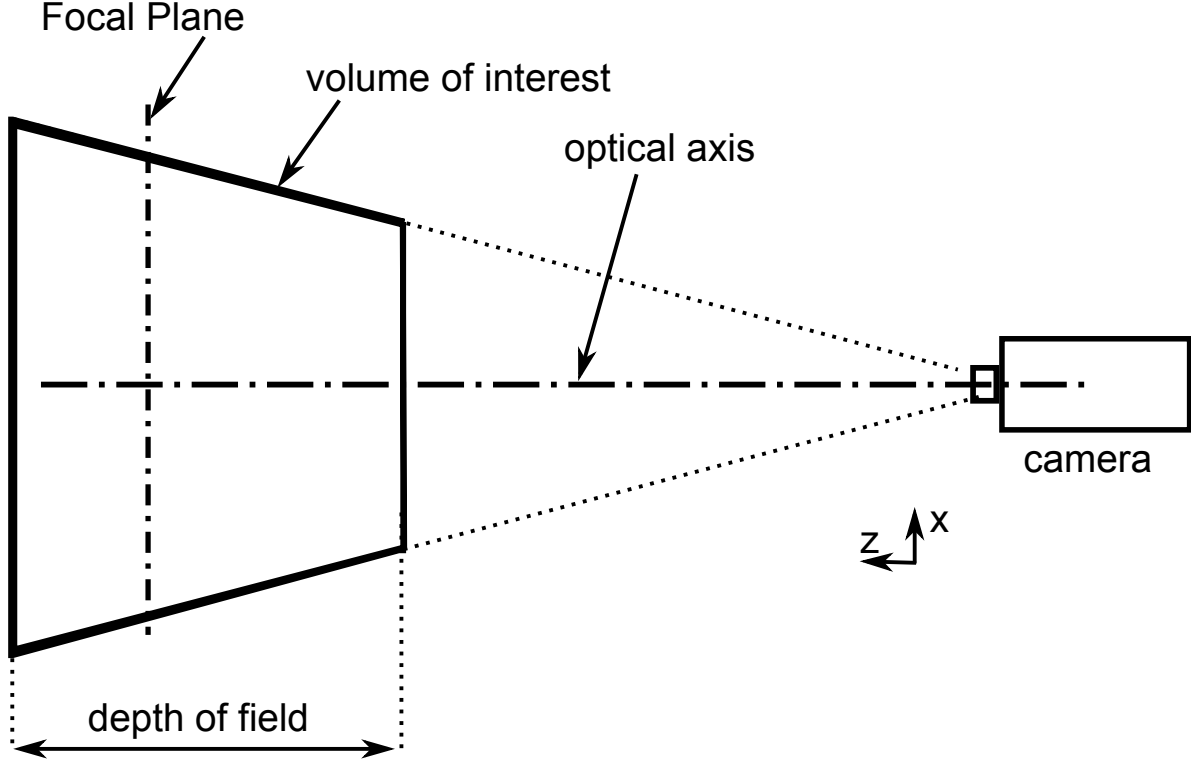
Figure 6.1: Schematic showing the experimental setup.

For practical purposes, the VOI is discretized into $N_x \times N_y \times N_z$ small volumes called voxels. For this work, N_x, N_y, and N_z are the number of voxels in the x, y and z directions respectively. As the plenoptic camera is used for imaging the background through the VOI, N_x and N_y are equal to the number of micro-lenses in the x and y directions respectively. As the micro-lenses are equi-distance apart in x and y direction, the length of the voxels (l) in x and y direction for a given plane are equal.

$$l_c = \frac{p_{micro}}{M_c} \qquad \text{for}, c = 1, 2, 3 \ldots N_z + 1 \qquad (6.4)$$

In Equation 6.4, l is the length of the voxel in x or y direction, M represents the magnification and p_{micro} represents the pitch of the microlenses. As there are N_z layers of voxels in the z direction and the FOV increases along the z-axis away from the camera, magnification of the FOV on the front plane of the voxel is different from the back plane.

When accounted for the difference, there are $N_z + 1$ magnification values excluding the magnification of the setup (M). Subscript c in the above equation refers to the cth plane, from $N_z + 1$ planes, in the z-direction.

The depth of a voxel measured parallel to the optical axis is given by b and is a constant for all voxels in the volume.

$$b = \frac{\text{DOF}}{N_z} \tag{6.5}$$

To expand on the calculation of weights and algorithm execution, a simpler version of the plenoptic camera that was used in evaluating the MART equation in Chapter 5 is assumed. In the assumed plenoptic camera, there are 7×7 pixels behind each micro-lens resulting in a 7×7 set of perspective views. Perspective view from the center of the camera array (perspective view 25) is used as the reference for discretizing the VOI.

BOS measurements for the discretized volume are mathematically expressed as:

$$\triangledown \phi \left(X_i, Y_i \right) = \triangledown \sum_{j \in N_i} w_{i,j} n \left(x_j, y_j, z_j \right) \tag{6.6}$$

Where, N_i indicates the voxels in the neighborhood of the line of sight of the ith pixel and $w_{i,j}$ is the weight coefficient associated with the jth voxel [129]. When moving from Equation 6.3 to Equation 6.5, it is important to remember that the refractive index, n, is no longer a continuous function but the average value in a voxel.

Weight coefficient seen in Equation 6.5 $(w_{i,j})$ is defined as the fraction of the voxel at location (x_j, y_j, z_j) in the VOI influencing the OPD associated with the ith pixel. Figure 6.2 shows a reference volume with 4 voxels and 2 light rays (one in blue and other in red). The two light rays belong to the same perspective view and each light ray represents the line of sight of a single pixel. Part of the volume of voxel 1 influencing the blue light ray is shown in the image as a quadrilateral with square shading inside $(V1b)$ and the part of the volume influencing the red light ray is shaded with stripes $(V1r)$. Using this information, the weight

coefficient associated with voxel 1 and the blue ray is given by:

$$w_{1b} = \frac{V1b}{V1b + V1r} \tag{6.7}$$

and the weight coefficient associated with voxel 1 and the red ray is given by:

$$w_{1r} = \frac{V1r}{V1b + V1r} \tag{6.8}$$

The sum of the two weight coefficients is equal to 1.

$$w_{1b} + w_{1r} = 1 \tag{6.9}$$

Figure 6.2: Figure showing the weight coefficient distribution.

To keep the explanation simple, generating weights in 2D is described. This same process can be extended to 3D. Figure 6.3 shows the 2D discretization of the VOI. The

outermost solid lines represent the VOI and the smaller quadrilateral boxes represent the voxels. As discussed, the volume of the individual voxels increase when moving away from the camera along the z-direction. A red reference voxel and a blue reference light ray are shown Figure 6.3.
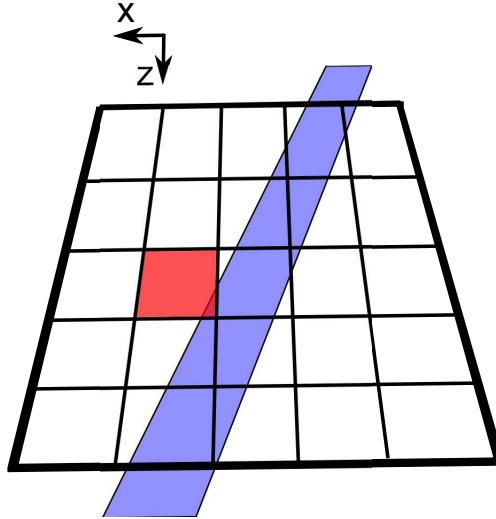
Figure 6.3: Discretization of the volume of interest in 2D.

6.1.2 Nomenclature

The zoomed in view of the reference voxel and the light ray in Figure 6.3 is shown in Figure 6.4. To start with, the interaction between the two edges of the voxel parallel to the x-axis and the light ray is considered. For the sake of argument, the edge closer to the camera is called the top edge and the edge away from the camera is called the bottom edge. L_{x1} is the vector distance between the center of the voxel edge and the center of the light ray. Mathematically,

$$L_{x1} = v_{j1} - r_{i1} \tag{6.10}$$

where, L represents the vector distance, r and v refer to the centers of the light ray and the voxel respectively. Subscripts i and j represents the ith pixel and j^{th} voxel, 1 refers to the

top edge and x refers to the axis parallel to the edge. Similarly L_{x2} represents the vector distance at the bottom edge.
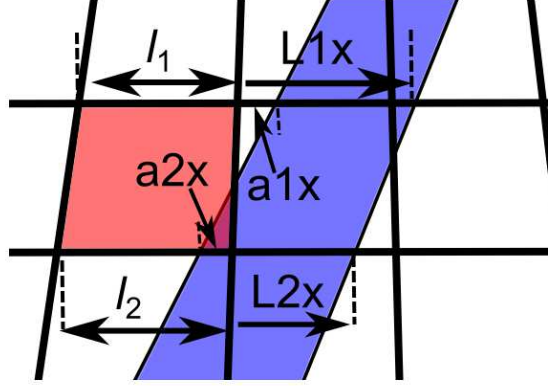
Figure 6.4: Zoomed in view of the interaction of light and the red voxel, shown in Figure 6.3, with the nomenclature.

The normalized vector distance is given by:

$$\tau_{x1} = \frac{L_{x1}}{l_1} \qquad (6.11)$$

where, τ_{x1} is the normalized vector distance between the center of the light ray and the center of the top edge of the voxel and l_1 is the length of the top edge. Similarly, τ_{x2} and l_2 belong to the bottom edge.

Absolute distances between the inner corner of the voxel and the inner corner of the light ray are given by a_{x1} and a_{x2}. Mathematically, they are defined as:

$$a_{x1} = |(|L_{x1}| - l_1)| \qquad (6.12)$$

$$a_{x2} = |(|L_{x2}| - l_2)| \qquad (6.13)$$

102

6.1.3 Problem

Considering the above terminology, 4 types of interactions can be defined between the light ray and the top edge of the voxel depending on the value of τ_{x1}.

1. $\tau_{x1} < -1$

2. $-1\tau_{x1} < 0$

3. $0\tau_{x1}1$

4. $1 < \tau_{x1}$

Thus, each edge of the voxel perpendicular to the z-axis may interact with the light ray in one of the four ways. In a 2D reconstruction problem there are 2 edges perpendicular the z-axis and in 3D, there are 4 edges. Thus in 2D, there are 16 possible ways a voxel may interact with the light ray and there are 256 possible interactions in 3D.

The 16 possible cases in 2D are divided into 2 categories:

1. When $\tau_{x1} \times \tau_{x2} \geq 0$, the interaction is called positive interaction, and

2. When $\tau_{x1} \times \tau_{x2} < 0$, the interaction is called negative interaction.

This categorization divides the 16 cases, putting eight cases in category 1 and the other 8 in category 2. Interactions in category 1 and category 2 cases are shown in Figures 6.5 and 6.6 respectively. The dotted and the solid trapezoids represent the light ray and the voxel respectively.

6.1.4 Calculations

The 8 cases shown in category 1 are simple and easy to calculate the weight coefficient. In these cases, when the light ray interacts with the voxel, the interaction is either a simple triangle or a trapezoid. When the interaction is a trapezoid, the weighting coefficient is given

Case 1
$\tau_{x1} > 1$
$\tau_{x2} > 1$

Case 2
$\tau_{x2} > 1$
$1 >= \tau_{x2} >= 0$

Case 3
$1 >= \tau_{x1} >= 0$
$\tau_{x2} > 1$

Case 4
$1 >= \tau_{x1} >= 0$
$1 >= \tau_{x2} >= 0$

Case 5
$0 > \tau_{x1} >= -1$
$0 > \tau_{x2} >= -1$

Case 6
$0 > \tau_{x1} >= -1$
$-1 > \tau_{x2}$

Case 7
$-1 > \tau_{x1}$
$0 > \tau_{x2} >= -1$

Case 8
$-1 > \tau_{x1}$
$-1 > \tau_{x2}$
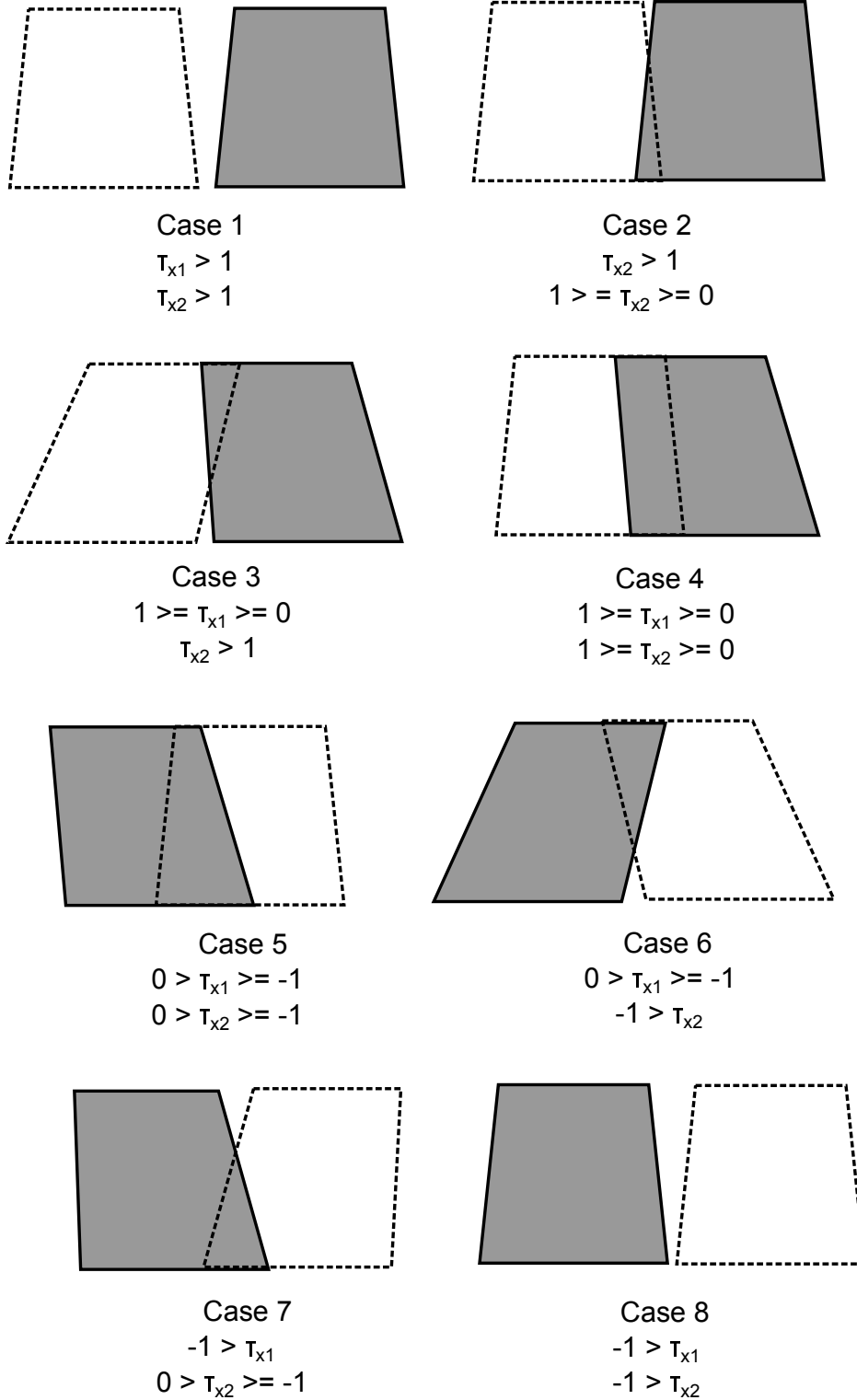
Figure 6.5: Possible interactions in category 1 $(_{x1} \times _{x2} 0)$.

Case 9
$\tau_{x1} > 1$
$-1 > \tau_{x2}$

Case 10
$1 >= \tau_{x1} >= 0$
$-1 >= \tau_{x2}$

Case 11
$\tau_{x1} > 1$
$0 > \tau_{x2} >= -1$

Case 12
$1 >= \tau_{x1} >= 0$
$0 > \tau_{x2} >= -1$

Case 13
$0 > \tau_{x1} >= -1$
$1 >= \tau_{x2} >= 0$

Case 14
$1 > \tau_{x1}$
$1 >= \tau_{x2} >= 0$

Case 15
$0 > \tau_{x1} >= -1$
$\tau_{x2} > 1$

Case 1
$-1 > \tau_{x1}$
$\tau_{x2} > 1$
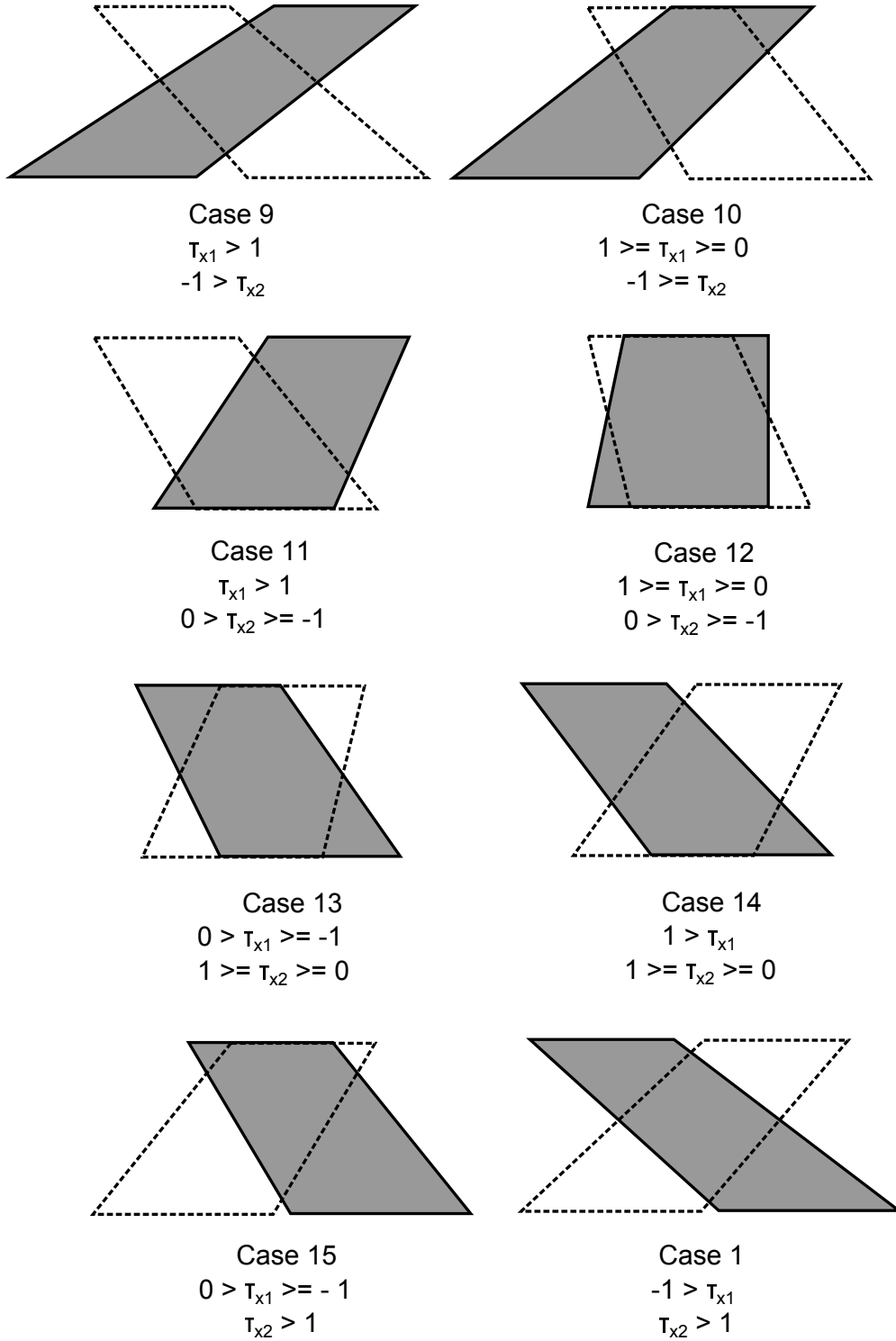
Figure 6.6: Possible interactions in category 2 ($_{x1} \times _{x2} < 0$).

by:

$$w = \frac{a_{x1} + a_{x2}}{l_1 + l_2} \tag{6.14}$$

When the interaction is a triangle, the height of the triangle of interaction is required. In Figure 6.7, a triangular interaction of the voxel and the light ray is shown (case 2 from category 1 shown in Figure 6.5). The angle made by the right edge of the light ray and the angle made by the left edge of the voxel with the z-axis are given by θ_r and θ_v respectively. These angles are known from the experimental setup. Using these angles, the height of the triangle is given by:

$$h = b - a_{x1} \times \text{abs} \left(\frac{\tan\left(\frac{\pi}{2} - \theta_r\right) \tan\left(\frac{\pi}{2} - \theta_v\right)}{\left(\frac{\pi}{2} - \theta_r\right) - \left(\frac{\pi}{2} - \theta_r\right)} \right) \tag{6.15}$$

Once calculated, the height of the triangle is used to calculate the weight coefficient by using:

$$w = \frac{a_{x2} h}{(l_1 + l_2) b} \tag{6.16}$$
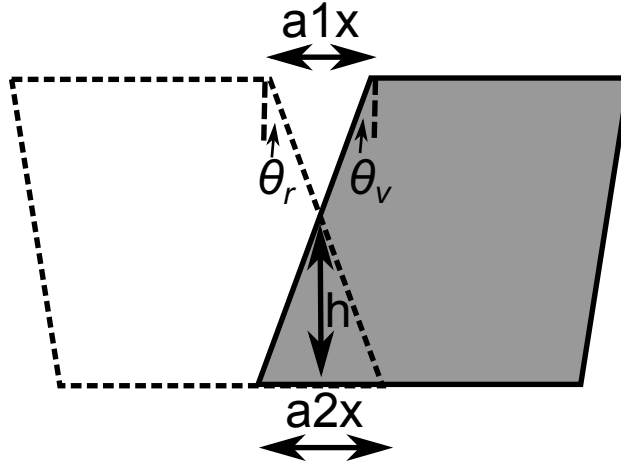
Figure 6.7: Simple case with triangular interaction.

The interactions in category 2 are more complex when compared to the cases in category 1. As an example, case 9 shown in Figure 6.6 is discussed here. To calculate the weight

coefficient for this interaction, the problem is divided into simpler cases. This simplification is shown in Figure 6.8.

In Figure 6.8, the area of the light ray in gray between the dashed lines is the area of interaction and forms a quadrilateral. In such complex situation it is easy to calculate the interaction by subtracting the blue quadrilateral regions from the area of the voxel. Thus,

$$w = \frac{\left(\frac{(l_1+l_2)b}{2} - \text{sum of the two blue regions}\right)}{\left(\frac{(l_1+l_2)b}{2}\right)} \tag{6.17}$$
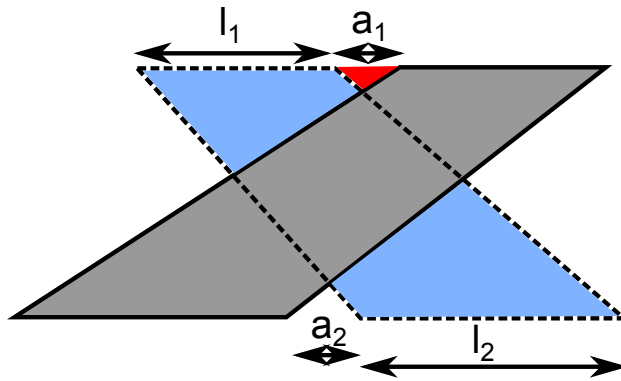
Figure 6.8: One of the complex cases from category 2 (case 9).

The two blue regions are also quadrilateral in shape and need more information than available to calculate their area. The areas of these quadrilaterals can be obtained from further simplification into simple triangles. For example, area of the top blue region is calculated by:

$$\text{area of top blue region} = \text{area of the triangle formed by the combined}$$
$$\text{region shaded in blue and red} - \text{area of the red triangle} \tag{6.18}$$

Areas of these triangles are calculated similar to the process discussed for the triangular interaction.

When extending the ideas from 2D to 3D, the interaction becomes more complex. The shapes of the interaction volumes seen in 3D are rectangular pipe with varying area of the rectangle along the z-axis, triangular pipe with varying depth of the pipe when moving from the base to the top of the triangle, and rectangular and triangular pyramids. These shapes are shown in Figure 6.9.
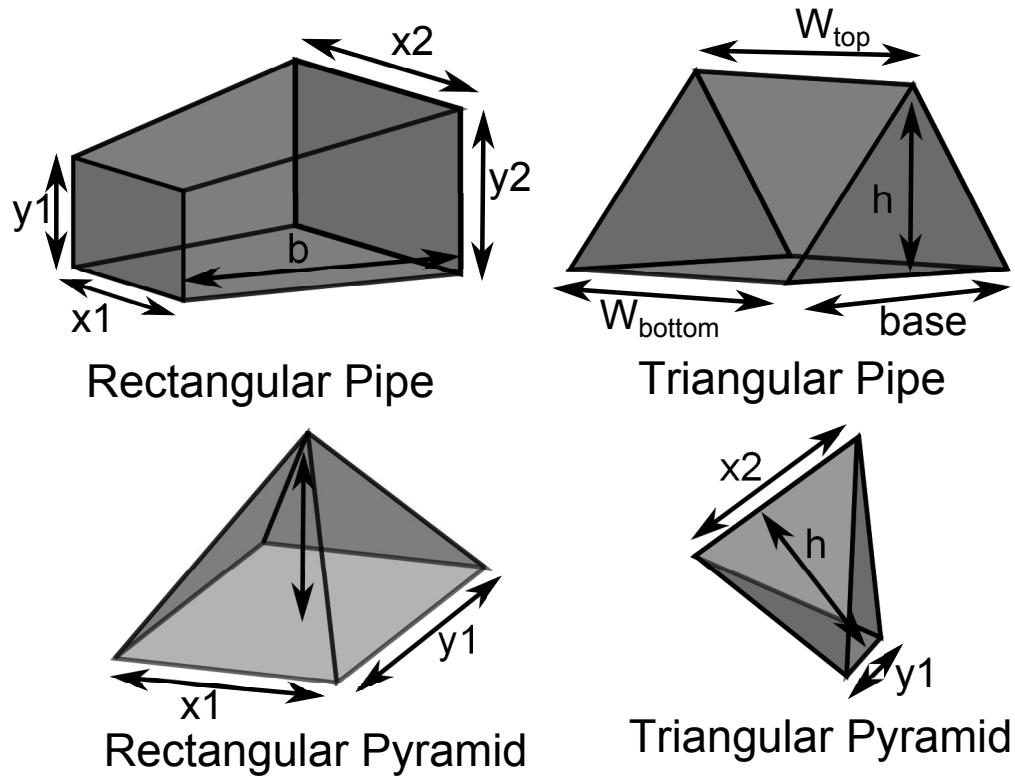
Figure 6.9: Shapes of the 3D volume interactions.

Volume measurement for each interaction is given by:

$$w_{Rpipe} = \frac{(x1 \cdot y1 + x2 \cdot y2)}{(l_{x1} \cdot l_{y1} + l_{x2} \cdot l_{y2})} \tag{6.19}$$

$$w_{Tpipe} = \left(\frac{base \cdot h \cdot w_{top}}{2} - \frac{base \cdot h \cdot (w_{top} - w_{base})}{2} \right) \cdot \frac{2}{(l_{x1} \cdot l_{y1} + l_{x2} \cdot l_{y2})\, b} \tag{6.20}$$

$$w_{Rpyramid} = \left(\frac{x1 \cdot x2 \cdot h}{3}\right) \cdot \frac{2}{(l_{x1} \cdot l_{y1} + l_{x2} \cdot l_{y2})\, b} \qquad (6.21)$$

$$w_{Tpyramid} = x1 \cdot h \cdot x1 \left(\frac{1}{2} - \frac{1}{3}\right) \cdot \frac{2}{(l_{x1} \cdot l_{y1} + l_{x2} \cdot l_{y2})\, b} \qquad (6.22)$$

6.2 Iterative Execution of MART

Things to remember before starting the reconstruction process:

1. The influence of a voxel on a perspective view is independent of its influence on any other perspective view.

2. The sum of all weight coefficients associated with a voxel and a perspective view has a maximum value of 1.

3. The sum of all weight coefficients associated with a voxel and all the perspective views for the assumed plenoptic camera (there are 7×7 perspective view) has a maximum value of 49.

$$\sum_{i=1}^{49} \sum w_{i,j} \leq 49 \qquad (6.23)$$

6.2.1 Execution

In this subsection, the steps associated with the reconstruction process are detailed.

1. Consider the example of the plenoptic camera with 100×100 microlens and 7×7 pixels under each microlens, which results in 7×7 perspective views. The VOI is discretized into $100 \times 100 \times 100$ voxels. For this setup, if the weights are calculated with double precision, then the total data containing weights is equal to a little more than 2GB. To keep the reconstruction fast without affecting the performance of the computer, calculate the weights for the volume associated with each perspective view separately and store them in separate files.

2. Initialize the density of all voxels in the VOI to 1.

3. Calculate the average density at each voxel due to every pixel in every perspective view using the MART equation.

4. If it is the first iteration, repeat step 3, else, calculate one of the three errors:

(a)

$$\text{Simple error}: e = \frac{\sum\limits_{x_j=1}^{N_x} \sum\limits_{y_j=1}^{N_y} \sum\limits_{z_j=1}^{N_z} |g^k(x_j, y_j, z_j) - g^{k-1}(x_j, y_j, z_j)|}{N_x N_y N_z} \qquad (6.24)$$

(b)

$$\text{RMS error}: e_{rms} = \left(\frac{\sum\limits_{x_j=1}^{N_x} \sum\limits_{y_j=1}^{N_y} \sum\limits_{z_j=1}^{N_z} \left[g^k(x_j, y_j, z_j) - g^{k-1}(x_j, y_j, z_j)\right]^2}{N_x N_y N_z} \right)^{1/2} \qquad (6.25)$$

(c)

$$\text{Nomralized error}: e_{norm} = \left(\frac{\sum\limits_{x_j=1}^{N_x} \sum\limits_{y_j=1}^{N_y} \sum\limits_{z_j=1}^{N_z} |g^k(x_j, y_j, z_j) - g^{k-1}(x_j, y_j, z_j)|}{\sum\limits_{x_j=1}^{N_x} \sum\limits_{y_j=1}^{N_y} \sum\limits_{z_j=1}^{N_z} g^k(x_j, y_j, z_j)} \right) \qquad (6.26)$$

5. Compare the calculated error with the stop criteria (degree of accuracy suitable for the work). Stop the iteration process if the error meets the criteria, else repeat steps 3-5. In this work, the simple error defined in step 4 is used.

   In this work, generation of the weighting function, simulation of models for testing the algorithm and the MART reconstruction were performed using the C++ programming language. All C++ codes written in this work were written and executed in the Microsoft Visual Studio 2013 environment with the compilers provided with it. Parallel processing was

enabled with the openmp package for C++. The simulations were run on a computer with AMDs A8-5500 processor with 10 GB memory.

The simulated models used in Chapter-5 had a magnification of 1 with a 7×7 array of cameras looking into the VOI. Each camera was modeled to have 100×100 pixel sensor. The VOI in these models was discretized into $100 \times 100 \times 100$ voxels. As mentioned, the weight function associated with individual cameras were store separately. Generating the complete weighting function for the above experimental configuration required 90 min of computing time.

The weighting function in this work is stored as a vector. The influence of all voxels in the volume on a single pixels are stored in subsequent elements of the vector followed by the influence on the next pixel. If the plane of voxels parallel to xy plane is considered a layer, then for the current configuration, there are utmost of 9 (3×3) voxels in a layer that influence the information of the pixel. This was used to reduce the size of the weighting function file size by storing only the information of the 9 voxels that may influence the pixel along with the information about location of the top right voxel in the 3×3 array of voxels.

For example, one of the extreme cases in the models simulated in Chapter-5 is the bottom right corner pixel in camera 1. Figure 6.10 shows schematic images of how the line of sight of the pixel interacts with layers 1 and 2. Only the voxels whose information is stored in the weighting function are shown in these images. The solid boxes in the images represent the voxels and the dashed box represents the light ray reaching the pixel. Numbers on the top and left show the column and row numbers of the voxels and the numbers in the voxels represent the fraction of the volume of the voxel that influences the information captured by the pixel associated with the light ray. From Figure 6.10(a), vector that represents the influence of layer 1 on the bottom right corner pixel of camera 1 is given by:

$$l1p10000 = [84,\ 84,\ 0,\ 0,\ 0,\ 0,\ 0.3111,\ 0.2138,\ 0,\ 0.2138,\ 0.2613] \qquad (6.27)$$

Where, $l1$ represents the layer, $p10000$ represents the pixel number. Pixels are number from the top left corner of the camera and navigating along the row. The first two elements in the vector represent the row and column of the voxel in the top left corner of the 3×3 array of voxels shown in Figure 6.10(a). The weighting vector that shows the influence of the whole volume on the pixel is given by:

$$VOIp10000 = [l1p10000,\ l2p10000,\ \dots l100p10000] \tag{6.28}$$

And the vector representing the weight function of the whole camera is given by:

$$C1 = [VOIp1,\ VOIp2,\ \dots VOIp10000] \tag{6.29}$$

Where, $C1$ is the vector with the complete weighting function for camera 1 that is stored in a single file.
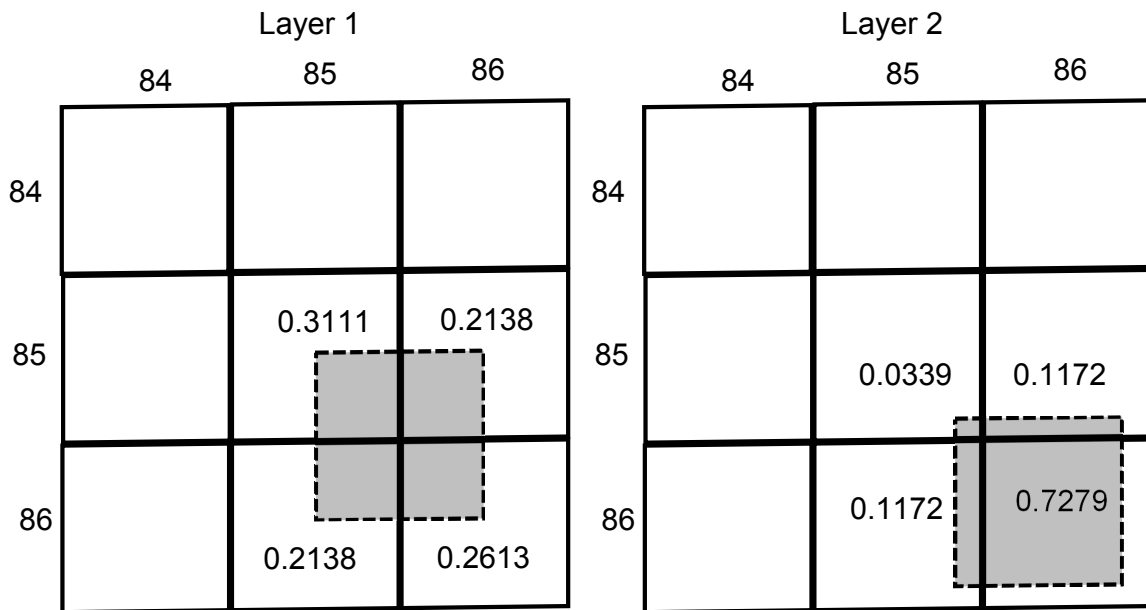
Figure 6.10: Schematic images showing the influence of layers 1 and 2 with the bottom right pixel in camera 1.

Current implementation of the weighting function and the reconstruction were optimized for memory and time, but, further optimization is possible. Optimization of the current implementation will be investigated in future studies.

To demonstrate the reconstruction capabilities of the reconstruction of choice and the developed weighting function implementation, the model with positive disturbance from Chapter-5 is used here. Reconstruction process for the model with the above mentioned computer required 150-180 min of computing time for 15 iterations. Figure 6.11 shows layer 9 from the simulated volume containing two inhomogeneities. Figure 6.11 shows the same layer from the reconstructed volume at different iterations. From the images in Figure 6.11, the convergence of the reconstructed volume towards the solution with increasing iterations is clearly visible giving us the confidence on the developed weighting function. In the next chapter, the performance of the reconstruction technique is further tested and analyzed with simulated flow fields.
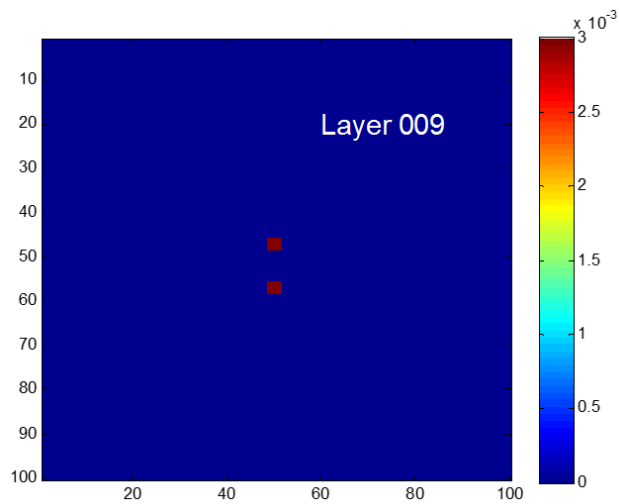
Figure 6.11: Layer 9 from the simulated model showing the presence of positive inhomogeneities.
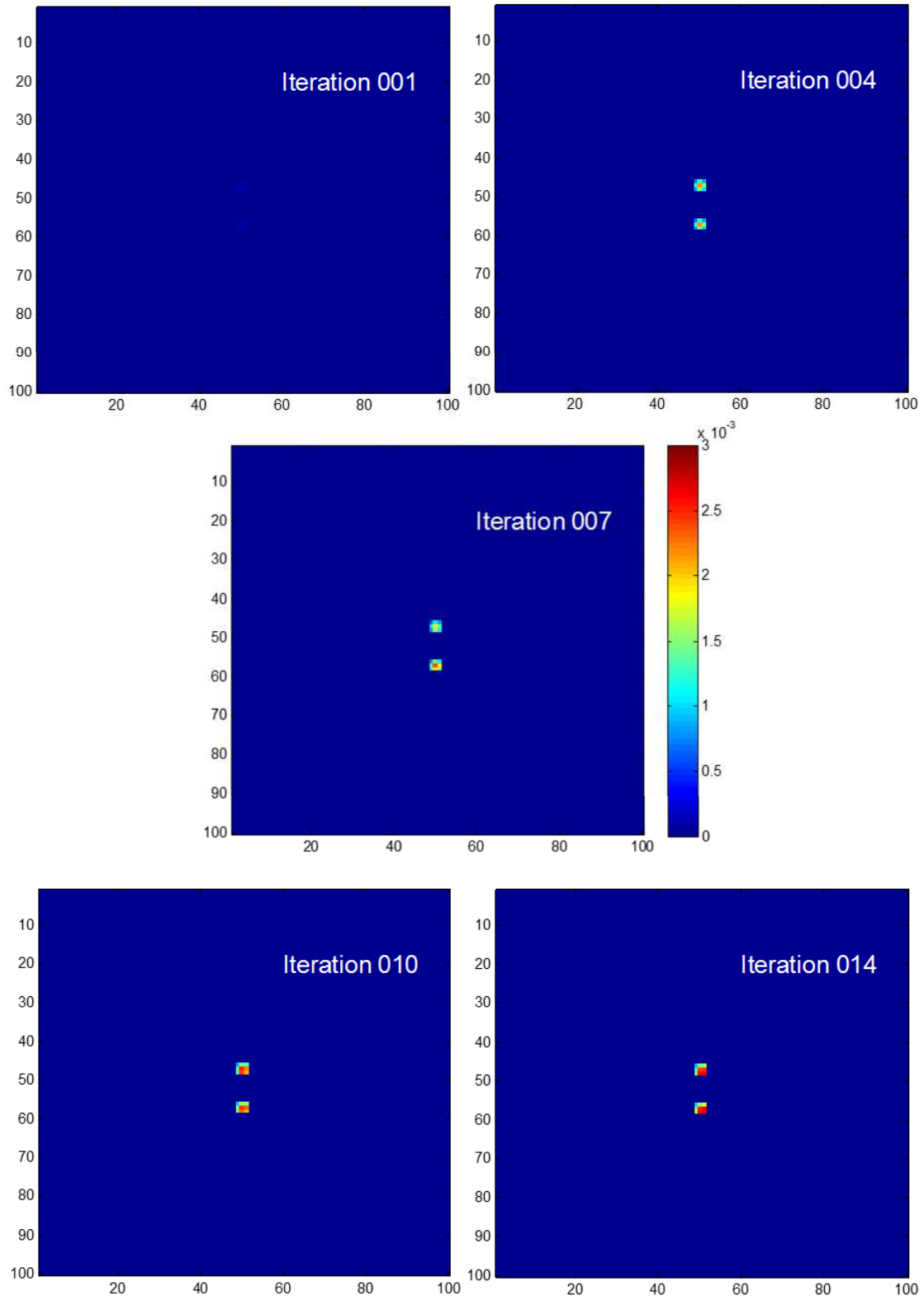
Figure 6.12: Layer 9 from the reconstructed volume obtained after different number of iterations showing the evolution of the solution with iterations.

Chapter 7

Simulated Experiments and Results

So far in this dissertation, capabilities of BOS and the plenoptic camera were discussed in Chapters 3 and 4 respectively, followed by a brief description and the choice of the reconstruction technique for this work in Chapter 5 and the algorithm execution in Chapter 6. In this chapter and the following chapter, observations from the study done to show the performance of the 3DDMT developed are present. The results and observations in this research are divided into simulated and physical experiments. Results from the simulated experiments are presented in this chapter and the physical experiments are presented in Chapter 8.

Simulated experiments mimicking the 3DDMT were performed to test:

1. the modulation transfer function (MTF) for the technique,

2. its accuracy to reconstruct the 3D flow field using a simulated flow field with perfect input data, and

3. its accuracy to reconstruct the 3D flow field with less than perfect, noisy, input data.

Simulations were modeled to mimic the plenoptic camera with 100×100 microlens and 7×7 pixels under each microlens, as described in Chapter 5. Magnification of the system for the simulations was set at 1 ($M = 1$) and the physical dimensions for experimental setup were calculated with the equations developed in Chapter 3. Dimensions used in these simulations are given in Table 7.1.

Physical Quantity	Value (m)
f	0.05
p_{micro}	123e-6
f_{micro}	500e-6
s_o	0.1
s_i	0.1
s_{near}	0.0758
s_{far}	0.1471
DOF	0.0713
M	1
CC	1

Table 7.1: Table showing the physical quantities calculated with the equations developed in Chapter-3.

7.1 Modulation Transfer Function

In imaging systems, MTF is the measure of the sharpness with which it captures the images. The MTF is represented as a function of spatial frequency. Williams and Burns in 2000 [130], described the MTF as the measure of the spatial frequency response (SFR) of cameras as a function of aperture, field position and defocusing optical phenomenon. For a given imaging system MTF of the system is a function of the MTF of its components such as the lens, image sensor (digital or film) etc. Studying MTF in this work is to measure the limitations of the concept and not to study the MTF of the individual components.

Mathematically, image captured through an optical system can be written as:

$$p(x, y) = q(x, y) * *r(x, y) \tag{7.1}$$

where, $r(x, y)$ is the real space imaged, $q(x, y)$ is the impulse function of the optical system, $p(x, y)$ is the projection image on the image sensor, and $**$ denotes 2D convolution. Fourier transform of Equation 7.1 is given by:

$$P(\xi_x, \xi_y) = Q(\xi_x, \xi_y)R(\xi_x, \xi_y) \tag{7.2}$$

P, Q and R are the individual Fourier transforms of p, q and r respectively. Q in Equation 7.2 is referred to as the transfer function. In classic optical system, Q is referred to as the optical transfer function (OTF) and the modulus of OTF is called the MTF [131].

$$\text{MTF}_{\text{Hz}} = |\text{OTF}| = |Q(\xi_x, \xi_y)| \tag{7.3}$$

In the above equation, Hz in the subscript refers to the frequency at which MTF is calculated. In simple form, MTF can be written as:

$$\text{MTF}_{\text{Hz}} = \frac{Mod_p}{Mod_r} \tag{7.4}$$

Where, Mod_p and Mod_r are the modulation of the image/projection and the real space respectively and the modulation is measured as:

$$Mod = \frac{I_{max} - I_{min}}{I_{max} + I_{min}} \tag{7.5}$$

Where, I_{max} and I_{min} are the maximum and minimum intensities.

Before the emergence of digital cameras, the knife-edge technique (KET) was used to estimate the MTF of a spatially continuous imaging system (eg. film camera) [132–135]. In KET, an image of a sharp discontinuity is imaged with radiance uniformity and edge regularity. This image is then scanned and sampled for the edge feature using a microdensitometer, an instrument used to measure optical densities, perpendicular to the edge. An edge profile thus obtained is then used to derive the point spread function using either discrete first derivative or parametric fit of the data. The modulus of the discrete Fourier transform is then computed to give the MTF [136]. Detailed information on the KET is out of the scope of this work. Readers are directed to the references for more information.

With the emergence of the digital cameras in the 90's and early 2000, use of KET to estimate the MTF was found inaccurate [136, 137]. Reichenbach et al. [137] detailed the

problems associated with the application of KET to estimate the MTF for digital cameras. KET was designed for a continuous oversampled image, whereas, the digital cameras register data only at fixed points resulting in undersampled data. Sampling of the scanned image in KET is done to facilitate the processing by manipulating the sampling rate and orientation. To address the issues associated with estimating the MTF for digital cameras, other techniques were developed that used one of the three targets:

1. slant edge target,

2. sinusoidal wave target, and

3. grill target.

Slant Edge Target

One of the earliest attempts to characterize the performance of the digital cameras was detailed by Reichenbach et al. [137] in 1991. In their paper they refer to the slant edge technique (SET) as the extension of KET. Burns in 2000 [136] noted that the use of digital cameras for imaging the slant edge eliminates the use of external instruments such as the microdensitometer, for sampling the image of the edge.

Figure 7.1 shows an example of SET. In SET, an edge set at an angle to the rows of pixels of the camera is imaged, shown in Figure 7.1(a). The response of the pixels in a digital camera is shown in Figure 7.1(b) with dashed line and the comparative ideal analog response shown by the solid line. Once imaged, the possible edge location for each row is calculated with sub-pixel accuracy using one of the techniques described in literature [138–140]. After accurately locating the edge in each row, they are aligned and super imposed, as shown in Figure 7.1(c). This produces a super resolved sampling, beyond Nyquist frequency, of the edge as required by KET to estimate the MTF of the digital camera. To standardizing the SET measurement technique for measuring MTF of digital cameras, a reference target (shown in Figure 7.2) and the SET measurement technique was detailed in the ISO-12233 documents.
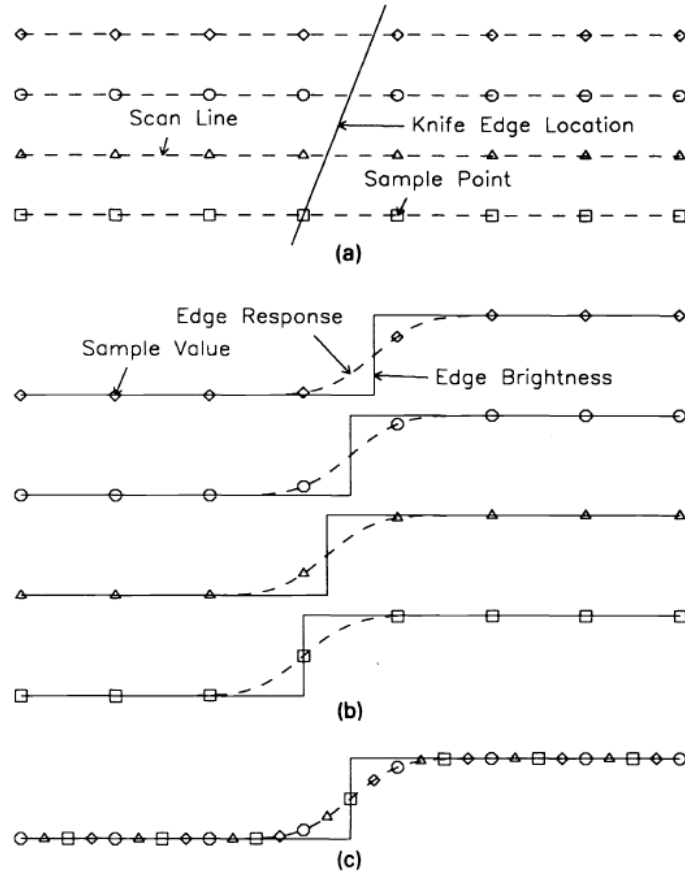
Figure 7.1: Registering scans with shifted with knife edge. (a) Sampling grid with knife edge skewed from perpendicular. (b) Knife-edge shift in successive scans. (c) Combined scan with registered edges [137].

Sinusoidal Wave Target

Figure 7.3 shows a typical sinusoidal wave target (SWT) used for estimating the MTF for cameras. The upper and the lower rows contain boxes with different gray scale values and the two middle rows contain the sinusoidal patterns with varying frequencies. Each sinusoidal pattern has a single frequency thus allowing the calculation of MTF for individual frequencies directly.

As, each individual frequency is imaged separately, the SWT to measure the MTF helps in detection/isolation of a problem and has high signal-to-noise ratio [131]. When using the sinusoidal wave for estimating the MTF of the system, use of single frequency with each target can prolong the process when a range of frequencies are used.

119
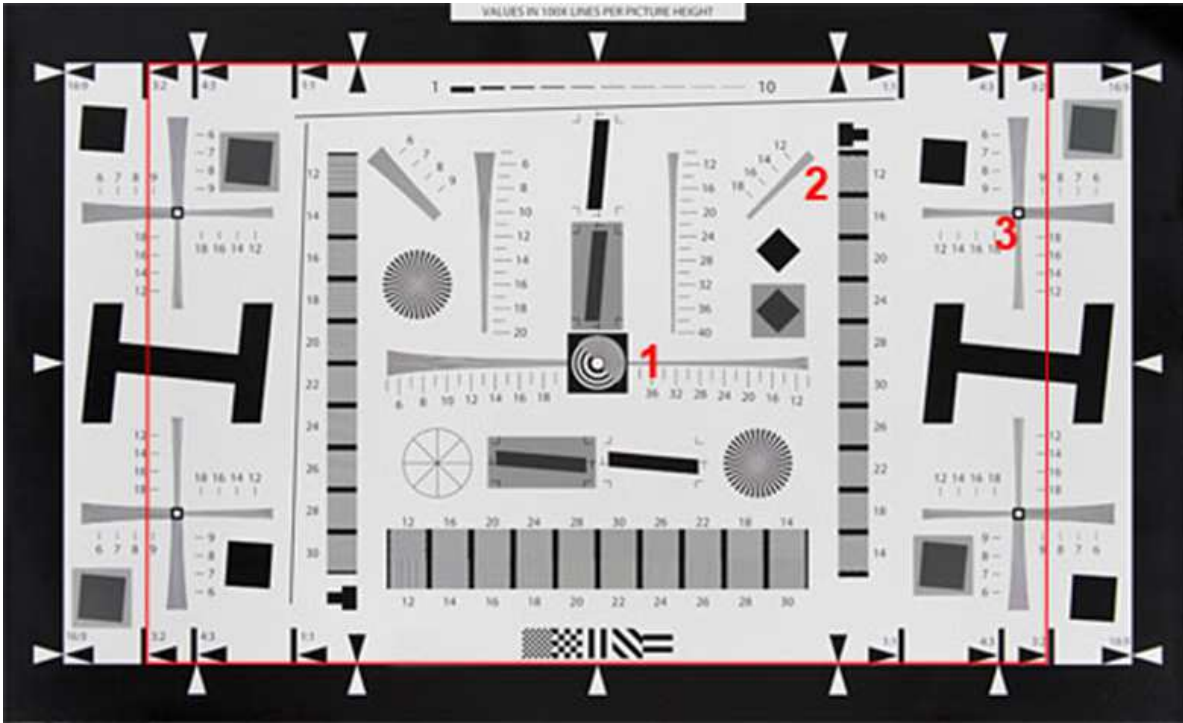
Figure 7.2: Images shows the target recommended for using with the slant-edge technique [141].
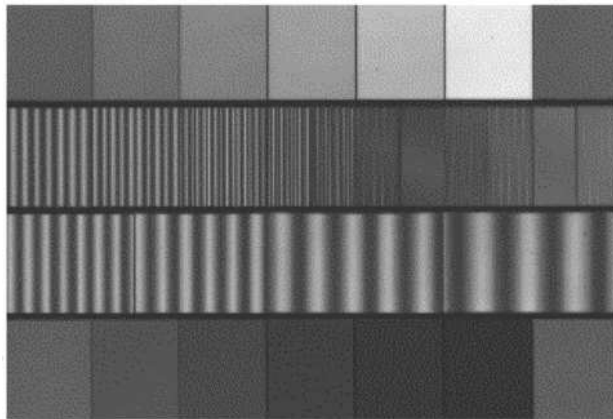
Figure 7.3: Images shows the target recommended for using with the slant-edge technique [142].

Grill Target

The grill target method of measuring the MTF is also known as the bar target. In some of the works this is also referred to as knife-edge target method. The different names

for the technique come from the fact that the target imaged consists of lines with varying frequencies and the sharp edges. The lines in the target are either aligned parallel to the rows or the columns of the pixels of the imaging sensor.

Figure 7.4 shows the grill target referred to as the USAF 1951 resolution target used for measuring the resolution of the imaging systems. The bars in the target are divided into 5 groups, -2, -1, 0, 1 and 2, and each group has 6 elements (sets of grills). Resolution measurement when using this target is given by:

$$resolution = 2^{group + \frac{element - 1}{6}} \qquad (7.6)$$
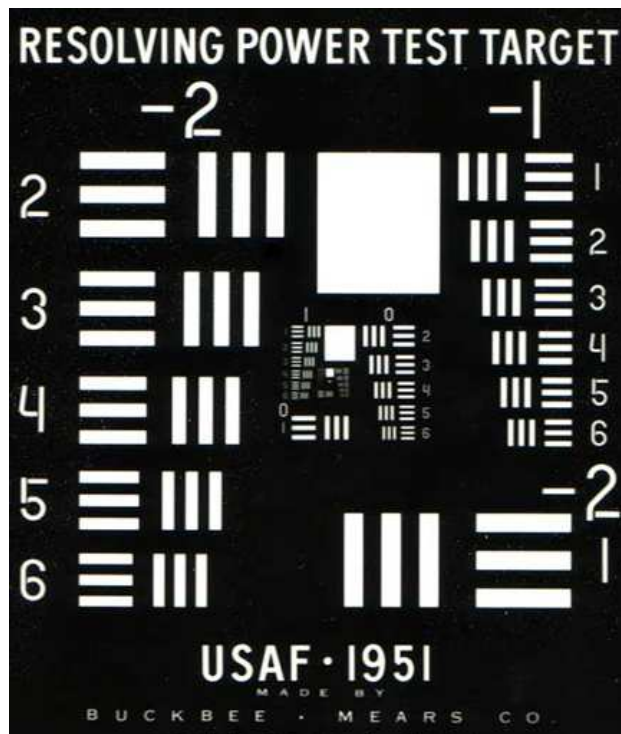
Figure 7.4: USAF target for measuring the resolution of the imaging systems.

Equation 7.6 measures the resolution in terms of lines per millimeter, fundamental frequency of the grill. For example, let's consider group -2 and element 1, when substituted in Equation 7.6 gives 0.25 lines per millimeter. Measuring MTF from the grill target is different from the formula given in Equation 7.4 as there are more than one frequency in any

grill target. Nill in 2001 [131] addressed the issue of comparing the MTF from a sinusoidal target with that obtained from a grill target. Because the two are different, to distinguish the MTF of the grill target from that of the sinusoidal target, MTF from the grill target is referred to as the contrast transfer function (CTF). Nill used Coltman formulas to convert MFT to CTF and vice versa.

$$\text{MTF}_{\text{HZ}} = \frac{\pi}{4}\left[\text{CTF}_{\text{HZ}} + \frac{1}{3}\text{CTF}_{3\text{HZ}} - \frac{1}{5}\text{CTF}_{5\text{HZ}} + \frac{1}{7}\text{CTF}_{7\text{HZ}} + \frac{1}{11}\text{CTF}_{11\text{HZ}} - \frac{1}{13}\text{CTF}_{13\text{HZ}}\dots\right]$$
(7.7)

$$\text{CTF}_{\text{HZ}} = \frac{\pi}{4}\left[\text{MTF}_{\text{HZ}} - \frac{1}{3}\text{MTF}_{3\text{HZ}} + \frac{1}{5}\text{MTF}_{5\text{HZ}} - \frac{1}{7}\text{MTF}_{7\text{HZ}} + \frac{1}{9}\text{MTF}_{9\text{HZ}} - \frac{1}{11}\text{MTF}_{11\text{HZ}}\dots\right]$$
(7.8)

For this work, the SWT was selected to estimate the MTF of the 3DDMT. Using the SWT for MTF measurement allows to measure MTF at a single frequency and keeps the process simple and straight forward. An example of the model is shown in Figure 7.5.

MTF analysis of the 3DDMT was done with varying frequencies of the sinusoidal wave. Frequency of the sinusoidal wave was varied by varying the wavelength. For analysis, 4, 8, 10, 20, 30, 40, and 50 microlens size wavelengths were used. Figure 7.5 shows the slices from the VOI with density varying as a sinusoidal wave with 30 microlenses long wavelength (MLW). Figure 7.5(a) shows cross-sectional plane coinciding the focal plane of the setup, xy plane. Figures 7.5(b) and 7.5(c) show the planes parallel to xz and yz planes respectively. Planes in Figures 7.5(b) and 7.5(c) divide the volume in to two equal parts. From Figures 7.5(b) and 7.5(c), it is evident that the cross section of the volume increases along the z-axis away from the camera lens. If noticed, the color distribution in the plane in Figure 7.5(c) varies from the front of the VOI to the back. Though, the actual density is constant along the

plane, discretization of the VOI results in decreasing average density from the front to the back of the VOI as the volume of individual voxels increase from the front to the back.
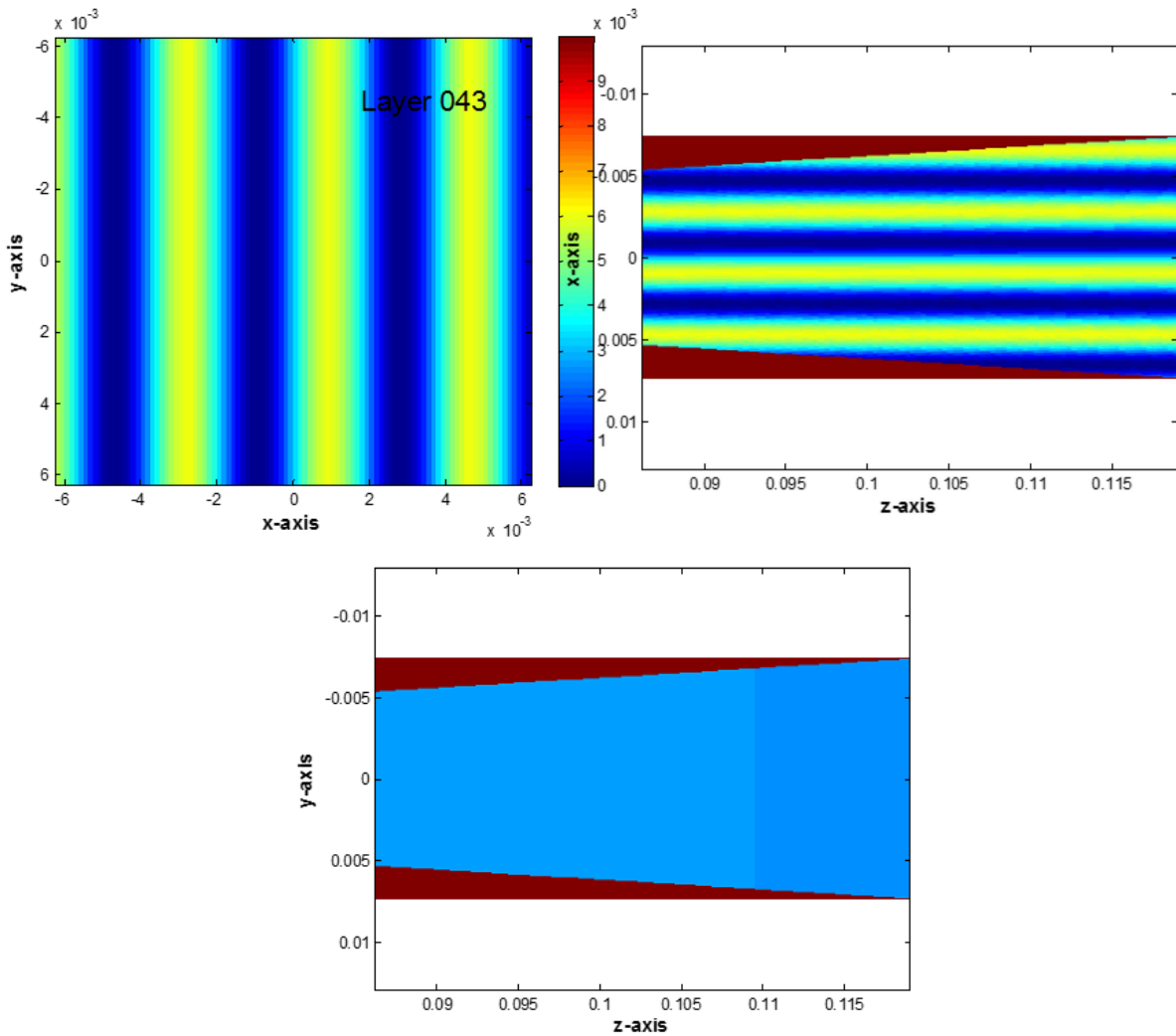
Figure 7.5: Figure showing the percentage error distribution in the calculated OPD.

All images in Figure 7.5 were generated using MATLAB. Because the size of the voxels and the cross-section varied along the z-axis, plotting the xz and the yz planes with standard options resulted in plots with distortions that do not depict the actual shape of the VOI. To overcome the limitations, the VOI in x and y direction were divided with a common divisor into much smaller voxels. Doing so, the boundaries of the new smaller voxels may or may

not coincide with the boundaries of the original voxels thus causing the plots to have some jagged edges.

OPD measured due to the sinusoidal density distribution in the VOI as viewed by each camera was obtained by integrating the refractive index along the line of sight. Some of the perspective views simulated with the 30 MLW disturbance in the VOI are shown in Figure 7.6. In Figure 7.6, 5 perspective views from the array of 7×7 virtual cameras are shown. The numbering of the cameras used in this experiment is the same as the numbering scheme discussed in Chapter 5. From that discussion, cameras 1 and 43 are at the two ends of the left most column, cameras 7 and 49 are at the two ends of the right most column, cameras 1 and 7 belong to the top row and cameras 43 and 49 belong to the bottom row. Camera 25 is at the center of the array. As the sinusoidal nature of the disturbance was simulated in the x-direction, images captured in the perspective views change along the row (compare cameras 1 and 7 or cameras 43 and 49), whereas, the perspective views along the column show no difference (compare cameras 1 and 43 or cameras 7 and 49).

OPD measured from the simulations were used in the 3D reconstruction of the volume using the MART equation selected in Chapter 5 and given here in Equation 7.9 for convenience.

$$g\left(x_j, y_j, z_j\right)^{k+1} = g\left(x_j, y_j, z_j\right)^k \frac{1}{N_j} \sum_{i=1}^{N_T} \left(\frac{I\left(X_i, Y_i\right) + IC_i^k}{\sum_{j \in N_i} w_{i,j} g\left(x_j, y_j, z_j\right)^k} \right) \tag{7.9}$$

Results from the reconstructed volume with 30 MLW disturbance are shown in Figure 7.7. An averaging filter of size $3 \times 3 \times 3$ was used in the reconstruction process of this volume. All three plots are plotted with the same color scheme with the range of the color scheme varying from the smallest density value to the largest density value in the reconstructed volume. Qualitatively, the reconstructed volume matches the input volume. The features, such as the density value varying in a sinusoidal fashion, that are expected to see in the reconstructed volume are noticeable and follow the input volume pretty well.
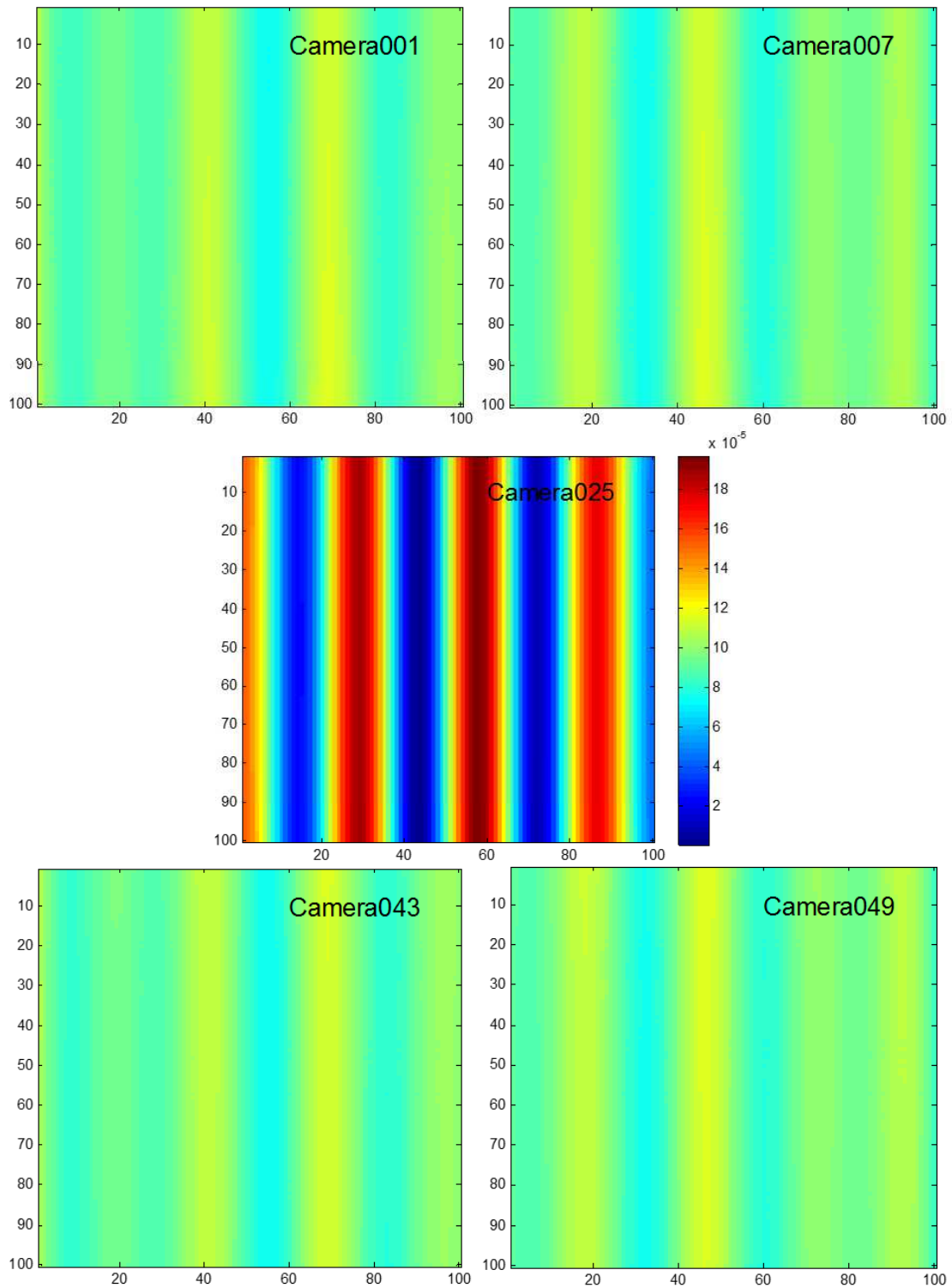
Figure 7.6: OPD measured for a) camera 1, b) camera 7, c) camera 25, d) camera 43, and e) camera 49.
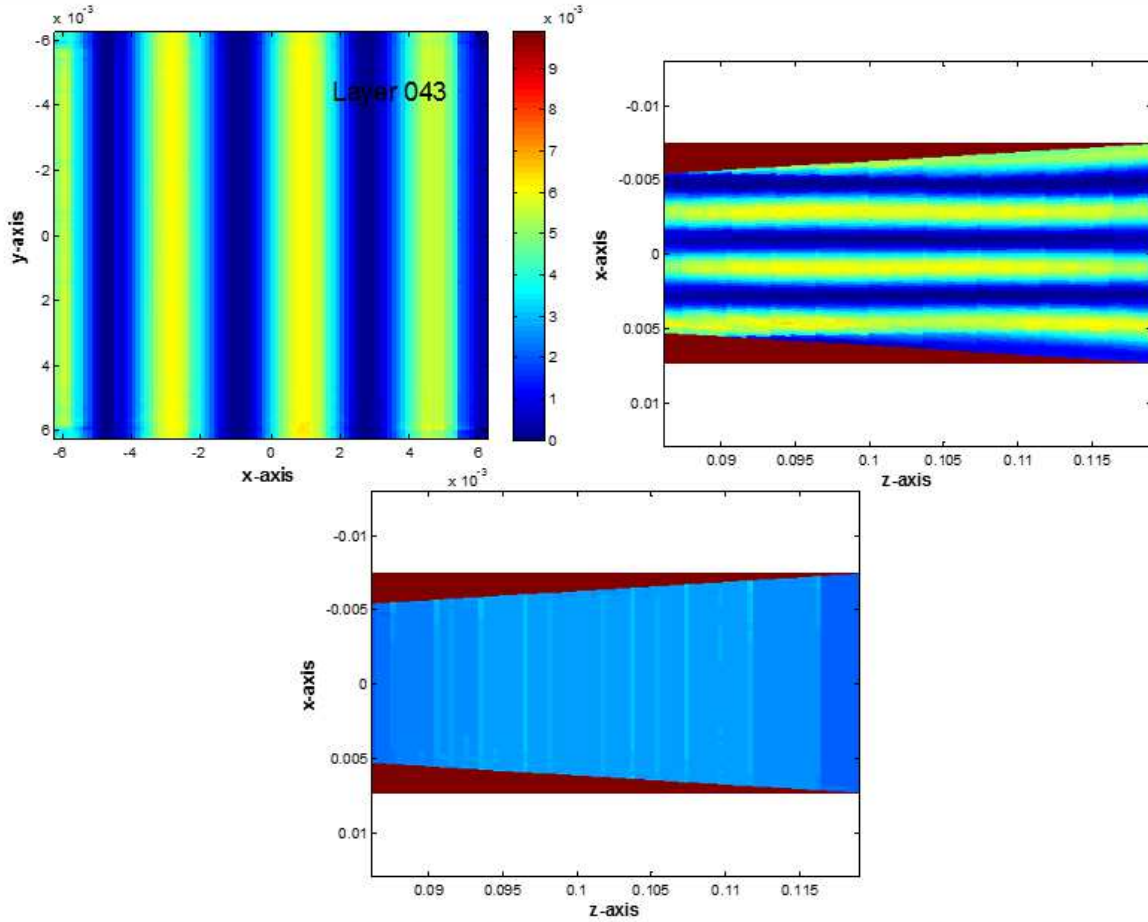
Figure 7.7: Results from the reconstructed volume. a) Sinusoidal distribution of the disturbance in the focal-plane (xy plane). b) Plane splitting the volume in two equal halves in xz plane. c) Plane splitting the volume in two equal halves in yz plane.

After the reconstruction of the 3D VOIs, data from the simulated volumes and the reconstructed volumes was used to calculate the MTF at different wavelengths using Equations 7.4 and 7.5. MTF values thus obtained are plotted against the sinusoidal wavelength and frequency in Figure 7.8. In Figure 7.8(a), MTF is plotted against the wavelength of the sinusoidal wave and in Figure 7.8(b) MTF is plotted against the frequency. The bold line in both plots represents the MTF measured for the reconstructed volume obtained with no averaging filter in the reconstruction process. The dashed line represents the reconstruction process with a $3 \times 3 \times 3$ pixel averaging filter. There are a couple of things that can be learned from these plots.

1. The reconstruction of the VOI was better when there was no averaging filter used in the reconstruction process, and

2. The performance of the reconstruction was good until the disturbance had a wavelength greater than or equal to 8 MLW and then drops off sharply.
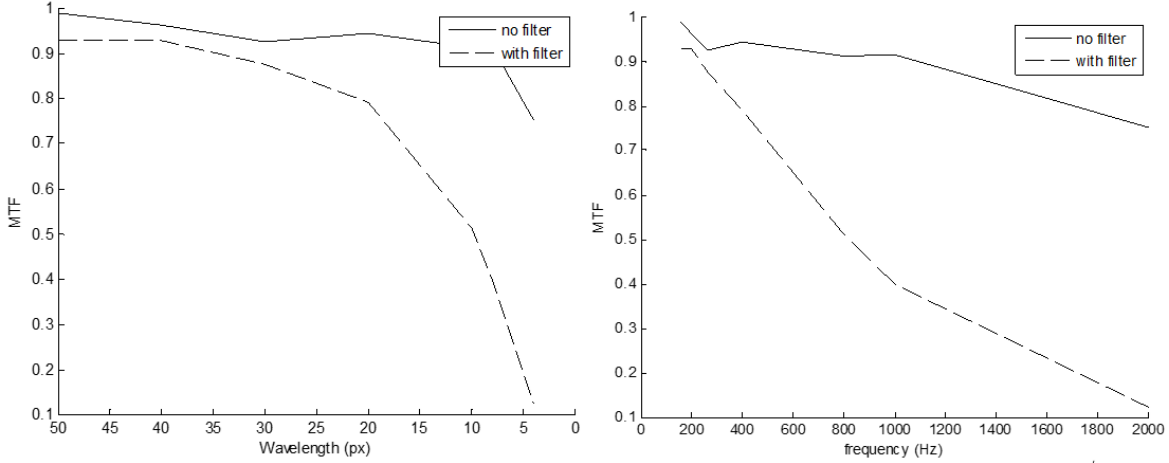
Figure 7.8: Plots showing MTF. a) MTF plotted against wavelength and b) MTF plotted against frequency.

From the observations, it is noted that the reconstruction without filter in the process is better than reconstruction with the filter and the performance of the reconstruction technique was good when the wavelength of the sinusoid was greater than 8 microlenses. The idea of filters is further tested and the results are presented in the next section. To understand the drop off of the performance of the reconstruction technique when the disturbance wavelength is below 8 microlenses (which is approximately 6.7 voxel length at the end of the DOF), plots showing the cross-section of the reconstructed volume with 4 and 8 MLW test cases are presented in Figure 7.9. The cross-sectional planes plotted in Figure 7.9 are the planes close to the focal plane of the experimental setup. In Figure 7.9(a), the cross-section from 4 MLW test case is shown and the aliasing effect in the reconstructed volume is unmistakable. In Figure 7.9(b), aliasing effect is not that obvious but a closer look reveals some aliasing.

These observations suggests that the Nyquist rate for the reconstruction is between 4 and 8 microlenses.
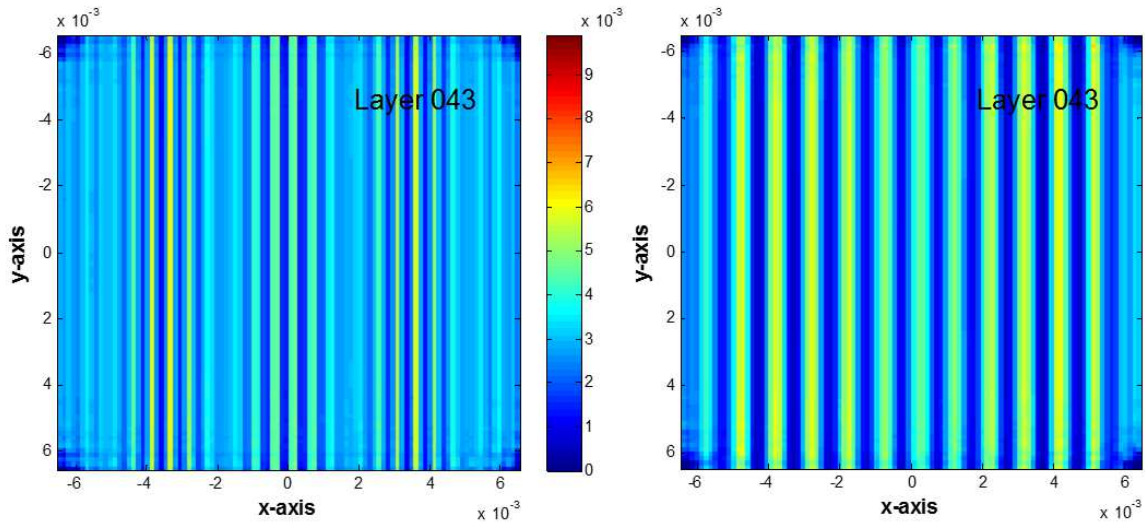
Figure 7.9: Cross-sectional plane from a) 4 voxel and b) 8 voxel sinusoidal wave density distribution.

7.2 Observations from Perfect Input Data

In this subsection, the goals are to:

1. compare the effect of averaging filter on the MART reconstruction technique,

2. study the performance of the 3DDMT with error analysis, and

3. apply the 3DDMT technique to a flow field with a shock in the FOV and study its performance.

To understand the effect of the filter size on the reconstructed volume, reconstruction was performed with no filter and with averaging filters of size $3 \times 3 \times 3$ and $5 \times 5 \times 5$. Results present here are from the reconstructions using no filter and with the filter size $3 \times 3 \times 3$ but similar observations were seen with the filter size $5 \times 5 \times 5$.

For visual comparison, the density distribution in the focal plane from both reconstructed volumes are shown in Figure 7.10. The slice of the volume in Figure 7.10(a) is from the reconstructed volume with the $3 \times 3 \times 3$ averaging filter in the reconstruction process and the slice of the volume in Figure 7.10(b) is from the reconstructed volume with no filter in the reconstruction process. Qualitatively, both volumes appear similar, but a closer comparison of the reconstructed volumes with the simulated or the expected volume would reveal more. Qualitative comparison of the two reconstructed volumes layer by layer with the simulated volume show that the use of the filter smoothens the reconstructed volume and has less artifacts. This smoothening of the density distribution in the volume also results in different range of density values in the two reconstructed volumes.
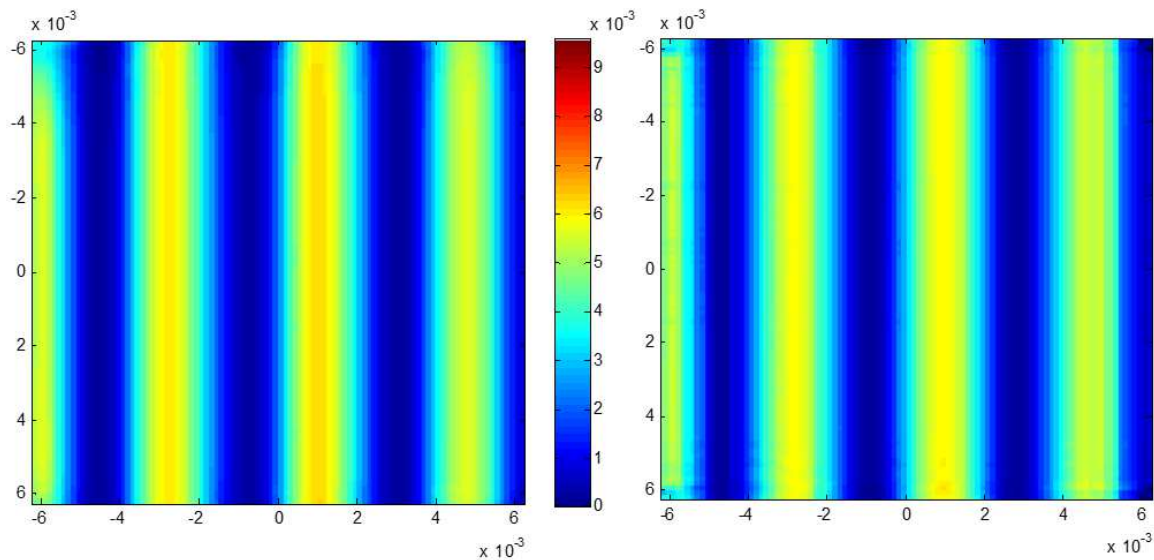
Figure 7.10: Cross-sectional plane from the reconstructed volume when a) 3×3 filter and b) no filter were used in the reconstruction process.

A better understanding of the reconstruction accuracy is obtained from error analysis. Figure 7.11 shows the error plots for both reconstructions. The dashed line represents the reconstruction with the filter and the bold line represents the reconstruction without the filter. The x-axis in the plots represents the iteration and the y-axis represents the error. As these are simulated experiments, errors in the reconstruction can be directly obtained by

comparing the reconstructed volume with the actual or simulated density distribution model. Error equations given in Equations 6.24, 6.25 and 6.26 in Chapter 6, given here again for the reference, are used for plotting the error plots in Figure 7.11.

Simple error:

$$e = \frac{\sum\limits_{x_j=1}^{N_x} \sum\limits_{y_j=1}^{N_y} \sum\limits_{z_j=1}^{N_z} |g^k(x_j, y_j, z_j) - g^{k-1}(x_j, y_j, z_j)|}{N_x N_y N_z} \tag{7.10}$$

RMS error:

$$e_{rms} = \left(\frac{\sum\limits_{x_j=1}^{N_x} \sum\limits_{y_j=1}^{N_y} \sum\limits_{z_j=1}^{N_z} \left[g^k(x_j, y_j, z_j) - g^{k-1}(x_j, y_j, z_j) \right]^2}{N_x N_y N_z} \right)^{1/2} \tag{7.11}$$

Normalized error:

$$e_{norm} = \left(\frac{\sum\limits_{x_j=1}^{N_x} \sum\limits_{y_j=1}^{N_y} \sum\limits_{z_j=1}^{N_z} |g^k(x_j, y_j, z_j) - g^{k-1}(x_j, y_j, z_j)|}{\sum\limits_{x_j=1}^{N_x} \sum\limits_{y_j=1}^{N_y} \sum\limits_{z_j=1}^{N_z} g^k(x_j, y_j, z_j)} \right) \tag{7.12}$$

From the plots, it is observed that the output from the reconstruction without any filters is better when compared with the output from the reconstruction with the filter. From Figure 7.11, when using the averaging filter, the error seems to reach a minimum at 13 or 14 iterations and the output diverges from the solution there after with increasing iterations. When using no filter in the reconstruction process, increasing iterations is resulting in the output to converging towards the solution. To further test the reconstruction process with no filter, iterations on the volume with 40 microlens wavelength were extended to more than 50 iterations. Results from the experiment are plotted in Figure 7.12. From the figure, we notice that the output from the reconstruction process with no filter seem to be approaching the solution even after 50 iterations.
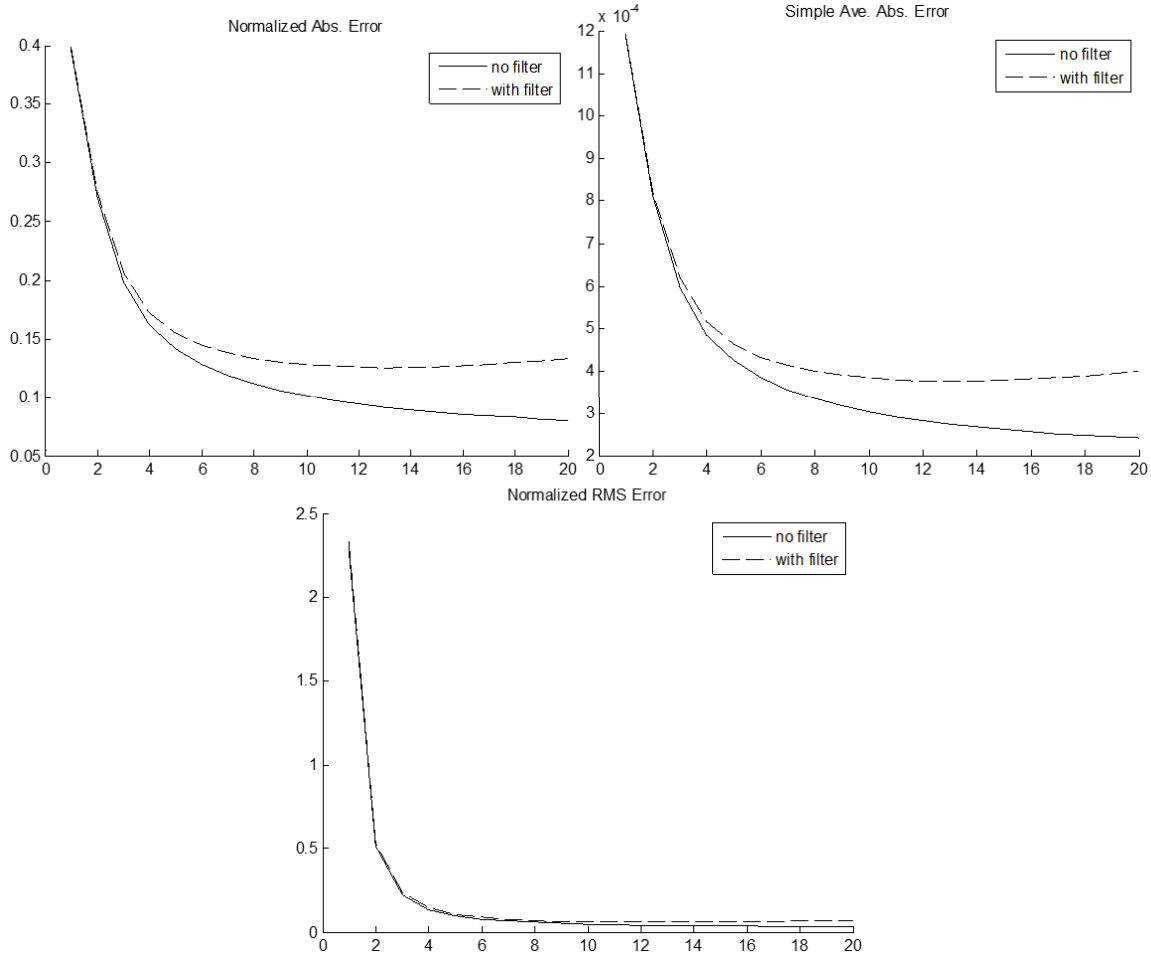
Figure 7.11: Error plots. a) Normalized Absolute error, b) Simple average absolute error, and c) Normalized RMS error.

In the 3D reconstruction processes such as the one used in this work, iterative, rate of convergence of the reconstruction process is as important as the accuracy. For comparison, the rate of convergence measured as the change in the volumetric density distribution from one iteration to the next are plotted in Figure 7.13. Rate of convergence from the two reconstruction methods, with and without filter, are compared. Reconstruction process with no filter is slow on convergence when compared with the process with filter. But, when using the filter in the reconstruction process, solution start to diverge after 13 or 14 iterations depending on the method of comparison. Similar trend is seen in the error plots in Figure 7.11. This trend observed here suggest that the reconstruction process without
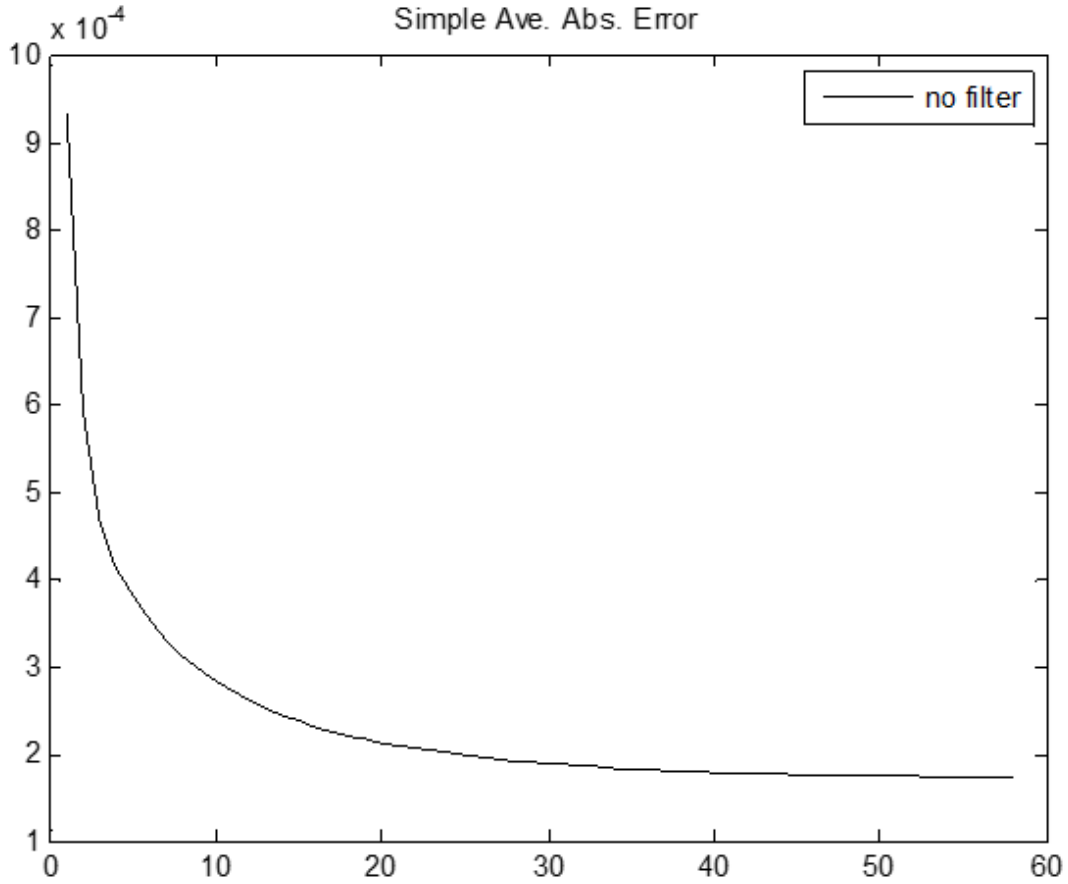
Figure 7.12: Plot showing the measured error in the reconstructed volume against iteration when the wavelength of the sinusoidal wavelength is 40 microlenses.

the filter is better for the volumetric reconstruction and the rate of convergence slows down after 13-14 iterations. Keeping these observations in view, from here on, the output from the reconstruction with no filter and 14th iteration are used to present the observations.

One of the best compressible flow examples to explore are the shock waves. As an example for application of the developed 3DDMT on real flow fields, in this work, a Mach 2.0 flow with the shock making a 45° angle with the x-axis, β angle in the $\theta-\beta-$M description of the oblique shocks, was adopted. Figure 7.14 shows the schematic of the flow field in the VOI. The dashed line in the image represents the optical axis or the z-axis of the setup. The region represented in red is the region behind the shock and has higher density. In the model shown in Figure 7.14, the shock is making an angle of 45° with the x-axis and 0°
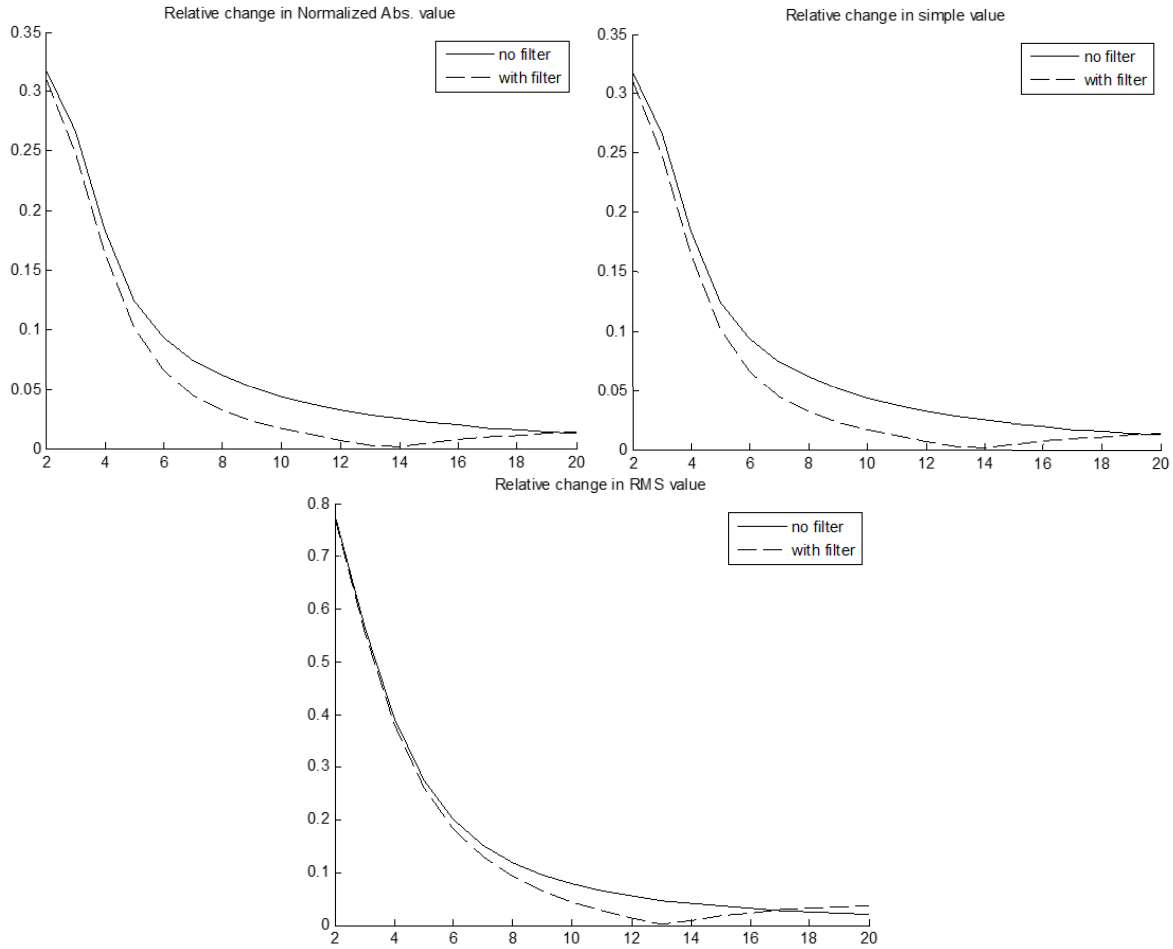
Figure 7.13: Rate of convergence of the reconstruction technique when using change in the a) Normalized absolute value, b) Simple summation, and c) RMS value.

with the z-axis. To further illustrate the geometry of the shock model used in this work, schematics of the cross-sectional planes taken parallel to the xz plane and xy plane are shown in Figure 7.15. In Figure 7.15(a), the schematic of a plane parallel to the xz-plane that divides the VOI into two equal halves is shown and in Figure 7.15(b), the schematic of the focal-plane from the modeled VOI is shown. The region in red represents the regions behind the shock. The angle α shown in Figure 7.15(a) represents the angle shock makes with the z-axis. In the experiments, the α angle was varied from $0°$ - $60°$ with the shock making a constant $45°$, shown in Figure 7.15(b), angle with the x-axis.
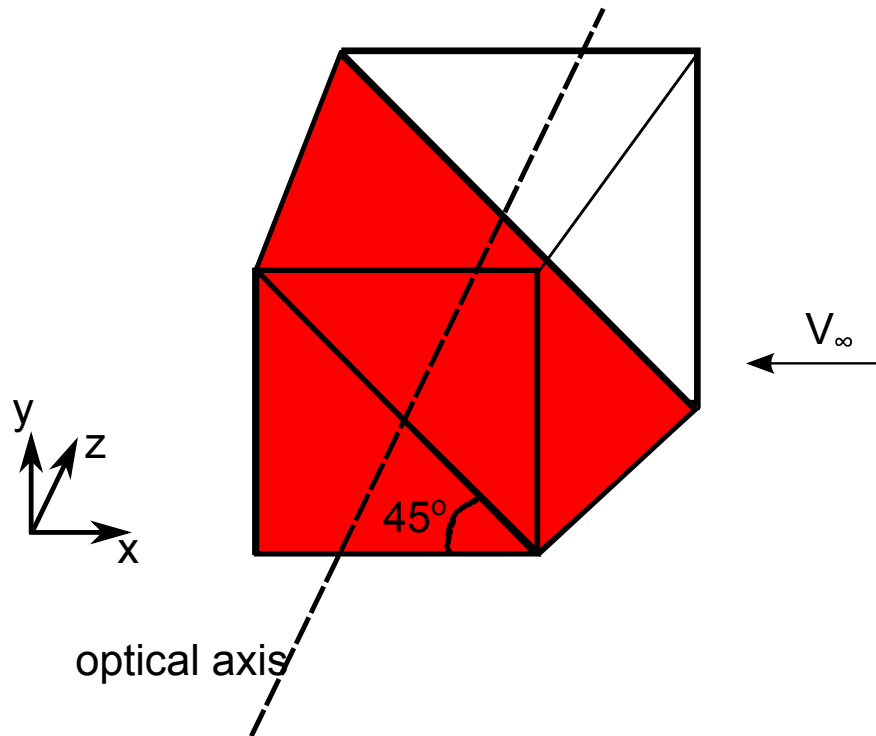
Figure 7.14: Schematic showing the Mach 2.0 flow with a shock making an angle of 45 with the x-axis.
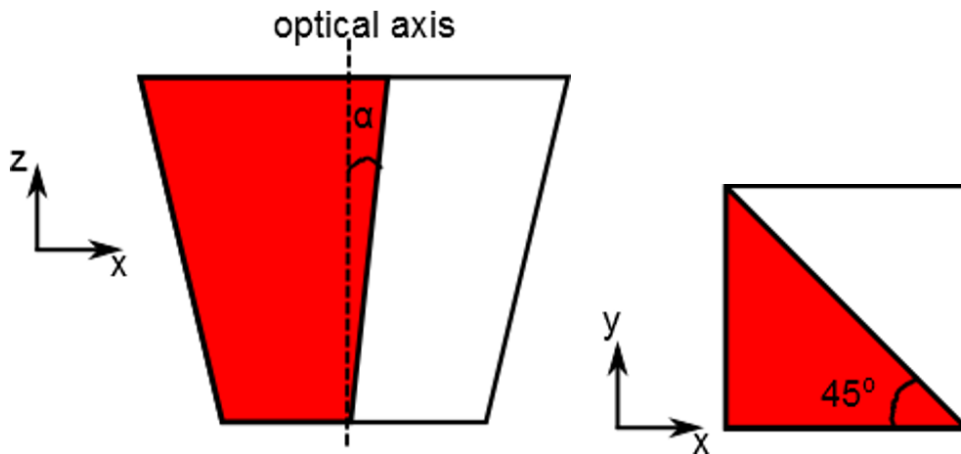
Figure 7.15: Cross-sectional views of the VOI with shock.

The perspective views 1, 7, 25, 43 and 49 (numbering scheme described in Chapter 5) generated with the shock making $0°$ angle with the z-axis, $\alpha = 0$, are shown in Figure 7.16. As expected, the perspective views from cameras lying on the main diagonal, cameras 1,

25, and 49, capture a sharp discontinuity due to the shock. The discontinuity in the images divides the image into two equal halves. As the location of the cameras move away from the main diagonal, the discontinuity in the image blurs, perspective views of cameras 7 and 43. The sharpness of the discontinuity in the perspective views from the cameras on the main diagonal, cameras 1, 9, 17, 25, 33, 41, and 49, is lost when the shock makes an angle greater than 0 with the z-axis, $\alpha > 0$. To show the effect, perspectives views from the simulation where the shock makes $20°$ angle with the z-axis, $\alpha = 20$, are shown in Figure 7.17.

Cross sectional planes of the volume for the two cases, $\alpha = 0$ and $\alpha = 20$, are shown in Figure 7.18 and Figure 7.19 respectively for comparison. Planes shown in these figures are taken from the beginning, center and the end of the DOF. The color distribution in the plots assume the free stream density as reference and plot the density variation with respect to it. In Figure 7.18, where the shock makes $0°$ with the z-axis, no change in the location of the shock is observed when moving through the volume along the z-axis. Whereas, when the shock makes the $20°$ angle, the location of the shock in the xy plane changes when moving through the volume.

Figure 7.20 shows the planes from the reconstructed volume with shock wave making $0°$ angle with the z-axis. The color bar is set to match the color bar on the slices shown from the simulated volume in Figure 7.18 for a quick reference. Plots in Figure 7.21 show the slices of the volume with error distribution. For most of the volume, the error is in the acceptable range below 10% as shown in Figure 7.21. The color bar in the plot represent the whole range of the error percentage in the reconstructed volume. The range on the color bar varies from 0-140, which can be misleading. To show the occurrence of the maximum error, plot of layer 77 is shown in Figure 7.22 with the maximum error occurring at the bottom right corner of the layer. A better sense of the error in the reconstructed volume is obtained from the mean and median errors. The mean and median error measured in the reconstructed volume are 1.9973% and 0.2863%, giving the confidence in the reconstruction process.
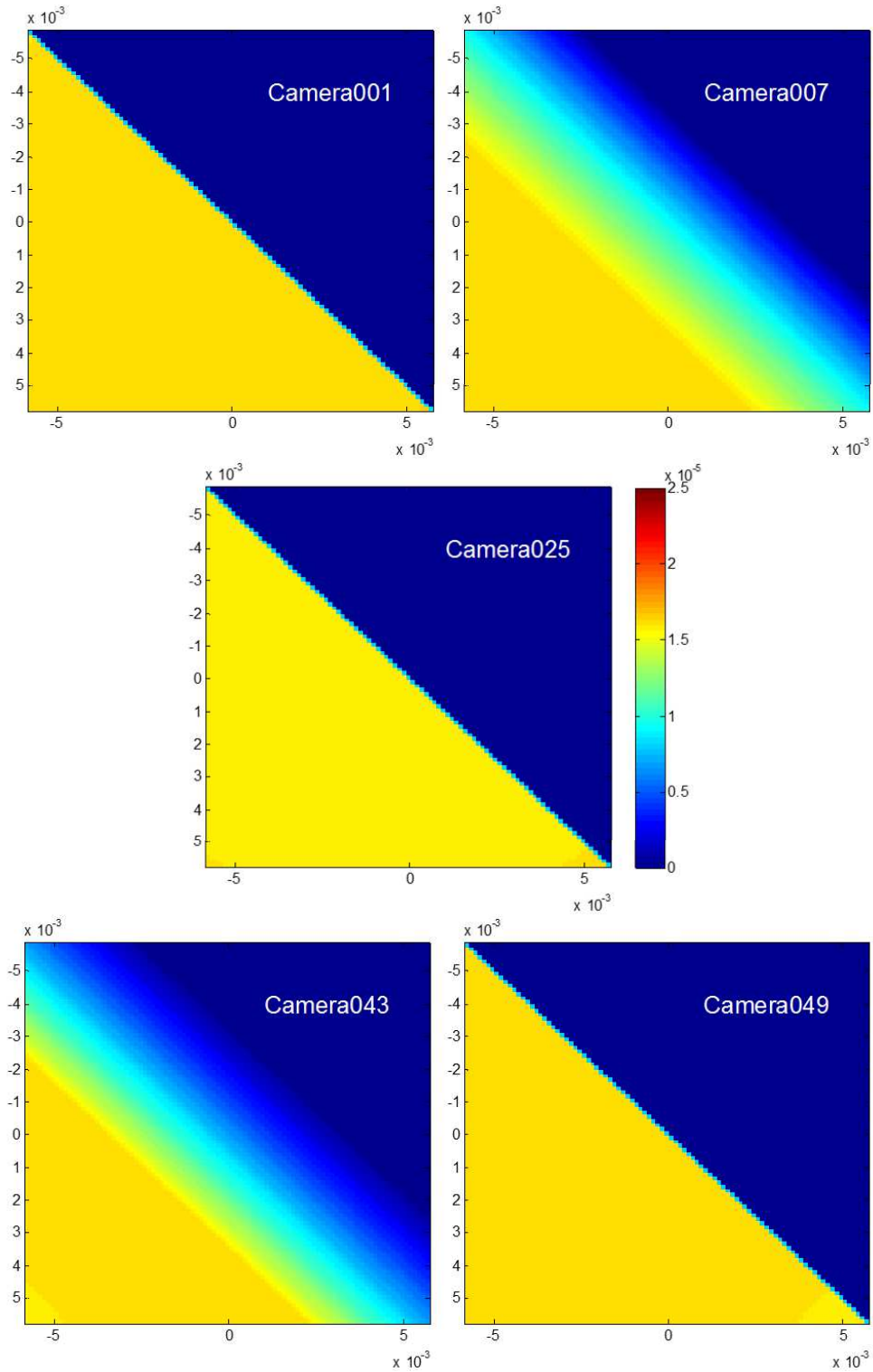
Figure 7.16: Perspective views of the shock flow with shock making 45° angle with the x-axis and 0° degree angle with the z-axis. Perspective views a) 1, b) 7, c) 25, d) 43 and e) 49 in the plenoptic camera array.
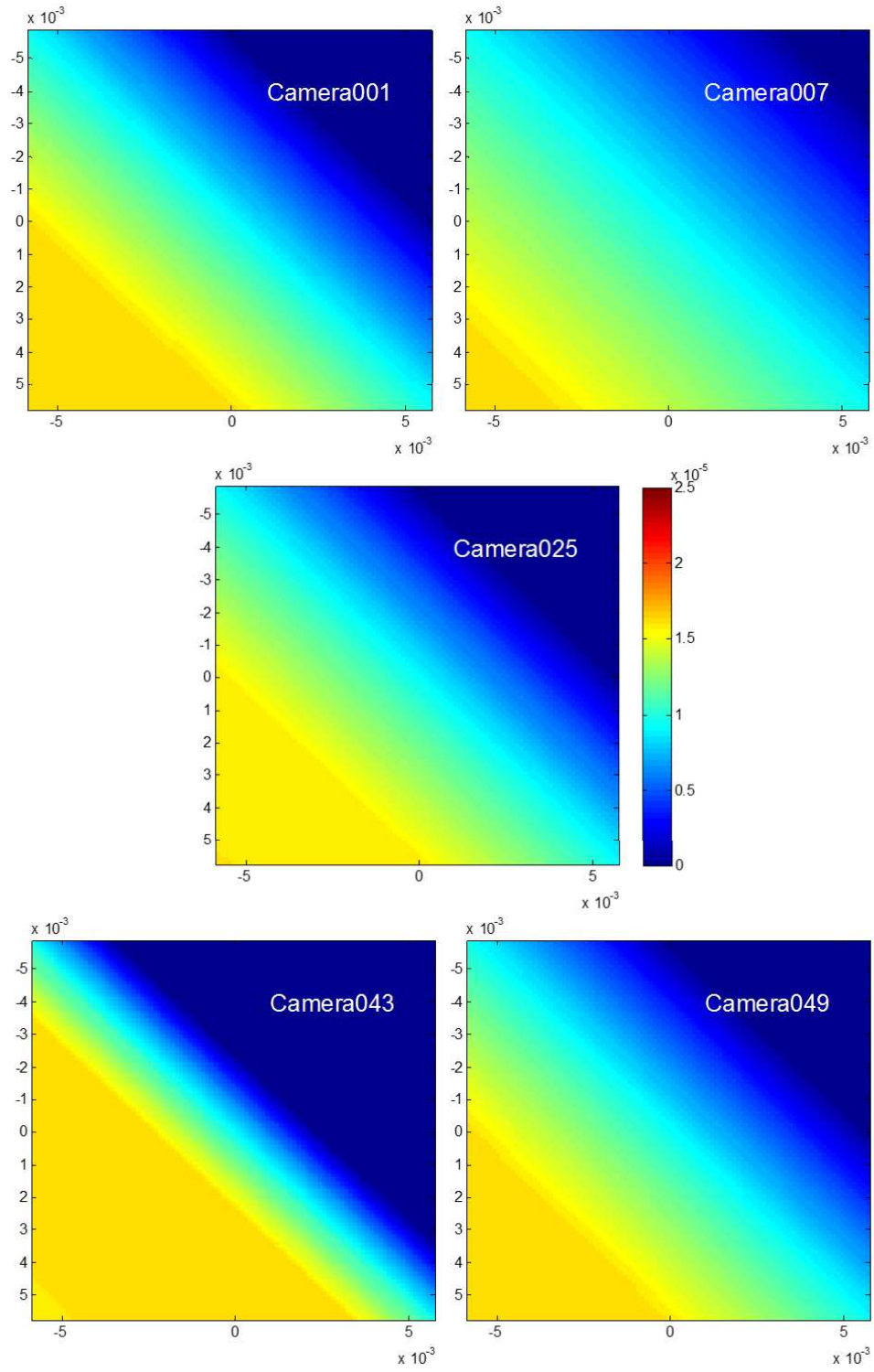
Figure 7.17: Perspective views of the shock flow with shock making $45°$ angle with the x-axis and $20°$ degree angle with the z-axis. Perspective views a) 1, b) 7, c) 25, d) 43 and e) 49 in the plenoptic camera array.
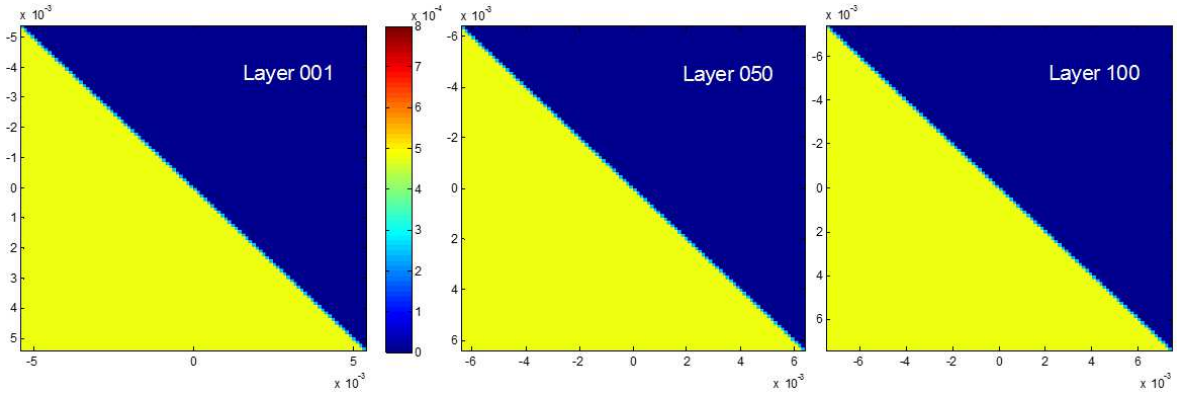
Figure 7.18: Cross-sectional planes from volume with shock making 0° angle with the z-axis. Planes taken from the a) front, b) center and c) end of the DOF.
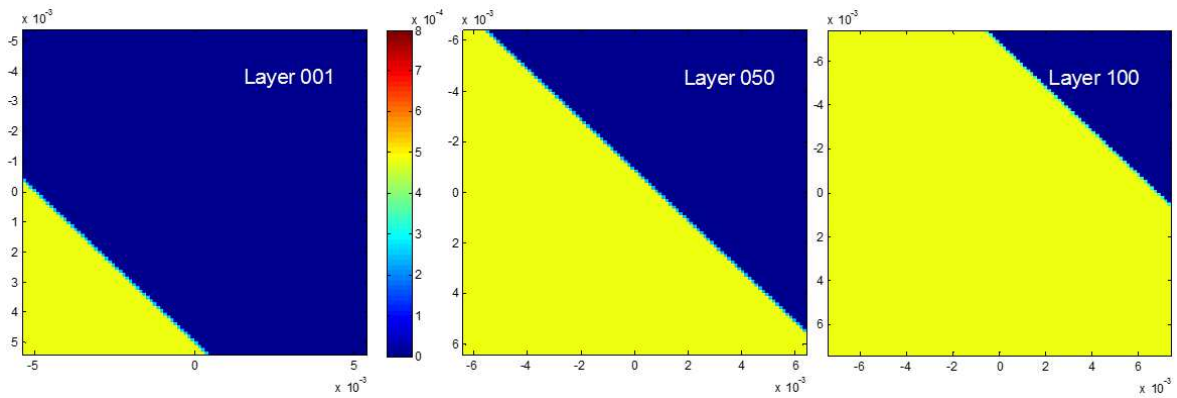
Figure 7.19: Cross-sectional planes from volume with shock making 20° angle with the z-axis. Planes taken from the a) front, b) center and c) end of the DOF.
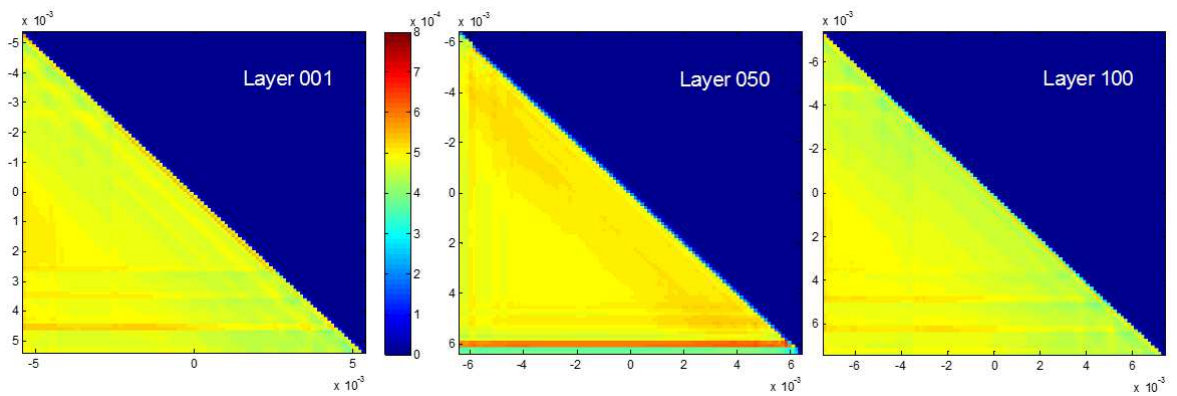
Figure 7.20: Cross-sectional planes from the reconstructed volume with shock making 0° angle with the z-axis. Plane from the a) front, b) center and c) end of the DOF.
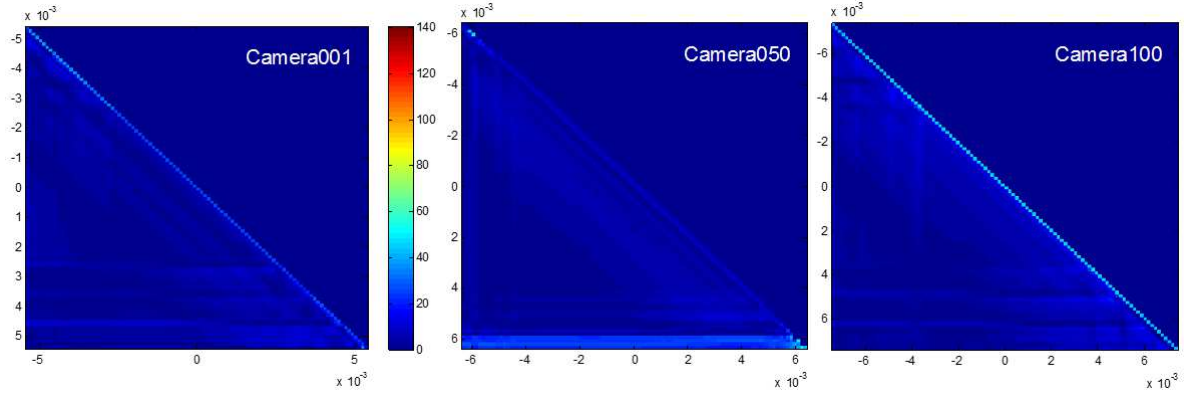
Figure 7.21: Cross-sectional planes from the reconstructed volume with shock making 0°
angle with the z-axis showing the percentage error distribution in the volume. Plane from
the a) front, b) center and c) end of the DOF.
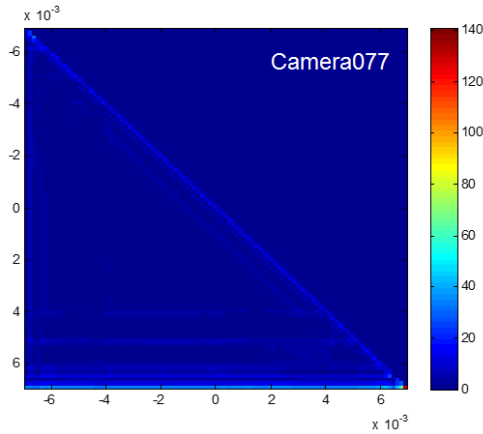
Figure 7.22: Image showing the occurrence of maximum error in the reconstructed volume.

In Figure 7.23, the total absolute error for the volume versus the angle of the shock
with the z-axis is shown. A 20 fold increase in the total error from 0° to 45° is noticed. To
better understand how the angle between the shock and the z-axis affects the 3DDMT, plots
of density distribution in the central plane of the FOV from cases with angles 6, 8, 12, 16,
20 and 25 degree are shown in Figure 7.24. As the angle goes beyond 7°, the discontinuity
in the density distribution representing the shock wave present in the volume is blurred.
The blurring of the shock increases with increasing angle. This is an expected trend as the

disparity angle for the plenoptic camera ranges from $-7°$ to $+7°$ for the experimental setup with setup magnification set at 1.
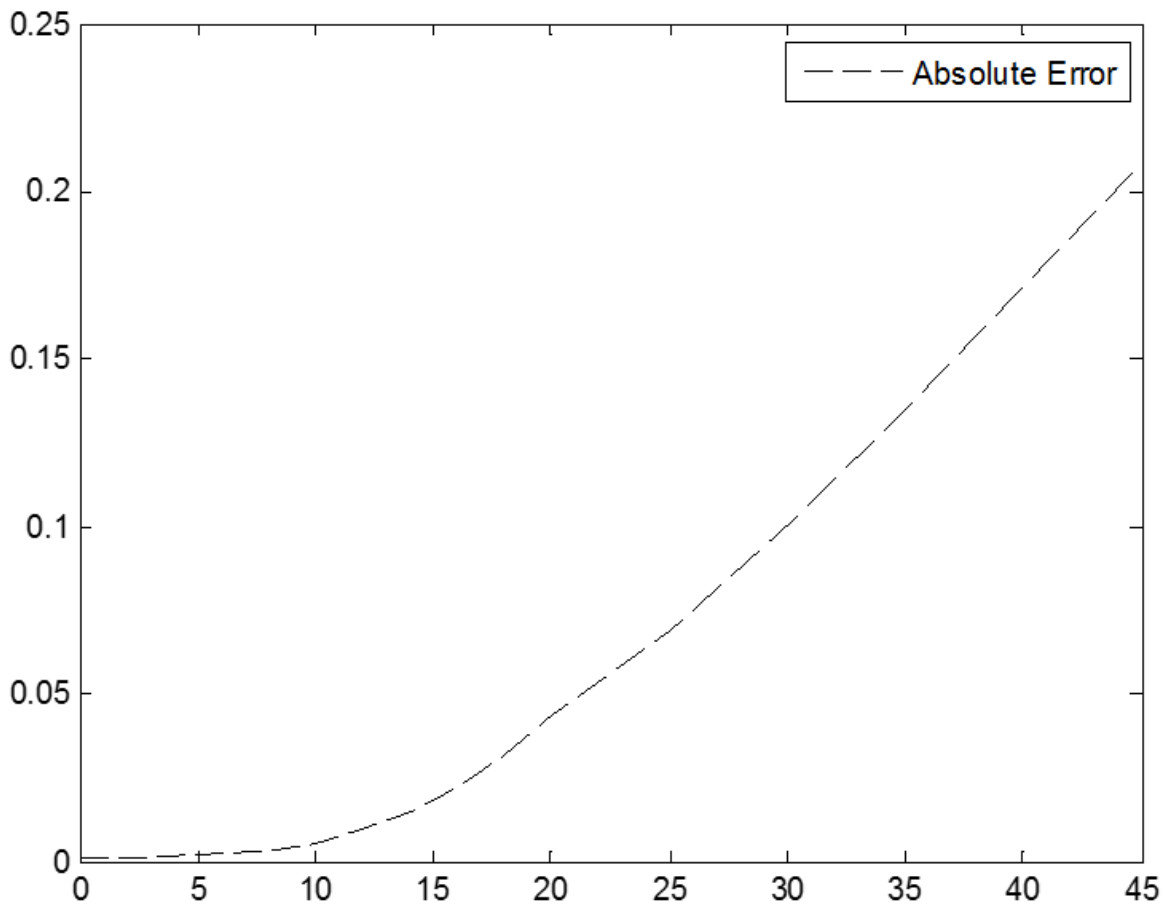
Figure 7.23: Absolute error vs angle with z-axis.

7.3 Results from Noisy Input

It is not always possible to have perfect input data for reconstruction. To account for the noisy input data, in this section, observations from the test to study the performance of the reconstruction process when the input data is noisy are presented. As seen in Chapter 3, data input obtained from the BOS process may contain systematic or random error. The systematic error can be accounted for with the calibration images, whereas the random error is hard to account for. In this subsection, the effect of the random error by introducing
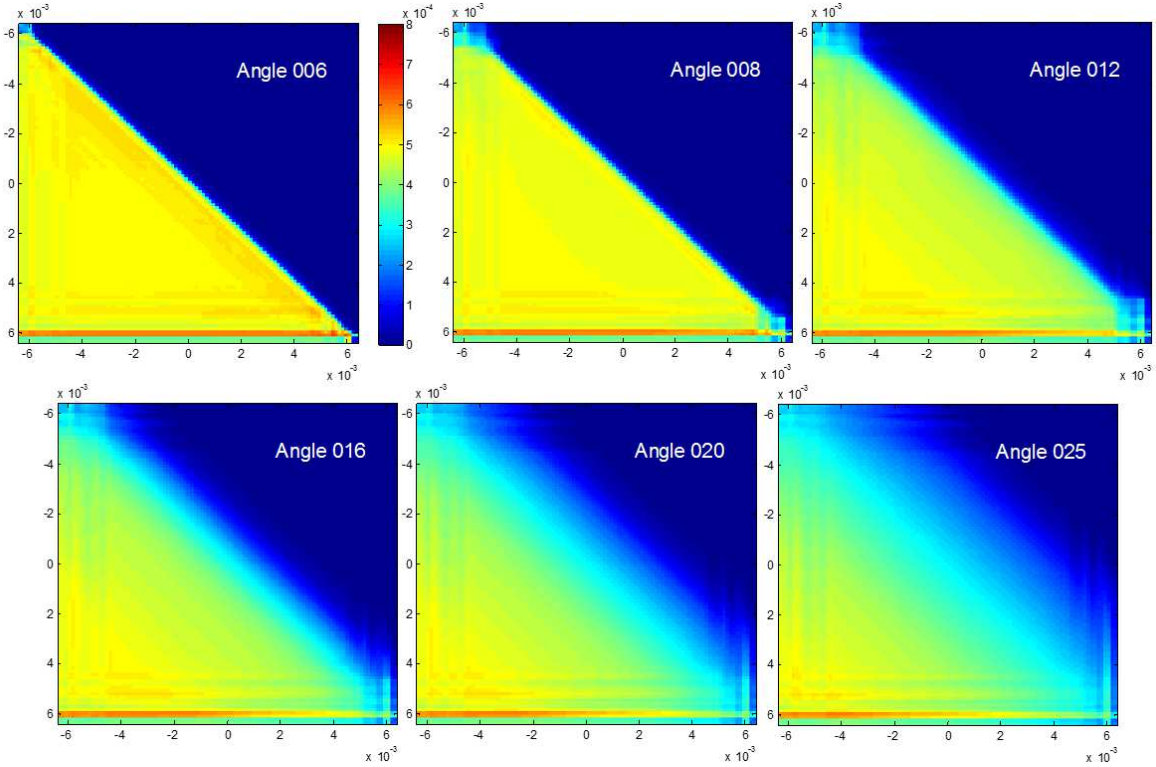
Figure 7.24: Density distribution in the central plane of volumes with the shock making an angle of a) 6, b) 8, c) 12, d) 16 e) 20 and f) 25 with the z-axis.

it into the deviation data obtained from the BOS images is studied. To study the effect of the error, four data sets with 0%, 1%, 5% and 10% error in the deviation were used in the reconstruction of the shock volume. Simulation with 0% error was used to account for the error introduced due to the Southwell's method for calculating the OPD on the overall reconstruction technique.

For visual reference, OPD data of the 25th perspective view from the four cases are shown in Figure 7.25. The effect of the introduced error is evident in these images with the presence of the artifacts in the images. In Figure 7.25(a), the presence of artifacts in the OPD distribution is observed, even when the input for the Southwell's method was perfect. Increasing the random error in the deviation data resulted in decreasing the artifacts in the OPD distribution, but an increase in the overall error was noticed.
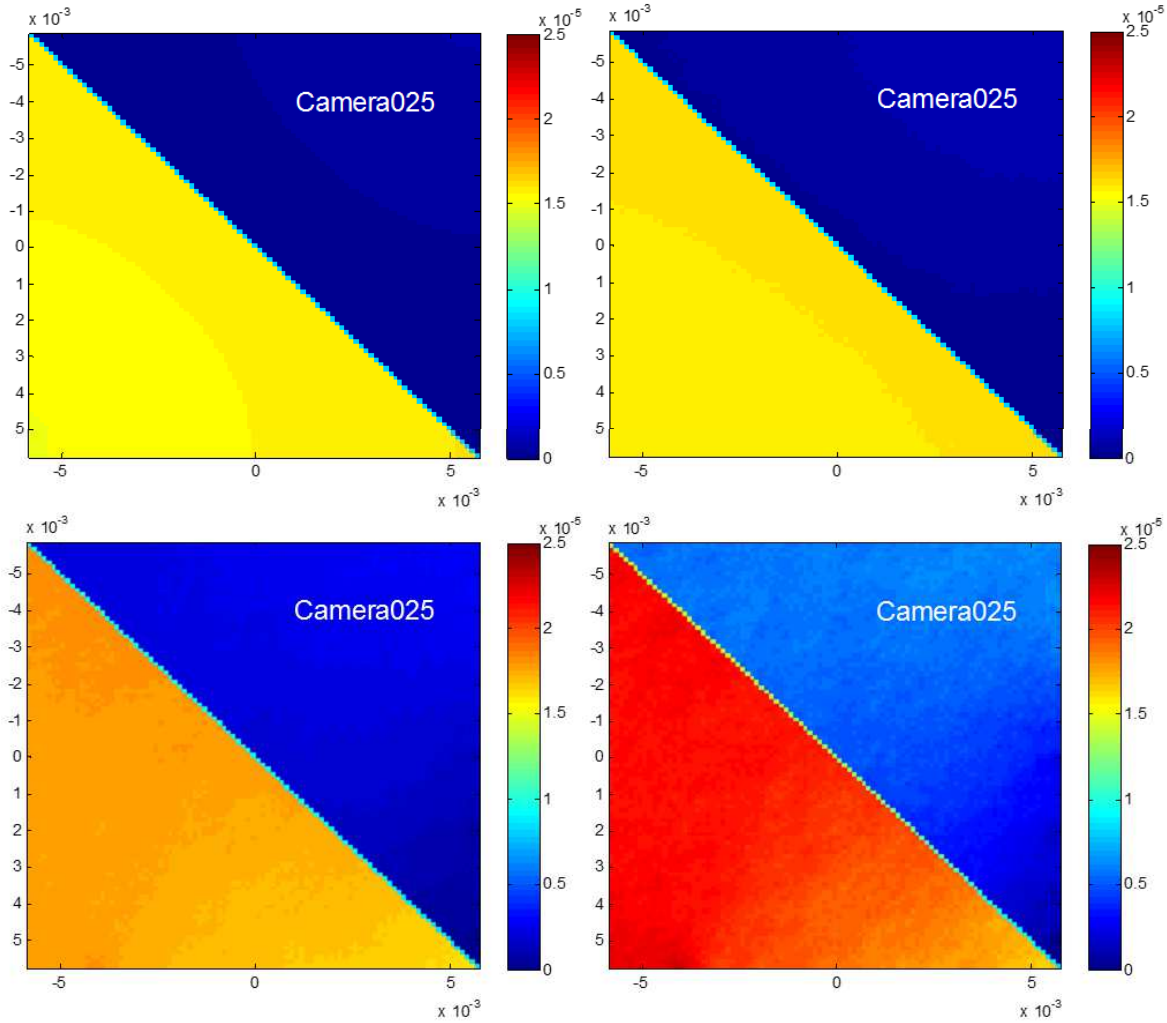
Figure 7.25: OPD obtained from Southwell's method for camera 25 in the plenoptic camera array for the four cases. a) no error, b) 1% error, c) 5% error, and d) 10% error.

Figures 7.26, 7.27, 7.28 and 7.29 show the slices of the VOIs reconstructed using the noisy deviation data. The slices in Figures 7.26, 7.27, 7.28 and 7.29 belong to cases with the 0, 1, 5 and 10 percent random error respectively. In all four cases, the reconstructed volumes show the location of the shock accurately in the volume with a sharp discontinuity in the density distribution. A more quantitative comparison of the of density distribution in these volumes with that of the simulated flow field is shown in Figure 7.30. In the Figure 7.30, absolute error calculated for the 5 cases:

1. perfect input data for reconstruction,

2. perfect input data for calculating OPD data using Southwell's method,

3. up to 1 percent random error introduced in the BOS deviation data,

4. up to 5 percent random error introduced in the BOS deviation data, and

5. up to 10 percent random error introduced in the BOS deviation data.

is plotted. x-axis in the plot shows the percentage error introduced into the data and the absolute error on the y-axis. The two cases at 0% error represent the perfect data as input to the 3D reconstruction technique and the perfect data as an input to the Southwell's method for generating OPD used in the 3D reconstruction technique. From the figure, it is observed that the increasing the percentage error in the input resulted in the increased error in the reconstructed volume. A better sense of the error in the reconstructed volume can be obtained from Table 7.2, where the error percentage for each case is calculated and tabulated against the case. From the table, we notice that a 5% error in the distortion data obtained from the BOS analysis that is used as the input to the Southwell's method resulted in a reconstructed volume with a mean and median error less than 10%. In Chapter 3, it was observed that distortion data obtained from BOS analysis when used with the Southwell's method to generate OPD data with less than 5% error. These two observations suggest that the reconstructed volume from the 3DDMT would have an overall error less than 10%, which is acceptable.
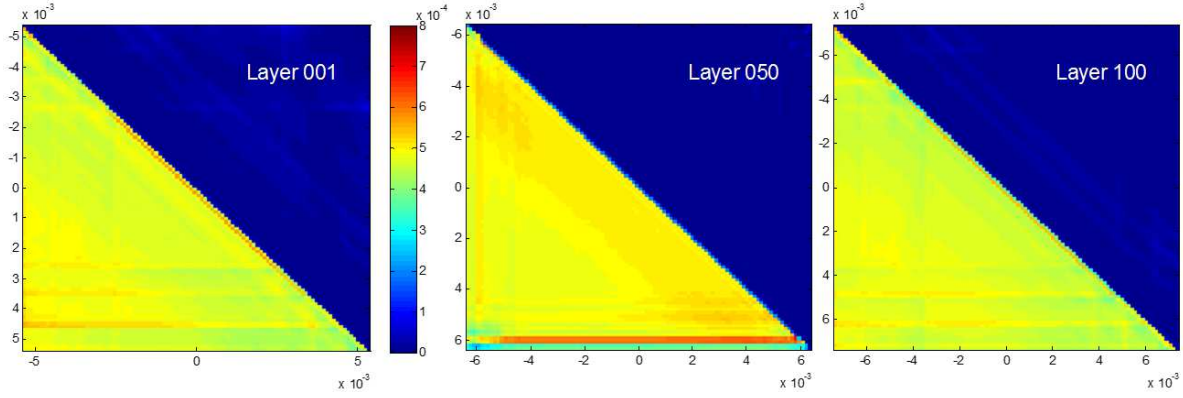
Figure 7.26: Planes from the a) beginning, b) center and c) end of the DOF of the reconstructed volume when no error is introduced.
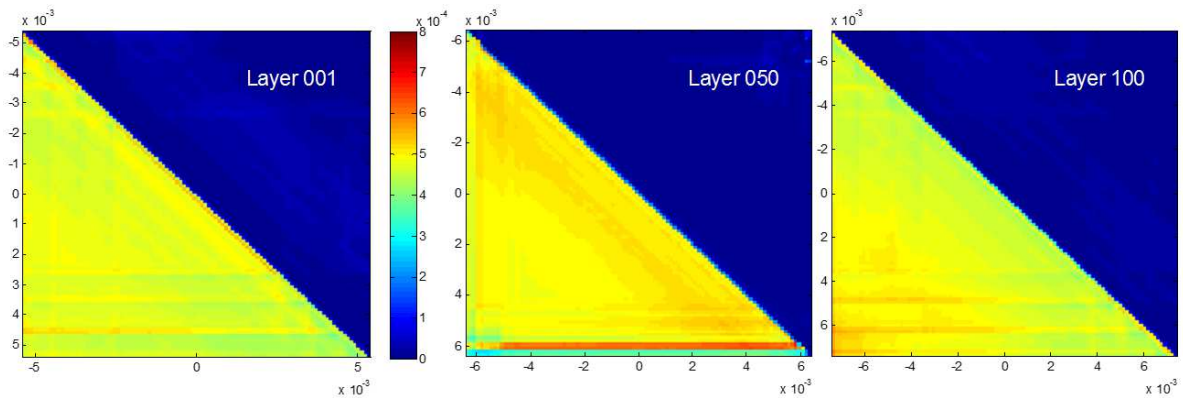
Figure 7.27: Planes from the a) beginning, b) center and c) end of the DOF of the reconstructed volume when 1% error is introduced.
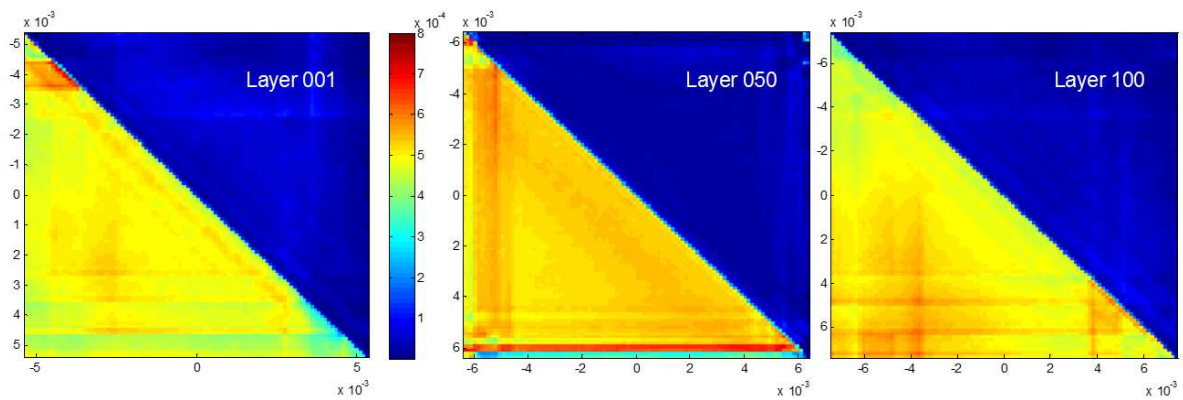
Figure 7.28: Planes from the a) beginning, b) center and c) end of the DOF of the reconstructed volume when 5% error is introduced.
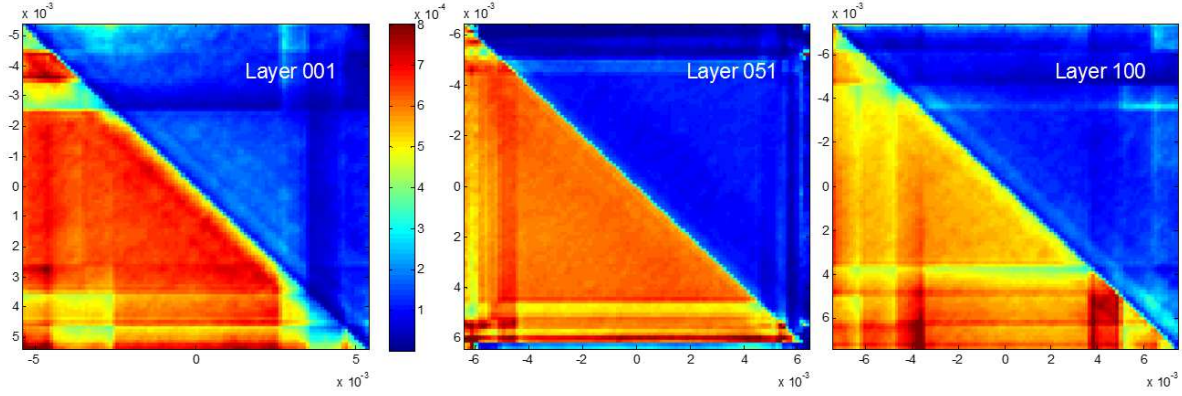
Figure 7.29: Planes from the a) beginning, b) center and c) end of the DOF of the reconstructed volume when 10% error is introduced.
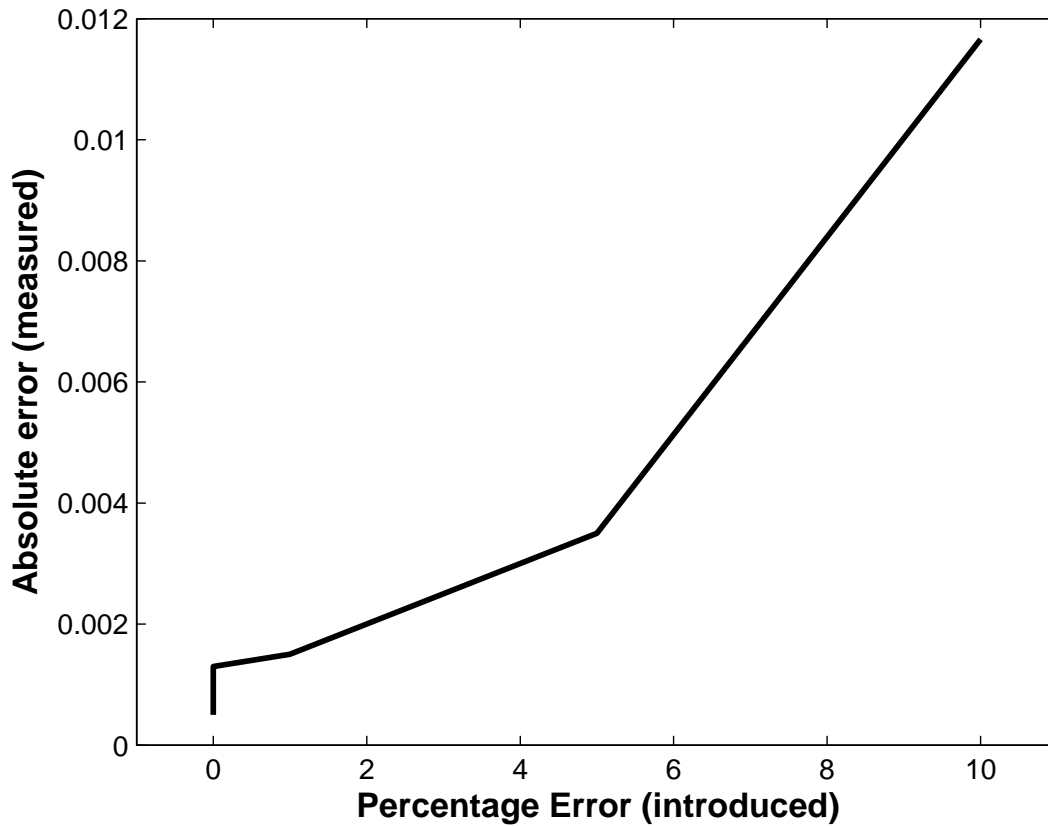
Figure 7.30: Error plot showing the influence of noise data on the reconstructed volume.

Data Type	Mean Error (%)	Median Error(%)
Perfect Data	1.9973	0.2863
0% error	2.4374	1.1831
1% error	2.9584	1.8331
5% error	9.1411	7.1738
10% error	21.9935	21.6185

Table 7.2: Mean and median measured in the reconstructed volume.

One last experiment conducted with the simulated model included using BOS images with a signal to noise ratio (SNR) of 10 to study its effect on the reconstruction. SNR is defined as the ratio of the desired signal to the noise signal or as the ratio of the contrast to the standard deviation of the noise. SNR is the standard measurement technique to measure and characterize the image sensors.

To study the effect of the SNR 10 in the BOS images on the whole 3DDMT, noise was introduced in the BOS images which were then analyzed using the PIV cross-correlation technique to obtain distortion data. The deviation/distortion measurement thus obtained was then used with the Southwell method to obtain the OPD measurement for individual perspective views which were in turn used in with the MART equation to reconstruct the 3D shock volume.

Error measurement obtained when the reconstruction volumes from the experiment were compared with the simulated shock volumes is plotted in Figure 7.31, represented by the solid line. x-axis in the plot refers to the angle the shock in the flow field makes with the z-axis and the y-axis shows the measure of the absolute error. For comparison, error calculated from the reconstructed volumes when the input data was perfect is plotted with a dashed line. The error in the volumes reconstructed with perfect data is small when compared to the volumes reconstructed with the SNR 10 data as long as the shock made less than 8° angle with the z-axis, $\alpha < 8$. For comparison at $\alpha = 0$, the error from the SNR 10 experiment is 3 times the error obtained with the perfect input data.
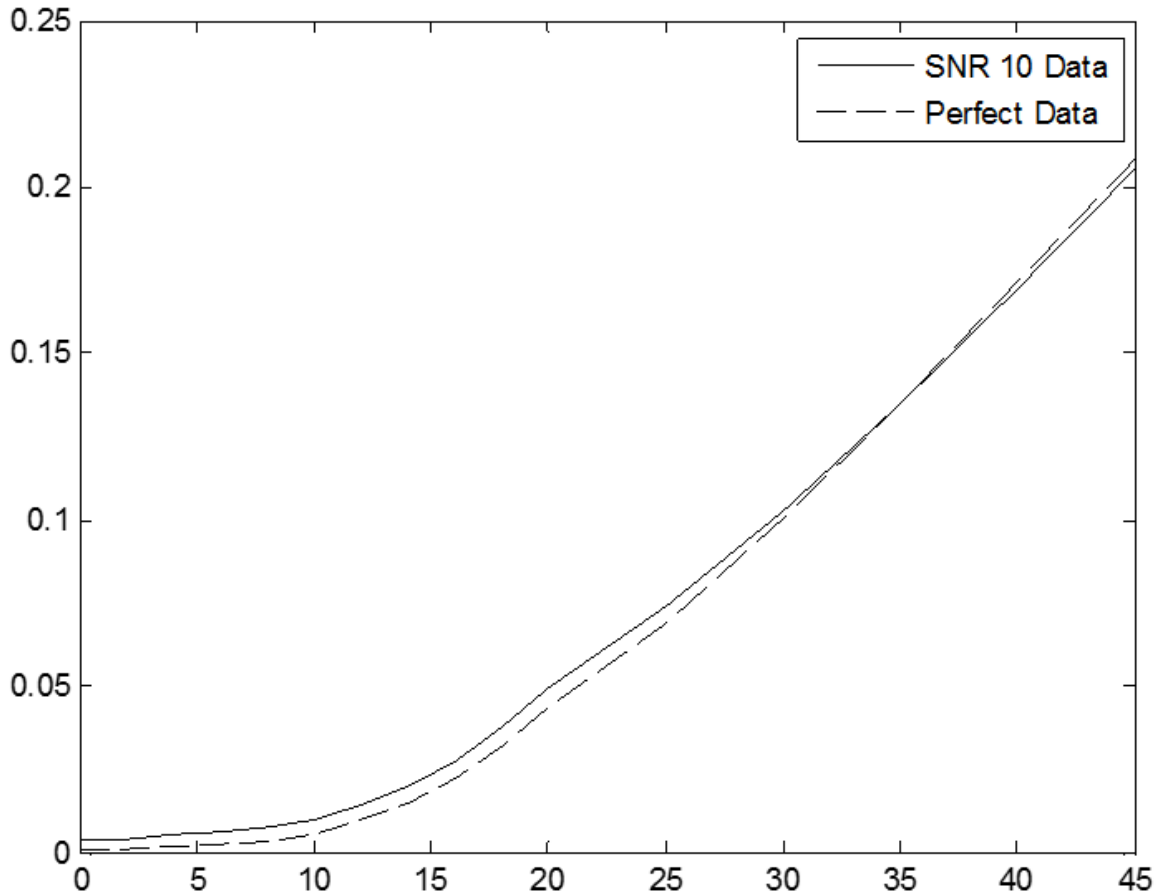
Figure 7.31: Absolute error measured for the volume reconstructed using data with SNR 10 vs angle with z-axis.

7.4   Summary

In this chapter, simulated experiments were used to study the MTF of the 3D reconstruction technique chosen for this work in Chapter 5. Experiments were also simulated to study the performance of the reconstruction technique with perfect and noisy data.

In the experiments conducted to study the MTF of the reconstruction technique, it was found that, for the experiments with magnification 1, the inhomogeneity with less than 8 microlenses (this is equivalent to 6.7 voxels lengths at the end of the DOF) showed aliasing effect in the reconstructed volume. When comparing the volumes reconstructed with and

without averaging filter in the reconstruction process, the MTF analysis showed that the reconstruction without filter gave more accurate output than the reconstruction with filter.

The simulated experiments analyzing the performance of the 3D reconstruction technique also showed that the output was more accurate without the use of the averaging filters in the reconstruction process. From the experiments, it was also observed that the rate of convergence of the 3D reconstruction technique towards a solution becomes an asymptote after 13 or 14 iterations when the reconstruction process uses no averaging filters.

Performance of the reconstruction technique was analyzed using an oblique shock making a 45° angle with the x-axis of the system. As long as the angle between the shock and the optical axis of the system was in the range of the disparity angles of the simulated plenoptic system, the reconstructed volume showed sharp discontinuity in the density distribution and locating the shock accurately. Analysis of the noisy data also showed encouraging results. The reconstructed volume had less than 10% mean error when BOS data used in the reconstruction had a maximum error of 5%. Observations also that, when the data used in the MART reconstruction had a SNR of 10, the reconstructed volume had 3 times the error when compared with the volume reconstructed with perfect input data.

In this chapter, simulated experiments and their observations were presented. In the next chapter, physical experiments and their observations are presented.

Chapter 8

Experimental Results

In this chapter, the real world applicability and challenges associated with the application of BOS with a plenoptic camera are studied. To do so, experiments studying the supersonic flow around a cone model were conducted. The goals in conducting the physical experiments are:

1. to show the application of BOS with a plenoptic camera for DP of inhomogeneous flow structures in a flow field,

2. to study the challenges associated with the application of the 3DDMT in real world facilities, and

3. to study the performance of the 3DDMT when applied to real world flow fields.

This chapter is divided into three main sections. In the first section, the details of the supersonic wind tunnel facility at AU are presented. In section two, a discussion on why BOS with a plenoptic camera can be used for DP is presented. This is followed by a conversation on the application of the developed 3DDMT to real flows in the third section.

8.1 Experimental Facility

Experiments were conducted in AUs supersonic blowdown wind tunnel with a 4" × 4" test-section. Air supplied to the test-section is provided by two storage tanks that store the compressed air at 125 psi. A 650 cfm compressor is used as the source to pump air into the two storage tanks. Air from the two storage tanks provide a runtime of about 2 minutes. This runtime is good to capture about 90-100 images at a constant Mach number of 2.0 at 1 frame per sec.

A schematic of the supersonic wind tunnel at AU is shown in Figure 8.1. In the top view, a schematic of the experimental setup is presented. In the side view, shown in Figure 8.1(b), a schematic of the cross-section of the test-section with its movable bottom is shown. The movable bottom wall of the test-section gives users the control to change the location of the throat of the test-section, in turn, giving control of the test-section flow field speeds. Changing the location of the throat, users can vary the flow field Mach number between 1.2 and 3.5.

a) Top View

b) Side View
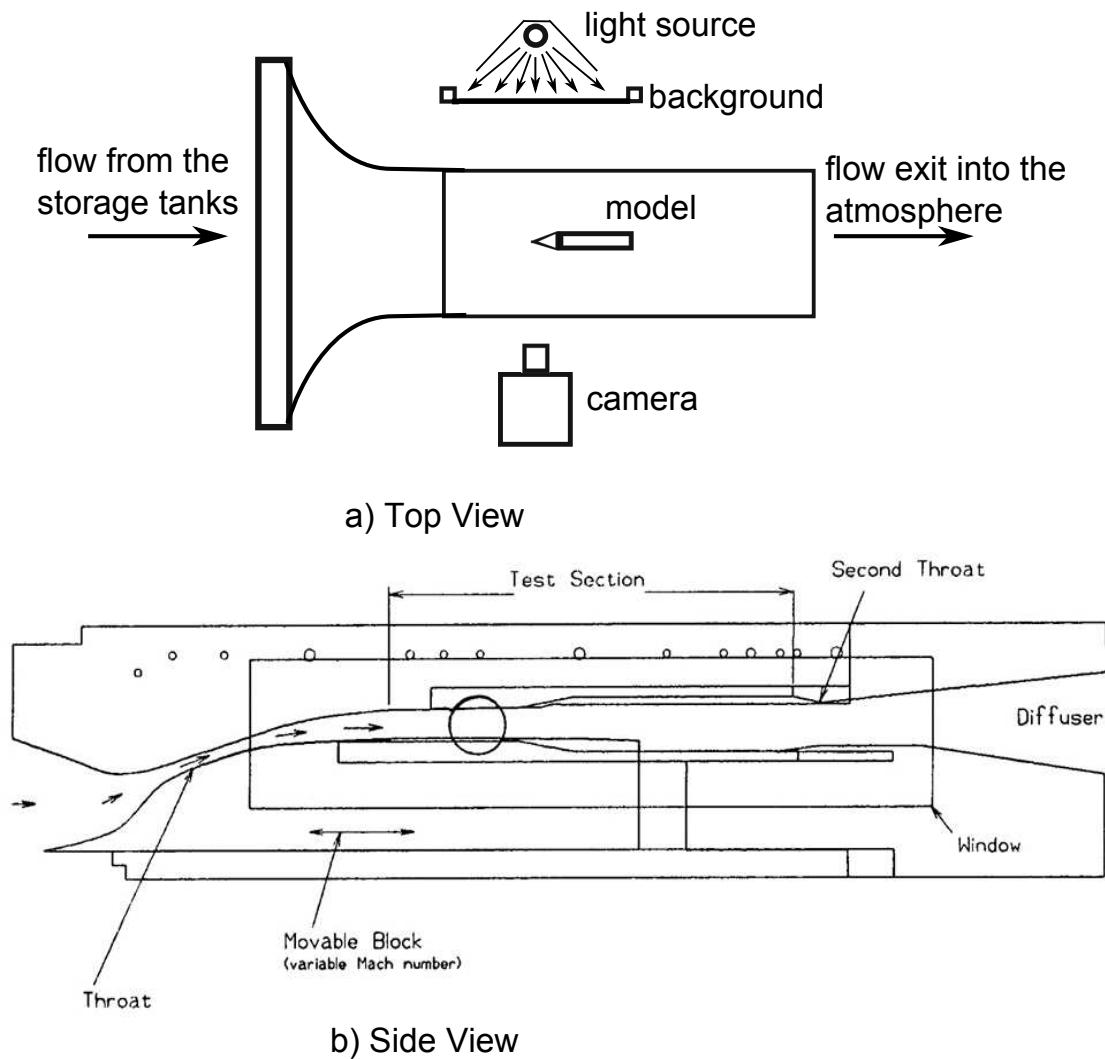
Figure 8.1: (a) Top view schematic showing the experimental setup. (b) Cross section of the tunnel showing the movable block that allows the control of the Mach number in the test section [143].

The top wall of the test section has ports to measure the static pressure in the test-section. The two side walls are made of glass giving optical access to the wind tunnels test-section. A sting located downstream of the test-section of the tunnel is used to mount the models. An external control to the sting mounts provides the user with the ability to change the pitching angle of the model. Air leaving the test-section is diverted to the top of the facility to exhaust the air into the atmosphere.

8.2 Depth Perception

Measuring the depth of objects from the images of a scene is of interest in many fields such as computer vision, robotics, astronomy, driver assist technology in automobiles etc.. Early measurement techniques, were based on the stereo or binocular vision of the humans. Algorithms developed by Falkenhagen [144], Muhlmann et al. [145], Okutomi et al. [146] and Huguet et al. [147] use the disparity measured between a pair of stereo images for estimating the depth.

Early depth estimation systems included binocular imaging systems with two horizontally separated cameras, and the depth measurement was given by:

$$z' = \frac{Bf}{d} \tag{8.1}$$

where, z' is the depth estimation, B is the horizontal distance between the two cameras, f is the focal length of the lenses on the cameras, assuming both cameras have the same focal length lenses, and d is the disparity measured in the images captured with the two cameras [148]. A schematic of the experimental setup for Equation 8.1 is shown in Figure 8.2. The above equation suggests that a large separation between the cameras results in a sensitive system. Large separation between the cameras can cause problems such as occlusion and photometric distortions. These issues were addressed in various studies using surface interpolation techniques [149, 150], area based techniques [151, 152] or by using

151

multiple cameras [148, 153]. To simplify the use of multiple cameras, Adelson and Wang in 1992 [90] showed the application of a single plenoptic camera for depth measurement. In this section, the ideas of measuring depth from the disparity in the perspective views, and the implementation of BOS with a plenoptic camera are combined to develop a depth measurement technique to locate the inhomogeneous flow structures in a flow field.
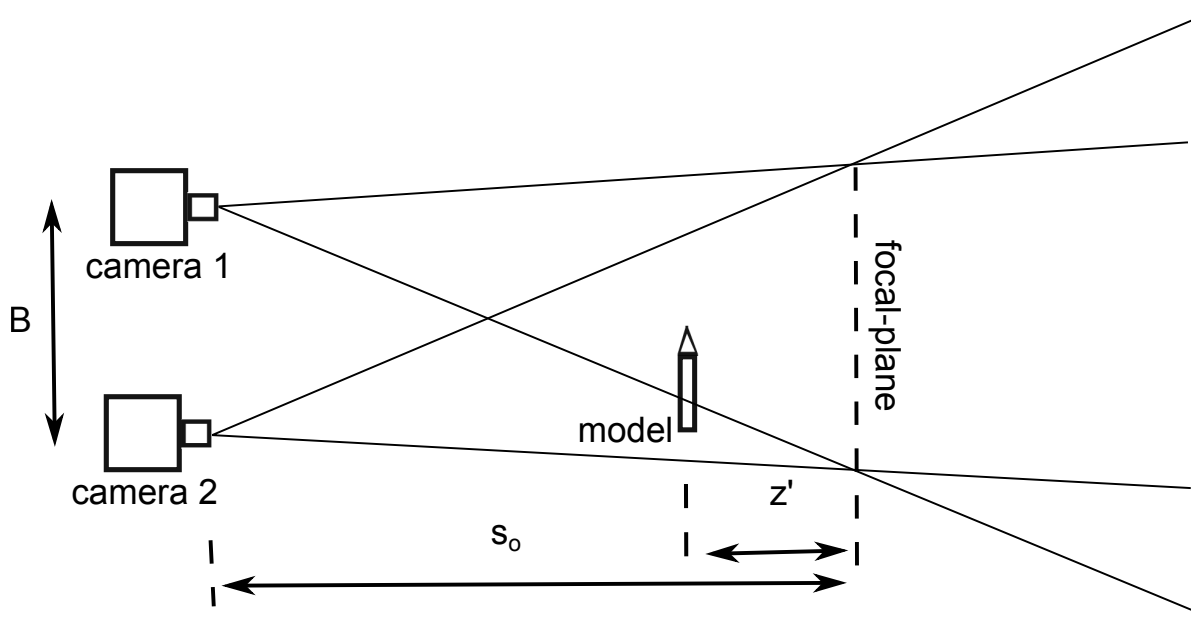
Figure 8.2: Schematic of a stereo depth perception experiment.

8.2.1 Method used for Depth Measurement

Figure 8.2 shows the schematic of a stereo depth perception experiment. In the image the two cameras shown are conventional cameras imaging a model in their FOV. The disparity in the location of the model in the images obtained from the two is given by $\vec{d}$. The arrow on d suggest that the measured disparity is a vector value. When the model is placed at the focal plane, the disparity in the images from the two cameras is zero. If the model is placed closer than the focal plane, as shown in Figure 8.2, the disparity measurement obtained when comparing the image from camera 2 with camera 1 is less than zero. Now, if the model is moved away from the camera and placed farther than the focal plane of the system, the sign

of the disparity changes from negative to positive. This effect can be noticed in Figure 8.3. In the original plenoptic image (shown in Figure 4.7 in Chapter 4), the Nikon camera bag is in focus. In the perspective views shown in Figure 8.3, the books in the back and the cameras in the front come into focus. Now, when the text on the book in the back and the Nikon lens cap in the front of the bag are compared, the lens cap in the bottom image moves to the left and the text on the book moves to the right in comparison with the image on the top. This information is used in the vector equation given below to obtain the $\vec{z}$ location of the objects.

$$\vec{z} = \frac{\vec{d}s_o}{BM - \vec{d}} \tag{8.2}$$

Here, M is the magnification of the setup and s_o is the object distance. A negative $\vec{z}$ value means that the object in the scene is closer than the focal plane and the distance between the camera and the object is given by $s_o + \vec{z}$.

8.2.2   Depth Perception Experiments

In Chapter 5, synthetic volumes were generated to demonstrate the applicability of the tomographic reconstruction technique to flow fields. In those synthetic volumes, inhomogeneties were placed at different depths in the VOI. When imaged analytically by integrating the optical path length of the light, the location of each inhomogeneous structure in the perspective views changed from one perspective view to the other. This was the effect of the distance between the inhomogenities and the nominal focal plane of the plenoptic camera in that setup. To exhibit similar effect and its use for DP, experiments and their results are presented in this section.

To demonstrate the DP capabilities of BOS with a plenoptic camera, experiments were conducted at AUs supersonic wind tunnel. The 29 MP Imperx camera with the hexagonal lenslet array was used for imaging the background through the test section of the tunnel. A 135 mm lens with 36 mm long extension tubes was used on the lens to obtain a magnification
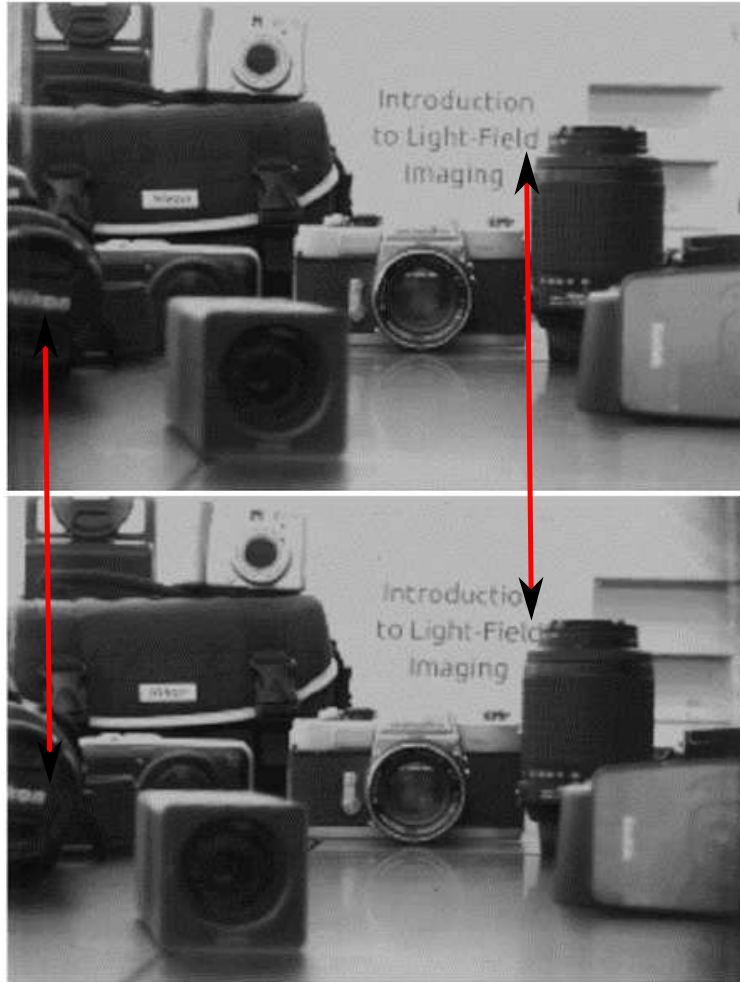
Figure 8.3: (a) Left and (b) right perspective views.

of 0.378. The aperture on the camera lens was set to an image side f-number of 2.9. With the given camera conditions, the distance between the camera and the nominal focal plane was approximately 492 mm. The details of the experiment are presented in Table 8.1 and a schematic of the experimental setup is shown in Figure 8.4. For the above experimental setup, a depth-of-field (DOF) of 154 mm was achieved in the perspective views with a circle of confusion (CC) of 1.

Figure 8.5 shows a ruler image captured in the DP experiments to measure the size of the FOV at the nominal focal plane. In the image, a blunt model used in the experiments is also visible. Three different backgrounds were used in these experiments, one with only

Focal length	135 mm
s_o	492 mm
Distance between the model and the focal plane	76.2 mm
Distance between the background and the focal plane	160 mm
M	0.378
Image side f-number	2.9
Effective f-number	1

Table 8.1: Table showing the details of the depth perception experiment.
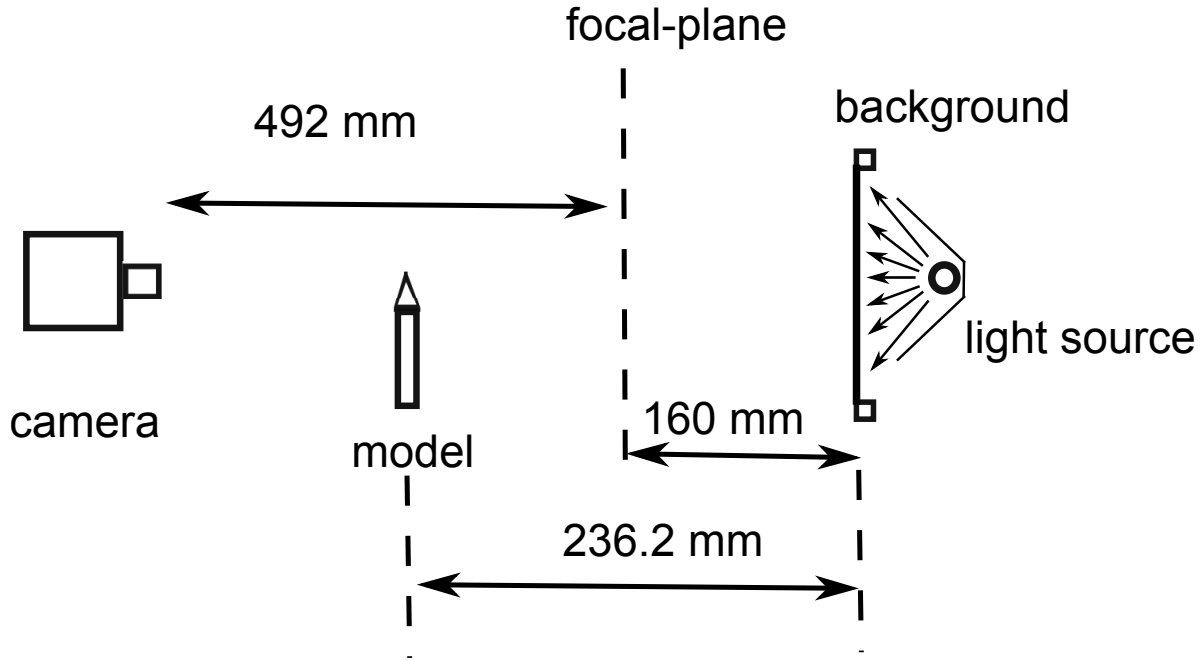
Figure 8.4: Schematic of the experimental setup used in the depth perception experiments.

vertical lines, one with only horizontal lines and one with both vertical and horizontal lines in it. The lines in these backgrounds were 1.78 mm (0.07 in) apart. The separation between the lines was chosen so that the lines are close enough for capturing the discontinuity due to the shock in the flow field and to be able to use the images for BOS analysis. Placing the lines closer than the selected separation resulted in the loss of contrast between the black and white lines. Placing them farther apart lost the information about the shock in the images.
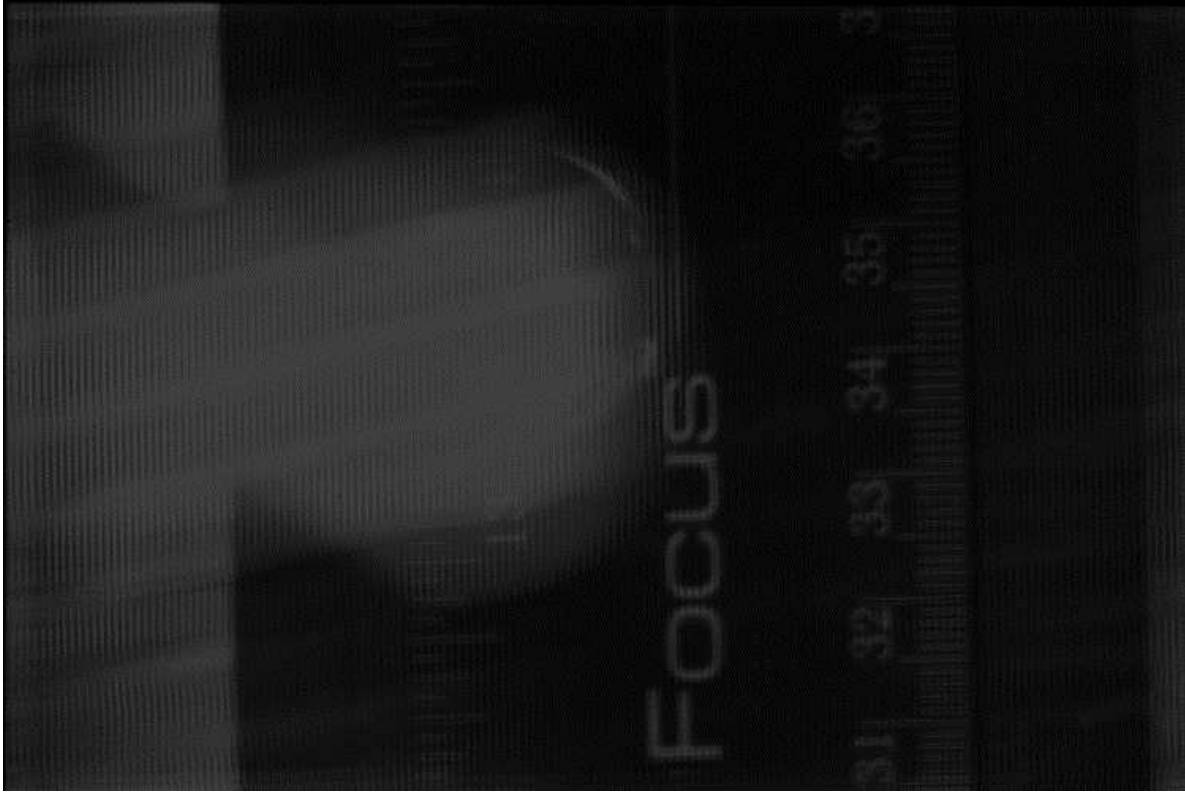
Figure 8.5: Image of the ruler captured in the DP experiments with a blunt model in the field-of-view.

Background images were captured with and without the flow in the tunnel. When imaging the background with the flow in the tunnel, the wind tunnel was set to operate at Mach 2.0. The shock in the VOI was generated with either a cone or a hemisphere model. A schematic and the image of the cone model used in the experiments are shown in Figure 8.6. A perspective view of the imaged background with the cone in Mach 2.0 flow is shown in Figure 8.7. The original raw image obtained from the plenoptic camera used in generating the perspective view in Figure 8.7 is shown in Figure 8.8. Plenoptic images captured were processed with the program called LFIT, discussed in Chapter 4, developed in house to generate perspective views. A set of 11×11 perspective views was generated from the plenoptic images in this experiment. The generated perspective views are labelled 1 to 121. A schematic of how the perspective views are labelled is shown in Figure 8.9.

The model and the background are out of focus in the original image, but, when the perspective views are generated, the effective aperture size decreases by the number of pixels under each microlens resulting in large DOF, discussed in Chapter 4. The effective DOF causes the model and the background to appear in-focus in perspective views, as seen in the sample perspective in Figure 8.7.
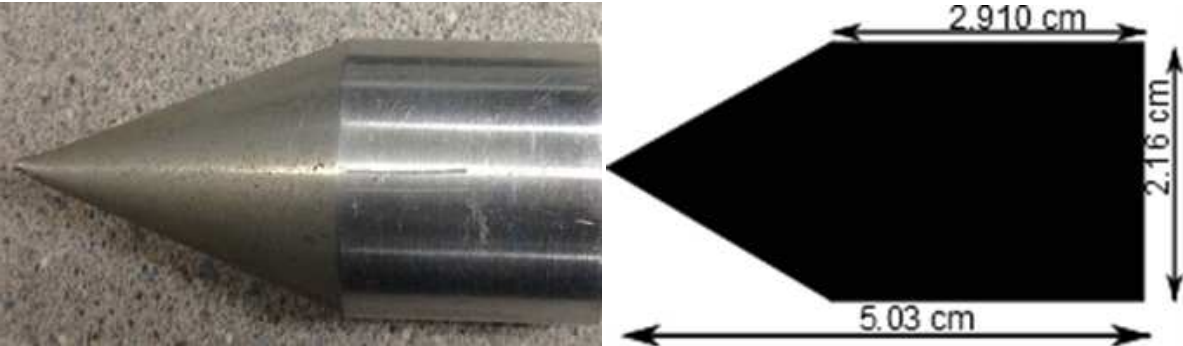
Figure 8.6: a) Model and b) schematic of the cone used in the experiments.
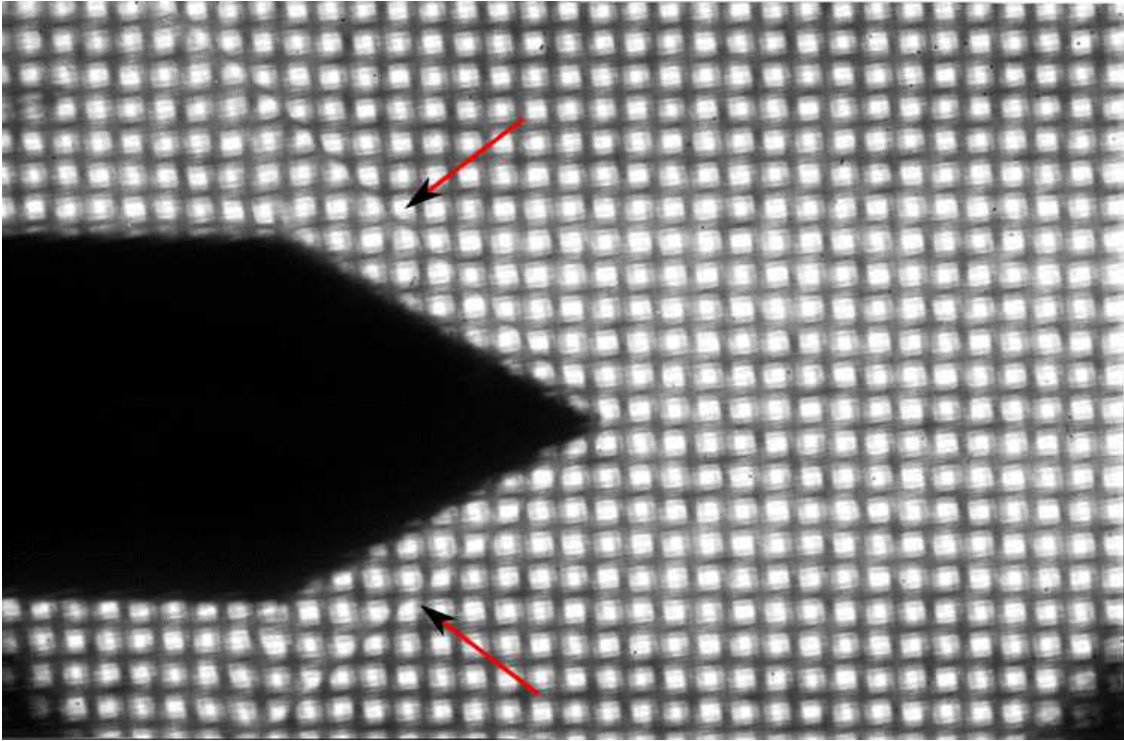
Figure 8.7: Perspective view with Mach 2.0 flow in the FOV highlighting the captured shock.
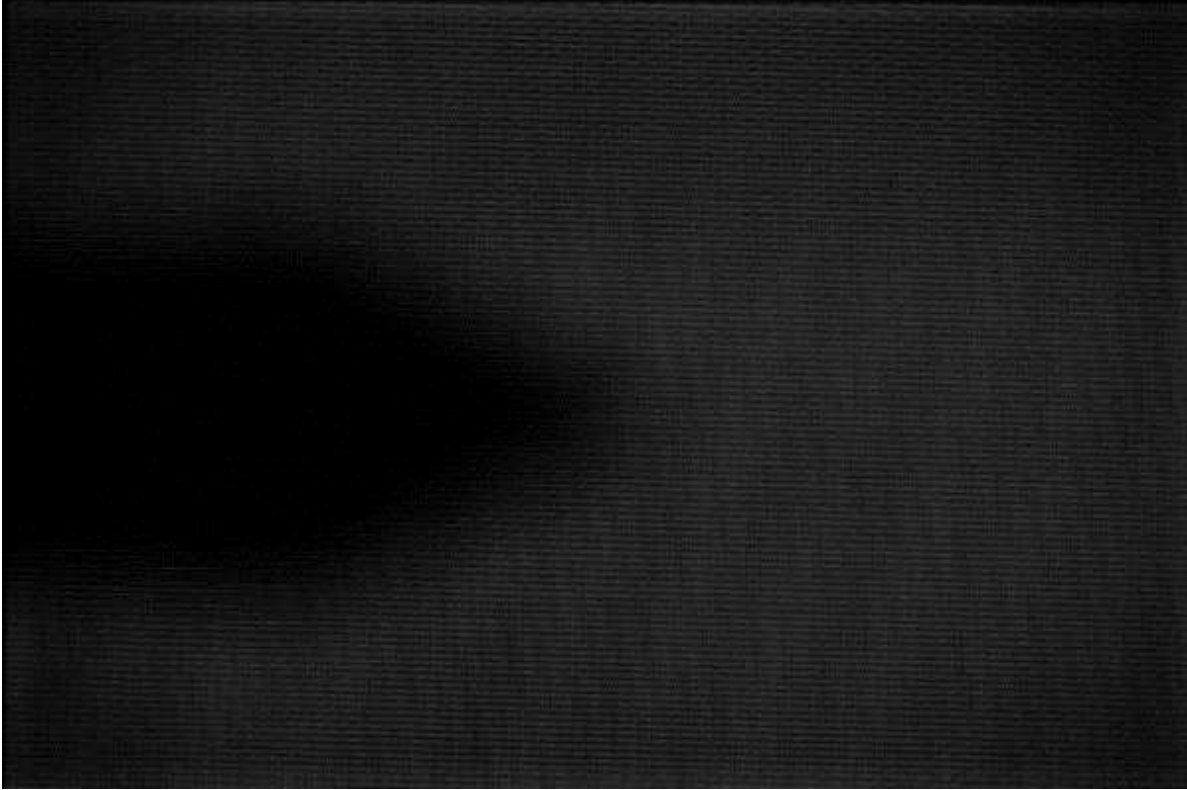
Figure 8.8: Raw image of the background captured with the plenoptic camera in the depth perception experiments.

$$\begin{bmatrix} 1 & \cdots & 11 \\ \vdots & \ddots & \vdots \\ 111 & \cdots & 121 \end{bmatrix}$$

Figure 8.9: Schematic showing the labelling of the perspective views generated in the physical experiments.

The backgrounds used in these experiments have regular patterns. Any distortions in such patterns are discernable with naked eyes. The perspective view in Figure 8.7 was captured with the Mach 2.0 flow in its FOV. Therefore, the distortions in the image caused due to the shocks present in the flow field are expected to see, emerging from the tip of the nose of the cone. The two arrows in the image point to these expected shocks captured

158

in the image and are visible to naked eye without any image processing, except generating perspective views from the plenoptic image.

In Chapters 5 and 7, five different perspective views for each model were presented to show the difference in the measured OPL with changing perspective. In this section, to study how BOS with a plenoptic camera can be used for DP, two different perspectives of the BOS images are compared directly. Figure 8.10 compares the perspective views 56 and 66 that are in a single row and Figure 8.11 compares the perspective views 6 and 116 that are in a single column. The vertical line in Figure 8.10 and the horizontal line in Figure 8.11 highlights the disparity in the location of the cone in both pairs of images.
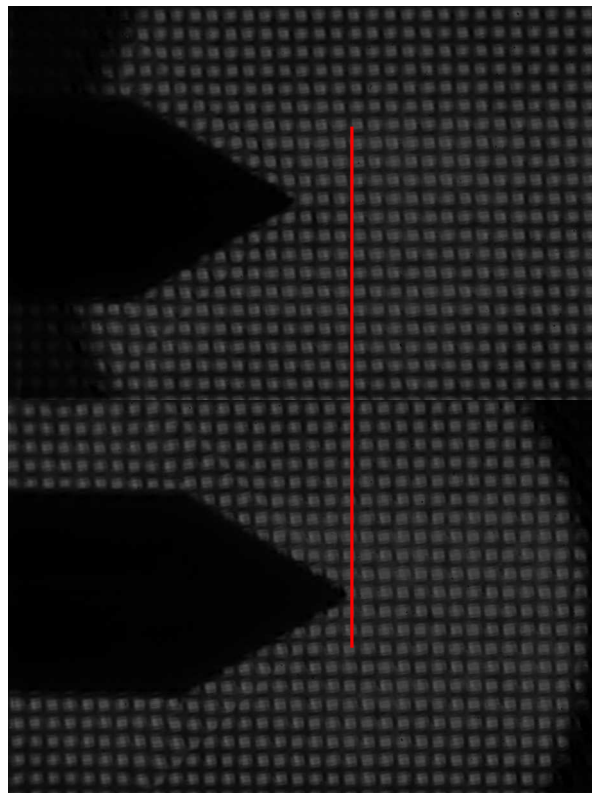
Figure 8.10: Perspective views 56 and 66 from the two ends of the middle row of perspective views with a vertical red line highlighting the disparity in the location of the cone. a) Perspective view 66. b) Perspective view 56.

Figure 8.12 shows a perspective view superimposed with the disparity measured between the two perspective views, 6 and 116, using cross-correlation technique used in the PIV
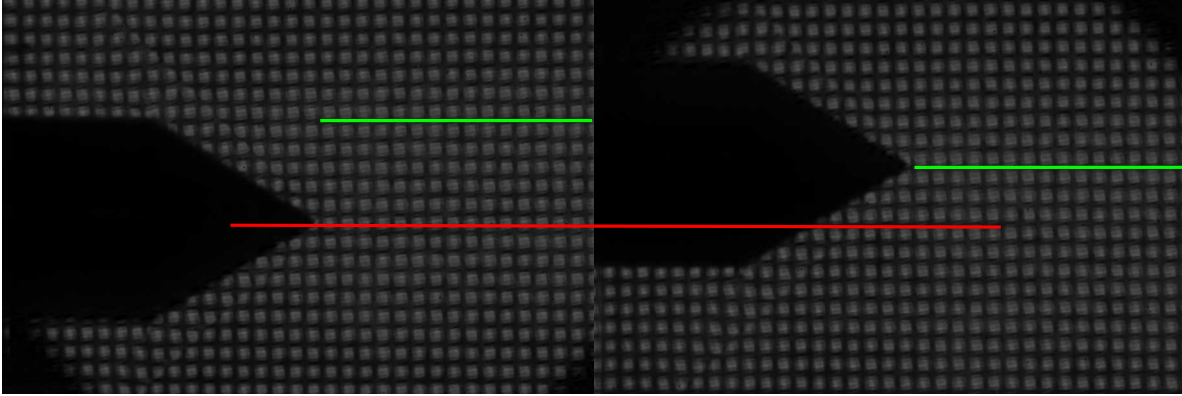
Figure 8.11: Perspective views 6 and 116 from the top and bottom of the middle column of perspective views with a horizontal red line highlighting the disparity in the location of the cone. a) Perspective view 116. b) Perspective view 6.

analysis. From the observations in the last subsection and the experimental setup, the background and the cone in the image are expected to move in opposite directions, but the regular pattern of the background which finds correlation in all directions is biased by the movement of the model resulting in inaccurate correlation vectors. So, to find the disparity in the perspective views, the perspective view images were first converted to binary with a threshold of 0.05 using the MATLAB command im2bw. These binary images were then processed with the edge function defined in MATLAB to define the edge of the cone in the images. An example of the output image from the process is shown in Figure 8.13. Disparity in the location of the cone in any two perspective views was then calculated by measuring the movement of the edges in the two.

The disparity measurement thus obtained was used in Equation 8.2 to obtain the location of the cone in the VOI. For example, when the perspective views 6 and 116 are considered, the disparity in the location of the horizontal edges of the cone in the two was -90 pixels. This translates to about -8.9 mm in the focal plane. As the measured disparity at the image plane is converted to disparity at the nominal focal plane, a modified version of Equation 8.2, given in Equation 8.3, is used for calculating the $\vec{z}$. d_{fp} in Equation 8.3 is the disparity measured at the nominal focal plane. From the experimental setup, B for the

160
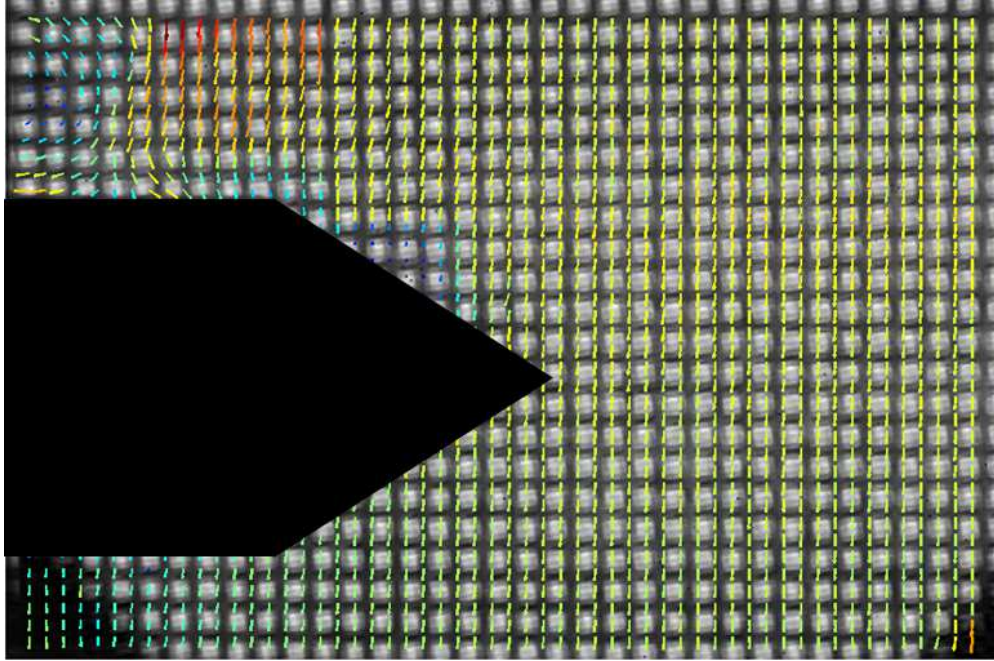
Figure 8.12: Image showing a perspective view superimposed with the correlation vectors obtained by cross-correlation two pespective views from a single column of perspective views.
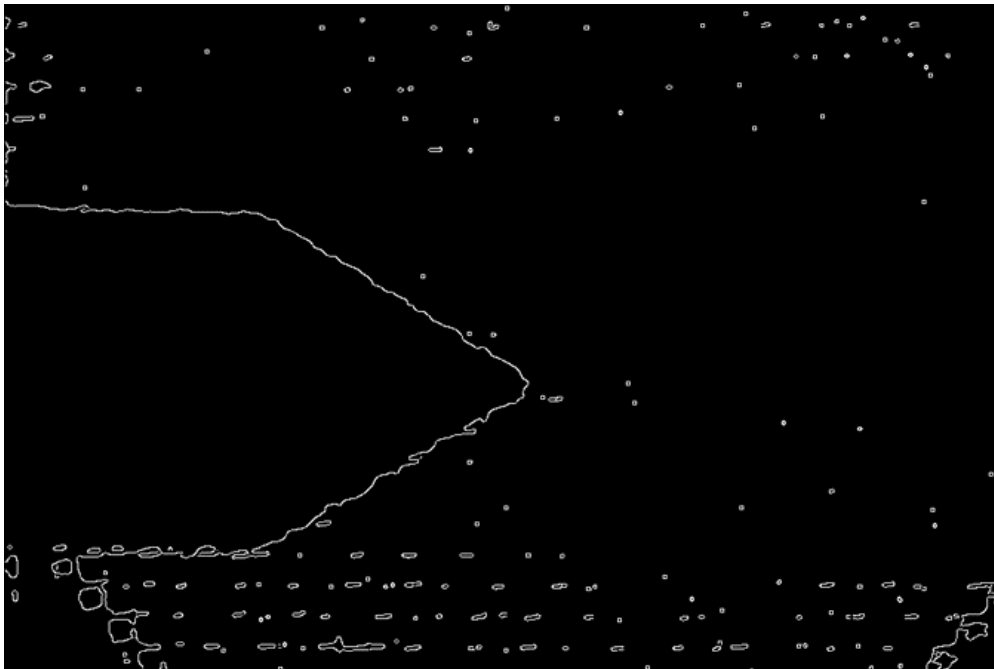
Figure 8.13: Example of an edge image generated by processing a perspective view.

two perspective view was equal to 43 mm and s_o was equal to 492 mm. For this example, $\vec{z}$ value of -83.7 mm was obtained. From the disparity measurement measured by comparing multiple pairs of perspective view, an average $\vec{z}$ of -85.6 mm with a standard deviation of -6 mm was obtained.

$$\vec{z} = \frac{d_{fp}s_o}{BM - d_{fp}} \tag{8.3}$$

$$d_{fp} = \frac{d}{M} \tag{8.4}$$

Figure 8.14 shows the perspective view 61 superimposed with the distortion data obtained by correlating the no flow image and the corresponding image with flow in it. Distortion was measured using the cross-correlation techniques used in PIV analysis. The vector data used in Figure 8.14 was obtained by analyzing the images with interrogation regions of size 32×32 pixels with an overlap of 16 pixels. A much denser correlation data was used in generating the displacement data image shown in Figure 8.15. The data used in Figure 8.15 was obtained by analyzing the images with interrogation region size of 16×16 pixels with 14 pixel overlap. The image shown in Figure 8.15 was obtained by plotting the distortion data as an image using MATLAB.

Images generated by plotting the distortion data were then compared to measure the disparity in the location of the shock. This was done in two stages, as described above. The distortion images were first processed to generate binary images and then generate edge images. These edge images were then compared to measure the disparity between them. This disparity information was used in calculating the location of the shock in the VOI. When the same set of perspectives views, 6 and 116, used in the above example were used, a disparity of -42 pixels was found. This -42 pixel disparity means -8 mm disparity at the focal plane and a $\vec{z}$ value of -76.9 mm. From the disparity information obtained by comparing
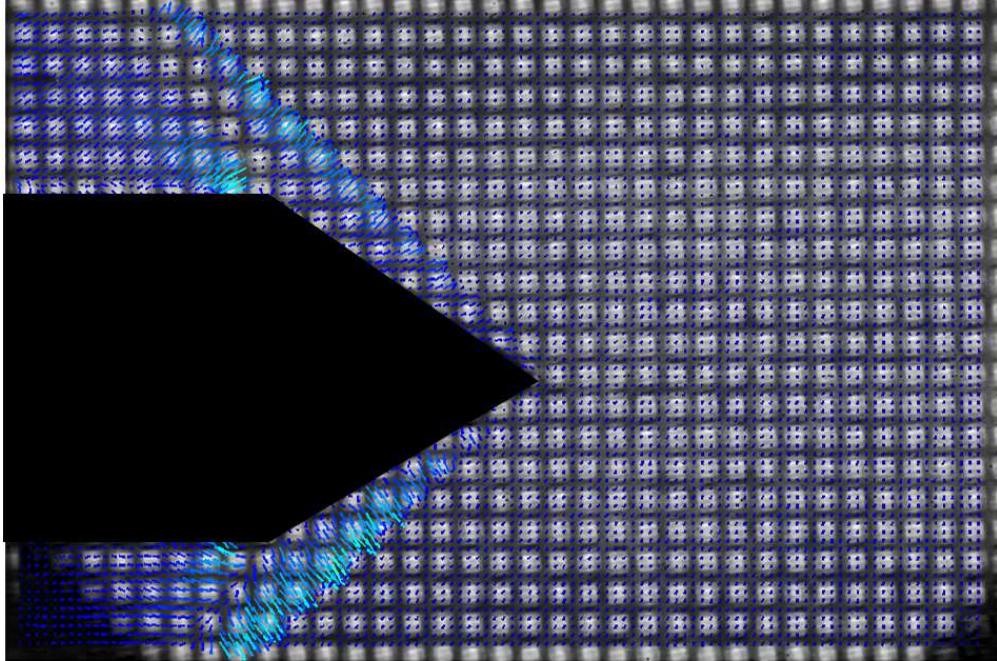
Figure 8.14: Image showing a perspective view superimposed with vectors of the measured distortion.
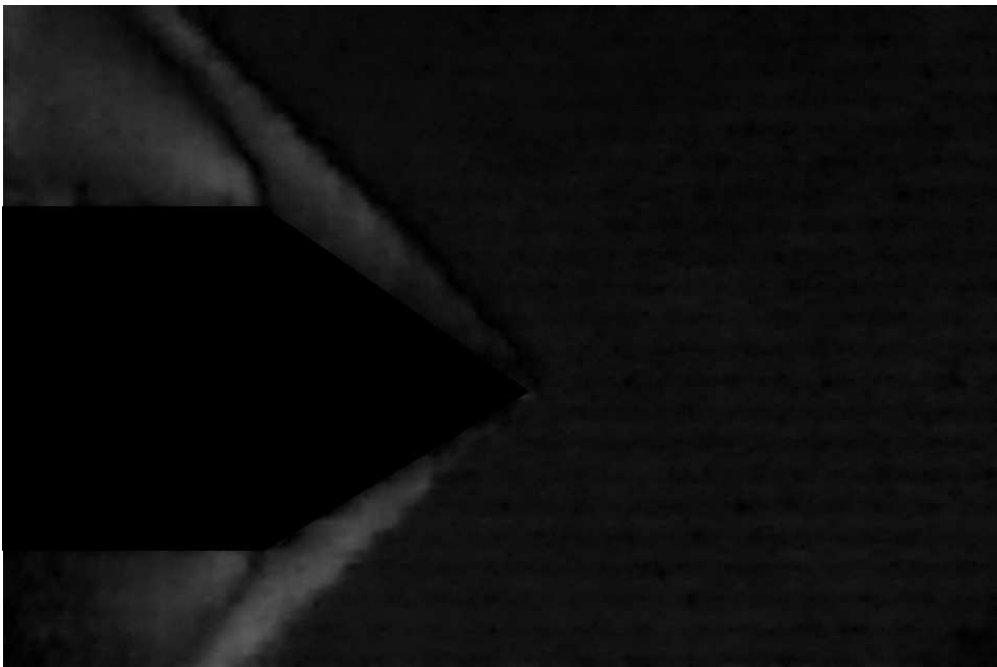
Figure 8.15: Image showing the distribution of the measured distortion obtained from BOS analysis.

multiple pairs of perspective views, an average $\vec{z}$ value of -80.4 mm with a standard deviation of -8 mm was found.

From the experimental setup, the location of the cone and the shock with respect to the camera are known. As the shock is generated at the tip of the cone, the location of the shock is the same as the location of the cone. From the experimental setup, it is known that the cone is 416 mm away from the camera. From the experimental observations, it was found that the cone was 406.4 mm (492 85.6) and the shock was 411.6 mm (492-80.4) away from the camera. The locations of the cone and the shock in the VOI were located with less than 3% error.

8.3 3DDMT Experiments

3DDMT experiments were also conducted in AUs supersonic wind tunnel. Experiments were conducted with a cone model placed in a Mach 2.3 flow. BOS images of the flow field were captured with the 29 MP plenoptic camera using a 60 mm macro lens. Although, the image side f-number of the camera lens was set to 3.2, the effective $f\#$ of the perspective views is 44.8. The magnification and circle of confusion of the setup were set at 0.48 and 2 microlenses respectively.

Focal length	60 mm
s_o	183.7 mm
s_{near}	124.6 mm
s_{far}	349.3 mm
M	0.5093
Image side f-number	3.2
Effective f-number	44.8
Circle of confusion	2 microlenses

Table 8.2: Table showing the details of the 3DDMT experiment.

A schematic of the experimental setup is shown in Figure 8.16. Though the basic idea of capturing the BOS images with plenoptic camera through a compressible flow is the same in both the DP and the 3DDMT experiments, there is slight difference in the placement of

the model in the two. In the 3DDMT experiments, the model was placed closer to the focal-plane, keeping the whole flow field in the DOF (i.e. the front window of the wind tunnel was placed at the near DOF of the camera). Whereas, the model in the depth perception experiments was placed in front of the focal-plane closer to the front of the DOF of the setup to highlight the disparity in the perspective views as a function of the distance from the focal-plane.
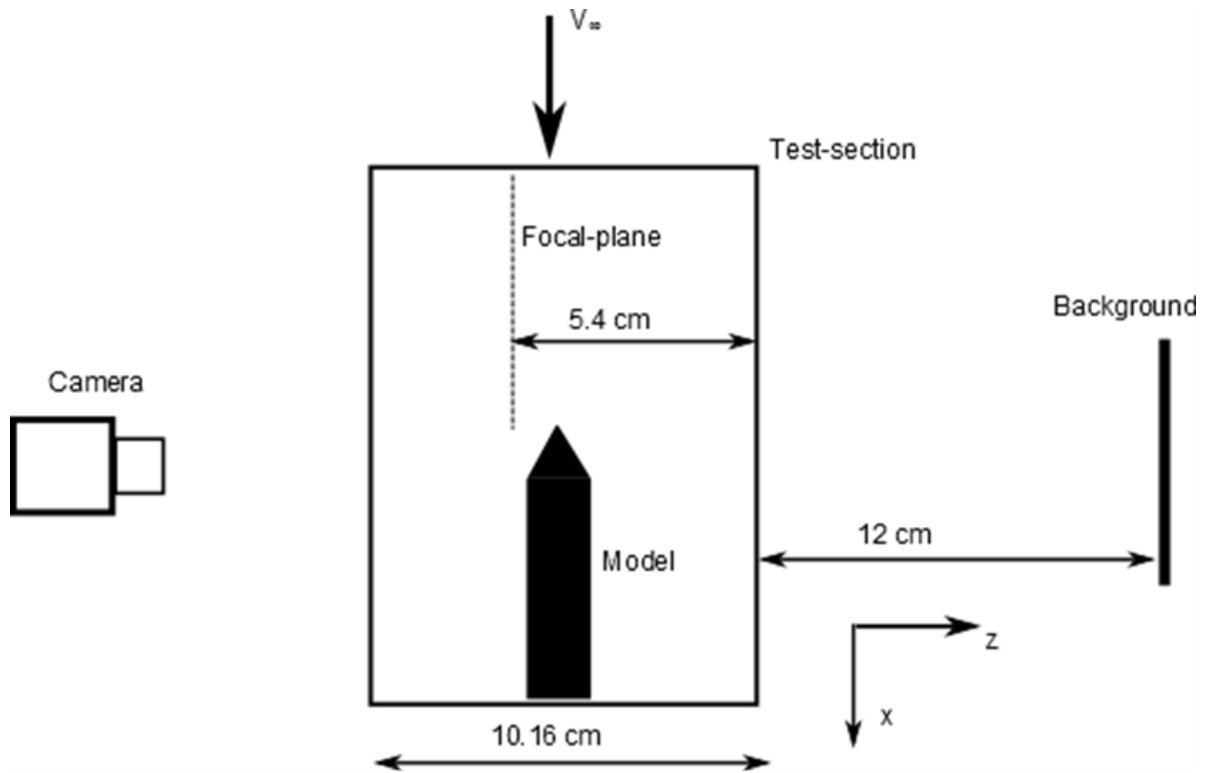
Figure 8.16: Schematic showing the experimental setup used for the 3DDMT experiments.

With the above experimental setup, a FOV of approximately 76.2×50.8 sq.mm (3×2 sq. inches) at the focal plane was achieved. A plenoptic image of a ruler was used for focusing and measuring the FOV is shown in Figure 8.17. A BOS image captured in these experiments is shown in Figure 8.18. The model in the images is sharper than in the plenoptic image shown in Figure 8.8, as it is placed near the focal-plane of the setup. Perspective views were generated using LFIT v2.1 with a super sampling of 2. Figure 8.19 shows a perspective view generated from the raw image in Figure 8.18. For reasons to be discussed, the background

165

is different than the uniform grid pattern used earlier. There are 904×603 pixels in each perspective view and a total of 11×11 perspective views were generated from each plenoptic image. Perspective views are labelled as discussed in the last section.
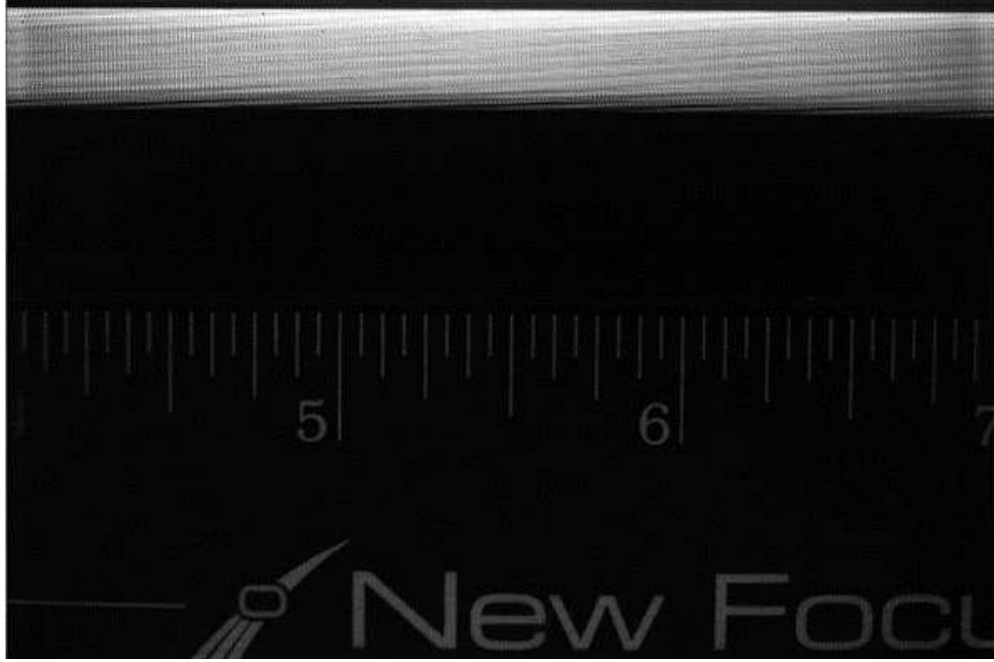
Figure 8.17: Image of the ruler captured with the ruler placed at the focal-plane showing the size of the FOV.

The experimental setup described above for the 3DDMT experiments was used for performing physical and simulated experiments. The physical experiments were first conducted in the lab whose conditions were then used in developing the analytical model for comparison. But, in this section, the discussion about the physical experiments is presented after the simulated experiments to develop an understanding about the expectations of the observations from the physical experiments. But, before the simulated experiments and the observations from them are presented, the analytical solution of a flow around the cone placed in a supersonic flow is discussed. When presenting the density distribution in the VOI or in the reconstructed volumes, density difference distribution is used. Density difference at any point is defined as the difference between the density at the location and the freestream density.
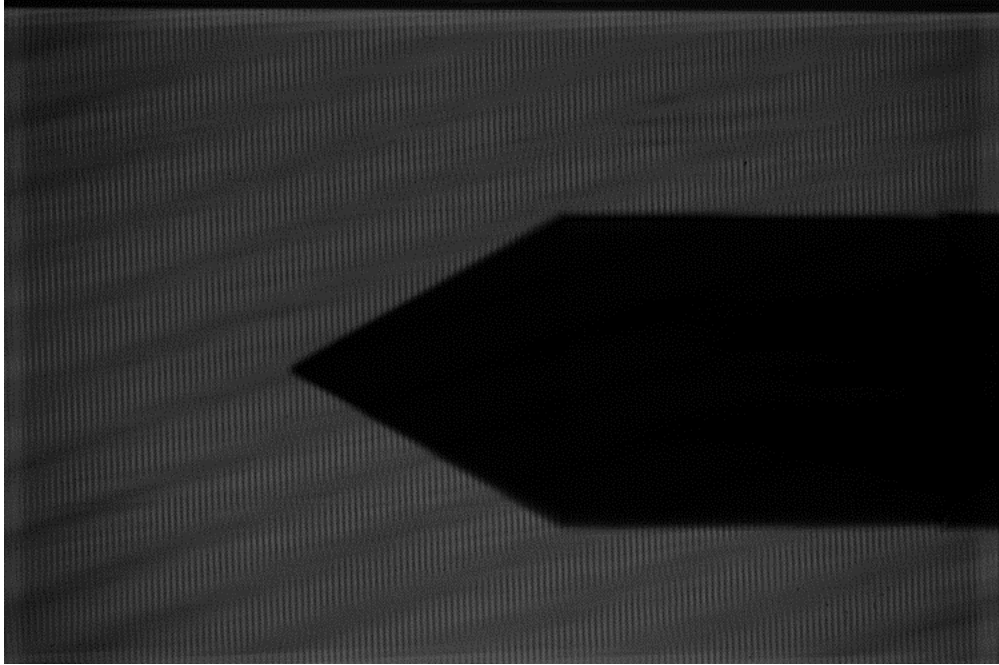
Figure 8.18: Raw BOS image captured with the plenoptic camera in the 3DDMT experiments.
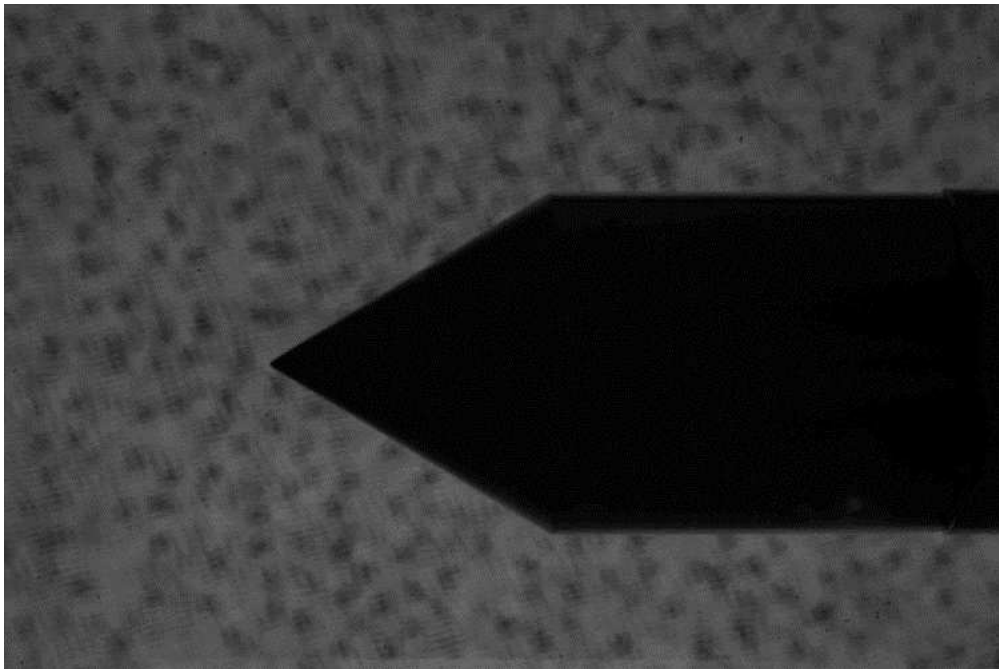
Figure 8.19: Perspective view 66 generated from the plenoptic image shown in Figure 8.18.

8.3.1 Analytical Solution of the Cone in Supersonic Flow

An analytical solution of a cone in supersonic flow was found using the Taylor-Maccoll (TM) differential equations (Equations 1 and 2) [154].

$$\frac{\gamma - 1}{2}\left[V_{max}^2 - V_r^2 - \left(\frac{dV_r}{d\theta}\right)^2\right]\left[2V_r + \cot\theta\frac{dV_r}{d\theta} + \frac{d^2V_r}{d\theta^2}\right] - \frac{dV_r}{d\theta}\left[V_r\frac{dV_r}{d\theta} + \frac{dV_r}{d\theta}\left(\frac{d^2V_r}{d\theta^2}\right)\right]$$

(8.5)

$$V_\theta = \frac{dV_r}{d\theta}$$

(8.6)

where, γ is the ratio of the specific heats of air and V_{max}^2 is twice the theoretical stagnation enthalpy of the freestream.

Figure 8.20 shows the schematic of a cone placed in a supersonic flow. In the figure, the cone model has a cone angle of θ_c with the cone axis coinciding with the x-axis. A conical shock in the flow field makes an angle of θ_s with x-axis. Consider any ray starting from the tip of the cone making an angle θ, such that $\theta_c\theta\theta_s$. The velocity of the flow field at any point on the ray is given by the two orthogonal components, V_r and V_θ parallel and perpendicular to the ray respectively. Given the Mach number of the freestream velocity and cone angle, the velocity components at any point on the ray can be solved using the TM equations.
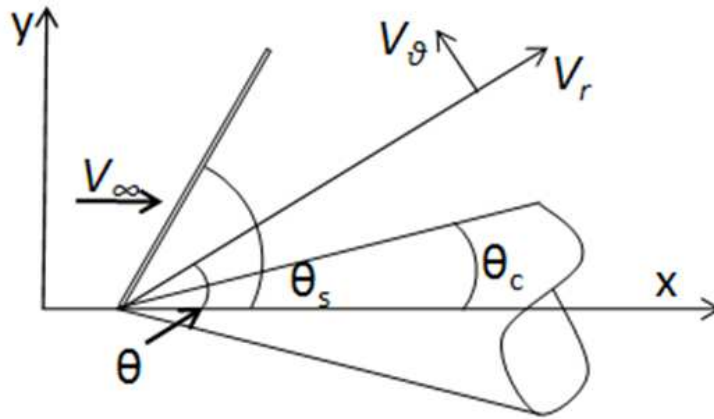
Figure 8.20: Schematic of the cone model.

8.3.2 Simulated Experiments

Simulated experiments were conducted on a model of a cone in supersonic flow mimicking the physical experiments. The density distribution around the cone for the experiments was modeled using the analytical solution described in subsection 8.3.1.

Simulated experiments were designed mimicking the conditions of the physical experiments in Microsoft Visual Studio environment using C++. In the physical experiments, there were 11×11 perspective views, giving a total of 121 perspective views from each plenoptic image. The same number of perspective views were simulated. The analytical volume used in the simulated experiments was designed to have be 25% bigger in x and y directions so that the information at the edges was not lost. The discretization scheme used in the physical experiments was also used in the simulated experiments.

Figure 8.21 shows a slice of the simulated volume taken parallel to the xz plane dividing the volume into two equal halves. The asymmetric nature of the inhomogeneity around the axis of the cone due to the shape of the VOI is seen here. This is further observed in the slices of the volume shown in Figure 8.22. The lines in Figure 8.21 represent the slices of the volume shown in Figure 8.22 and Figure 8.23. The lines parallel to the x-axis represent the planes parallel to the xy plane and are shown in Figure 8.22. The line parallel to the z-axis represents the plane parallel to the yz plane and is shown in Figure 8.23.

In the images in Figure 8.22, only the density variation in the volume is shown. The dark blue region in the images represents the freestream density, red represents the cone in the volume and the region with light green to yellow color represents the density difference distribution after the shock. The color bar on the image at Figure 8.22(c) represents the absolute density difference between the density at the point and the density of the freestream. To give the sense of where in the volume does the inhomogeneity starts appearing, five different layers are shown. When navigating through the VOI from the camera to the background, inhomogeneity in the VOI starts to appear in the 103rd layer and disappear after the 256th layer with the tip of the cone appearing in 168th and 169th layer.
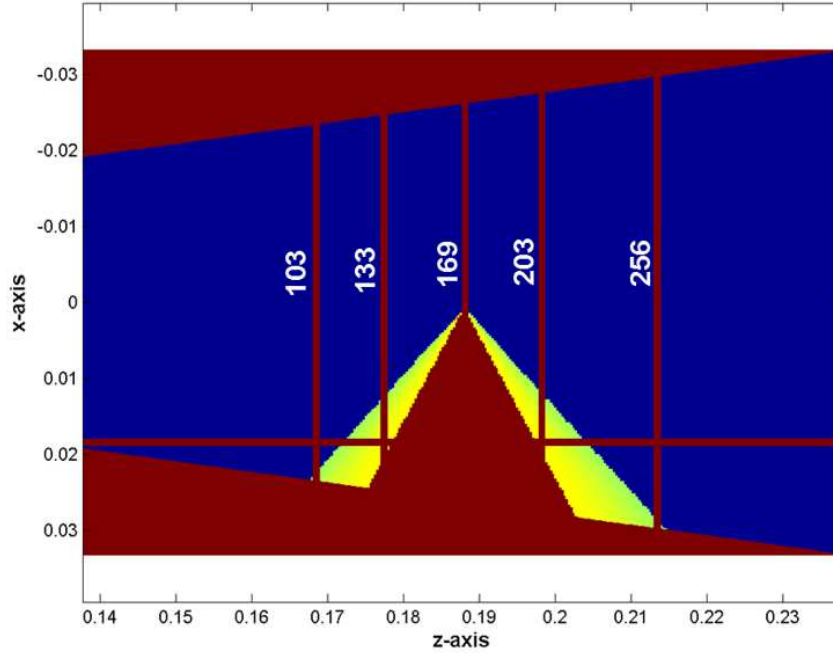
Figure 8.21: Slice of the analytical volume taken parallel to the xz-plane dividing the volume into two equal halves. Image also shows the slices of volume shown in Figures 8.22 and 8.23.

As the cone placed in the supersonic flow is symmetric about its axis, the flow is expected to generate a symmetric density distribution around the cone. That means, if the inhomogeneity in density distribution starts appearing in 103rd layer, then it is expected to disappear around layers 232 or 233 if the designed VOI was a cube. Given the designed VOI has the FOV that increases along the z-axis, the inhomogeneity disappear after the 256th layer. This was visualized in Figure 8.21.

Figure 8.23 shows the slice of the volume taken parallel to the yz plane and passing through the right vertical edge of the plane of the VOI facing the camera. The increasing FOV of the VOI is clearly visible. The region in red represents either the region out of the VOI or the cone. The plots in Figure 8.21 and Figure 8.23 show the region where the inhomogeneity in the density is confined to in the modeled volume.
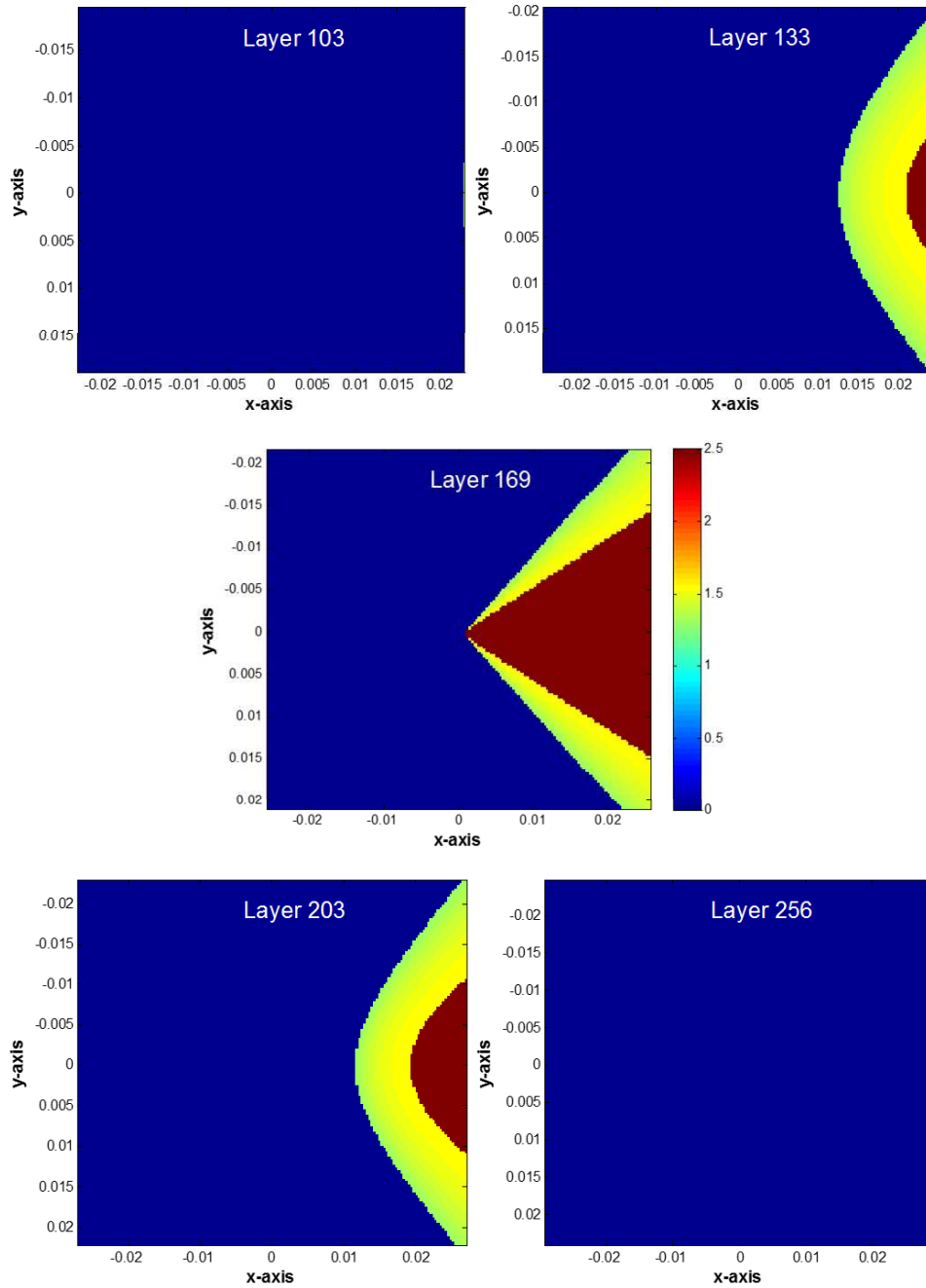
Figure 8.22: Slices of the cone model solution obtained from TM equations.

The 3D volume generated from the TM equations was used in the simulated experiments to obtain 121 perspective views. OPD values were calculated by integrating the inhomogeneous density along the line of sight of the pixel.
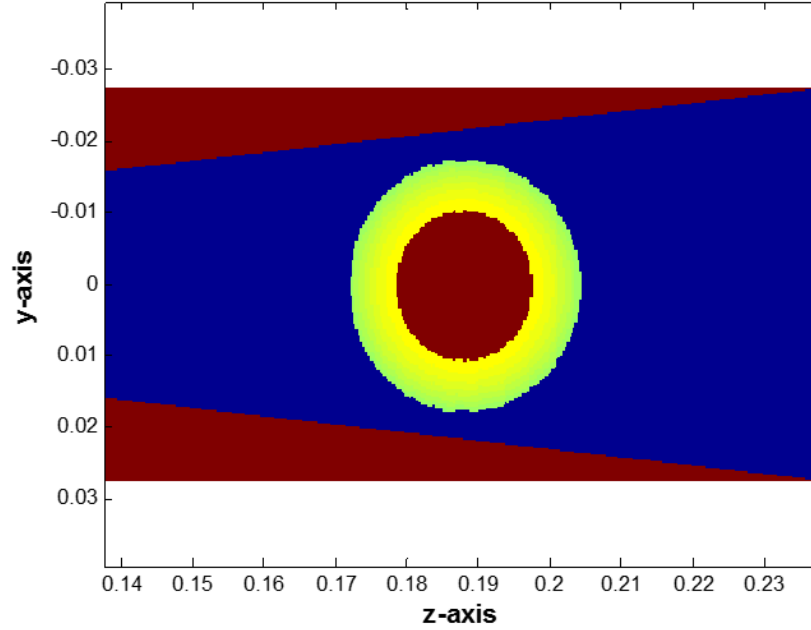
Figure 8.23: Slice of the VOI taken parallel to the yz plane coinciding with the right vertical edge of the plane of the VOI facing the camera.

A few of the generated perspective views are shown in Figure 8.24. The dark blue region in these images represent the OPD for light rays passing through the volume without any interaction with the region after shock. The light blue to green region represents the OPD of light rays that have some interaction with the flow field after the shock and the region in red represents the pixels whose light rays were blocked by the cone in the volume.

From Figure 8.24, it is hard to see the difference between any two perspective views. Therefore, to visualize the difference between the perspective views, an image showing the difference measured between the perspective views 11 and 121 is shown in Figure 8.25. Data used for the plot was obtained by subtracting the OPD of perspective view 121 from the OPD of the perspective view 11. The inner triangle is the region where the cone was observed in both the perspective views. The dark red region at the upper edge of the triangle is where the cone extends in perspective view 11 and the dark blue at the lower edge of the triangle is where the cone extends in perspective view 121. Triangles at the top and bottom of the image show the difference in OPD measured between the two perspective views.

172
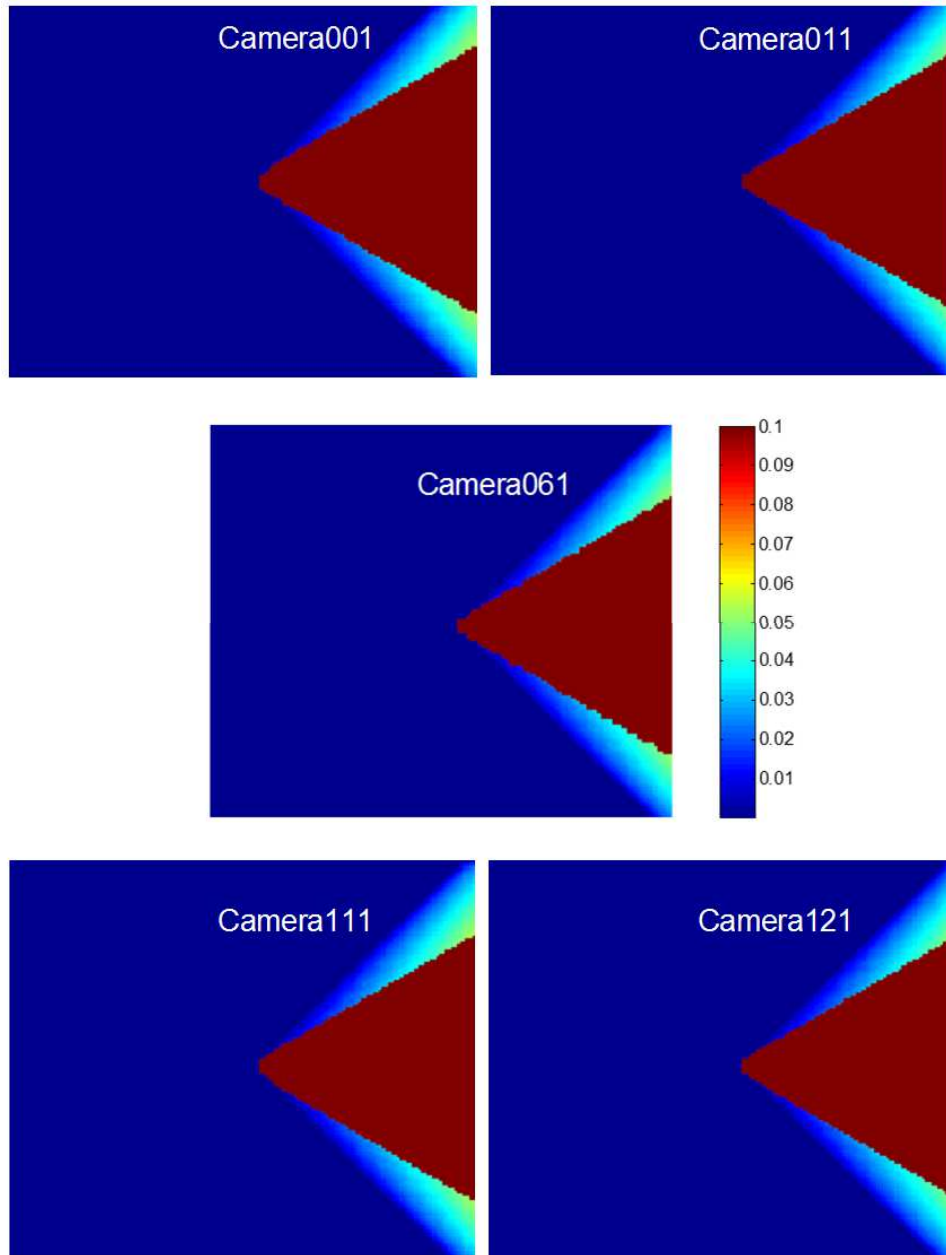
Figure 8.24: Perspective views simulated from the generated 3D volume using TM equations.

Perspective views of the simulated model designed using the TM solution were used with the MART algorithm in reconstructing the volume. Slices from this reconstructed volume showing the density difference distribution are shown in Figure 8.26. From the images in Figure 8.26, presence of inhomogeneity in all layers of the VOI is observed. These observation are in contrast to the original volume seen in Figure 8.22. Presence of inhomogeneity in all
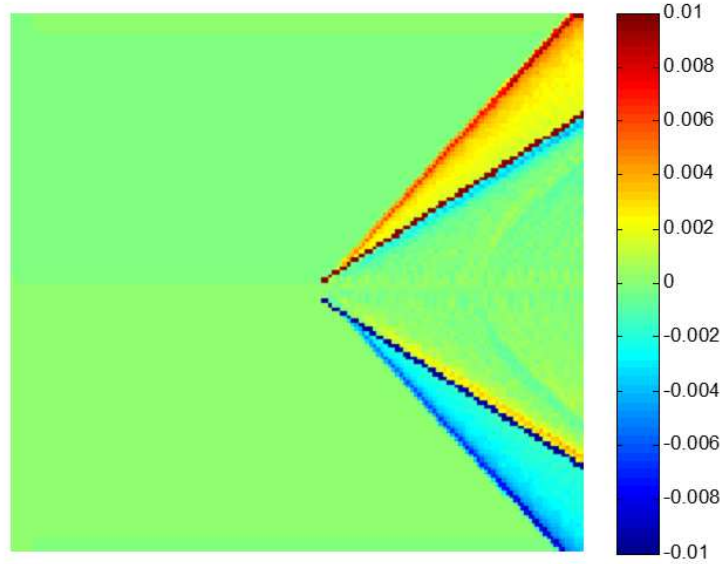
Figure 8.25: Difference between the perspective views 11 and 121.

layers of the reconstructed volume is the result of the limited maximum angular disparity in perspective views. With the current setup, the maximum angular disparity of $5.44°$ ($-2.72°$ to $+2.72°$) was achieved in both x and y directions. This limited angular disparity in the perspective views limit MARTs reconstruction ability as the cone shock makes a range of angles with z-axis, $-180°$ to $+180°$. As seen in the results of the simulated experiments in Chapter 7, where, Mach 2.0 flows with the shock making a $45°$ angle with the x-axis was used to study the performance of the developed 3DDMT. In the experiments simulated in Chapter 7, when the angle between the z-axis and the shock exceeded $7°$, the shock in the reconstructed volume was blurred. The maximum angular disparity in those experiments was around $14°$. Thus, the limited angular disparity in the perspective views result in the smearing of the measured density difference in all layers of the reconstructed volume.

To get a different viewpoint of the reconstructed volume, slices taken parallel to xz plane and yz plane are shown in Figure 8.27. In the plane dividing the volume into two equal halves and parallel to xz plane, presence of the cone in the center of the volume results in occlusion and no observations can be made. Therefore to show the smearing effect, in
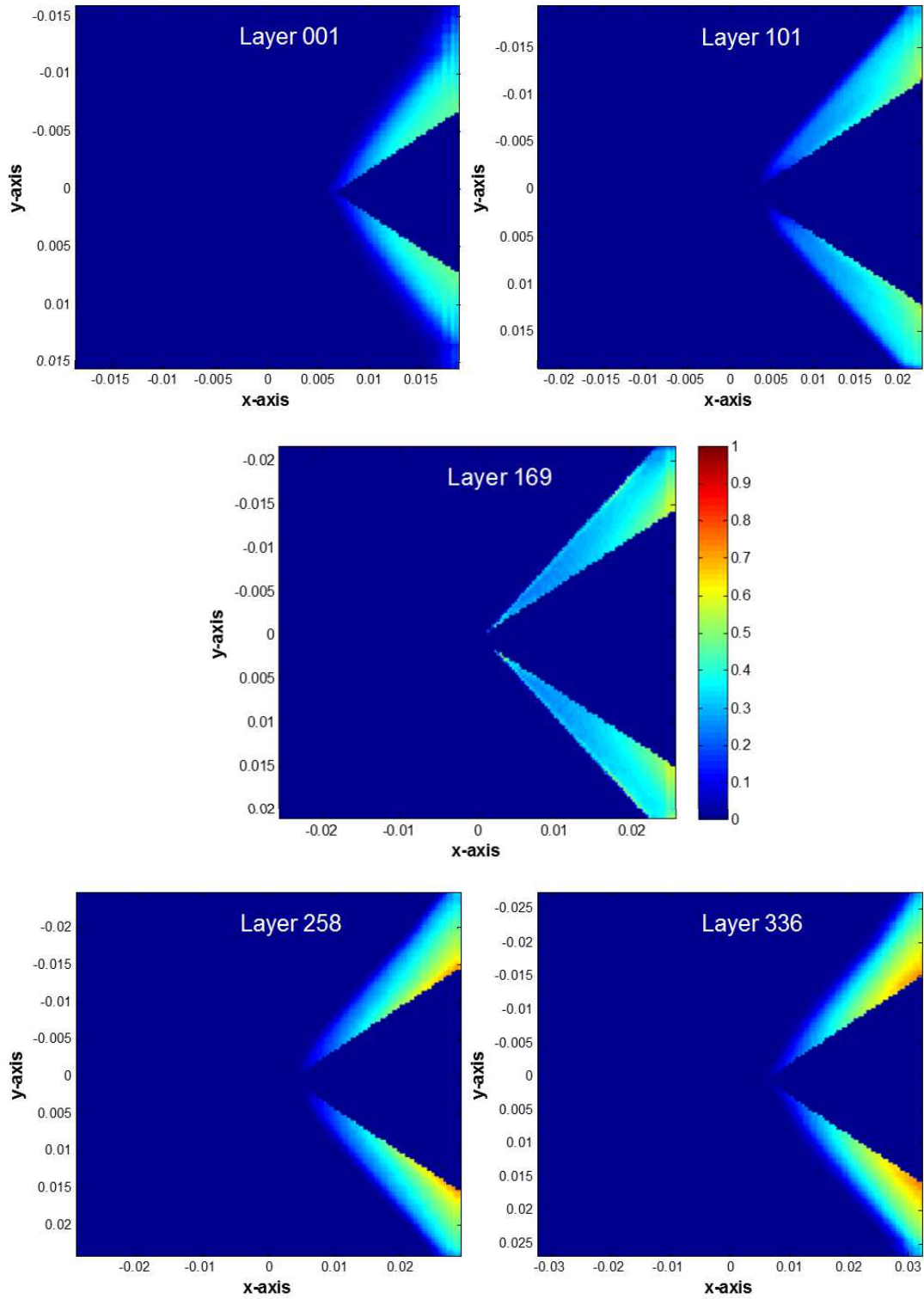
Figure 8.26: Slices from the reconstructed volume using data from simulated perspective views.

Figure 8.27(a), a plane making 0.4° angle with the xz plane at the camera aperture is shown. The density difference present in the volume is hardly noticeable in the image as there is occlusion of information due to the presence of cone in the volume. Figure 8.27(b) shows a slice of the volume taken parallel to the yz plane coinciding with the right edge of the face of the volume facing the camera. Presence of the inhomogeneity from the start to the end of the volume is obvious from the image.
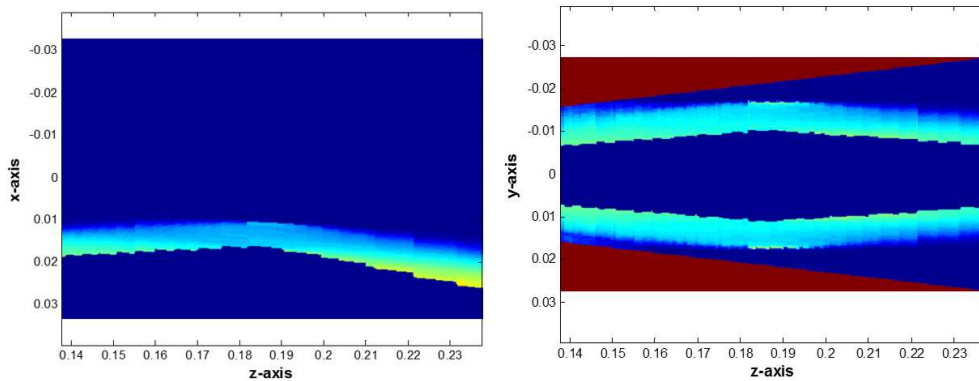
Figure 8.27: Slices of the reconstructed volume with simulated data. Plane a) making a 0.4° angle with the xz-plane and b) parallel to the yz-plane.

8.3.3 Physical Experiments

In Figures 8.18 and 8.19, sample perspective view and the plenoptic image used to generate it are shown. Notice the background in the perspective view shown in Figure 8.19, the background in the image is a random high contrast dot pattern background generated in MATLAB. A sample of the background is shown in Figure 8.28. The random dot pattern background was used as the use of the wavelet background with the plenoptic camera was challenging.

Figure 8.29 shows a wavelet background. It is a perspective view generated from the BOS image captured with the plenoptic camera. Figure 8.30 shows two 2D Fourier transforms. The Fourier transform image in Figure 8.30(a) shows the expected frequency distribution in a background image for effective use in BOS analysis. But, it is clear from the frequency
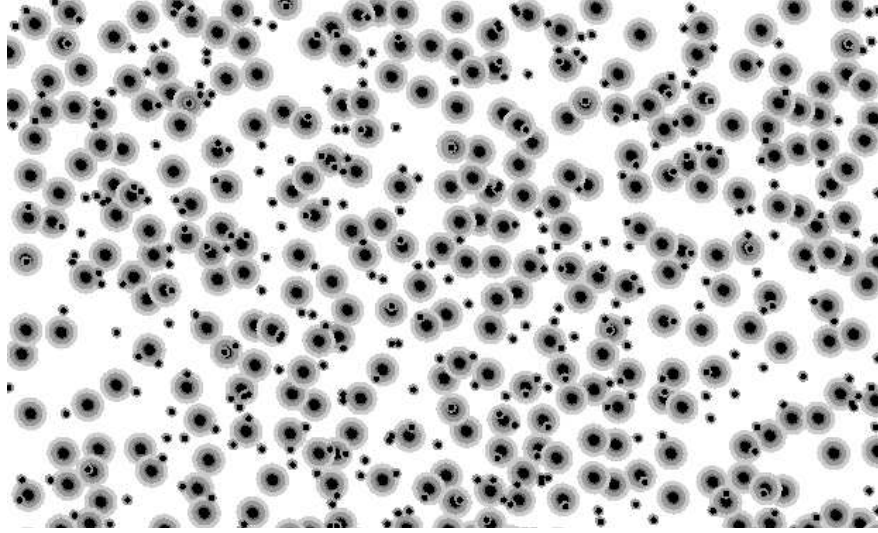
Figure 8.28: High contrast background used in the 3DDMT experiments.

plots that the band limit nature of the wavelet background seen in Figure 8.30(a) is lost in Figure 8.30(b). The low frequency information present in the perspective views of the plenoptic images is noticeable. This loss of bandlimited nature makes the use of wavelet background with optical flow techniques challenging. Using wavelet background along with optical flow techniques in BOS with a plenoptic camera is still a possibility, but this requires more work. To avoid the challenges for now, the high contrast dot pattern background shown in Figure 8.28 was used along with the PIV techniques to compare the reference background with the distorted background to generate distortion data.

In Figure 8.31, a zoomed in top half of the perspective view 66 is shown. Although the random dot pattern with high contrast was used as the background, when captured with the plenoptic camera some of the contrast in the background is lost. The loss in the contrast can be attributed to the blurring caused due to the experimental setup. The circle of confusion (CC) of the setup was set to 2 microlenses resulting in blurring of the background in the images.

In Figure 8.31, a line above the model is highlighted with an arrow. This line is the image of a scratch on the back wall of the tunnel. This scratch in both BOS images, reference
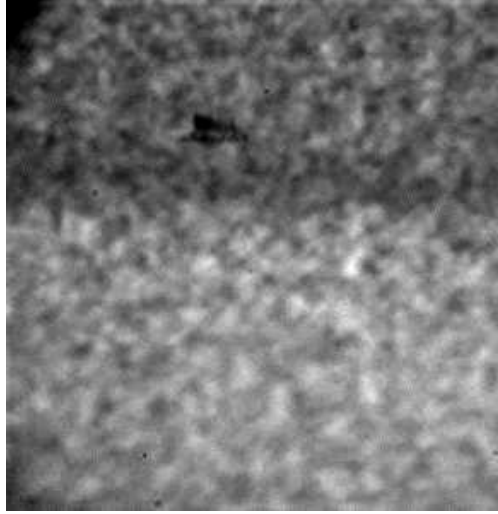
Figure 8.29: Images of the wavelet background captured in a perspective view generated from a plenoptic image.
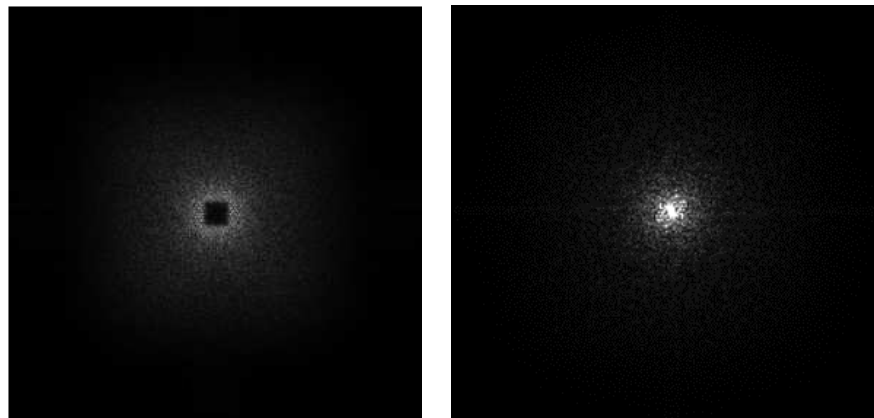
Figure 8.30: a) Expected FFT of the wavelet background and b) FFT of the wavelet background captured in a perspective view generated from a plenoptic image captured with the plenoptic camera.

and the distorted, resulted in false correlation and there was not a clear line of sight from the background to the camera at this location. Figure 8.32 shows the perspective view in Figure 8.31 super imposed with the x-component of the distortion data measured with PIV techniques. The effect of the scratch on the wall on measured distortion is evident in this image. To avoid the effect of the scratch on the measured data, cropped images were used to measure distortion data. Some portion of the region in the front of the cone belonging
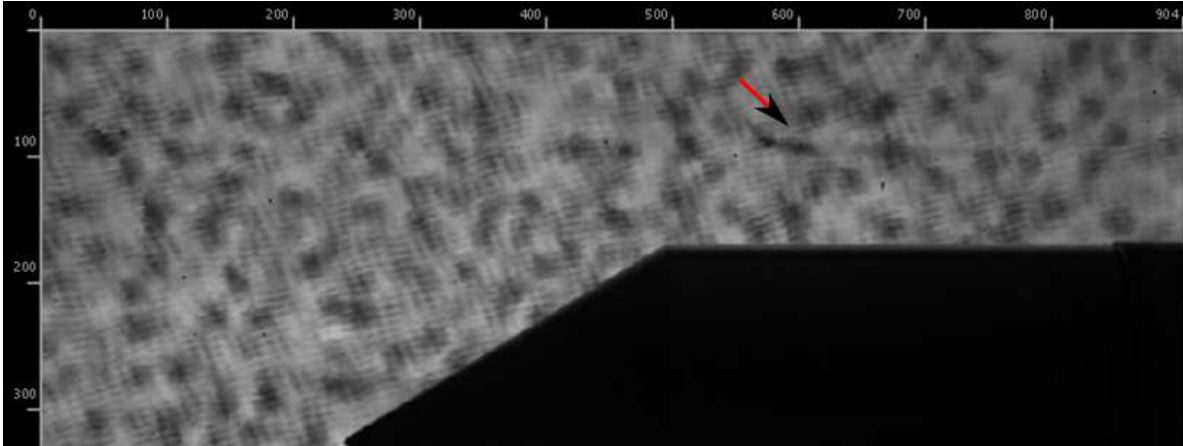
Figure 8.31: Top half of the perspective view 66.

to the freestream was also cropped as the average distortion measured in the region was two orders smaller than the distortion measured due to the shock. Cropping the freestream portion of the images also helped in speeding the volumetric reconstruction process. As an example, a point in the freestream region in Figure 8.33 is highlighted. The highlighted point suggest that the effect of cropping the freestream on the reconstructed wavefront is negligible. These cropped images were analyzed with PIV algorithms with an interrogation region size of 16×16 pixels and 12 pixel overlap. Because cropped images were used, only 72×110 vectors were obtained from each pair of perspective images.
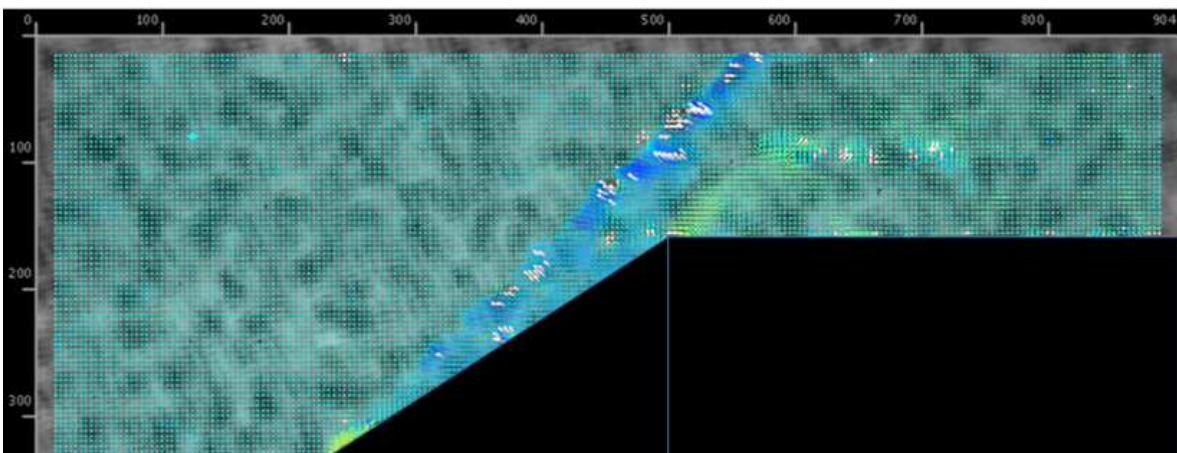
Figure 8.32: Image generated by super imposing the x-component of the distortion data obtained by PIV processing of the perspective view 66 shown in Figure 8.31.
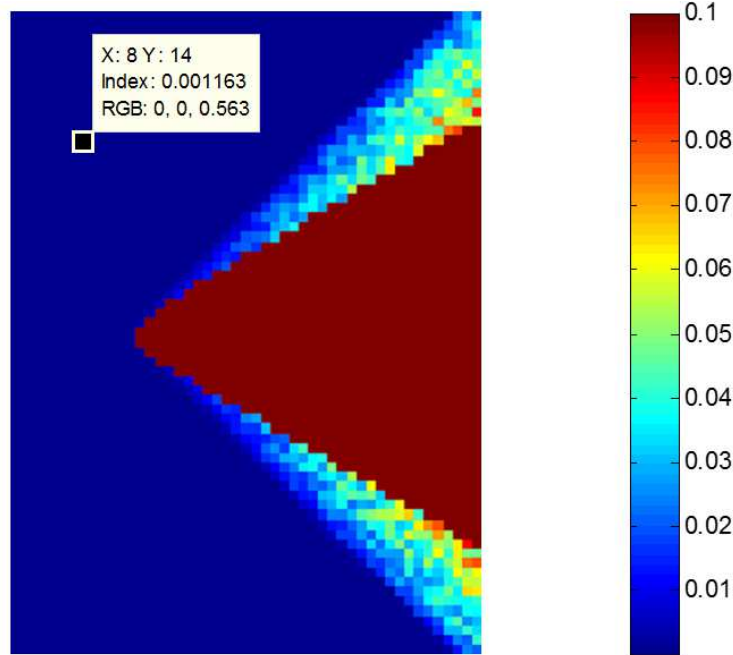
Figure 8.33: OPD data of perspective view 66 obtained by processing the BOS data with the Southwell method.

Distortion data obtained using the 2D cross-correlation was used with the Southwells method to obtain OPD data. Figure 8.33 shows the measured OPD distribution of the perspective view 66. OPD, thus obtained from all 121 perspective views was used in reconstructing the density distribution of the flow field.

For tomographic reconstruction of the volume, the VOI was discretized using the technique described in Chapter 6. The number of voxels in the x and y direction were equal to the number of interrogation regions in x and y direction obtained from PIV analysis. Though, the width and height of the VOI increased when going from the camera to the background, the number of voxels per layer was kept constant. The size of each voxel in the z-direction was equal to the width of a voxel at the nominal focal plane of the setup. Thus, there were a total of $72 \times 110 \times 336$ voxels in the VOI.

A slice of the model volume taken parallel to the xz plane dividing the volume into two equal halves is shown in Figure 8.34. The slice is superimposed with the lines showing the location of the slices taken from the reconstructed volume to present in Figure 8.35. The

slices shown in Figure 8.35 are parallel to the xy plane. The uniform dark blue region in the front, is the region with freestream where, zero density difference is expected. The triangular region in the slices is the region whose information is occluded by the cone in the VOI.
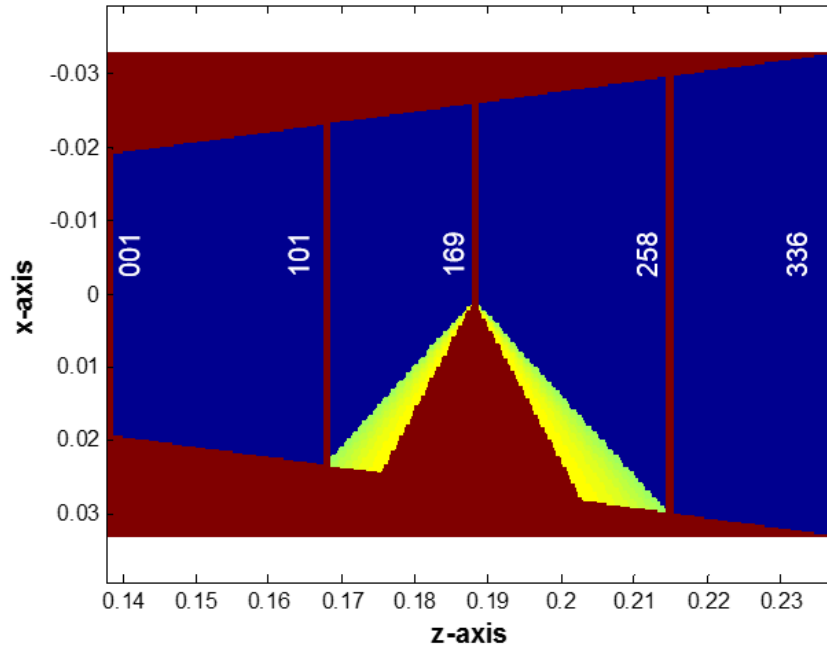
Figure 8.34: Slice of the modeled volume parallel the xz plane and dividing the volume into two equal halves. The lines in the image locate the slices shown in Figures 8.35 and 8.36 from the volume reconstructed using the experimental data.

A few observations can be made from the images in Figure 8.35:

1. Shock is blurred in layers layers in the front and the back layers of the DOF. As the experiments are performed with a 2 microlens circle of confusion blurring is expected in layers away from the focal plane.

2. A sharp shock is observed at the center of the reconstructed volume where the focal plane of the experiments is expected.

3. As expected, the density difference values in the reconstructed volume increase from the shock to the cone.
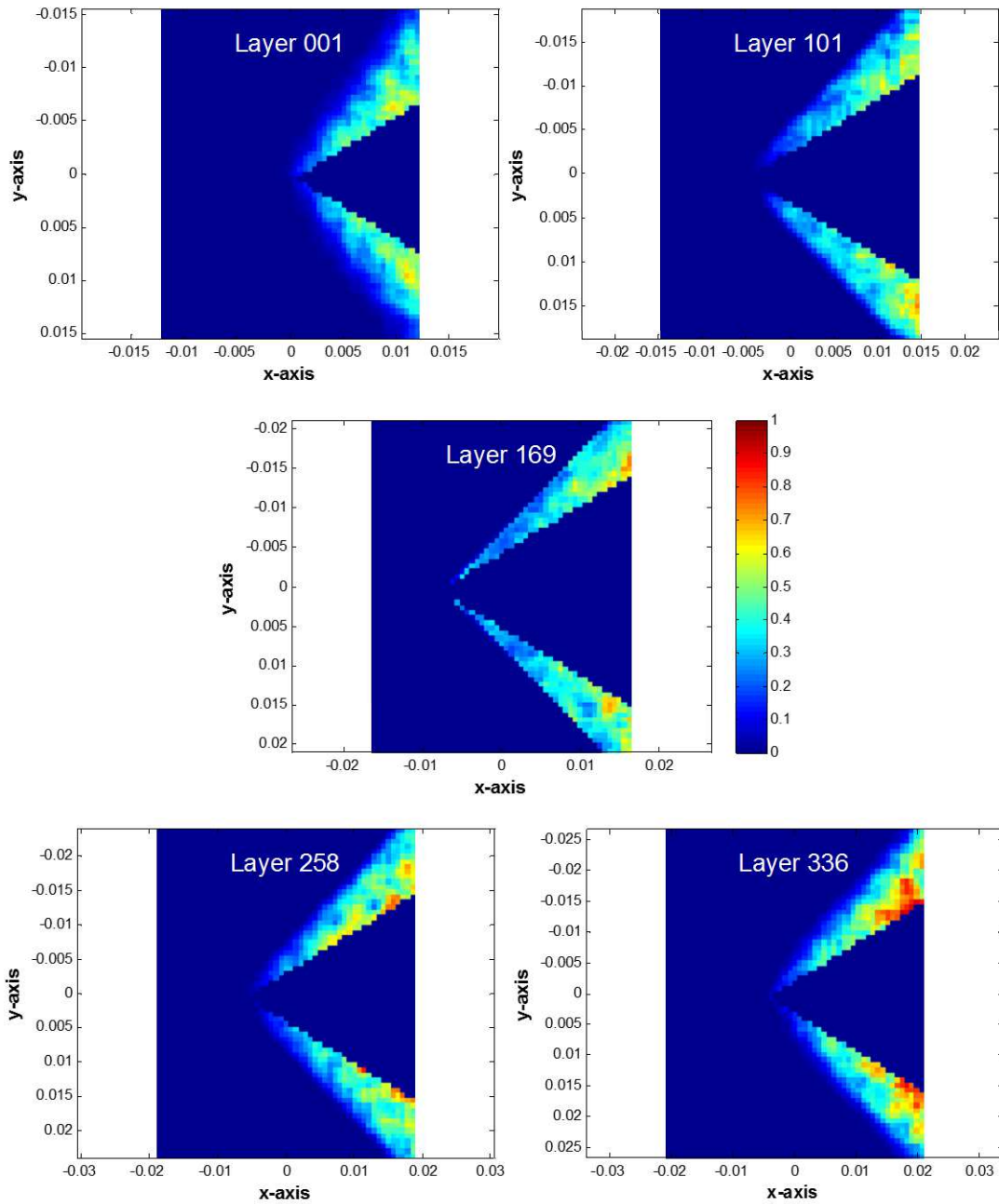
Figure 8.35: Slices of the reconstructed volume taken parallel to xy plane demonstrating the distribution of the density difference in the reconstructed volume.

4. Presence of the density difference value in all layers of the reconstructed volume suggest smearing of the measured density difference.

To better visualize the smearing of the measured density difference in the reconstructed volume two slices of the volume are shown in Figure 8.36. The image in 8.36(a) shows the slice of the volume that makes $0.4°$ angle with xz plane that divides the reconstructed volume in two equal halves. Plot in Figure 8.36(b) is taken parallel to the yz plane. Both slices show the presence of density difference in all layers of the reconstructed volume.
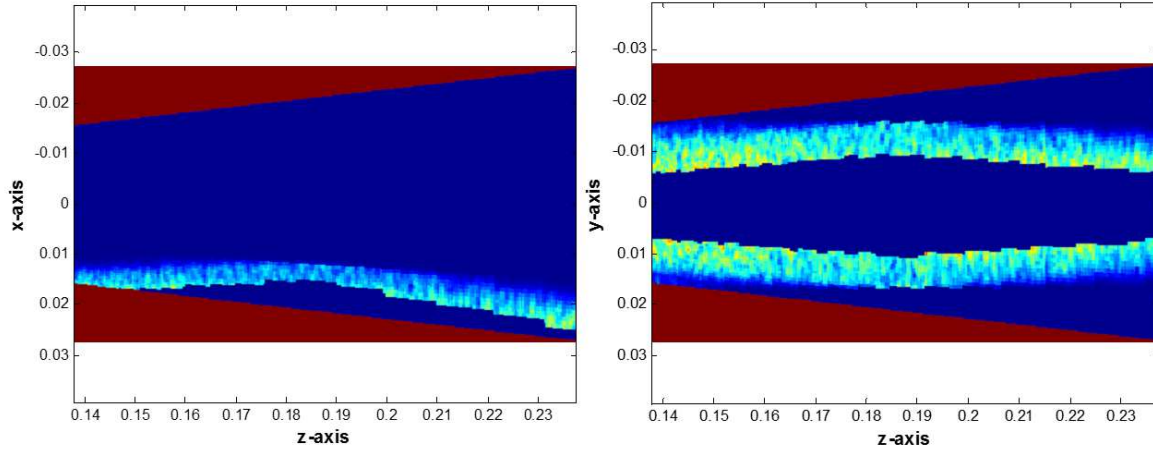
Figure 8.36: Slices of the volume reconstructed using experimental data taken parallel to the xz plane and yz plane demonstrating the smearing of the density difference in the reconstructed volume.

8.3.4 Observations from the 3DDMT Results

Visually comparing the reconstructed volumes obtained from the two, physical and simulated experiments, the pattern of the density difference distribution in the two seem to match well. An example of comparison is shown in Figure 8.37. In the figure two slices taken halfway through the VOI and parallel to the xy plane are shown. Figure 8.37(a) is taken from the reconstructed volume obtained in the simulated experiments and the Figure 8.37(b) is take from the reconstructed volume obtained from the physical experiments. In both experiments, the density difference distribution is observed in all layers of the reconstructed volume. When compared quantitatively, the difference between the total density difference measured in the two reconstructed volumes is less than 6%, at 5.3%.

183
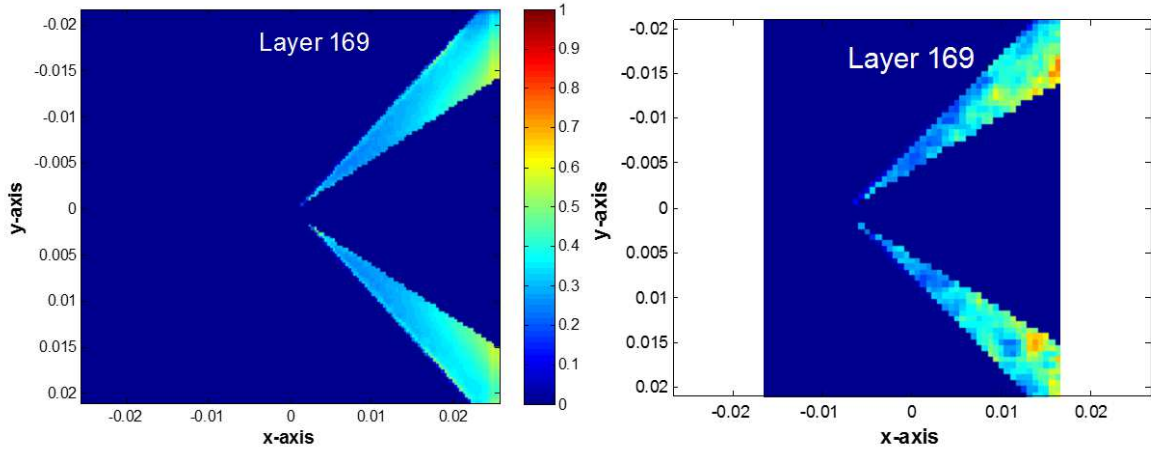
Figure 8.37: Slices of the reconstructed volume taken parallel to xy plane. a) Simulated experiment, and b) physical experiment.

The smearing of the density difference in all layers of the reconstructed volume was seen in the results from both, physical and simulated, experiments. This smearing of the density difference in the reconstructed volumes was caused by the limited maximum angular disparity measured in the perspective views. In Figure 8.38, the maximum angular disparity that can be achieved in the perspective views generated form a plenoptic image is plotted against the magnification of the setup. The setup conditions used in plotting the data in Figure 8.38 are the same as the setup conditions of the physical experiments, i.e., the 29 MP plenoptic camera with the 60 mm lens. From the plot, it can be conclude that the maximum angular disparity that can be achieved is directly proportional to the magnification number of the setup.

To further test the effect of angular disparity on the volumetric reconstruction, a special case was simulated. A set of 11 perspective views were generated for the same cone model developed in the simulated experiments. All 11 perspective views were generated as if they are all in a single column and are focused on the same plane. A schematic of the setup is shown in Figure 8.39. The maximum angular disparity in this experiment was set to 90°.

A reconstructed volume from the 90° angular disparity experiment is compared with the simulated cone model (SCM) and the reconstructed volume from the simulated experiment
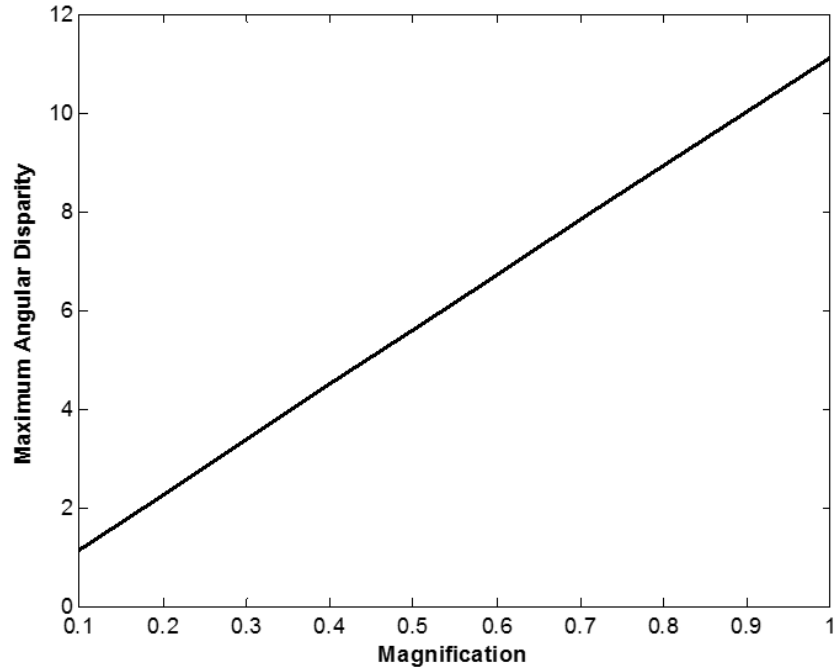
Figure 8.38: Plot showing the maximum angular disparity as a function of magnification for the current experimental setup.
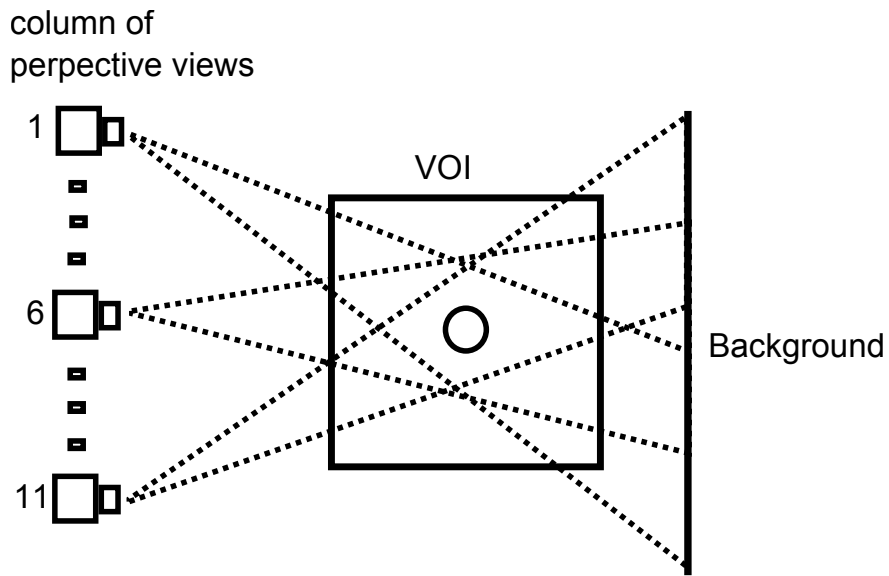
Figure 8.39: Schematic of the simulated experimental setup with 90 angular disparity.

that mimics the physical experiments. In the simulated experiments mimicking the physical experiments, the VOI was reconstructed without any assumptions restrictions or any prior

knowledge of the flow field. Therefore, for the sake of discussion, it is referred to as the generalize reconstruction technique (GRT). For visual comparison, layers 65, 123 and 171 are selected from the three volumes. A schematic showing the location of the layers chosen in the volume is shown in Figure 8.40. The slice of the volume shown in Figure 8.40 was taken from the SCM. The slice is parallel to the xz-plane dividing the volume into two equal halves. From the model, layer 65 is closer to the camera with no shock and has uniform density distribution. Layer 123 was chosen such that the inhomogeneity due to the shock is present in it but the cone is not. Layer 171 was chosen because it has both the density variation due to shock and the cone in it.
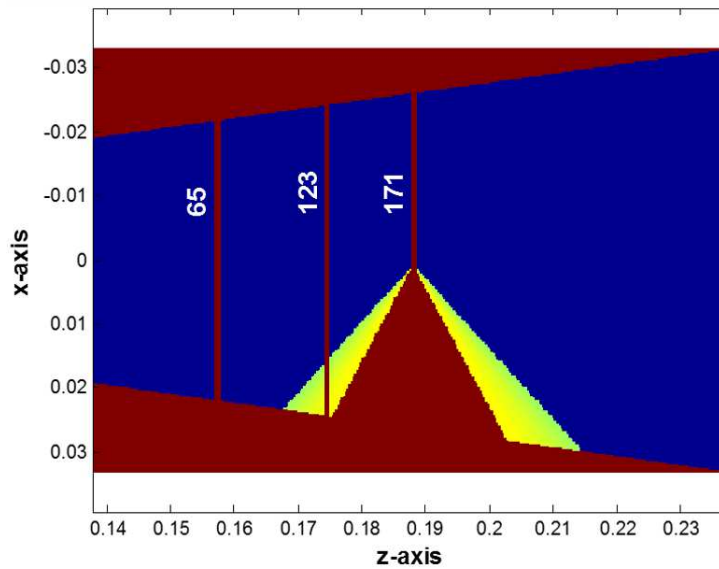
Figure 8.40: Schematic showing the layers used for comparison of the reconstructed volumes from the special cases with the simulated volume and the volume reconstructed from the simulated experiment mimicking the physical experiments.

Figure 8.41 shows the selected layers from the three volumes placed in a 3×3 array. The images in column one of the array are taken from the SCM, the images in column two are taken from the GRT and the images in the third column are taken from the $90°$ disparity experiment. As seen in the results from the GRT, the measured density difference is smeared in all layers of the reconstructed volume. The smearing of the density difference results in under predicting the magnitude of the density difference in the layers where the

186

inhomogeneity in the volume is expected. Increasing the angular disparity to 90°, decreased the amount of smearing but resulted in a jagged pattern. From the images in row 2, it is observed that the 90° angular disparity in the perspective views predicted the shape of the inhomogeneity better. The jagged pattern observed in the slices is caused due to the 5° angular disparity between any two consecutive perspective views.
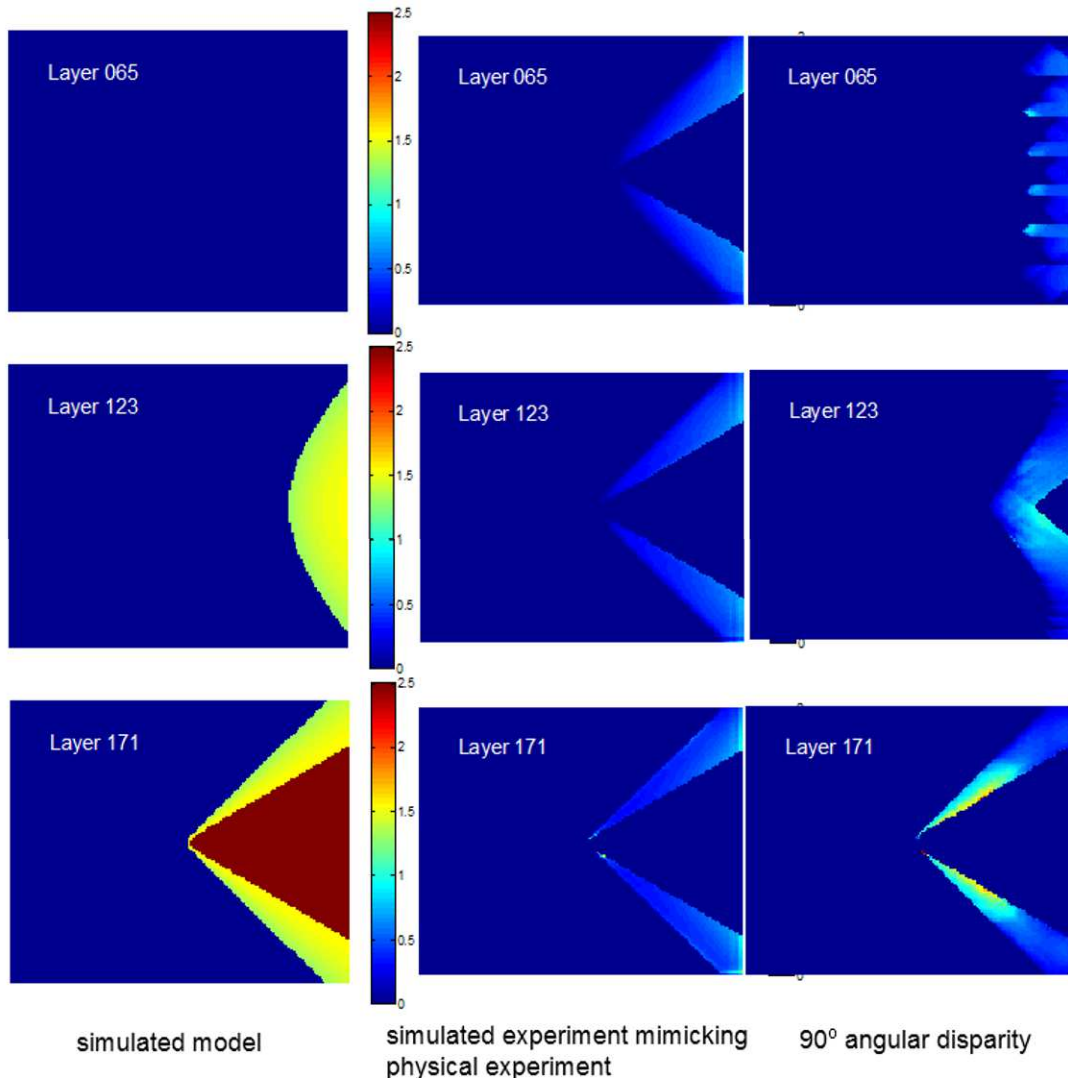
Figure 8.41: Slices comparing the expected volume, volume reconstructed with the generalized reconstruction technique and the volume reconstructed with a maximum angular disparity of 90°.

In the setup shown in Figure 8.39, the viewing angle of the camera 6 in y-direction is approximately 13° and the viewing angle of either the camera 1 or camera 11 is approximately

6.54°. In this experiment, the goal was to see how increasing the disparity angle of a plenoptic camera affected the reconstructed volume, therefore, the planes of all the perspective views were kept parallel to each other. One way to increase disparity in the perspective views without decreasing the viewing angle of the perspective views is to use multiple cameras to capture the BOS information. A schematic of the multiple camera setup is shown in Figure 8.42.
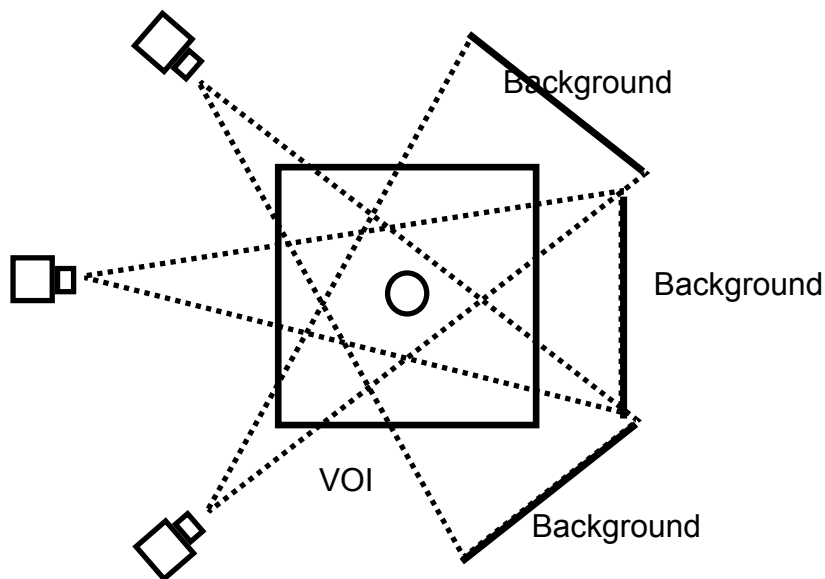
Figure 8.42: Schematic showing multiple camera setup to capture BOS images.

To address the smearing of the density difference in the reconstructed volume, a case specific reconstruction technique (CSRT) was used with the perspective views from the simulated experiments with 121 perspective views. Prior knowledge about the flow around the cone was used in the iterative reconstruction process. The information about the Mach number of the flow field and the cone angle of the model used in the experiments was used in the TM equation to calculate the cone angle of the shock. This cone angle was then used to calculate the layers where the inhomogeneity in the VOI was expected. The iterative volumetric reconstruction of the density distribution was limited to these layers.

Figure 8.43 shows the comparison of the volume reconstructed from this CSRT with the expected result, SCM, and the GRT. Images are plotted in a 3×3 array where the first

column of images are from the expected result, the second column of images are from the GRT and the third column of images are from the CSRT.
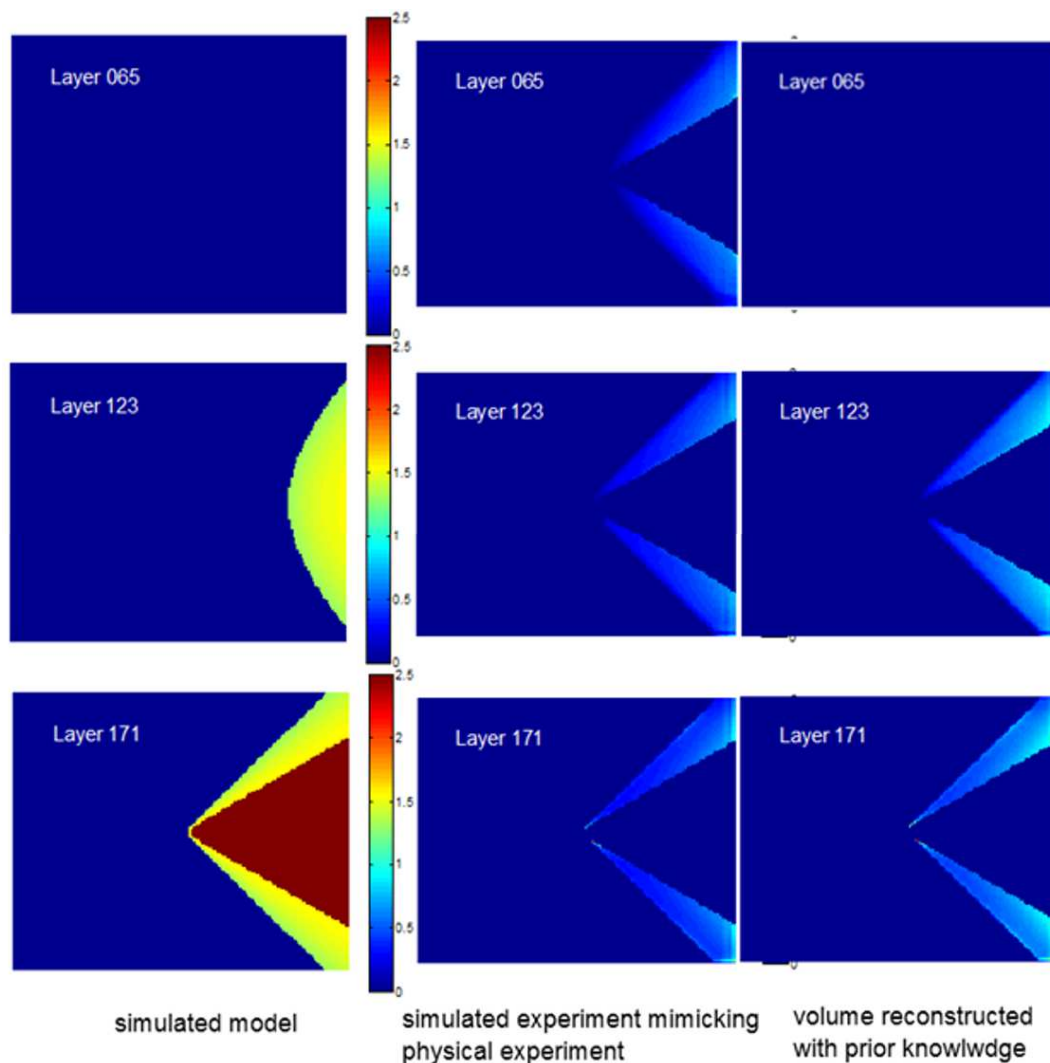
Figure 8.43: Slices comparing the expected volume, volume reconstructed with the generalized reconstruction technique and the special case reconstruction with priori knowledge about the flow field.

Comparing the layer 65 from the three cases, we notice that the layer 65 from the CSRT show uniform density distribution. This is an expected result, as the layer 65 has no inhomogeneity in the model and was left out of the iterative reconstruction process. Comparison of the layers 123 and 171 show that the density distribution between the CSRT and the GRT is similar. In both reconstructions, measured density difference is smeared in the layer.

189
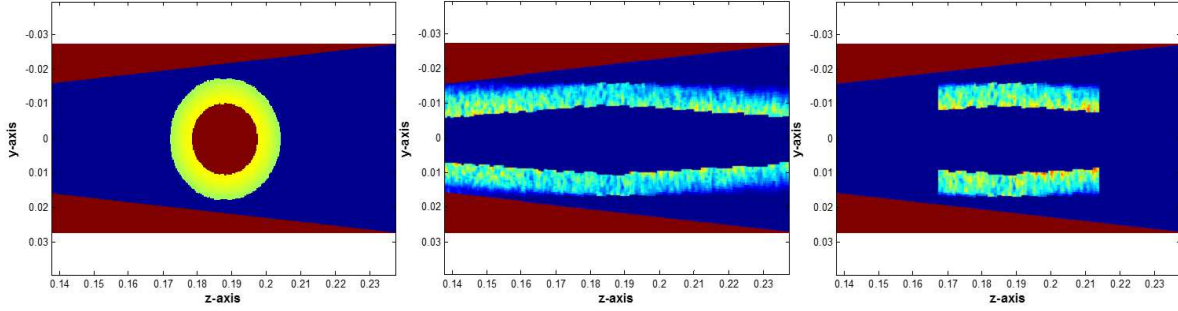
Figure 8.44: Slices comparing the expected volume, volume reconstructed with the generalized reconstruction technique and the special case reconstruction with priori knowledge about the flow field. Slices of the volume are taken parallel to the yz plane.

Because the reconstruction process was limited to the layers where the inhomogeneity was expected, the magnitude of the density difference distribution was about 1.4 times higher than the magnitudes observed in the GRT.

8.4 Summary

In this chapter, the application of BOS with the plenoptic camera for locating the inhomogeneous structures in an inhomogeneous flow field and for 3-dimensional density measurement of an inhomogeneous flow field were tested. Physical experiments to test the performance of BOS with the plenoptic camera for these applications were conducted in AUs supersonic wind tunnel facility.

In the depth perception experiments, perspective views were processed to generate binary images. These binary images were then processed to generate edge images to find the desired edges and sharp discontinuity due to shock in the perspective views. The edge images were then used to measure the movement of the edges and shocks from one perspective view to the other. This disparity information was used in Equation 8.3 to find the location of the cone and the shock generated due to the cone placed in the Mach 2.0 flow. Measurement of the location of the cone and the shock from the experiments closely matched the expected

results with less than 3% deviation. Although a good match between the experimental and expected results was found, further investigation of the technique is needed.

The 3DDMT experiments were conducted in three stages, physical experiments, simulated experiments and special case simulated experiments. In all the experiments, a cone model placed in a Mach 2.3 flow field with the magnification of the setup set at 0.48 and 2 microlens circle of confusion. As expected, some blurring is seen in the layers away from the focal plane of the setup. Near the focal plane of the setup, the discontinuity in the density measurement was reconstructed sharply and the pattern of density distribution, increasing density from the shock to the cone, matched the expected pattern.

The flow field investigated here in Chapter 8 is more complicated than the flow field investigated in Chapter 7. The shock in the flow field in this chapter made a range of angles, $-180°$ to $180°$, with the optical axis of the setup and the large size of the cone and the conical shock surrounding it cause occlusion of information about the flowfield that can be captured in the BOS images. As a result of occlusion, the reconstructed volume showed smearing of the measured density difference in all layers of the reconstructed volume. This effect was seen in volumes reconstructed in both the simulated and the physical experiments.

To address the smearing of the measured density difference, a few special cases of simulated experiments were conducted. Though, the smearing of the measured density difference was observed in the volumes reconstructed in these experiments, using the prior knowledge about the flow field or increasing the maximum disparity angle in the perspective views resulted in improving the output from the reconstruction process. When using the prior knowledge about the flow field in the reconstruction process, the magnitude of the inhomogeneity distribution increased by an average of 1.4 times. In the experiments, where the maximum disparity in the perspective views was increase to $90°$, the shape of the inhomogeneity distribution in front of the cone better matched with the expected result.

Chapter 9

Conclusions

In this dissertation, a novel idea of implementing background oriented schlieren (BOS) with the plenoptic camera was investigated. In the process, applications of BOS with the plenoptic camera for depth perception (DP) of inhomogeneous flow structures and for the measurement of 3-dimensional (3D) density distribution in an inhomogeneous flow field were also investigated.

The BOS measurement technique is non-intrusive with the ability to measure the properties of a flow field without any external influence on the flow. The conventional BOS is simple and easy to setup. The conventional BOS equation assumes that the aperture on the camera capturing the BOS images is a pinhole and that the distortions captured in the BOS images are the result of the interaction of a nominally planar wavefront with a thin inhomogeneous interface. When conducting the BOS experiments in a laboratory, these assumption are invalid, as the aperture on the camera is finite and the limited space for experiments results in a concave wavefront. To understand the performance of BOS in a laboratory, the assumptions made in a conventional BOS were relaxed to rework and develop a new BOS equation. The two primary constraints in the development of the equation were that

1. both the inhomogeneous medium and the background are in nominal focus, and

2. the field of view (FOV) of the system was fixed.

From the developed equation, it was found that, when the FOV of the experiment is fixed, the effect of the focal length of the lens on the sensitivity was negligible. Rather, the sensitivity of the system was better characterized by the f-number ($f\#$) of the system. The analysis

also showed the applicability of the BOS technique in space-limited environments and offered guidelines for optimizing the BOS experiment.

For the first time, the idea of implementing BOS with a plenoptic camera was conceived and explored. When using plenoptic camera for BOS imaging, the capability to generate multiple perspective views from a single plenoptic image gives the ability to perform BOS analysis of the flow field from multiple directions without requiring multiple cameras. Using a single image from the plenoptic camera to capture multiple perspective views also eliminates the cumbersome process of aligning and calibrating multiple cameras for the purpose. Another advantage of BOS imaging with plenoptic camera is that, all the perspective views are captured at the same instance. When using the plenoptic camera for BOS analysis, multiple perspective views with BOS data are obtained. The obvious extension to using the plenoptic camera for BOS imaging is to use the BOS data from these perspective views to study 3D properties of the flow field. The ideas of applying BOS with a plenoptic camera for:

1. Locating inhomogeneous flow field structures in 3D space, and

2. Measuring 3D density distribution of compressible flow fields

were conceived and tested.

When a scene is imaged with the plenoptic camera, the objects in the scene move from one perspective view to the other. In the DP experiments, it was observed that the disparity measured between any two perspective views depends on the angular disparity of the perspective views, and the location of the object in the scene measured from the focal-plane of the image. By quantifying the disparity between the distortions measured in different perspective views, inhomogeneous structures in an inhomogeneous flow field can be located. With the use of BOS with a plenoptic camera, we were able to locate both the model and the shock in a supersonic flow field with less than 3% error.

In computed tomography, light from a known source is passed through the VOI at different angles to form projections. These projections are used for reconstructing the density information of the VOI. This idea was used in the development of a 3D density measurement technique (3DDMT) using BOS with the plenoptic camera. Experiments, both simulated and physical, were conducted to study the performance of the 3DDMT. In simulated experiments, a simple 3D oblique shock flow was used and in physical experiments a supersonic flow with a cone generating a cone shock was used. Observations from these experiments can be summarized as:

1. When using the 3DDMT to measure density distribution in a simple 3D shock flows, the reconstructed volume accurately represented the flow field as long as the angle between the shock and the optical axis of the setup was in the range of the angular disparity measured in the perspective views.

2. In the flow field with the cone shock, the angle between the shock and the optical axis of the setup varied from $-180°$ to $180°$ resulting in the smearing of the measured density difference. Though the reconstructed volume was not an accurate representation of the flow field, discontinuity due to shock near the focal plane and the density distribution pattern were observed to match the expected result.

The limitations observed in these experiments were caused by the limited angular disparity measured in the perspective view generated from the plenoptic images. The limited maximum angular disparity measured in the plenoptic images is a function of the f-number on the camera lens and the magnification of the setup.

As the idea of implementing BOS with a plenoptic camera is still nascent, further study is needed to exploit the full potential. Some ideas for further investigation are presented here.

1. A limitation of BOS is the reduced resolution that is obtained due to the size of the microlenses. The resolution of the BOS data is further reduced if the BOS data is

obtained by cross correlation algorithms used in PIV analysis. To address the issue, use of optical flow techniques along with a wavelet background is suggested. This requires a study to understand the relation between the wavelet background and the resolution of the plenoptic camera.

2. In this work we were successfully able to measure the location of the cone and the shock generated due to its placement in a supersonic flow field. But this capability of the BOS with a plenoptic camera needs further investigation to understand its behavior in the presence of multiple inhomogeneous structures.

3. Although limited, simulated experiments using multiple cameras and prior knowledge about the flow field improved the output from the 3D reconstruction technique and gave comparatively better density distribution. One of the limitation of the multiple camera experiment conducted in this study was the use of the volume discretization technique developed for a single plenoptic camera. An exploration of a 3DDMT using multiple camera with the volume of interest shaped as a regular rectangular cube is suggested.

4. In 1999, Raffel et al. [67] captured BOS images of an inhomogeneous flow field using multiple cameras and generated BOS data by comparing two BOS images captured simultaneously by two different cameras. This eliminated the need of a reference image to measure distortion. As multiple perspective views are obtained with a single plenoptic image in BOS with a plenoptic camera, it is worth investigating their use in generating the BOS data without using any reference images for applications where it is hard to obtain one.

Bibliography

[1] Abhijit Biswas, Norman Page, Jerry Neal, David Zhu, Malcolm Wright, Gerardo G. Ortiz, William H. Farr, and Hamid Hemmati. Airborne optical communications demonstrator design and pre-flight test results, 2005.

[2] Nicholas De Lucca, Stanislav Gordeyev, and Eric Jumper. The airborne aero-optics laboratory, recent data, 2012.

[3] C. Hogge and R. Butts. Frequency spectra for the geometric representation of wavefront distortions due to atmospheric turbulence. *Antennas and Propagation, IEEE Transactions on*, 24(2):144–154, Mar 1976.

[4] M A Vorontsov, D V Pruidze, and V I Shmal'gauzen. Adaptive optics methods in interferometry. *Soviet Journal of Quantum Electronics*, 12(7):868, 1982.

[5] Pierre Lna. Adaptive optics: a breakthrough in astronomy. *Experimental Astronomy*, 26(1-3):35–48, 2009.

[6] Francesco dOvidio, Jordi Isern-Fontanet, Cristóbal López, Emilio Hernández-García, and Emilio García-Ladona. Comparison between eulerian diagnostics and finite-size lyapunov exponents computed from altimetry in the algerian basin. *Deep Sea Research Part I: Oceanographic Research Papers*, 56(1):15–31, 2009.

[7] Thomas Peacock and George Haller. Lagrangian coherent structures:: The hidden skeleton of fluid flows. *Physics today*, 66(2):41, 2013.

[8] Arne Melsom, François Counillon, Joseph Henry LaCasce, and Laurent Bertino. Forecasting search areas using ensemble ocean circulation modeling. *Ocean Dynamics*, 62(8):1245–1257, 2012.

[9] M. Aldén, H. Edner, G. Holmstedt, S. Svanberg, and T. Högberg. Single-pulse laser-induced oh fluorescence in an atmospheric flame, spatially resolved with a diode array detector. *Appl. Opt.*, 21(7):1236–1240, Apr 1982.

[10] Brett E. Battles and Ronald K. Hanson. Laser-induced fluorescence measurements of {NO} and {OH} mole fraction in fuel-lean, high-pressure (110 atm) methane flames: Fluorescence modeling and experimental validation. *Journal of Quantitative Spectroscopy and Radiative Transfer*, 54(3):521 – 537, 1995.

[11] Michael Smith, Alexander Smits, and Richard Miles. Compressible boundary-layer density cross sections by uv rayleigh scattering. *Opt. Lett.*, 14(17):916–918, Sep 1989.

[12] Robert L Johnson. Numerical simulation of tomographic reconstruction for the study of turbulence using optical wavefront sensor measurements. *Air Force Interim Report*, 1, 1993.

[13] Bryon L Pedersen. Experimental verification of tomographic reconstruction of turbulent air flow structure using optical wavefront measurements. Technical report, DTIC Document, 1993.

[14] L McMackin, B Masson, N Clark, K Bishop, R Pierson, and E Chen. Hartmann wave front sensor studies of dynamic organized structure in flowfields. *AIAA journal*, 33(11):2158–2164, 1995.

[15] L Venkatakrishnan and G E A Meier. Density measurement using the background oriented schlieren. *Experiments in Fluids*, 37:237–247, 2004.

[16] Bradley Atcheson, Ivo Ihrke, Wolfgang Heidrich, Art Tevs, Derek Bradley, Marcus Magnor, and Hans-Peter Seidel. Time-resolved 3d capture of non-stationary gas flows. In *ACM transactions on graphics (TOG)*, volume 27, page 132. ACM, 2008.

[17] Masanori Ota, Kenta Hamada, Hiroko Kato, and Kazuo Maeno. Computed-tomographic density measurement of supersonic flow field by colored-grid background oriented schlieren (cgbos) technique. *Measurement Science and Technology*, 22(10):104011, 2011.

[18] Gordon Wetzstein, Ramesh Raskar, and Wolfgang Heidrich. Hand-held schlieren photography with light field probes. In *Computational Photography (ICCP), 2011 IEEE International Conference on*, pages 1–8. IEEE, 2011.

[19] Marc Levoy, Ren Ng, Andrew Adams, Matthew Footer, and Mark Horowitz. Light field microscopy. *ACM Transactions on Graphics (TOG)*, 25(3):924–934, 2006.

[20] Kyle Lynch, Tim Fahringer, and Brian Thurow. Three-dimensional particle image velocimetry using a plenoptic camera. In *50th AIAA Aerospace Sciences Meeting*, 2012.

[21] Alan C Eckbreth. *Laser diagnostics for combustion temperature and species*, volume 3. CRC Press, 1996.

[22] R. Miles and W. Lempert. Two-dimensional measurement of density, velocity, and temperature in turbulent high-speed air flows by uv rayleigh scattering. *Applied Physics B*, 51(1):1–7, 1990.

[23] K. Fiedler, O. Sieber, and C. Jakiel. Quantitative density measurements by rayleigh scattering behind a plane turbine cascade. *AIAA Journal*, 35(8):1303–1308, Aug 1997.

[24] J. Panda and R. G. Seasholtz. Measurement of shock structure and shockvortex interaction in underexpanded jets using rayleigh scattering. *Physics of Fluids (1994-present)*, 11(12), 1999.

[25] Amy Mielke, Kristie Elam, and C Sung. Rayleigh scattering diagnostic for measurement of temperature, velocity, and density fluctuation spectra. In *44th AIAA Aerospace Sciences Meeting and Exhibit*, pages 9–12, 2006.

[26] RichardB. Miles and DanielM. Nosenchuck. Three-dimensional quantitative flow diagnostics. In Mohamed Gad-el Hak, editor, *Advances in Fluid Mechanics Measurements*, volume 45 of *Lecture Notes in Engineering*, pages 33–107. Springer Berlin Heidelberg, 1989.

[27] N. J. Dam, M. Rodenburg, R. A. L. Tolboom, G. G. M. Stoffels, P. M. Huisman-Kleinherenbrink, and J. J. ter Meulen. Imaging of an underexpanded nozzle flow by uv laser rayleigh scattering. *Experiments in Fluids*, 24(2):93–101, 1998.

[28] M Carla Escoda and Marshall B Long. Rayleigh scattering measurements of the gas concentration field in turbulent jets. *AIAA Journal*, 21(1):81–84, 1983.

[29] P. E. DIMOTAKIS, H. J. CATRAKIS, and D. C. FOURGUETTE. Flow structure and optical beam propagation in high-reynolds-number gas-phase shear layers and jets. *Journal of Fluid Mechanics*, null:105–134, 4 2001.

[30] John W. Daily. Laser induced fluorescence spectroscopy in flames. *Progress in Energy and Combustion Science*, 23(2):133 – 199, 1997.

[31] G.A Massey and C. Lemon. Feasibility of measuring temperature and density fluctuations in air using laser-induced o2fluorescence. *Quantum Electronics, IEEE Journal of*, 20(5):454–457, May 1984.

[32] F. Lemoine and B. Leporcq. An efficient optical pressure measurement in compressible flows: Laser-induced iodine fluorescence. *Experiments in Fluids*, 19(3):150–158, 1995.

[33] K.P. Gross, R.L. McKenzie, and P. Logan. Measurements of temperature, density, pressure, and their fluctuations in supersonic turbulence using laser-induced fluorescence. *Experiments in Fluids*, 5(6):372–380, 1987.

[34] A. Lozano, B. Yip, and R.K. Hanson. Acetone: a tracer for concentration measurements in gaseous flows by planar laser-induced fluorescence. *Experiments in Fluids*, 13(6):369–376, 1992.

[35] J. Z. Reid, K. P. Lynch, and B. S. Thurow. Density measurements of a turbulent wake using acetone planar laser-induced fluorescence. *AIAA Journal*, 51(4):829–839, 2013.

[36] DW Sweeney and CM Vest. Reconstruction of three-dimensional refractive index fields from multidirectional interferometric data. *Applied Optics*, 12(11):2649–2664, 1973.

[37] RJ Santoro, HG Semerjian, PJ Emmerman, and R Goulard. Optical tomography for flow field diagnostics. *International Journal of Heat and Mass Transfer*, 24(7):1139–1150, 1981.

[38] John K Kittleson and Yung H Yu. Transonic rotor flow-measurement technique using holographic interferometry. *Journal of the American Helicopter Society*, 30(4):3–10, 1985.

[39] Keith E Bennett, Gregory W Faris, and Robert L Byer. Experimental optical fan beam tomography. *Applied optics*, 23(16):2678–2685, 1984.

[40] Gregory W Faris and Robert L Byer. Quantitative optical tomographic imaging of a supersonic jet. *Optics letters*, 11(7):413–415, 1986.

[41] Ray Snyder and Lambertus Hesselink. Measurement of mixing fluid flows with optical tomography. *Optics letters*, 13(2):87–89, 1988.

[42] Wolgang Merzkirch. *Flow visualization*. Elsevier, 2012.

[43] T. Asanuma. *Flow Visualization: Proceedings of the International Symposium on Flow Visualization*. Series in thermal and fluids engineering. Hemisphere Publishing Corporation, 1977.

[44] Eric P Magee and Byron M Welsh. Characterization of laboratory-generated turbulence by optical phase measurements. *Optical Engineering*, 33(11):3810–3817, 1994.

[45] Slavica Ristić. Flow visualization techniques in wind tunnels–optical methods (part ii). *Scientific Technical Review, ISSN*, 206:2007, 1820.

[46] Christian Söller, R Wenskus, P Middendorf, GEA Meier, and F Obermeier. Interferometric tomography for flow visualization of density fields in supersonic jets and convective flow. *Applied optics*, 33(14):2921–2932, 1994.

[47] Daniel W Jewell. Flow visualization of a turbulent shear flow using an optical wavefront sensor. Technical report, DTIC Document, 1994.

[48] B C Platt and R Shack. History and principles of shack-hartmann wavefront sensing. *Journal of refractive surgery Thorofare NJ 1995*, 17(5):S573–S577, 2003.

[49] Costin Curatu, George Curatu, and Jannick Rolland. Fundamental and specific steps in shack-hartmann wavefront sensor design. pages 628801–628801–9, 2006.

[50] L. McMackin, J. B. Wissler, N. Clark, E. Chen, K. Bishop, and R. Pierson. Hartmann sensor and dynamic tomographical analysis of organized structure in flow fields. *NASA STI/Recon Technical Report N*, 96:11369, June 1994.

[51] Lenore McMackin, Ronald Hugo, R Pierson, and C Truman. High speed optical tomography system for imaging dynamic transparent media. *Optics express*, 1(11):302–311, 1997.

[52] Robert E Pierson, Ellen Y Chen, Kenneth P Bishop, and Lenore J McMackin. Modeling and measurement of optical turbulence by tomographic imaging of a heated air flow. In *SPIE's 1996 International Symposium on Optical Science, Engineering, and Instrumentation*, pages 130–141. International Society for Optics and Photonics, 1996.

[53] Ronald J Hugo and Lenore J McMackin. Conditionally sampled two-dimensional optical wavefront measurements in the near-nozzle region of a heated axisymmetric jet. In *SPIE's 1996 International Symposium on Optical Science, Engineering, and Instrumentation*, pages 50–61. International Society for Optics and Photonics, 1996.

[54] Robert E Pierson, Ellen Y Chen, Kenneth P Bishop, and L McMackin. Evaluating effective resolution of an optical tomographic imaging system using a narrow-band correlation metric. In *Image Processing, 1996. Proceedings., International Conference on*, volume 3, pages 535–538. IEEE, 1996.

[55] L McMackin, RJ Hugo, KP Bishop, EY Chen, RE Pierson, and CR Truman. High speed optical tomography system for quantitative measurement and visualization of dynamic features in a round jet. *Experiments in fluids*, 26(3):249–256, 1999.

[56] G.E. Elsinga, B.W. van Oudheusden, F. Scarano, and D.W. Watt. Assessment and application of quantitative schlieren methods: Calibrated color schlieren and background oriented schlieren. *Experiments in Fluids*, 36(2):309–325, 2004.

[57] Louis W Ehrlich. An ad hoc {SOR} method. *Journal of Computational Physics*, 44(1):31 – 45, 1981.

[58] L. Venkatakrishnan. Density measurements in an axysimmetric underexpanded jet using background oriented schlieren technique. *AIAA Journal*, 43(7):1574–1579, 2005.

[59] L. Venkatakrishnan and P. Suriyanarayanan. Density field of supersonic separated flow past an afterbody nozzle using tomographic reconstruction of bos data. *Experiments in Fluids*, 47(3):463–473, 2009.

[60] Kai Berger, Ivo Ihrke, Bradley Atcheson, Wolfgang Heidrich, Marcus A Magnor, et al. Tomographic 4d reconstruction of gas flows in the presence of occluders. In *VMV*, pages 29–36, 2009.

[61] Kai Berger, Kai Ruhl, Mark Albers, Y Schroder, Alexander Scholz, J Kokemuller, Stefan Guthe, and M Magnor. The capturing of turbulent gas flows using multiple kinects. In *Computer Vision Workshops (ICCV Workshops), 2011 IEEE International Conference on*, pages 1108–1113. IEEE, 2011.

[62] H Richard and M Raffel. Principle and applications of the background oriented schlieren (bos) method. *Measurement Science and Technology*, 12(9):1576, 2001.

[63] H. Richard, M. Raffel, M. Rein, J. Kompenhans, and G.E.A. Meier. Demonstration of the applicability of a background oriented schlieren (bos) method. In *Laser Techniques for Fluid Mechanics*, pages 145–156. Springer Berlin Heidelberg, 2002.

[64] G. E. A. Meier. Hintergrund schlierenmessverfahren. *Deutsche Patentanmeldung*, DE 199 42 856 A1, 1999.

[65] M. Raffel, C.E. Willert, S.T. Wereley, and J. Kompenhans. *Particle Image Velocimetry: A Practical Guide.* Experimental Fluid Mechanics. Springer, 2007.

[66] R.J. Adrian and J. Westerweel. *Particle Image Velocimetry*. Cambridge University Press, 2011.

[67] M. Raffel, H. Richard, and G. E. A. Meier. On the applicability of background oriented optical tomography for large scale aerodynamic investigations. *Experiments in Fluids*, 28(5):477–481, 2000.

[68] O.K. Sommersel, D. Bjerketvedt, S.O. Christensen, O. Krest, and K. Vaagsaether. Application of background oriented schlieren for quantitative measurements of shock waves from explosions. *Shock Waves*, 18(4):291–297, 2008.

[69] G. Meier. Computerized background-oriented schlieren. *Experiments in Fluids*, 33(1):181–187, 2002.

[70] Erik Goldhahn and Jrg Seume. The background oriented schlieren technique: sensitivity, accuracy, resolution and application to a three-dimensional density field. *Experiments in Fluids*, 43(2-3):241–249, 2007.

[71] YuXin Zhao, ShiHe Yi, LiFeng Tian, Lin He, and ZhongYu Cheng. An experimental study of aero-optical aberration and dithering of supersonic mixing layer via bos. *Science China Physics, Mechanics and Astronomy*, 53(1):81–94, 2010.

[72] O.A. Yevtikhiyeva, N.M. Skornyakova, and A.V. Udalov. An investigation of the error of the background schlieren method. *Measurement Techniques*, 52(12):1300–1305, 2009.

[73] Ardian B. Gojani and Shigeru Obayashi. Assessment of some experimental and image analysis factors for background-oriented schlieren measurements. *Appl. Opt.*, 51(31):7554–7559, Nov 2012.

[74] Michael J. Hargather and Gary S. Settles. A comparison of three quantitative schlieren techniques. *Optics and Lasers in Engineering*, 50(1):8 – 17, 2012. Advances in Flow Visualization.

[75] Klinge, T. F., Kirmse, and J. Kompenhans. Application of quantitative background oriented schlieren (bos): investigation of a wing tip vortex in a transonic wind tunnel. In *PSFVIP 4, is the Fourth Symopsium on Flow Visualization and Image Processing*, June 2003.

[76] W. Merzkirch. *Flow Visualization*. Academic Press, 1987.

[77] R. Goldstein. *Fluid Mechanics Measurements, Second Edition*. Taylor & Francis, 1996.

[78] Frank Träger. *Springer handbook of lasers and optics*. Springer Science & Business Media, 2007.

[79] R. Kingslake. *Optics in Photography*. Press Monographs. SPIE Optical Engineering Press, 1992.

[80] Robert L. Cook and Tony DeRose. Wavelet noise. *ACM Trans. Graph.*, 24:803–811, July 2005.

[81] R.T. Frankot and R. Chellappa. A method for enforcing integrability in shape from shading algorithms. *Pattern Analysis and Machine Intelligence, IEEE Transactions on*, 10(4):439–451, Jul 1988.

[82] Farid U. Dowla, James M. Brase, Scot S. Olivier, and Charles A. Thompson. Fast fourier and wavelet transforms for wavefront reconstruction in adaptive optics, 2000.

[83] Tiangong Wei and Reinhard Klette. Regularization method for depth from noisy gradient vector fields. *Technical Report 115*, 45:7, 2002.

[84] Lisa A. Poyneer, Donald T. Gavel, and James M. Brase. Fast wave-front reconstruction in large adaptive optics systems with use of the fourier transform. *J. Opt. Soc. Am. A*, 19(10):2100–2111, Oct 2002.

[85] W. H. Southwell. Wave-front estimation from wave-front slope measurements. *J. Opt. Soc. Am.*, 70(8):998–1006, Aug 1980.

[86] Thomas Brox, Andrs Bruhn, Nils Papenberg, and Joachim Weickert. High accuracy optical flow estimation based on a theory for warping. In Toms Pajdla and Ji Matas, editors, *Computer Vision - ECCV 2004*, volume 3024 of *Lecture Notes in Computer Science*, pages 25–36. Springer Berlin Heidelberg, 2004.

[87] A Gershun. The light field. *trans. by Moon, P., and Timoshenko, G., Journal of Math and Physics*, 18:51–151, 1939.

[88] James T Kajiya. The rendering equation. In *ACM Siggraph Computer Graphics*, volume 20, pages 143–150. ACM, 1986.

[89] Edward H Adelson and James R Bergen. The plenoptic function and the elements of early vision. *Computational models of visual processing*, 1(2):3–20, 1991.

[90] Edward H Adelson and John Y. A. Wang. Single lens stereo with a plenoptic camera. *IEEE transactions on pattern analysis and machine intelligence*, 14(2):99–106, 1992.

[91] Ren Ng, Marc Levoy, Mathieu Brédif, Gene Duval, Mark Horowitz, and Pat Hanrahan. Light field photography with a hand-held plenoptic camera. *Computer Science Technical Report CSTR*, 2(11), 2005.

[92] Ren Ng. *Digital light field photography*. PhD thesis, stanford university, 2006.

[93] Kyle Lynch. Development of a 3-d fluid velocimetry technique based on light field imaging. 2011.

[94] Timothy W Fahringer and Brian S Thurow. Tomographic reconstruction of a 3-d flow field using a plenoptic camera. In *42nd AIAA Fluid Dynamics Conference and Exhibit*, volume 2826, 2012.

[95] Parry Moon and Domina Eberle Spencer. The photic field. *Cambridge, MA, MIT Press, 1981. 265 p.*, 1, 1981.

[96] Marc Levoy and Pat Hanrahan. Light field rendering. In *Proceedings of the 23rd annual conference on Computer graphics and interactive techniques*, pages 31–42. ACM, 1996.

[97] Steven J Gortler, Radek Grzeszczuk, Richard Szeliski, and Michael F Cohen. The lumigraph. In *Proceedings of the 23rd annual conference on Computer graphics and interactive techniques*, pages 43–54. ACM, 1996.

[98] Jingyi Yu and Leonard McMillan. General linear cameras. In *Computer Vision-ECCV 2004*, pages 14–27. Springer, 2004.

[99] Jeffrey T Bolan, Kyle C Johnson, and Brian S Thurow. Enhanced imaging of reacting flows using 3d deconvolution and a plenoptic camera. 2014.

[100] L.D. Stroebel, J. Compton, I. Current, and R. Zakia. *Photographic materials and processes*. Focal Press, 1986.

[101] Jeffrey T Bolan, Kyle C Johnson, and Brian S Thurow. Preliminary investigation of three-dimensional flame measurements with a plenoptic camera. 2014.

[102] http://imperx.com/ccd-cameras/, march 22, 2015.

[103] Steve Webb. Historical experiments predating commercially available computed tomography*. *The British journal of radiology*, 65(777):835–837, 1992.

[104] Avinash C Kak and Malcolm Slaney. *Principles of computerized tomographic imaging*, volume 33. Siam, 1988.

[105] Lawrence A Shepp and Yehuda Vardi. Maximum likelihood reconstruction for emission tomography. *Medical Imaging, IEEE Transactions on*, 1(2):113–122, 1982.

[106] Charles L Byrne. Iterative image reconstruction algorithms based on cross-entropy minimization. *Image Processing, IEEE Transactions on*, 2(1):96–103, 1993.

[107] Charles L Byrne. Block-iterative methods for image reconstruction from projections. *IEEE transactions on image processing: a publication of the IEEE Signal Processing Society*, 5(5):792–794, 1995.

[108] A.J. Rockmore and A. Macovski. A maximum likelihood approach to emission image reconstruction from projections. *Nuclear Science, IEEE Transactions on*, 23(4):1428–1432, Aug 1976.

[109] H Malcolm Hudson and Richard S Larkin. Accelerated image reconstruction using ordered subsets of projection data. *Medical Imaging, IEEE Transactions on*, 13(4):601–609, 1994.

[110] Charles L Byrne. Accelerating the emml algorithm and related iterative algorithms by rescaled block-iterative methods. *Image Processing, IEEE Transactions on*, 7(1):100–109, 1998.

[111] Charles Byrne. Iterative algorithms for deblurring and deconvolution with constraints. *Inverse Problems*, 14(6):1455, 1998.

[112] Edward J Hoffman, Sung-Cheng Huang, Michael E Phelps, and David E Kuhl. Quantitation in positron emission computed tomography: 4. effect of accidental coincidences. *Journal of computer assisted tomography*, 5(3):391–400, 1981.

[113] Arthur P Dempster, Nan M Laird, and Donald B Rubin. Maximum likelihood from incomplete data via the em algorithm. *Journal of the royal statistical society. Series B (methodological)*, pages 1–38, 1977.

[114] Jeffrey A Fessler and Alfred O Hero. Space-alternating generalized expectation-maximization algorithm. *Signal Processing, IEEE Transactions on*, 42(10):2664–2677, 1994.

[115] Allan Macleod Cormack. Representation of a function by its line integrals, with some radiological applications. ii. *Journal of Applied Physics*, 35(10):2908–2913, 1964.

[116] Mark E Davison. The ill-conditioned nature of the limited angle tomography problem. *SIAM Journal on Applied Mathematics*, 43(2):428–448, 1983.

[117] A Caponnetto and M Bertero. Tomography with a finite set of projections: singular value decomposition and resolution. *Inverse problems*, 13(5):1191, 1997.

[118] Michael J Jackson, Daryl R Tweeton, and S Biilington. Seismic crosshole tomography using wavefront migration and fuzzy constraints: Application to fracture detection and characterization. *Ground Water Management*, 11:741–754, 1992.

[119] Dean Verhoeven. Limited-data computed tomography algorithms for the physical sciences. *Applied optics*, 32(20):3736–3754, 1993.

[120] Richard Gordon, Robert Bender, and Gabor T Herman. Algebraic reconstruction techniques (art) for three-dimensional electron microscopy and x-ray photography. *Journal of theoretical Biology*, 29(3):471–481, 1970.

[121] Gabor T Herman, Arnold Lent, and Stuart W Rowland. Art: mathematics and applications: a report on the mathematical foundations and on the applicability to real data of the algebraic reconstruction techniques. *Journal of Theoretical Biology*, 42(1):1–32, 1973.

[122] Peter Gilbert. Iterative methods for the three-dimensional reconstruction of an object from projections. *Journal of theoretical biology*, 36(1):105–117, 1972.

[123] Richard Gordon. A tutorial on art (algebraic reconstruction techniques). *Nuclear Science, IEEE Transactions on*, 21(3):78–93, 1974.

[124] AH Andersen and Avinash C Kak. Simultaneous algebraic reconstruction technique (sart): a superior implementation of the art algorithm. *Ultrasonic imaging*, 6(1):81–94, 1984.

[125] Yair Censor. Finite series-expansion reconstruction methods. *Proceedings of the IEEE*, 71(3):409–419, 1983.

[126] A Lent. A convergent algorithm for maximum entropy image restoration with a medical x-ray application. In *Proceedings of the Society of Photographic Scientists and Engineers Conference*, pages 238–243. SPSE, 1977.

[127] Gabor T Herman. *Application of maximum entropy and Bayesian optimization methods to image reconstruction from projections*. Springer, 1985.

[128] Cristian Badea and Richard Gordon. Experiments with the nonlinear and chaotic behaviour of the multiplicative algebraic reconstruction technique (mart) algorithm for computed tomography. *Physics in medicine and biology*, 49(8):1455, 2004.

[129] G. E. Elsinga, F. Scarano, B. Wieneke, and B. W. van Oudheusden. Tomographic particle image velocimetry. *Experiments in Fluids*, 41:933–947.

[130] Don Williams and Peter D. Burns. Diagnostics for digital capture using mtf, 2001.

[131] Norman B Nill. Conversion between sine wave and square wave spatial frequency response of an imaging system. Technical report, DTIC Document, 2001.

[132] R. V. Shack. Characteristics of an image-forming system. *Journal of Research of the National Bureau of Standards*, 56(5):245–260, 1956.

[133] BERGE TATIAN. Method for obtaining the transfer function from the edge response function. *J. Opt. Soc. Am.*, 55(8):1014–1019, Aug 1965.

[134] RICHARD BARAKAT. Determination of the optical transfer function directly from the edge spread function. *J. Opt. Soc. Am.*, 55(10):1217–1219, Oct 1965.

[135] R. M. Simonds. Two-dimensional modulation transfer functions of image scanning systems. *Appl. Opt.*, 20(4):619–622, Feb 1981.

[136] Peter D. Burns. Slanted-edge mtf for digital camera and scanner analysis, 2000.

[137] Stephen E. Reichenbach, Stephen K. Park, and Ramkumar Narayanswamy. Characterizing digital image acquisition devices. *Optical Engineering*, 30(2):170–177, 1991.

[138] Ali J Tabatabai and O Robert Mitchell. Edge location to subpixel values in digital imagery. *Pattern Analysis and Machine Intelligence, IEEE Transactions on*, (2):188–201, 1984.

[139] Edward M Mikhail, Mark L Akey, and OR Mitchell. Detection and sub-pixel location of photogrammetric targets in digital images. *Photogrammetria*, 39(3):63–83, 1984.

[140] M. Mazumdar, B. K. Sinha, and C. C. Li. Comparison of several estimates of edge point in noisy digital data across a step edge. In *Proc. Conf. on Computer Vision and Pattern Recognition*, page 2733. IEEE, 1985.

[141] Conversion between sine wave and square wave spatial frequency response of an imaging system. Technical report.

[142] Sine m-13-60-rm, applied image inc., 1653 east main street, rochester, ny 14609 usa. Technical report.

[143] http://www.mae.virginia.edu/arl/facilities.php. Technical report.

[144] Lutz Falkenhagen. Depth estimation from stereoscopic image pairs assuming piecewise continuos surfaces. In *Image Processing for Broadcast and Video Production*, pages 115–127. Springer, 1995.

[145] Karsten Mühlmann, Dennis Maier, Jürgen Hesser, and Reinhard Männer. Calculating dense disparity maps from color stereo images, an efficient implementation. *International Journal of Computer Vision*, 47(1-3):79–88, 2002.

[146] M. Okutomi and T. Kanade. A multiple-baseline stereo. *IEEE Trans. Pattern Anal. Mach. Intell.*, 15(4):353–363, April 1993.

[147] Frederik Huguet and Frédéric Devernay. A variational method for scene flow estimation from stereo sequences. In *Computer Vision, 2007. ICCV 2007. IEEE 11th International Conference on*, pages 1–7. IEEE, 2007.

[148] Takeo Kanade, Hiroshi Kano, Shigeru Kimura, Atsushi Yoshida, and Kazuo Oda. Development of a video-rate stereo machine. In *Intelligent Robots and Systems 95.'Human Robot Interaction and Cooperative Robots', Proceedings. 1995 IEEE/RSJ International Conference on*, volume 3, pages 95–100. IEEE, 1995.

[149] William Hoff and Narendra Ahuja. Surfaces from stereo: Integrating feature matching, disparity estimation, and contour detection. *Pattern Analysis and Machine Intelligence, IEEE Transactions on*, 11(2):121–136, 1989.

[150] Charles V Stewart, Robin Y Flatland, and Kishore Bubna. Geometric constraints and stereo disparity computation. *International Journal of Computer Vision*, 20(3):143–168, 1996.

[151] Takeo Kanade and Masatoshi Okutomi. A stereo matching algorithm with an adaptive window: Theory and experiment. *Pattern Analysis and Machine Intelligence, IEEE Transactions on*, 16(9):920–932, 1994.

[152] Andrea Fusiello, Vito Roberto, and Emanuele Trucco. Efficient stereo with multiple windowing. In *2013 IEEE Conference on Computer Vision and Pattern Recognition*, pages 858–858. IEEE Computer Society, 1997.

[153] Trina D Russ and Anthony P Reeves. High accuracy depth measurement using multi-view stereo. In *proceedings of International Conference on Vision Interface, VI*, pages 103–110, 1999.

[154] John D Anderson. *Modern compressible flow: with historical perspective*. McGraw Hill Higher Education, 1990.